IMPROVEMENTS OF RENEWABLE ENERGY: CAVITATION TREATMENT AND OPTIMIZATION OF HYBRID SYSTEM FOR REMOTE AREAS

by

Mohammad D. Qandil

A Dissertation Submitted in

Partial Fulfillment of the

Requirements for the Degree of

Doctor of Philosophy

in Engineering

at

The University of Wisconsin-Milwaukee

August 2021

ABSTRACT

IMPROVEMENTS OF RENEWABLE ENERGY: CAVITATION TREATMENT AND OPTIMIZATION OF HYBRID SYSTEM FOR REMOTE AREAS

by

Mohammad D. Qandil

The University of Wisconsin-Milwaukee, 2021
Under the Supervision of Professor Ryoichi S. Amano

The optimization of turbines hydrofoils is to improve the efficiency and lifetime of the hydro turbines. Air treatment is one of the methods to reduce the cavitation effect and improve hydro turbines performance. It is necessary to utilize Computational Fluid Dynamics (CFD) analysis and to generate cavitation at different Angle of Attack (AoA) for the hydrofoil and test a variety of designs of air injection slots through the hydrofoil to optimize the best design. StarCCM+ software is used for CFD simulations. The hydrofoil is tested in a square water tunnel with water entering the tunnel at different velocities for each AoA ranges from 9.1 m/s to 12.2 m/s. While the cavitation can be identified by a unique number (Averaged Vapor Volume Fraction), the work done created an inverse correlation between this number and the cavitation number at the same AoA. The validation and comparison were accomplished through three steps: visual validation, CFD simulation results, and image processing. The VVF scenes and high-speed camera images were compared and validated, visually, the cavitation behavior and pattern. The image processing confirmed the percentages of the cavitation area, numerically and experimentally, with almost matching values.

The cavitation behavior was observed first without aeration, then followed by air injection simulations to investigate the effect of aeration. The air was introduced at 101.3 kPa (0 psig) at AoA of 0, 6, 9, and 12 degrees. The Vapor Volume Fraction (VVF) and the output mechanical power were monitored throughout the simulations. The data acquired from the simulations were compared for both 6 and 3 air slots over the hydrofoil. It was observed that the cavitation was mitigated in the computer simulations reaching up to 97.9% as an average reduction for the 6 air slots, while the 3 air slots case was reduced by 93%.

Using fossil fuels as the primary way to generate electricity causes a significant effect on the environment. In 2019 more than 64% of the electricity in the United States of America was generated using fossil fuel resources, while renewable energy (RE) resources contributed to only 17% of the U.S. electricity generation for the same year. Due to the complex terrain distribution of many states in the U.S., a massive opportunity of utilizing RE resources in rural and remote areas can reduce the cost of electrical grid installation for such areas. In this study, a typical residential building with an average energy utilization of 30.25 kWh/day with a demand peak of 5.34 kW was considered a case study in each state to optimize a hybrid RE system and find the best alternative electrical grid system. This study presents the best configuration between Solar and Wind energy with different types of energy storage. It was discovered that the photovoltaic (PV) solar panels - diesel generator with battery best services in all states. The daily radiation and diesel prices substantially affect the Levelized Cost of Energy (COE) values in each state.

A remote residential building, commercial building, and industrial facility having different load profiles were considered as the case studies' loads. The load profile for each case was found to have a substantial effect on how the system's power produced a scheme. For the residential building, PV panels contributed more than 75% of the total power production for some cases, the

contribution reduced for the commercial building case study to 65% and dropped for the industrial facility case to almost 35%. Different fuel source (natural gas) for the generator was considered in the third-round simulations. It was found that the natural gas generator which has a lower installation and running cost than the diesel generator, reduces the net present cost, the COE, PV size, and the number of batteries at all states.

TABLE OF CONTENTS

TABLE OF CONTENTS vi

LIST OF FIGURES xi

LIST OF TABLES xvi

LIST OF NOMENCLATURE xvii

ACKNOWLEDGMENTS xx

Chapter 1 : Introduction 1

1.1 Renewable Energy 1

1.1.1 Photovoltaic Technology 3

1.1.2 Wind Energy 4

1.1.3 Hydropower 5

1.1.4 Renewable energy in the U.S. 5

1.2 Hydrofoils 7

1.3 Cavitation Phenomenon 8

1.4 Problem Statement 13

1.4.1 Cavitation Treatment 13

1.4.2 Optimization for a hybrid renewable system 14

Chapter 2 : Literature Review 16

2.1 Cavitation in Hydraulic System 16

2.1.1 Cavitation Treatment 18

2.2 Hybrid micro-grid 20

Chapter 3 : Cavitation Treatment 25

3.1 Research Outline 25

3.2 Methodology 25

3.2.1 The Geometry of Hydrofoil and Water Tunnel 25

3.2.2 Flow Physical Equation 26

3.2.3 Creating Mesh and Physical Parameters 28

3.3 Experimental Work 29

3.3.1 Constraints 29

3.3.2 Setup Configuration 31

3.3.3 Instrumentation 36

3.3.3.1 Ultimaker 2+ 36

3.3.3.2 Flow Meters 37

3.3.3.3 Variable Speed Driven Pump 38

3.3.3.4 FASTCAM Mini UX50 39

3.4 Results 40

3.4.1 Mesh Independent Study 40

3.4.2 CFD Validation 44

3.4.3 CFD – Experimental Validation Results 45

3.4.4 Correlations of VVF and The Cavitation Number (σ) 51

3.5 Cavitation Treatment Simulations 61
3.5.1 Modified New Hydrofoil Design 61
3.5.2 Simulations Without Aeration 62
3.5.3 Air Injection Simulations 63
3.5.4 CFD Results: Constant Water Inlet Velocity 63
3.5.4.1 Case 1: No Aeration 63
3.5.4.2 Case 2: 0 PSI with 6 Air Injection Slots 66
3.5.4.3 Effect of Air 70
3.5.4.4 Case 3: 0 PSI with 3 Air Injection Slots 72
3.5.5 Results Comparison 73
Chapter 4 : Optimization of Hybrid Systems in Remote Areas 78
4.1 Introduction 78
4.2 HOMER Software 78
4.3 Sites Overview 79
4.3.1 Load Profile 80
4.3.2 Solar Irradiation 82
4.3.3 Wind Speed 83
4.4 Hybrid System Components 84
4.4.1 Diesel Generator 85
4.4.2 Photovoltaic Array 86

4.4.3 Wind Turbine 90
4.4.4 Battery 92
4.4.5 Converter 93
4.4.6 Economical Aspects and Constraints 94
4.4.7 Summary 96
4.5 Optimization Results 97
4.5.1 System Configuration 97
4.5.2 Cost Summary 101
4.5.3 Electrical Aspects 102
4.5.4 Results Comparison 103
4.5.5 CO_2 Emission 106
4.6 Different Scenarios 107
4.6.1 Sensitivity Analysis 107
4.6.2 Different Applications 110
4.6.3 Fuels of the Generator 118
Chapter 5 : Conclusions and Future Work Recommendations 119
5.1 Research Conclusions 119
5.1.1 Conclusions of the Cavitation Characteristics 119
5.1.2 Conclusions of the Cavitation Treatment Simulations 120
5.1.3 Conclusion of the Hybrid Systems Optimization in Remote Areas 121

5.2 Future Work Recommendations 123

5.2.1 Recommendation for the Cavitation Treatment 123

5.2.2 Recommendation for the Hybrid System 123

References 125

Appendices 143

Appendix A: Sites Data 143

Appendix B: Electrical production for each stat at 2018 diesel price, 1.0 PV cost multiplier, and 1.0 wind turbine cost multiplier for Home application 145

Appendix C: Emissions outputs for each stat at 2018 diesel price, 1.0 PV cost multiplier and 1.0 wind turbine cost multiplier for Home application 149

Appendix D: Electrical production for each stat at 2018 diesel price, 1.0 PV cost multiplier, and 1.0 wind turbine cost multiplier for Commercial building application 154

Appendix E: Emissions outputs for each stat at 2018 diesel price, 1.0 PV cost multiplier and 1.0 wind turbine cost multiplier for Commercial building application 158

Appendix F: Electrical production for each stat at 2018 diesel price, 1.0 PV cost multiplier, and 1.0 wind turbine cost multiplier for Industrial facility application 163

Appendix G: Emissions outputs for each stat at 2018 diesel price, 1.0 PV cost multiplier and 1.0 wind turbine cost multiplier for Industrial facility application 167

Curriculum Vitae 172

LIST OF FIGURES

Figure 1: Estimated RE share of global electricity production, end-2019 [3] 2

Figure 2: RE capacity and growth rate in the last decade [3] 2

Figure 3: The daily wind cycle [8] 4

Figure 4: RE share of U.S. electricity production, end-2019 [13] 6

Figure 5: RE generation in U.S. electricity generation, 1950-2019 [13] 7

Figure 6: Percentage of annual RE production per country [4] 7

Figure 7: Phase change in the pressure-temperature diagram [16] 9

Figure 8: Localized cavitation damage on a pump blade [19] 10

Figure 9: Severe cavitation erosion as witnessed on a Francis turbine [20] 10

Figure 10: Severe cavitation erosion as witnessed on a Francis turbine [22] 11

Figure 11: Cavitation cloud as seen on the suction side of a hydrofoil [24] 12

Figure 12: Sheet cavitation observed on the suction side of a hydrofoil [25] 13

Figure 13: CAD model for NACA 66-012 hydrofoil 26

Figure 14: CAD model for water tunnel 26

Figure 15: Experimental setup 32

Figure 16: (a) Upper tank (b) Ball valve installed on the downpipe 32

Figure 17: CAD model for the new set-up design 33

Figure 18: Water tunnel CAD model 33

Figure 19: Experimental setup of the water tunnel: (a) The whole setup. (b) 15.2 cm circle pipe to an 8 cm square section Nozzle. (c) 8 cm square straightener. (d) 8 cm square section to a 15.2 cm circle pipe Diffuser. (e) 8x8 cm square straight water tunnel. (f) Hydrofoil 35

Figure 20: The 3D printed NACA66-012 hydrofoil for the experimental testing 36

Figure 21: Ultimaker 2+ 3D printer 37

Figure 22: Flowmeters installed on the filling and overflow lines 38

Figure 23: Pump-motor set and VSD 39

Figure 24: High-speed camera 40

Figure 25: Mesh scene of the whole simulation domain 40

Figure 26: Mesh scene for the entire system at 3.8 million cells and 12 prism layers 42

Figure 27: Mesh scene around the hydrofoil at 3.8 million cells and 12 prism layers 43

Figure 28: Mean of wall y+ values at the hydrofoil 43

Figure 29: Mean of convective Courant number nearby the hydrofoil 43

Figure 30: Comparison of coefficients of drag for 0 and 9 AoA 44

Figure 31: Comparison of coefficients of lift for 0 and 9 AoA 45

Figure 32: Visual comparison no aeration 9 AoA : (a) experimental (b) CFD VVF scene .. 46

Figure 33: Experimental image processing for 9 AoA at 18.3 m/s water inlet velocity: (a) original image, (b) enhanced contrast, (c) binary converted image 48

Figure 34: CFD image processing for 9 AoA at 18.3 m/s water inlet velocity: (a) original image, (b) grayscale converted image, (c) binary converted image 49

Figure 35: 12 AoA at 18.3 m/s water inlet velocity case image processing: (a) experimental binary image, (b) CFD binary image 50

Figure 36: VVF around hydrofoil at different cavitation number for 6 degrees AoA 52

Figure 37: Absolute pressure around hydrofoil at different cavitation number for 6 degrees AoA 53

Figure 38: Velocity Magnitude around the hydrofoil at cavitation number of 0.3 for (0,6,9 & 12) degrees AoA 54

Figure 39: Dependence of cavitation number vs Reynolds number 55

Figure 40: VVF at different cavitation number for (0, 6, 9 & 12) degrees AoA 56

Figure 41: Drag coefficient variation for different (σ) values at different AoA 57

Figure 42: Lift coefficient variation for different (σ) values at different AoA 57

Figure 43: Drag coefficient variation for different VVF values at different AoA 59

Figure 44: Lift coefficient variation for different VVF values at different AoA 59

Figure 45: Lift to drag ratio at different cavitation number for (0, 6, 9 & 12) degrees AoA 61

Figure 46: CAD model for modified NACA 661-012 hydrofoil with 6 air slots 62

Figure 47: VVF around hydrofoil – no aeration case at 22.8 m/s water inlet velocity for (0, 6, 9 & 12) degrees AoA 64

Figure 48: Absolute pressure CFD scenes – no aeration case at 22.8 m/s water inlet velocity for (0, 6, 9 & 12) degrees AoA 65

Figure 49: VVF around hydrofoil – 0 psi with 6 air slots case at 22.8 m/s water inlet velocity for (0, 6, 9 & 12) degrees AoA 68

Figure 50: Absolute pressure CFD scenes – 0 psi with 6 air slots case at 22.8 m/s water inlet velocity for (0, 6, 9 & 12) degrees AoA 69

Figure 51: Volume fraction distribution for air (right scenes), and water vapor (left scenes) around hydrofoil after 0.2s– 0 psi with 6 air slots case at 22.8 m/s water inlet velocity for (0, 6, 9 & 12) degrees AoA 71

Figure 52: CAD model for modified NACA 661-012 hydrofoil with 3 air slots 72

Figure 53: Absolute pressure – with aeration (on right) and without aeration (on left) cases at 22.8 m/s water inlet velocity for (0, 6, 9 & 12) degrees AoA 75

Figure 54: No aeration - VVF at different water velocity for (0, 6, 9 & 12) degrees AoA ... 75

Figure 55: 0 PSI - VVF at different water velocity for (0, 6, 9 & 12) degrees AoA 75

Figure 56: No aeration - Cavitation number at different water velocity for (0, 6, 9 & 12) degrees AoA..... 76

Figure 57: 0 PSI - Cavitation number at different water velocity for (0, 6, 9 & 12) degrees AoA..... 77

Figure 58: General scheme of a residential PV-Wind hybrid energy system 78

Figure 59: Topographic map of the United States [116] 80

Figure 60: Average electricity load for a typical home in each state [117]..... 81

Figure 61: Average daily load profile for a typical Commercial building in a Whole Year 82

Figure 62: Average daily load profile for a typical Industrial facility in a Whole Year 82

Figure 63: U.S. annual average solar GHI for 2017 [118]..... 83

Figure 64: U.S. Average wind speed per state for 2017 [119] 84

Figure 65: U.S. Average diesel price per state for 2018 [121]..... 86

Figure 66: PV's input window in HOMER 88

Figure 67: PV's azimuth and slope angles..... 89

Figure 68: Proposed wind turbine power curve [127]..... 91

Figure 69: Comparison between hybrid system batteries [130] 93

Figure 70: Operating reserve's input window in HOMER..... 95

Figure 71: Optimization results for the Wisconsin state case study 98

Figure 72: U.S. Average COE per state at 2018 diesel price, 1.0 PV cost multiplier, and 1.0 wind turbine cost multiplier for a typical Home..... 101

Figure 73: Cost summary window for Wisconsin case study 102

Figure 74: Monthly averaged electrical energy production for Wisconsin case study 103

Figure 75: COE, diesel price, and daily radiation for each state 105

Figure 76: OST with 1.0 PV cost multiplier for Wisconsin case study 108

Figure 77: OST with 0.5 PV cost multiplier for Wisconsin case study 108

Figure 78: OST with 1.0 PV cost multiplier for the Oregon case study 109

Figure 79: OST with 0.5 PV cost multiplier for the Oregon case study 109

Figure 80: OST with 1.0 PV cost multiplier for Texas case study..... 110

Figure 81: OST with 0.5 PV cost multiplier for Texas case study..... 110

Figure 82: U.S. Average COE per state at 2018 diesel price, 1.0 PV cost multiplier, and 1.0 wind turbine cost multiplier for a typical Commercial building..... 111

Figure 83: U.S. Average COE per state at 2018 diesel price, 1.0 PV cost multiplier, and 1.0 wind turbine cost multiplier for a typical Industrial facility 112

Figure 84: Cash flow summary for a Home case study for Wisconsin stateFigure 85: Cash flow summary for Commercial building case study for Wisconsin state 113

Figure 86: Cash flow summary for Industrial facility case study for Wisconsin state..... 114

Figure 87: DMap of the Generator for three applications in Wisconsin case study: a) Home b) Commercial building c) Industrial facility..... 117

Figure 88: Fuel Cell block diagram [136]..... 124

Figure 89: Diagram of an Electrolyzer cell and the basic principle of operation [137] 124

LIST OF TABLES

Table 1: Partial list of high-speed water tunnels around the world organized by mass flow rate..... 30

Table 2: Mesh independent test results..... 42

Table 3: No aeration case summary of CFD results..... 65

Table 4: 0 PSI with 6 air slots case summary of CFD results..... 70

Table 5: 0 PSI with 3 air slots case summary of CFD results..... 72

Table 6: Summarized input data..... 96

Table 7: System architecture for 2018 diesel price, 1.0 PV cost multiplier, and 1.0 wind turbine cost multiplier..... 99

Table 8: Comparison of three stats at 2018 diesel price, 1.0 PV cost multiplier and 1.0 wind turbine cost multiplier..... 104

Table 9: Electrical production for three stats at 2018 diesel price, 1.0 PV cost multiplier, and 1.0 wind turbine cost multiplier Home application..... 106

Table 10: Emissions outputs for three stats at 2018 diesel price, 1.0 PV cost multiplier and 1.0 wind turbine cost multiplier..... 107

Table 11: Electrical production for three stats at 2018 diesel price, 1.0 PV cost multiplier, and 1.0 wind turbine cost multiplier for different applications..... 115

Table 12: Comparison of three stats at 2018 fuel prices, 1.0 PV cost multiplier and 1.0 wind turbine cost multiplier for home application..... 118

LIST OF NOMENCLATURE

2D	Two dimensional
3D	Three dimensional
AoA	Angle of Attack
A	Plan area of the hydrofoil
AC	Air Conditioning
Ah	Ampere Hour
ASTM	American Society for Testing and Materials
COE	Levelized Cost of Energy
C	Rate of vapor collapse
CAD	Computer-aided design
CFD	Computational fluid dynamics
C_L	Lift coefficient
C_D	Drag coefficient
DC	Direct current
DOD	Depth of Discharge
EIA	Energy information administration
FC	Fuel Cell
GHI	Global Horizontal Solar Irradiance
GW	Gigawatts
GWC	Global Water Center
G	Rate of vapor generation
HOMER	Hybrid Optimization of Multiple Energy Resources
HPC	High-Performance Computing
HP	Horsepower
IEA	The International Energy Agency
LES	Large-Eddy Simulation
Li-Ion	Lithium-Ion
NACA	National Advisory Committee for Aeronautics
NOCT	Normal Operating Cell Temperature
NPC	Net Present Cost
NREL	National Renewable Energy Laboratory
OpenFOAM	Open Field Operation and Manipulation
OST	Optimal System Types

p	Local static pressure
PV	Photovoltaic
P_v	Vapor pressure at the given water temperature
P_s	Surrounding liquid pressure
R	Bubble radius
RANS	Reynolds Averaged Navier-Stokes
RE	Renewable Energy
Re	Reynolds Number
TSR	Tip Speed Ratio
u	Velocity component
u_{rf}	Reference frame velocity
URANS	Unsteady Reynolds average Navier-Stokes
U.S.	United States
v	Water velocity
VOF	Volume of fluid
VVF	Vapor Volume Fraction
VSD	Variable Speed Drive
WALE	Wall-adapting local-eddy

GREEK SYMBOLS

μ	Global phase dynamic viscosity
α_l	Phase volume fraction
σ	Cavitation number
φ	Source/sink term
ϕ	Fluid or flow property
ρ	Density, kg/m^3
ρ_l	Liquid phase density
∀	Volume
$\forall_c$	Volume in the cell

SUBSCRIPTS AND SUPERSCRIPTS

n	Total number of coexisted phases

LETTER-BASED SYMBOLS

$\vec{g}$	Gravitational acceleration

$\hat{t}$	Temporal cut-off value
$\widetilde{T}$	Favre-filtered static temperature
$\vec{u}$	Velocity vector
$\hat{x}$	Spatial cut-off value

ACKNOWLEDGMENTS

First of all, I would like to express my appreciation and thanks to my advisor Professor Ryoichi Amano, I would like to thank him for his tremendous continuous support and for encouraging my research and allowing me to grow as an independent researcher. His supervision has been priceless.

I would like to thank Professors, John Reisel, Istvan Lauko, Wilkistar Otieno, and Deyang Qu for serving on my dissertation committee and for giving me guiding comments during the preliminary exam and the final dissertation. Their input to my research is valuable and contributes to a better version of my work.

My acknowledgment extends to my research mates and colleagues and I wish them all the best in their future endeavors. Special thanks to my best friend and my colleague Ahmad Abbas and Ahmad Abdelhadi for their great assistance in testing and running the experimental setup. Additionally, I would like to thank an alumna of UW-Milwaukee Caleb Rozema for his help in designing the CAD work of the set-up. The research is funded by the US Department of Energy under DE-EE0007716.

Finally, thanks to my family and friends for their continuous support, encouragement, and inspiration.

With all the love I have in my heart and mind, I dedicate my work

To

My Family

Chapter 1: Introduction

1.1 Renewable Energy

Due to the instability of the conventional energy prices (oil, coal, and natural gas), along with its increased environmental impacts caused by CO_2 emissions polluting products; those traditional types of energy are losing interest in the field of energy research and development. On the other hand, the world is investing more and more in RE, especially in remote areas where electricity is hard to find. Major conventional resources for powering remote areas are either fossil fuel generators or electricity from a nearby grid. Both methods have considerably expensive running costs and varying implementation costs depending on the location.

Currently, RE plays a significant role in new power generation worldwide. Hydropower, wind, biomass, and PV are the leading RE streams with 99% of total renewable sources. These streams add up to hundreds of gigawatts in global energy generation. Further, these mitigate tons of greenhouse gas emissions [1][2].

As of 2018, renewable energies in their various forms accounted for an estimated 18.1% of the total final energy consumption worldwide. More electricity generated from RE each year, *Figure 1* shows the estimated RE share of global electricity production at the end of 2019, hydropower still accounted for 60% from the renewable electricity production as the highest share among the other RE sources, followed by wind power (21%), solar PV (9%) and bio-bower (8%) [3].

By comparing with other renewables, hydropower is the largest contributor as shown in *Figure 2* with a power capacity of 1,132 GW as of 2018 [3]. Although the growth rate of hydropower is not as high as wind and solar sources, however, hydropower is sharing almost 40% of the total RE sources in the world.

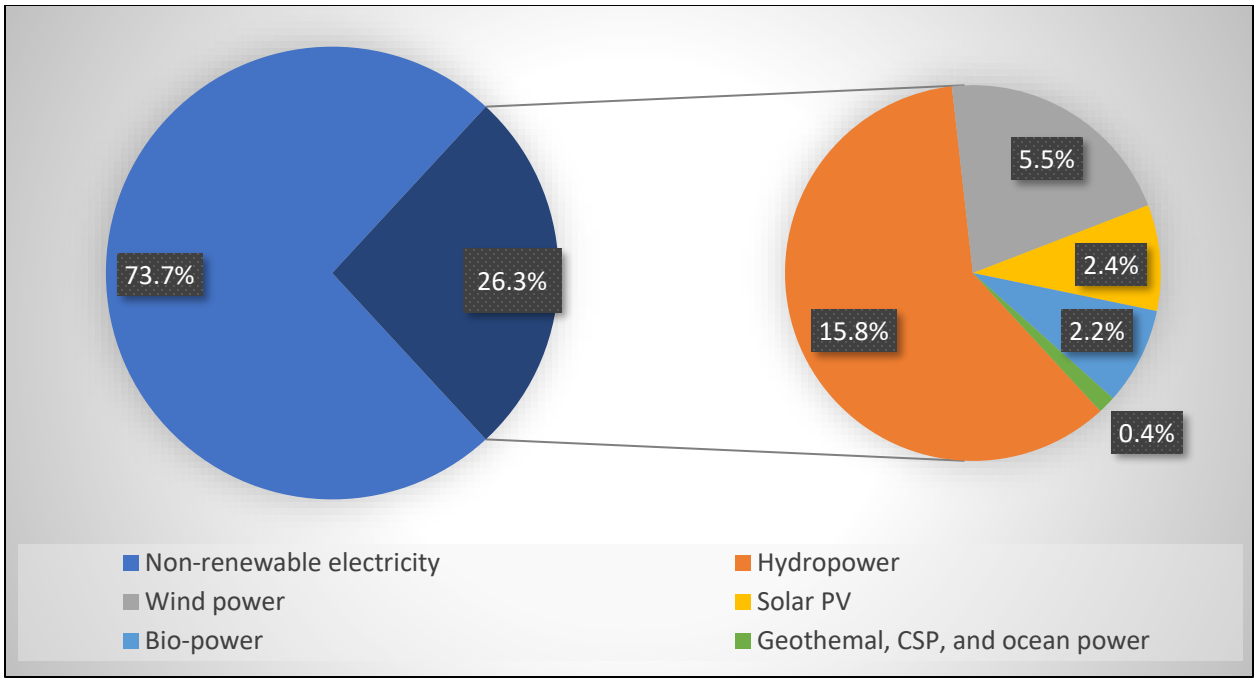

Figure 1: Estimated RE share of global electricity production, end-2019 [3]

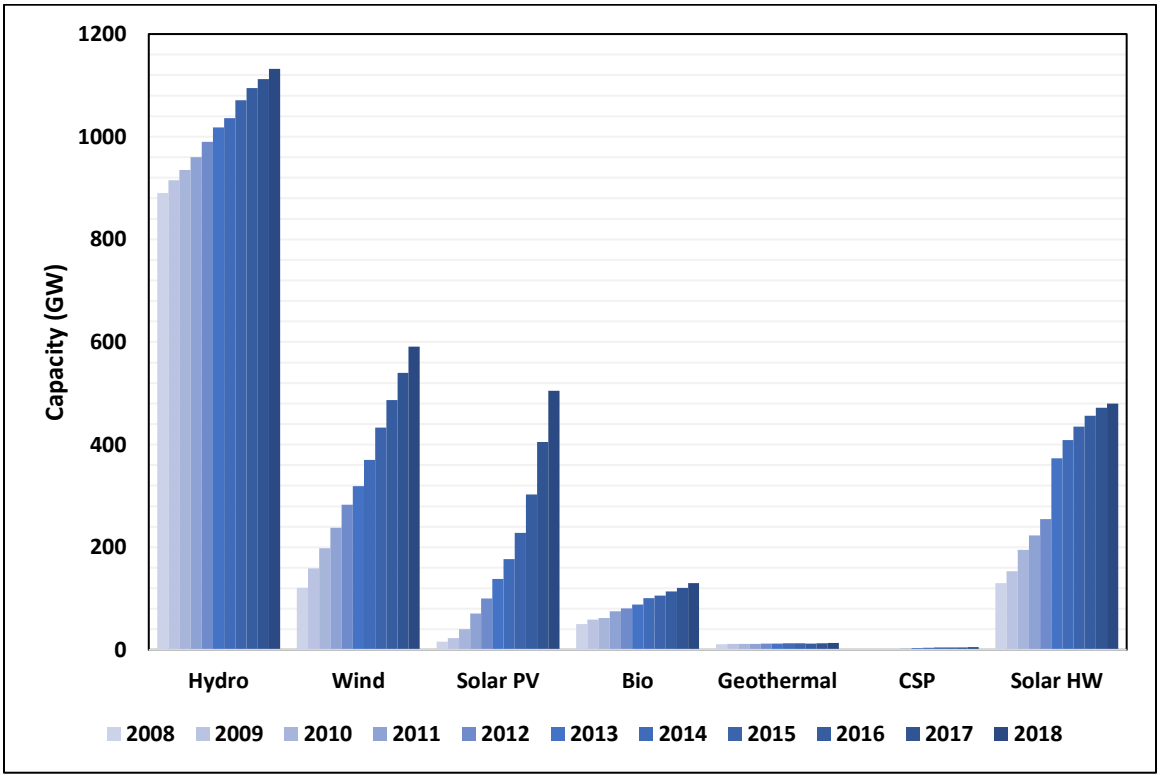

Figure 2: RE capacity and growth rate in the last decade [3]

1.1.1 Photovoltaic Technology

For billions of years, the sun has produced energy and is the ultimate source for all of the energy sources and fuels that we are using today, over time, humanity developed many technologies to get the benefit of solar energy. One method is to use solar thermal energy systems to heat places or generate electricity, another method is converting the sunlight into electricity using solar PV systems [4].

The discovery of photovoltaism is commonly ascribed to Becquerel (1839), who observed that photocurrents were produced on illuminating platinum electrodes, coated with silver chloride or silver bromide, and immersed in aqueous solution. The observation by Smith (1873) of photoconductivity in solid selenium led to the discovery of the PV effect in a purely solid-state device by Adams and Day (1877). The first practical PV device, a light meter consisting of a thin-layered 1.4 potentials of selenium sandwiched between an iron base plate and a semi-transparent gold top layer made by Fritts (1883), was promoted by the German industrialist Werner von Siemens [5].

Photovoltaic is a method of generating electrical power, it works by converting solar radiation into direct current (DC) electricity using semiconductors that exhibit the PV effect. PV power generation employs solar panels composed of several solar cells containing a PV material. Materials presently used for PVs include monocrystalline silicon, polycrystalline silicon, amorphous silicon, cadmium telluride, and copper indium gallium selenide/sulfide. Due to the growing demand for RE sources, the manufacturing of solar cells and PV arrays has advanced considerably in recent years [6].

Solar PV technology is growing rapidly, although from a small base to a total global capacity of 512 GW at the end of 2018, all solar PV power plants together produce only 2.2% of the world's

electricity output. By 2018 the worldwide PV capacity is projected to increase considerably from a low scenario of 320 GW to a high scenario of 430 GW within five years [7]. Installations may be ground-mounted or building-integrated, and PV systems are either grid-connected or stand-alone.

1.1.2 Wind Energy

The sun is heating the earth's surface by an uneven amount, which causes wind. The heating absorption rate for the earth's surface is different for the land and the water. The daily wind cycle is one of the examples of uneven heating. During the day the air above the land heats up faster than the air over the water (see *Figure 3*). Warm air over the land expands and rises, and heavier, cooler air rushes in to take its place, creating wind. At night, the winds are reversed because the air cools more rapidly over land than it does over water [8].

In the same way, the atmospheric winds that circle the earth are created because the land near the earth's equator is hotter than the land near the North Pole and the South Pole.

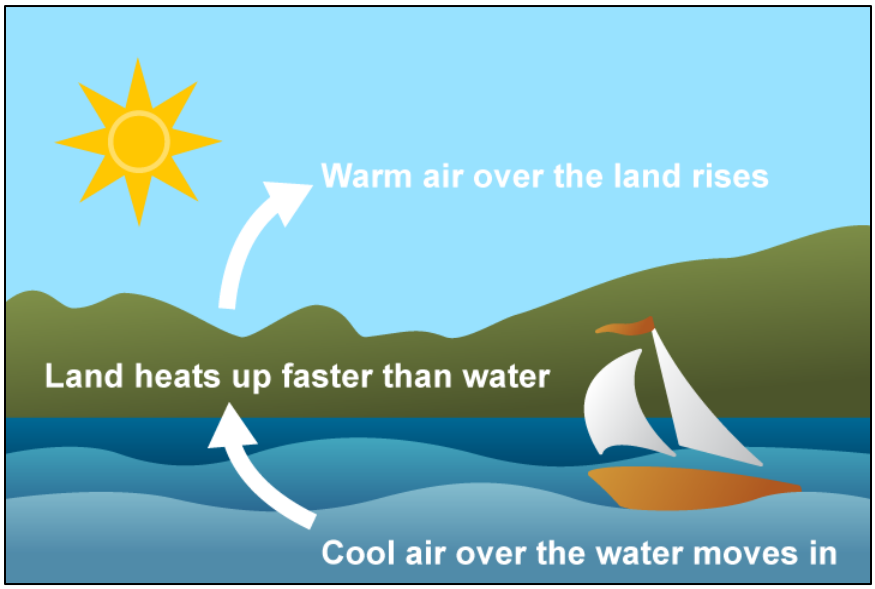

Figure 3: The daily wind cycle [8]

Today, wind energy is mainly used to generate electricity. Water-pumping windmills were once used throughout the U. S. and some still operate on farms and ranches, mainly to supply water for livestock [9].

1.1.3 Hydropower

Hydropower is the energy generated via the forces in flowing water such as in rivers, streams, and dams as well as tidal waves in oceans. It is considered one of the oldest sources of energy used to produce mechanical and electrical energy and was used to grind grains using paddle wheels. The amount of the available energy is dependent on the elevation difference in addition to the volume of water flowing. The energy is extracted using a turbine connected to an electrical generator that transforms the rotational energy into electricity [10][11].

Hydro turbines are classified into two main categories depending on the action of water on the blades: reaction and impulse. In the reaction turbines, such as Francis and Kaplan (propeller), a pressure casing encompasses the blades which are fully immersed in water and the blades are angled to lift forces through the pressure differences. The runner in the impulse turbines, such as Pelton, operates in air and the rotational movement is created by one or more jets of water impinging on the blades. Reaction turbines are most common in low to medium-head applications whereas impulse turbines are used in high-head applications [12].

1.1.4 Renewable energy in the U.S.

In the U.S., several RE sources are used to generate power such as hydro, wind, and solar. *Figure 4* shows the share percentage of each type of these sources in the production energy in 2019 based on the U.S. Energy Information Administration (EIA) report [13]. Currently, RE supplies 11.5% of U.S. electricity production. In 2019 wind become the third-largest source of U.S. generation capacity and the largest RE source with 44% of RE generation capacity.

With about 2,400 dams utilized for hydropower, it represents 40% of RE generating capacity. Solar energy comes in third place with 10% of the total RE generating capacity. Biomass fuels generate about 4% of the RE in the U.S. and 2% for geothermal power [13].

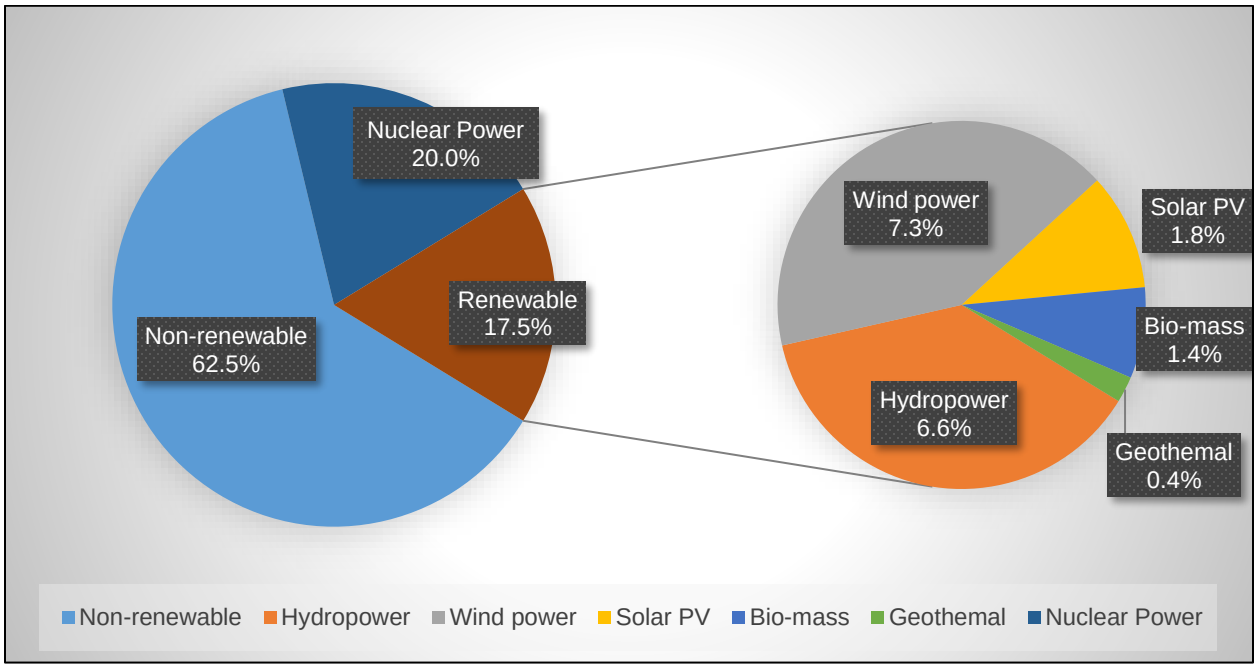

Figure 4: RE share of U.S. electricity production, end-2019 [13]

It can be inferred from *Figure 5* that hydroelectric power represents the highest contribution in generating electricity compared to other RE sources since the 1950s, although wind power started to have more contribution in the last two years [13].

The RE generation nearly doubled in the U.S. between 2008-2018 [12]. The United States is ranked second in the annual installed power generating capacity after China and followed by Brazil, India, and Germany as indicated in *Figure 6* [4].

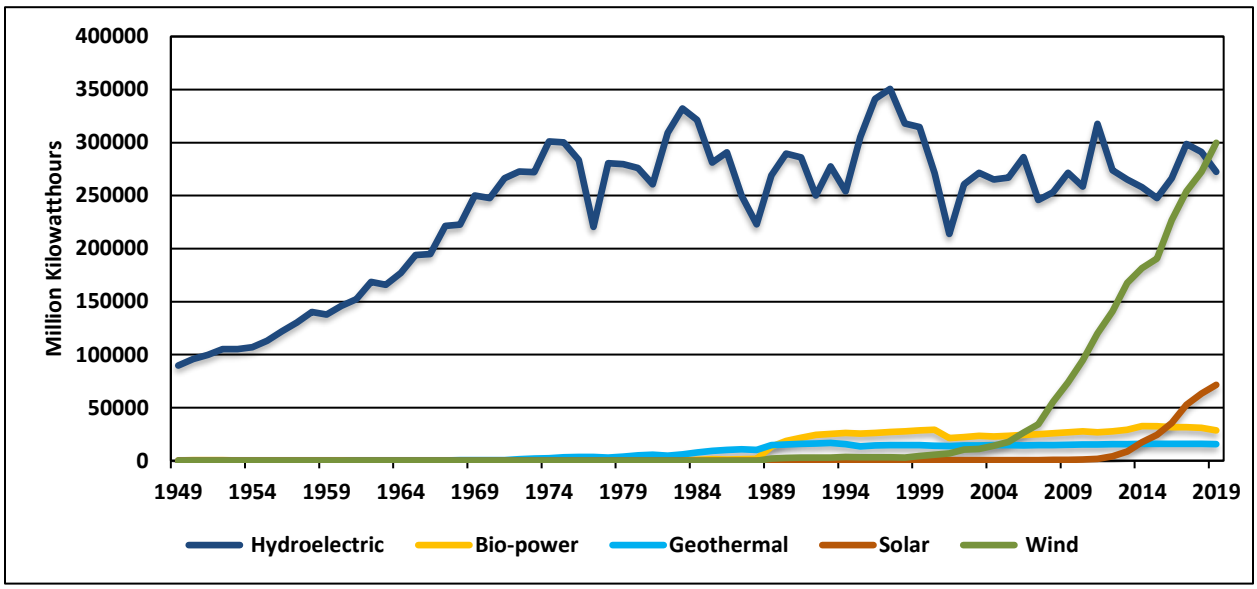

Figure 5: RE generation in U.S. electricity generation, 1950-2019 [13]

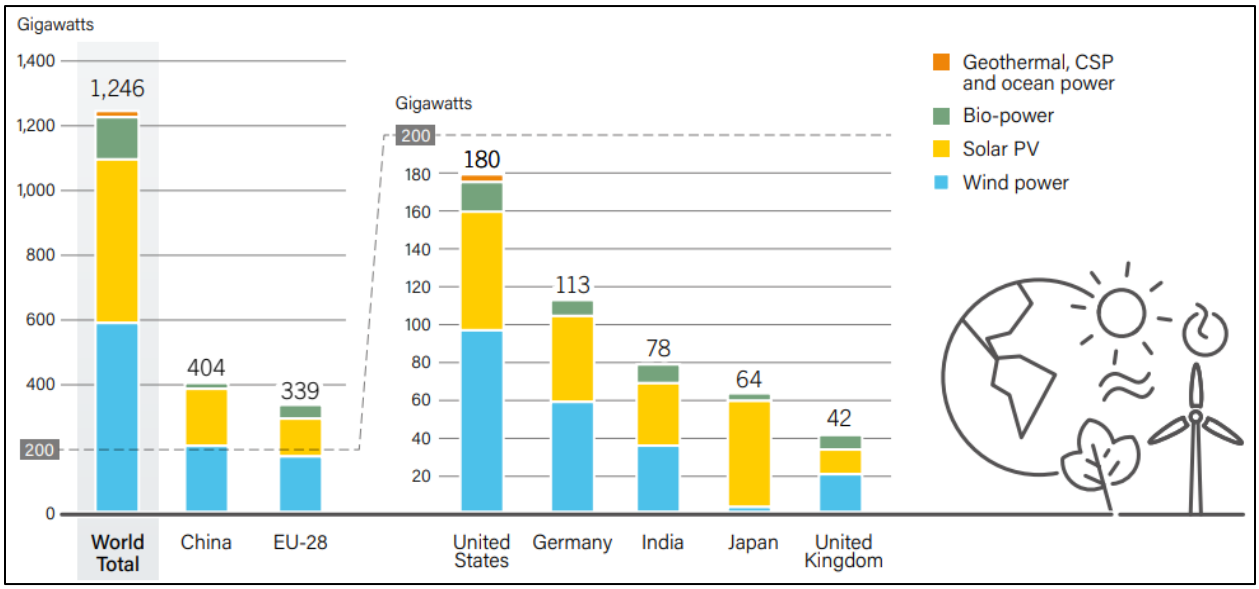

Figure 6: Percentage of annual RE production per country [4]

1.2 Hydrofoils

The basic principle of a standard hydrofoil craft is to raise a ship's hull from the water and support it dynamically on a wing-like foil lifting surface. The effect of lifting a ship's hull from the water includes the reduction of wave effects on the ship resulting in a smoother ride as well as a decrease in power required to maintain modestly high cruising speeds as the hull no longer suffers

drag effects from the water. Historically when designing hydrofoil craft, engineers and marine architects have relied on empirical methods and data for the selection of hydrofoil sections followed by costly and time-consuming experimental testing of scale and full-sized models [14].

Currently, hydrodynamic data is widely available for a large range of standardized geometric shapes such as wedges, plates, and circular arc hydrofoils as well as conventional cambered airfoil shapes. Symmetrical hydrofoil shapes have traditionally played important roles as both lifting surfaces and non-lifting support struts and fairings as the requirements for such structures including drag profiles and strength requirements are very similar to lifting hydrofoils [15].

The principle of hydropower is the extraction of kinetic and potential energy from a flow to convert it into mechanical energy and then to electrical power by utilizing the head. The hydro turbine is not a very new concept, however increasing demand for RE, leads to expansion and further investigation of the technology. Hydrofoils are used in hydraulic fluid machines (i.e. water turbines, pumps).

1.3 Cavitation Phenomenon

In a flow of liquid if the local pressure at a point falls below the vapor pressure of the fluid a phase change from liquid to vapor is likely to occur. This phase change from liquid to vapor due to this reduction in pressure is called cavitation. For this phenomenon to occur there is an additional requirement to a drop-in pressure, this requirement is the inclusion of points of weakness in the form of small gas or vapor inclusions operating as initiation sites for the breakdown of the liquid. These microbubbles within the fluid are termed cavitation nuclei and in the absence of such microbubbles, liquids can withstand negative absolute pressures in much the same way as solids. However, in any practical application, such weaknesses will occur in one of several forms. Although cavitation and boiling may seem similar since both represent a liquid to gas phase

change, however, the approach and the conditions of the phase transformation are different. Heating is the driving force of the phase change in a boiling phenomenon in which as the molecules are being superheated, they gain kinetic energy causing rupture of the liquid. Whereas, cavitation occurs due to a drop in the pressure at a roughly constant temperature breaking the tensile forces between the molecules and leading to liquid rupture. The difference between the two processes can be inferred from *Figure 7*. Boiling is represented by the constant pressure horizontal line, while cavitation is represented by the constant temperature vertical line.

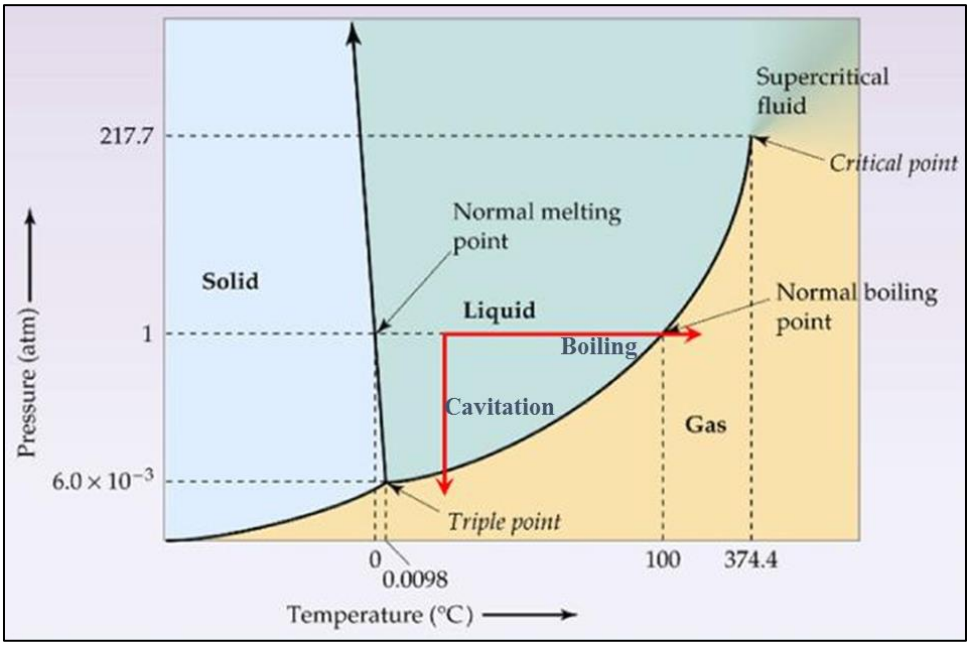

Figure 7: Phase change in the pressure-temperature diagram [16]

A dimensionless number called "Cavitation Number" σ indicates the possibility of the cavitation occurrence by correlating the design condition of the hydrofoil as well as the design flow conditions [17]. The cavitation number is defined as per the equation below:

$$\sigma = \frac{p - p_v}{\frac{1}{2}\,\rho \upsilon^2} \qquad \text{Eq. 1}$$

At high cavitation numbers, flow is mostly steady or near-steady, and tiny bubbles can be noticed traveling along with the flow. On the other hand, at low cavitation numbers, other

cavitation forms as sheet cavity and bubble cloud can be observed [18]. Cavitation has been associated with some adverse in turbomachinery applications including the most common problem: material damage. Due to the collapse of the bubbles nearby a solid surface, severe damage can occur to the runner, blades, impellers, and parts within the system. The collapse of the cavitation bubbles is a fierce process that creates localized large-amplitude shock waves and microjets in the fluid where the collapse occurs causing stresses on the adjacent solid surfaces [19]. Having the cavitation bubbles collapse repeatedly leads to fatigue failure, pitting, and eventually pieces of materials detachment. *Figure 8* and *Figure 9* represent examples of localized damage on a pump blade due to cavitation.

Figure 8: Localized cavitation damage on a pump blade [19]

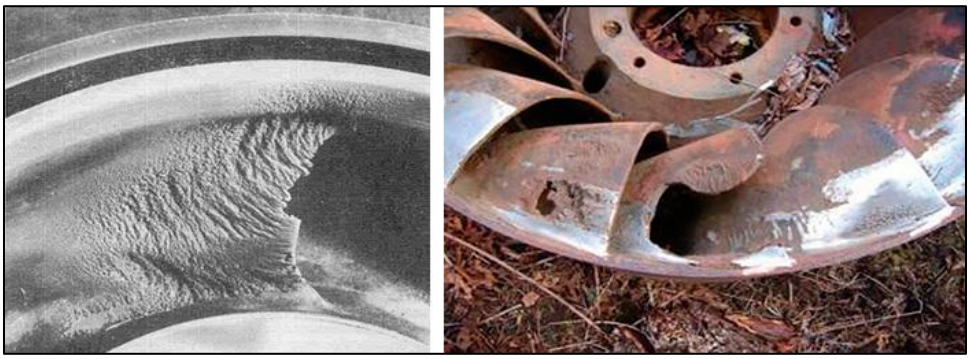

Figure 9: Severe cavitation erosion as witnessed on a Francis turbine [20]

Additionally, cavitation generates noise and vibrations which affects the stability and system performance. The high pressures that are caused momentary when the bubbles are compressed and collapsed result in noise and vibrations. Moreover, vibrations can initiate cracks especially in low-head turbine applications such as Kaplan turbines [19]. It occurs once the excitation frequency of the vortices coincides with one of the natural frequencies within the system leading to cracks in the turbomachinery components.

Large-scale cavitation structures can be classified into three main types: vortex, sheet, and cloud cavitation. Vortex cavitation can be recognized by the cavitation formed in the vortex core where the pressure is smaller significantly than the other regions in the flow domain. Vortices usually form inflows with a high Reynolds number such as pump impellers and swirling flow in the draft tube of a hydro turbine. Tip vortex cavitation is a form of cavitation that occurs when bubbles are trapped in the core of the tip vortex which is the low-pressure region [21]. Further reduction of the cavitation number will induce filling the vortex core with vapor. An example of a tip vortex cavitation is shown in *Figure 10*.

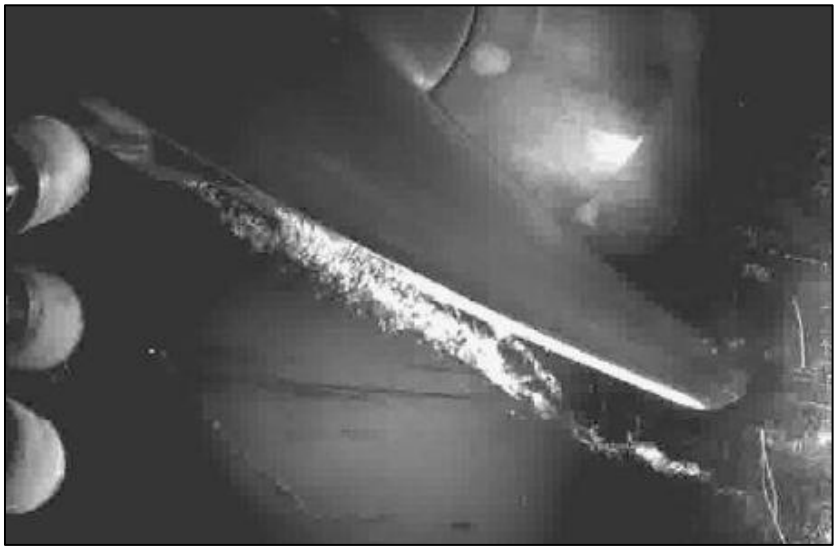

Figure 10: Severe cavitation erosion as witnessed on a Francis turbine [22]

Cloud cavitation is a periodic formation and collapse of multiple cavitation bubbles in the form of a cloud. It occurs due to the scattering of cavitating vortices and a result of a periodic disturbance imposed on the flow. The cloud cavitation can be observed in the interaction between the stator and rotor of pumps and hydro turbines as well as in ship propellers and the wake region. The collapse of the cloud cavitation is proved to cause more noise and a higher potential for damage than flows with no fluctuations [23]. *Figure 11* shows a cloud cavitation formation on the suction side of a hydrofoil.

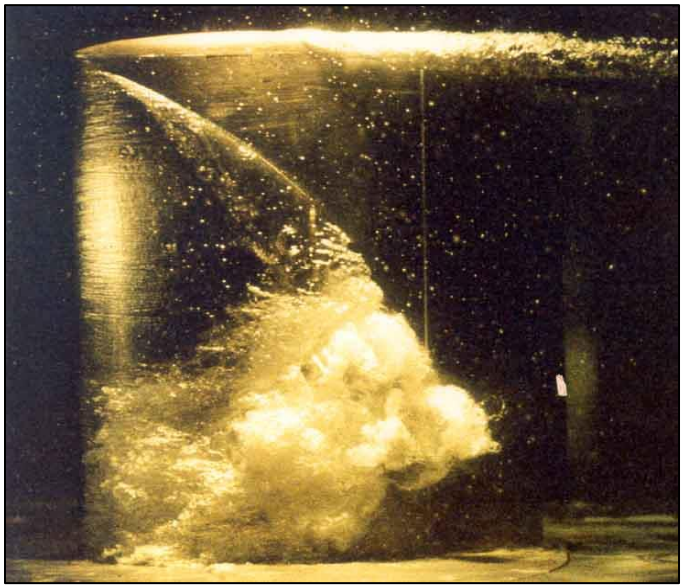

Figure 11: Cavitation cloud as seen on the suction side of a hydrofoil [24]

Sheet cavitation occurs when a region of separated flow is transformed into vapor and a "sheet" like zone is formed. It is observed as a vapor-filled separation zone or wake that is often called a fully developed or attached cavity. On a hydrofoil or a propeller blade, it is called sheet cavitation, whereas in pumps known as blade cavitation. An example of sheet cavitation is exhibited in *Figure 12*.

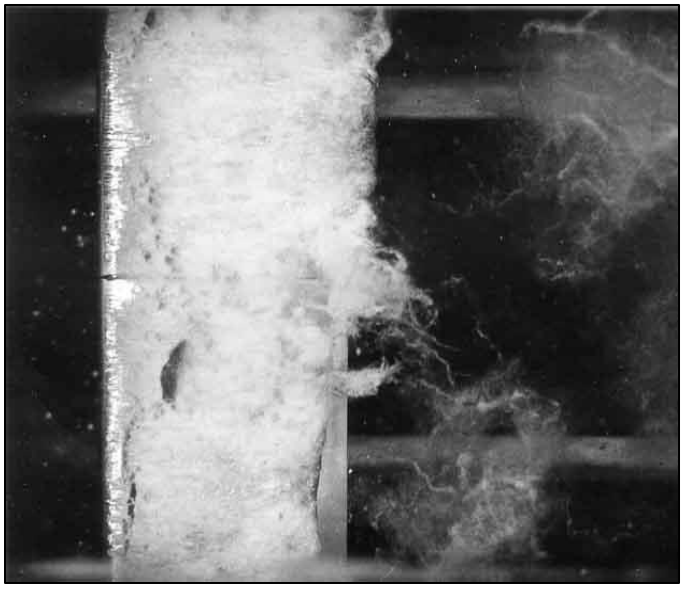

Figure 12: Sheet cavitation observed on the suction side of a hydrofoil [25]

1.4 Problem Statement

The study will cover two main topics:

1.4.1 Cavitation Treatment

- Compare the performance characteristics of NACA 66-012 hydrofoil in cavitation flows with previous experimental performance data for the same hydrofoil type.
- Evaluate the cavitation treatment for the conventional hydrofoil by utilizing CFD and by testing a three-dimensional (3D) printed model of the hydrofoil in a custom-built experimental setup.
- Introduce the air over the hydrofoil as a cavitation treatment, and the work is conducted by numerical modeling investigation of cavitating flow over a NACA 66-012 hydrofoil.
- Optimize the best configuration for the air slot openings over the hydrofoil to have the best cavitation treatment for each AoA.

- The CFD setup is based on 3D transient turbulent featuring the Large Eddy Simulation (LES) model, and STAR-CCM+ is the CFD software. In addition, the high-performance computing (HPC) cluster of the University of Wisconsin-Milwaukee is used for solving complex CFD simulations.

1.4.2 Optimization for a hybrid renewable system

The percentage of people who did not have access to electricity has been steadily decreasing over the last few decades worldwide. In 1990, around 29% of the world's population had no access to electricity; this has decreased to 13% in 2018, which means 860 million people still do not have access to electricity [26]. The 'access to electricity' term is defined by the International Energy Agency (IEA) as more than just the delivery of electricity to the household. It also requires households to meet a specified minimum level of electricity, which is set based on whether the household is rural or urban, and which increases with time [26].

In 2018, about 45% of the world population is estimated to be living in rural areas [27]. Presently, about 60 million people in the united states live in rural areas. About 97 percent of the U.S landmass is rural with 20 percent of the population lives there [28]. In many cases, utility grid extension is impractical owing to dispersed population or rugged terrain, thus stand-alone power systems are likely to be the most viable options. Various combinations of RE sources (such as wind, solar PV, etc.) and diesel generators with/without rechargeable batteries are currently being researched (for electricity production) and are marketed as cost-effective in a long run. In this context, one of the options to provide electricity to remote locations is the utilization of solar energy (one of the potential markets for PV installations is in remote areas) either with\without wind turbines and diesel generators. And the study follows the below main points:

- Prepare complete hybrid renewable system design with all components (PV panels, wind turbines, inverters, batteries, diesel generator …etc.) for utilizing the sun and the wind in powering remote areas in the U.S.
- Optimize the best configuration for each application case (residential, commercial, and industrial) for each state in the U.S., according to its application and load profile.
- Perform an economical study with life-cycle costing, to highlight the aspects of using renewable power over other conventional types of energy.
- Perform different scenarios for finding a suitable system type for each case.

Chapter 2: Literature Review

In this chapter, a comprehensive review of previous studies on different aspects of cavitation treatment and utilizing the RE sources in powering remote areas is presented.

2.1 Cavitation in Hydraulic System

The need for having a more efficient method to understand the unsteady cavitating flow has increased after many costly and time-consuming experimental tests on real ship propellers and pumps. Testing a stationary hydrofoil in a water tunnel was found to be a suitable solution to save time, cost, and simulate the real size and geometry of a turbomachine [29]–[35]. Many experiments were conducted for hydrofoils with two-dimensional nature and with different types of the National Advisory Committee for Aeronautics (NACA) airfoils.

Further investigations have been done on 3D hydrofoils taking into consideration varying the AoA and capture most of the changes, and the non-uniform loading occurs over the hydrofoil [36]–[39]. Keerman R. [40] is one of them in 1956 who experimented with symmetrical hydrofoil shapes. He found that those hydrofoils meet the general requirement for watercraft applications. Besides, a symmetric hydrofoil is easy to design with low cavitation numbers and high strength. Moreover, some researchers studied the ability to control the cavitation phenomena by using obstacles on the hydrofoil and change the direction of the cavitation progress [41].

As of now, many computational simulation software has been developed to help in solving the mathematical equations and capturing the cavitation progress in many cases. These simulations started with a two-dimensional (2D) geometry, and a 3D symmetric geometry along with simplified boundary conditions and that depends on the model used in the simulation like Unsteady Reynolds Averaged Navier-Stokes (URANS) or LES [42]–[49]. Huang et al. [50] validated the CFD work by doing a numerical estimation on NACA66 hydrofoil and showed how CFD could

provide close results to the experiment. However, these results showed some variations; these variations are normal experimental variations.

Schroeder et al. [50] studied the effect of cavitation on NACA0015 hydrofoil using the Open Field Operation and Manipulation (OpenFOAM) toolkit, which is another toolkit used to study the unsteady turbulent cavitation effects. This study made on a multi-phase solver with a liquid-vapor mix using Reynolds Averaged Navier-Stokes (RANS)/LES turbulence model on NACA0015 hydrofoil. The results obtained were found to be excellent, and similar to the experimental data concerning mean values, root means squared values and spectral contents for the same hydrofoil type NACA0015. Gosset et al. [51] reported simulation interphase change foam of cavitating flow on symmetrical section hydrofoil using the OpenFOAM. In their study, the investigators compared the results of the cavitating flow. The results showed that the interphase change foam gave better results than cavitating flow. Thus, what he attempted to prove is that OpenFOAM gives results with an order of magnitude to experimental results.

Nedyalkov et al. [52] reported a study on three different hydrofoil sections NACA0015, NACA64-424, and NACA63-424 bi-directional. These investigators found that the NACA63-424 bidirectional is more beneficial to be used for marine RE conversion than NACA64-424 unidirectional by deriving the lift and drag coefficient and the cavitation number for each of the three hydrofoils. Tabatabaei et al. [52] studied the icing of wind turbine blades in cold weather by using the RANS model to simulate the aerodynamic characteristics for some samples.

In many cases, it is hard to capture the effect of the walls if simplified symmetry conditions are used. Therefore, researchers tend to employ the full dimensions of the tunnel and the propellers in unsteady flow conditions to keep tracking most of the parameters included in the cavitation progress [10], [53]–[55].

2.1.1 Cavitation Treatment

Air introduction into a hydraulic system to mitigate the cavitation phenomenon is not a new technique. Although not commonly known, it is used to influence the cavitation behavior in an already cavitating flow by increasing the pressure in the system, thus reducing the potential of cavitation occurrence. Air injection can be introduced by the means of compressed air where the cavitation is anticipated to take place; low static pressure regions e.g.: suction side of a hydrofoil or leading edge of a hydro turbine.

There are previous studies and research conducted to investigate the effect of air introduction. Ardent et al. [56] investigated the use of air injection to alleviate the erosion caused by cavitation in a study to improve hydropower generation in a utility provider. The experimental work was performed on a specially instrumented hydrofoil and a NACA 0015 cross-section in a water tunnel and tested flows up to 20 m/s velocities. The vibration and cavitation noise was measured using an American Society for Testing and Materials (ASTM) vibratory apparatus and hydrophone. The pitting rate was inferred by measuring the impulse pressure and air was injected at the leading edge of the hydrofoil. The air injection was found to be an effective technique in minimizing cavitation erosion.

Zhi-Yong et al. [56] investigated the control of cavitation by aeration experimentally and theoretically at flow velocities 20-50 m/s. The pressure waveforms were measured with and without aeration and the variation of the compression ratios at different air concentrations was identified. The experimental results indicated that with aeration the pressure was increased significantly in the region where cavitation is anticipated. Additionally, the compression ratio increased with increasing air concentration.

Tomov et al. [57] studied the effect of aeration on a transparent horizontal venturi nozzle by injecting compressed air and capturing images using a high-speed camera. The study compared the experimental results of the aerated and non-aerated cavitation by image processing for three different regimes: sheet cavitation, cloud cavitation, and super-cavitation. The experimental study showed that the symmetrical cavitation structures were partially broken in the case of sheet cavitation and cloud cavitation, while were completely disappeared when the super-cavitation was achieved.

Rivetti *et al.* [57] investigated the effect of air injection on the tip vortex cavitation in a Kaplan hydro turbine. The experiments were carried out using a 0.34 m diameter turbine located vertically between an upper and lower tank. Air was introduced through twenty 3-mm-diameter holes located on a horizontal plane above the runner centerline. The data gathered through accelerometers, hydrophones, and high-speed cameras were analyzed. Although the turbine efficiency was slightly reduced, however, air injection helped in alleviating the erosion caused by the tip vortex cavitation and reduced the vibration in the whole system [58]. Other studies have been done on Kaplan turbines with different injection holes through the hub and led to a 90% reduction in the cavitation at some cases [59].

From all the above, it can be concluded that cavitation has a major impact on turbomachinery applications in which deteriorating the system performance and lifetime. Also, it limits the performance of hydro turbines due to the constraint of running at high rotational speeds. Thus, it is vital to address cavitation and introduce methods to alleviate the adverse caused by this phenomenon to improve the overall system performance and extend the lifespan of the turbomachinery components.

2.2 Hybrid micro-grid

The micro-grid concept can be understood as a hybrid power system comprising small-scale sources of power generation (conventional and renewable) and storage devices that supply energy to nearby loads through intelligent coordination of the whole. Micro-grids can be applied to two different types of systems: those designed for normal operation in connection with general electrical energy distribution networks, and those designed for operation in permanent isolation from such networks [60].

There are many areas of the world, often in rural areas far from power plants, that have no electricity [61], [62]. As a result of the distances involved, constraints imposed by features of the terrain, and the costs associated with the cabling of an electrical supply network, it is unlikely that many of these places will ever enjoy the benefits of installations connected to a main electrical grid [63]. However, numerous proposals have been made to cover the demand for power in such remote areas through the use of power systems not connected to a main electrical network [64], [65]. These systems are usually classified as ‘decentralized’, ‘autonomous’, ‘stand-alone’, or ‘remote’ [66].

Badran O. [67] introduced a study for the implementation of wind energy to drive water pumps, either directly by mechanical means or indirectly by a wind-driven electric generator. The study concludes that wind energy pumping systems are preferable over diesel ones as they are more reliable, require less maintenance, safer, and do not pollute the environment.

Hrayshat and Al-Soud [68] introduced a survey for use of PV-generator systems for water pumping applications in Jordan, where ten different locations in the country are chosen for this assessment. They concluded that four of ten sites are considered ‘‘adequate’’ for solar pumping, the other three sites are ‘‘promising’’, and the rest three sites are considered ‘‘poor’’.

Ashhab M., et al. [68] discussed the possibility of combining a PV solar system with another energy source to generate energy efficiently. The PV solar system was specified and designed. A prototype was designed and built, consisting of 8 PV panels, each of 250 W, in addition to a charge controller, an inverter, batteries, and an Air Conditioning (AC) unit. A data logging system was installed to collect relevant readings. The results showed that the system performance was promising for developing the research of the solar system. Based on the results, the PV solar system will be augmented with another efficient model to form a hybrid setup. A promising candidate for the other model was found to be the absorption system, which will potentially lead to an overall system that people can afford where energy is generated most efficiently.

Sopian et al. [68] Studied the optimization of a stand-alone PV hybrid system for a household in Malaysia using HOMER simulation software and showed that the least expensive system is composed of 2 kW PV and 1 kW wind turbine.

Karakoulidis K., et al. [68] analyzed an energy system combining RE sources, traditional sources, and batteries or hydrogen as a storage medium. The analysis utilizes the power load data from an electric machinery laboratory located in Kavala town, Greece. The modeling, optimization, and simulation of the proposed system were performed using HOMER software.

The simulation results indicate that for a hybrid system comprising of a 6 kW PV system together with a 16 kW diesel system and battery storage, the PV fraction/penetration was 41.7%. Using the proposed hybrid PV-diesel system with a battery instead of the diesel-only system results in a 33.8% fuel saving. The simulation results indicated that the replacement of conventional technologies, namely diesel generators and batteries by hydrogen technologies is technologically feasible, reduces emissions, noise, and fossil fuel dependence.

Abatcha H., et al. [69] showed how to design the aspects of a hybrid power system using the HOMER program as an optimization software, the study specified one sensitivity variable with two values; which were the slope of fuel consumption in Fuel Cell (FC) and the marginal fuel consumption of the FC. It showed that the Net Present Cost (NPC) and the cost of energy had increased due to the rise in fuel consumption in the FC from 0.03 to 0.05 L/hr./kW.

Balachander K., et al. [70] offered a study and design of a complete hybrid-renewable power system model for day-to-day load demand of Metropolitan cities in India. The sizing, optimization, and economic estimation of the systems were performed using HOMER software. HOMER solved the optimization problem to minimize the total cost and provides the optimum PV, wind turbine, battery, and FC ratings. It also provided a comparison between the three different suggested power system configurations. The study made a simulation across three different locations and found that the stand-alone PV-Battery system was the most suitable configuration for all locations.

Shiroudi A., et al. [71] investigated a stand-alone power system that consists of a PV array as a power supply and electrolyzer. They have been integrated and worked at the Taleghan renewable energies site in Iran. HOMER simulation software has been used to carry out the optimal design and techno-economic viability of the energy system. The simulation results demonstrated that the energy system is composed of a 10 kW PV array, 3.5 kW electrolyzer, 0.4 kW proton exchange membrane FC, 2.5 kW inverter, and 60 batteries (100 Ah and 12 V). The total initial capital cost, NPC, and cost of electricity produced from this energy system are $193,563, $237,509, and $3.35/kWh, respectively.

Lagorse J., et al. [72] evaluated three configurations of FC and PV hybrid systems based on economic constraints. The study used two approaches to size the system, analytical relations, and optimization with Matlab/Simulink. It also employed three major ways to gather two sources

(Battery storage, Hydrogen storage, and use of both), with a simulation model made for each configuration.

Jaber J., et al. [72] studied the use of conventional energy sources as well as RE resources for the space heating system. They showed that a space heating system based on RE resources is a favorable option due to its low cost-to-benefit ratio. Asgarpoor, et al. [73] introduced a method for designing a stand-alone PV system to improve the load point reliability, extend the operation life, and minimize the design cost.

Lagorse J., et al. [74] showed that a system composed of a PV generator, an FC, an electrolyzer, and a battery can deliver energy in a stand-alone installation at an acceptable cost. Gebre S., et al. [74] discussed the effect of using an optimal load-sharing strategy for PV/FC hybrid power systems with batteries. The simulation results showed that the sharing and control strategy is effective to achieve high power availability and reduced cycling of the battery. The study concluded that the solution relying on the only use of hydrogen storage was not feasible, the two other configurations were similar on the cost of view if the system's site can be reached to bring hydrogen, the configuration of (PV-Battery storage and FC supplied by an external tank) was the best choice unless the configuration of (PV-Battery storage and FC supplied by an electrolyzer) would prefer.

Kaldellis J., et al. [75] presented a study to determine the optimum dimensions of a stand-alone PV-diesel system, under the restriction of minimum long-term electricity generation cost, and accordingly obtain a comparison with diesel-only systems. Using developed methodology to a representative Greek island, with results obtained being rather encouraging for the implementation of the proposed solution.

Ma T., et al. [75] evaluated the operating performance of a stand-alone solar PV system over the complete year of 2011, with average electricity production from the PV system at 61.2 kWh/day and electric energy consumption at 49.5 kWh/day. The study found that the average AC power output ratio of the PV array to the entire system energy utilization ratio was 9.5% and 7.7% and noted that the output of the PV module decreased significantly with the increase in cell temperature. It was also found that the round-trip efficiency of the battery bank during the year was 74.3% with the state of charge values above 50% for 88% of the year. And the average yield, system losses, and capture losses during the year were 2.49 hrs/day, 0.59 hrs/day, and 1.86 hrs/day, respectively. The study suggested a way to better utilization of the RE output by training residents.

Kyriakidis I. [76] investigated the optimal size and operation of an energy storage system included in a hybrid renewable-based plant for the islanded power system of Agios Efstratios, and optimize the hybrid system based on specific economic and policy criteria, and evaluate the techno-economic feasibility of incorporating different battery types for energy storage.

Silva, et al., [77] presented the evaluation for the use of a PV-FC system with a battery to supply electric power in an isolated community in the Amazon region. The analysis showed that the optimal system's initial cost, net present cost, and electricity cost with the hydrogen storage system are $87,138, $102,323, and $1.35/kWh, respectively.

Chapter 3: Cavitation Treatment

3.1 Research Outline

This chapter presents a first step of studying the cavitation characteristics that occurs over a NACA 66-012 hydrofoil in a water tunnel test numerically using CFD, which helps to design and to set up the experimental setup and reducing the time and cost needed. The results are beneficial for applying to hydro energy machine components for improved energy harvesting technology [78][79].

This chapter's focus is to investigate the effect of air injection on the cavitation treatment over a hydrofoil. Air is being introduced through the air slots over the hydrofoil at different locations.

3.2 Methodology

NACA 66-012 hydrofoil is used in a water tunnel to conduct a simulation of the cavitation at different cavitation numbers for each AoA. Mesh independent test was made for NACA 66-012, and then predicting the phenomena of cavitation and its effect on the turbomachines performance by doing a correlation between the cavitation number, the Volume of Fluid (VOF) fraction and lift and drag coefficients for many AoA.

3.2.1 The Geometry of Hydrofoil and Water Tunnel

NACA 66-012 hydrofoil model was selected in this study due to the available data at different flow conditions [80]. The geometry of the hydrofoil was modeled by the standardized geometric entities; the hydrofoil is defined with a set of 26 (x, y) coordinates stations and ordinates as a percent of the chord. Each station refers to the percentage of the chord from the leading edge of the foil and ordinates the normal distance from the chord line to the surface of the foil.

The hydrofoil model was constructed by using the data from NACA [80]. *Figure 13* shows the Computer-aided design (CAD) model for the selected hydrofoil with the chord length and a span

of 8.4 cm (3.3-inch) and 7.4 cm (2.9-inch), respectively, with a thickness to chord ratio of 0.12. The CAD model for the water tunnel used in the simulation has a total length of eight chords, and a height of one span, and one span width, as can be seen in *Figure 14*.

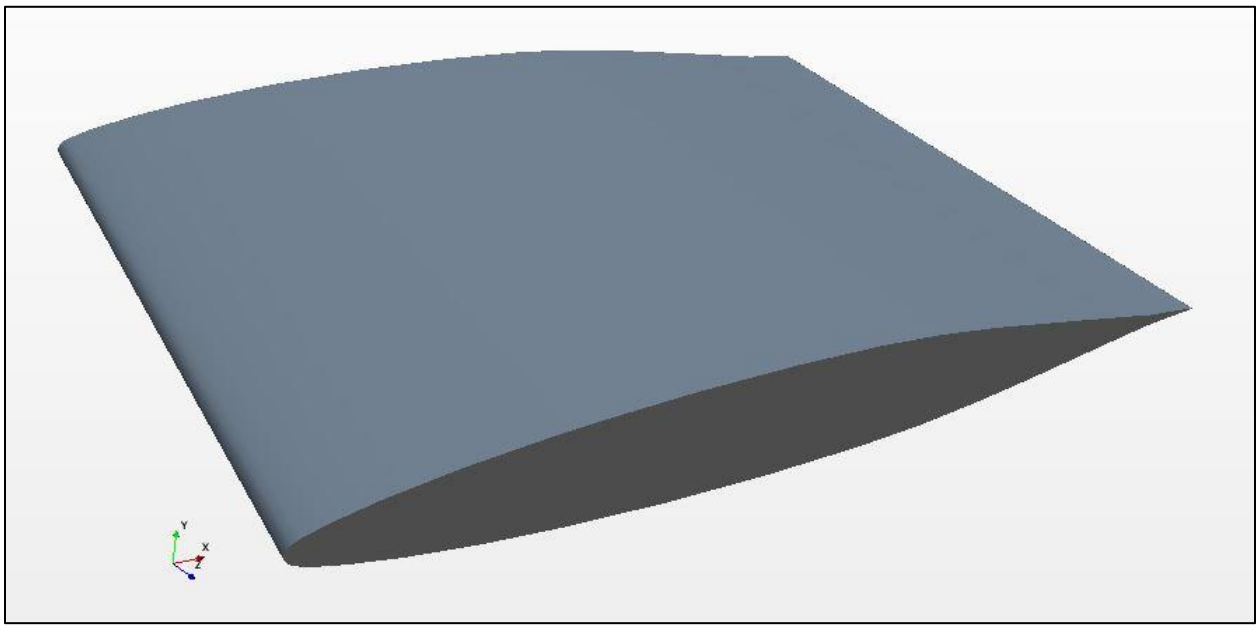

Figure 13: CAD model for NACA 66-012 hydrofoil

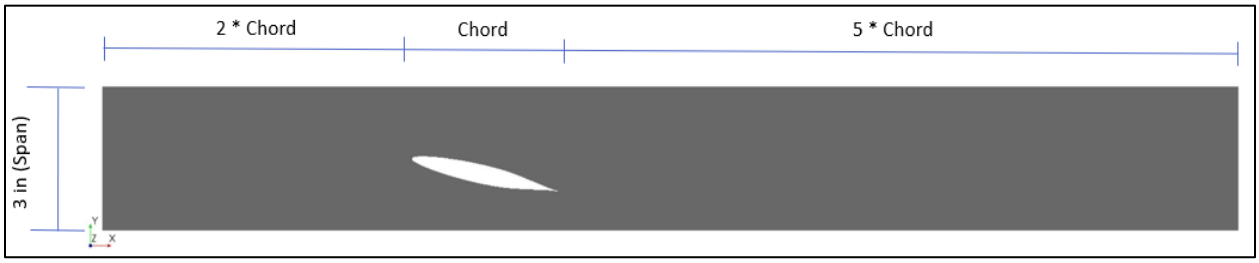

Figure 14: CAD model for water tunnel

3.2.2 Flow Physical Equation

The VOF was introduced briefly in 1976 by Noh and Woodward [36] followed by a full method description by Hirt and Nichols in 1981 [81]. In such approach, coexisted (n) fluids were accounted as a global one phase of fluid and how the flow properties were calculated as an averaged sum based on the presence percentage of each step in the computation cell by volume ratio $(\frac{\forall_l}{\forall_c})$ for the

VOF model [82]. Accordingly, the (l)th step volume fraction (α_l), and any similar property (ϕ) is calculated every time step as in Equations (2) and (3), respectively.

$$\alpha_l = \frac{\forall_l}{\forall_c} \quad \text{Eq. 2}$$

$$\phi = \sum_{l=1}^{n} \alpha_l \, \phi_l \quad \text{Eq. 3}$$

Since a conserved system is introduced, the volume fractions of the phases are also maintained in balance by solving the continuity equation (transport) for each volume fraction Equation (4):

$$\frac{\partial}{\partial t}\int_{\forall}^{\cdot} \alpha_l \, d\forall + \int_{A}^{\cdot} \alpha_l \, (u - u_{rf}) \, dA = \int_{\forall}^{\cdot} (\varphi_{\alpha_l} - \frac{\alpha_l}{\rho_l} \frac{D\rho_l}{Dt}) \, d\forall \quad \text{Eq. 4}$$

$(u - u_{rf})$: the phase motion relative to the reference frame motion

(φ_{α_l}): phase addition/reduction due to source/sink existence

Since Cavitation is the main issue here, and a rapid phase change causes it, the global density varies temporally and locally at a high rate, and the (φ_{α_l}) dominates another equation.

Equation (5) is a simplified equation that was derived from Equation (4) but non-conservative, and it was acquired to bypass the computational challenge because it becomes difficult to solve this behavior of the unsteady terms by the segregated flow method:

$$\int_{A}^{\cdot} \alpha_l \, (u - u_{rf}) \, dA = \sum_{l}^{\cdot} \int_{\forall}^{\cdot} (\varphi_{\alpha_l} - \frac{\alpha_l}{\rho_l} \frac{D\rho_l}{Dt}) \, d\forall \quad \text{Eq. 5}$$

Equation (5) represents the mass transfer rate of the vapor depending on the status of generation ($P_v > P_s$) or collapse ($P_v < P_s$) in case of cavitation. Equations (6) and (7) respectively, express the rate of generation (G) and the rate of collapse (C) [83]:

$$G = \frac{\rho_v \rho_L}{\rho} \alpha(1-\alpha) \frac{3}{R} \sqrt{\frac{2}{3} \frac{(P_v - P_s)}{\rho_L}} \quad \text{Eq. 6}$$

$$C = \frac{\rho_v \rho_L}{\rho} \alpha(1-\alpha) \frac{3}{R} \sqrt{\frac{2}{3} \frac{(P_s - P_v)}{\rho_L}} \quad \text{Eq. 7}$$

In the case of a mixture, the motion of the global phase is solved by the compressible flow momentum differential equation, taking into consideration the isothermal and Newtonian fluid conditions, as seen below in Equation (8):

$$\frac{d(\rho \vec{u})}{dt} + \nabla.(\rho \vec{u}\, \vec{u}) = \rho \vec{g} - \nabla P + \nabla.[\mu(\nabla \vec{u} + \nabla \vec{u}^T)] \quad \text{Eq. 8}$$

Two forces with their coefficients are calculated in this study; lift force occurs when the flow passes over the hydrofoil and acting perpendicular to the flow direction and the hydrofoil. The drag force, which is parallel with the flow direction. These coefficients are dimensionless and stated as follows in Equation (9) and (10):

$$C_L = \frac{Lift}{\frac{\rho}{2} v^2 A} \quad \text{Eq. 9}$$

$$C_D = \frac{Drag}{\frac{\rho}{2} v^2 A} \quad \text{Eq. 10}$$

3.2.3 Creating Mesh and Physical Parameters

Polyhedral mesher, prism layer, and surface remesher are the three types of mesh used in this simulation. Based on the literature review where the polyhedral mesher was found to be the best method to capture most of the phase change for the multi-phase flow as per the physics conditions for this case. The polyhedral mesher is considered an unstructured mesh, which is better than the structured mesh in capturing physics like separation and wake region. Twelve Prism layers, which are the boundary layer at the solid surfaces, were used. Surface remesher, which represents the mesh around the solid object inside the fluid.

The base size of 1.25×10^{-3} m, which is 10-50% from the smallest dimension inside the system was taken, based on the hydrofoil and water tunnel dimensions.

LES with Wall-Adapting Local Eddy (WALE) Sub-Grid Scale (SGS) model was selected for this case. As an implicit unsteady simulation, a time step of 2.5×10^{-5} seconds was chosen along with a total solution time of 0.2 seconds. Eulerian Multiphase (Liquid and Vapor) was defined with a 3D turbulent flow and implicit unsteady models to monitor the cavitation formation progress. Water enters the tunnel at various velocities for each AoA ranges from 12.2 m/s (40 ft/s) to 22.8 m/s (75 ft/s) AoA at different angles of attack (0, 6, 9, and 12 degrees). The outlet conditions were defined as pressure with the magnitude of atmospheric pressure (0 Pa gauge), and water vapor pressure is 2,338 Pa at 20 ˚C.

3.3 Experimental Work

3.3.1 Constraints

A water tunnel is the liquid equivalent of a wind tunnel. Both facilities use instrumentation to make fluid flow observations and collect valuable data from test articles. The data are used to paint a vivid picture of how bodies influence the flow and vice versa. Wind tunnels make observations in airflow and have been used in situations that range from measuring the drag and lift of airfoils [84][85] to observing the aerodynamic characteristics of a missile in supersonic conditions [86].

Water tunnels have been used to observe and record hydrodynamic loads to visualize the flow [87], and to study cavitation [88][89]. Water tunnels are specialized pieces of equipment; as a result, they are often designed and constructed to meet a specific use. *Table 1* lists high-speed water tunnels around the world and their ownership. The tables provide test section dimensions and allow for the comparison of tunnels using mass flow rate and speed. There are only four high-speed water tunnels owned by academic institutions within the United States.

Table 1: Partial list of high-speed water tunnels around the world organized by mass flow rate

Tunnel	Location	Test Section Size			Max Mass Flow Rate (kg/s)	Max Speed (m/s)	Reference (s)
		W (m)	H (m)	L (m)			
Large Cavitation Channel (LCC)	US Naval Surface Warfare Center - Carderock (USA)	3.05	3.05	13	167,445	18	[90]
LOCAT	Korea Research Institute of Ships and Ocean Engineering - KRISO (Korea)	1.80	2.80	12.5	75,600	15	[91][89]
Flow Noise Simulator (FNS)	Naval Systems Research Center (Japan)	2	2	10	60,00	15	[92]
HYKAT	HSVA (Germany)	1.60	2.80	11	53,760	12	[93]
Grand Tunnel Hydrodynamique (GTH)	Bassin d'Essais des Care’nes (France)	1.10	1.10	6	24,200	20	[94]
Medium cavitation tunnel	HSVA (Germany)	0.57	0.57	2.20	3,087	9.5	[95]
Mini-LCC	University of Michigan (USA)	0.22	0.22	0.93	1,210	25	[96]
ARL 12-inch Water Tunnel	Applied Research Lab at Penn State (USA)	0.11	0.51	0.76	1,178	21	[97]
UGA Water Tunnel	University of Georgia (USA)	0.30	0.30	1	1,017	11.3	[98]
St. Anthony Falls High-Speed Water Tunnel	University of Minnesota (USA)	0.19	0.19	1.30	722	20	[99][100]
Tunnel de Cavitation	Ecole Navale (France)	0.19	0.19	1	542	15	[99][101]
High-Speed Cavitation Tunnel (HiCaT)	University of New Hampshire (USA)	0.15	0.15	0.91	293	13	[89]
OSU 6-inch Water Tunnel	Oklahoma State University (USA)	0.15	0.15	1	225	10	[96]

Water tunnels are composed of several components that play an integral role in the performance of the tunnel. Key components of water tunnels include the pump, motor, diffuser, and test section [102]. Due to the high cost of having a similar water tunnel, a simpler setup was designed where the true water tunnel conditions can be simulated at a lower cost. In the designed test section it would be hard to measure the lift, drag, and cavitation number in the Global Water Center (GWC) lab.

3.3.2 Setup Configuration

Experimentation helps in verifying the numerical computations and can be used as a tool to validate the results obtained from the CFD simulations. It demonstrates the accuracy of the CFD results and can be used to proceed with the simulations with confidence. Additionally, it determines the credibility of the programming and computational results as well as examines the models through comparison with the experimental results.

The experimental setup was built in the Hydro Turbine lab at the University of Wisconsin-Milwaukee hosting a relatively low-head Kaplan turbine. The system was designed to accommodate a horizontal turbine configuration with an elevated tank, a discharge reservoir, and a circulating pump, as shown in *Figure 15*. The setup is installed on a T-slot table that houses the lower tank providing supports to the hydro turbine system and adjustable configuration. The maximum head that can be achieved through this setup is 2.75 m (9 ft). The upper tank has a capacity of 0.60 m^3 (21 ft^3), *Figure 16 (a)*, and the lower reservoir has a capacity of 0.45 m^3 (16 ft^3). The 10 HP pump circulates the water between the two tanks and is equipped with a Variable Speed Drive (VSD) to control the pump flow rate during testing. The water flowing into the turbine is also controlled through a ball valve installed vertically on the 0.15 m (6 in) downpipe as shown in *Figure 16 (b).*

Due to the space limitation and the high cost of building a high-speed water tunnel to test the hydrofoil, a modification for the current set-up has been designed. *Figure 17* shows the CAD model for the modifications required to be done on the current set-up, which includes replacing the current test reg with an 8×8 cm (3×3 in) square straight water tunnel with 0.7 m (26.5 in) long as shown in *Figure 18* and made of clear acrylic material. An intake nozzle from a 15.2 cm (6 in) circle pipe to an 8 cm (3 in) square section connected to an 8 cm (3 in) square straightener before

the water tunnel. After the tunnel, a diffuser 8 cm (3 in) square section returns for a 15.2 cm (6 in) circle pipe.

Figure 15: Experimental setup

(a)

(b)

Figure 16: (a) Upper tank (b) Ball valve installed on the downpipe

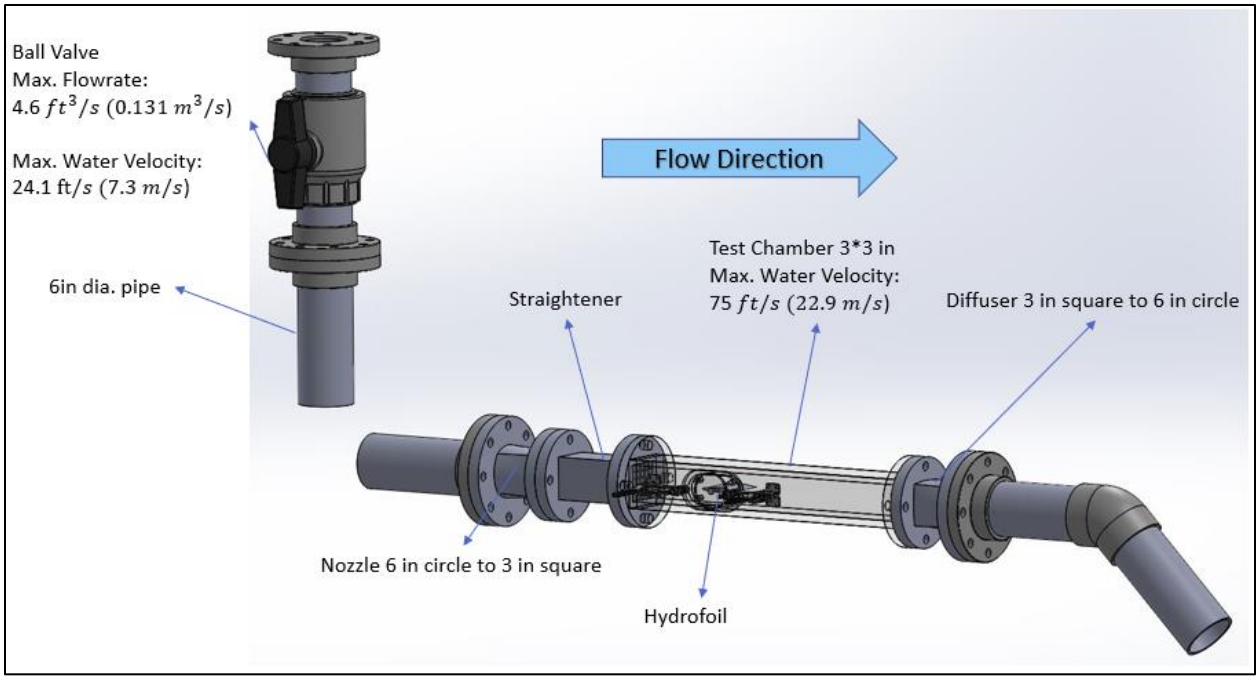

Figure 17: CAD model for the new set-up design

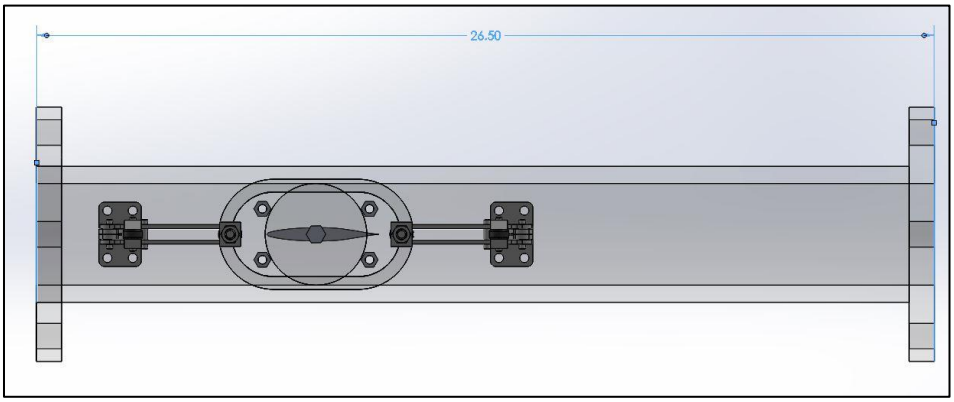

Side view

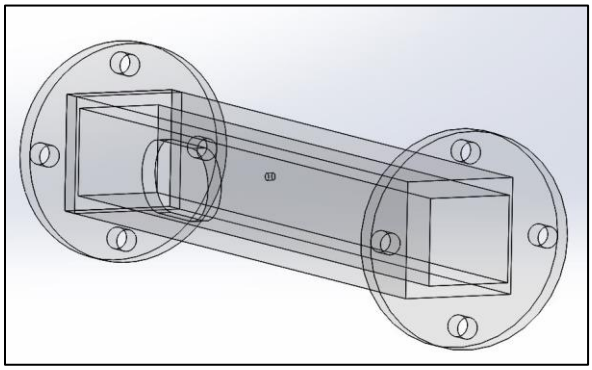

Side view

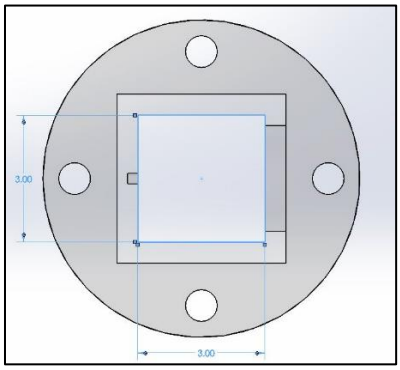

Front view

Figure 18: Water tunnel CAD model

The experimental setup of the Hydro Turbine Lab at the University of Wisconsin-Milwaukee (as explained previously) is used for the hydrofoil cavitation experimental testing. Minor changes were done on the setup to accommodate the hydrofoil assembly includes as shown in *Figure 19*. The maximum head that can be achieved through the setup is still 2.6 m (8.5 ft) with the same maximum flow rate of 0.31 m^3/s (4.6 ft^3/s).

Most of the experimental setup parts including the hydrofoil, the nozzle, the straightener, the water tunnel section, and the diffuser were designed and optimized through previous research conducted at the Hydro Turbine lab. Most of these parts along the supports were 3D printed using Eastman Amphora 3D Polymer AM3300 commercialized by ColorFabb as nGen [103]. *Figure 20* shows the 3D printed NACA 66-012 hydrofoil. The parts were designed using CAD modeling software to match the system configuration and requirements. Ultimaker 2+ [104] was utilized to 3D print the hydrofoil and supports used in the experimental setup.

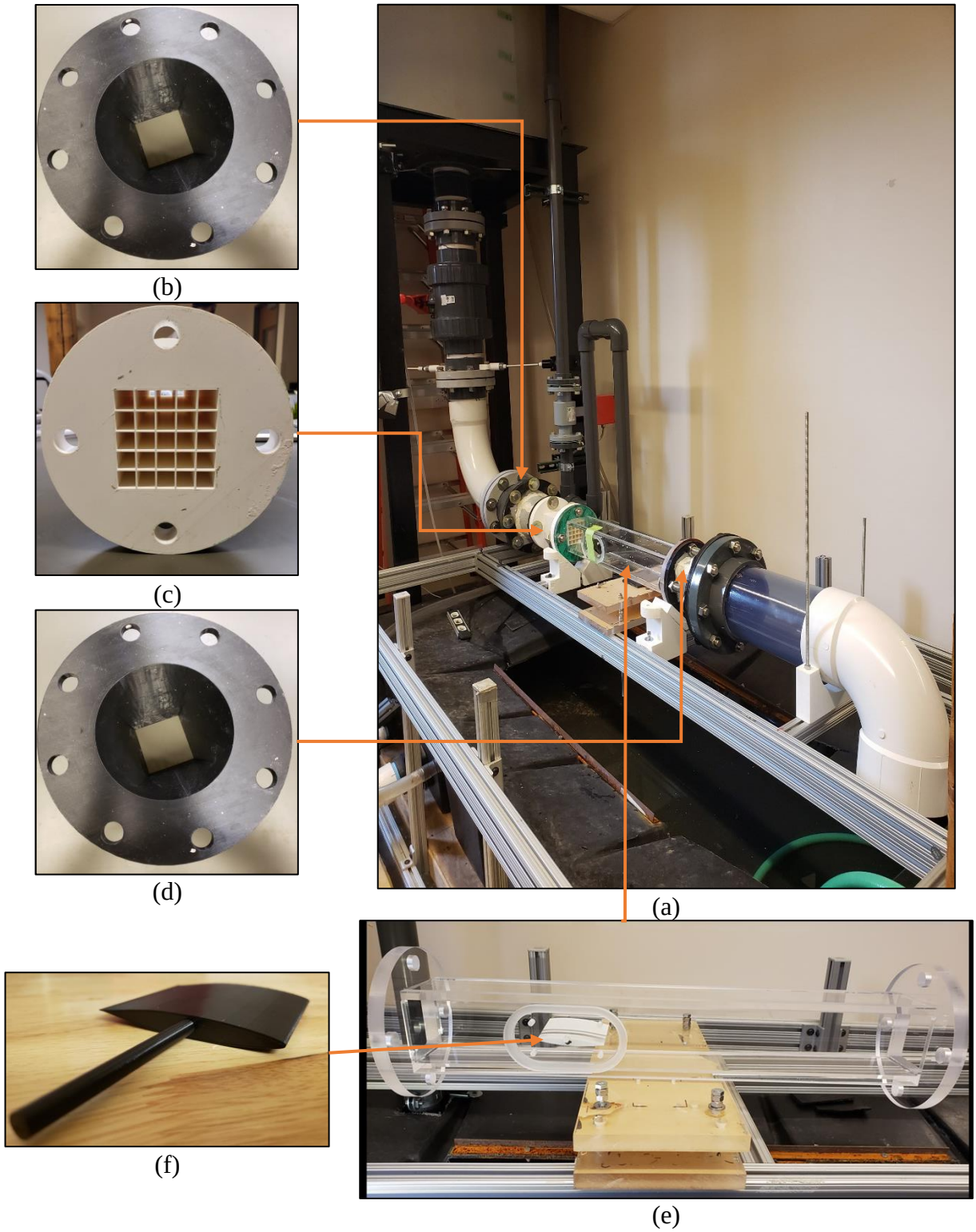

Figure 19: Experimental setup of the water tunnel: (a) The whole setup. (b) 15.2 cm circle pipe to an 8 cm square section Nozzle. (c) 8 cm square straightener. (d) 8 cm square section to a 15.2 cm circle pipe Diffuser. (e) 8x8 cm square straight water tunnel. (f) Hydrofoil

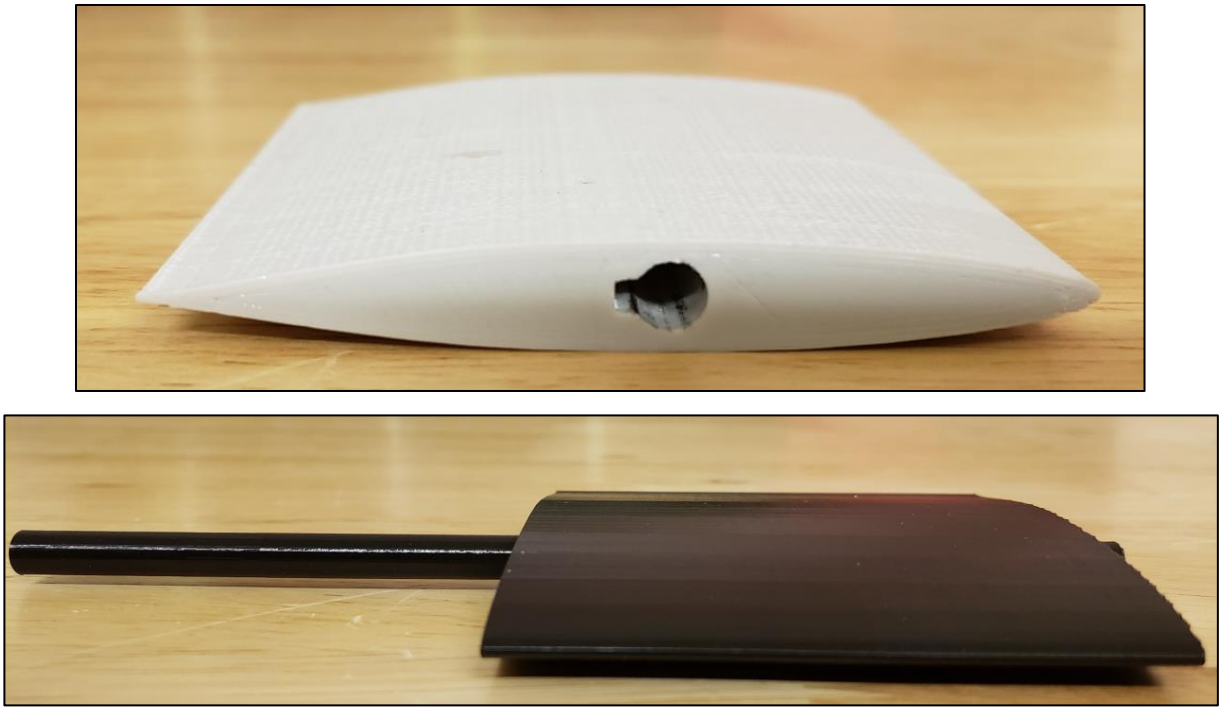

Figure 20: The 3D printed NACA66-012 hydrofoil for the experimental testing

3.3.3 Instrumentation

3.3.3.1 *Ultimaker 2+*

Ultimaker 2+ is a 3D printer with a printing platform of 22 x 22 x 20 cm that can print complex 3D parts at various layer resolutions. The printer has high flexibility and provides a wide range of filament materials in addition to printing nozzle sizes. The printing layer resolution can be as fine as 0.6 mm and the maximum printing speed can reach up to 24 mm^3/s [104]. *Figure 21* shows the 3D printer that was utilized to print the parts used in building the experimental setup.

Figure 21: Ultimaker 2+ 3D printer

3.3.3.2 *Flow Meters*

Flow rates in the experimental setup were monitored via two electromagnetic flowmeters. A 0.08 m flow meter was installed on the pump discharge pipe that fills the upper tank and a 0.051 m was installed on the overflow line of the upper tank. The difference between the two flow rates gives the flow rate going through the turbine while maintaining a constant head. The M-2000 M-series Mag Meter manufactured by Badger Meter was used in the experimentation. The meter has two DC-powered electromagnetic coils and a set of electrodes that create a magnetic field and sense when a conductive fluid like water passes through the meter. The voltage difference between the electrodes is directly proportional to the average velocity of the fluid and then converted to a flow rate. The meter has an accuracy of ±0.25% [105]. *Figure 22* presents the installed flow meters on the system.

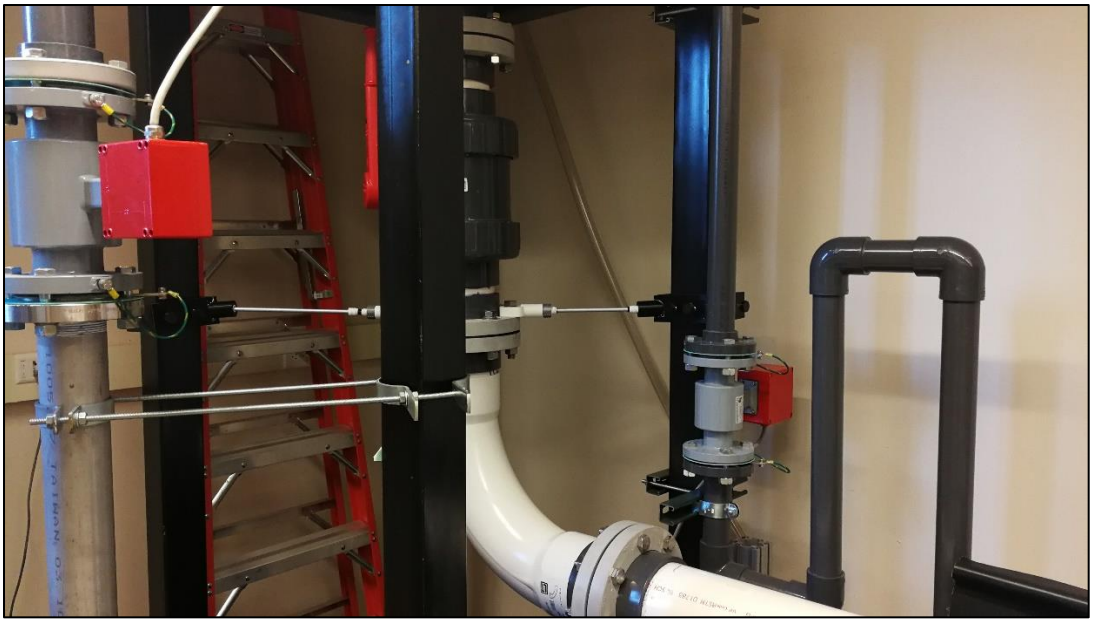

Figure 22: Flowmeters installed on the filling and overflow lines

3.3.3.3 *Variable Speed Driven Pump*

The water was lifted from the lower (sink) tank to the upper tank via a 10 HP (7,460 W) close-coupled centrifugal pump. The pump can provide a flow rate of up to 7.93 m^3/s (500 GPM) and a maximum head of 30 m (98.4 ft) [106]. The pump is equipped with a VSD to provide a closed control flow rate during the experimental testing. The ABB ACS310-03U-34A1-2 VSD is capable of controlling motors ranging from 7.5 HP to 10 HP with a digital output accuracy of 0.2% [107]. It also can change the speed manually as well as programmable control to provide an energy-efficient operation. The pump and the VSD installed in the experimental setup are indicated in *Figure 23*.

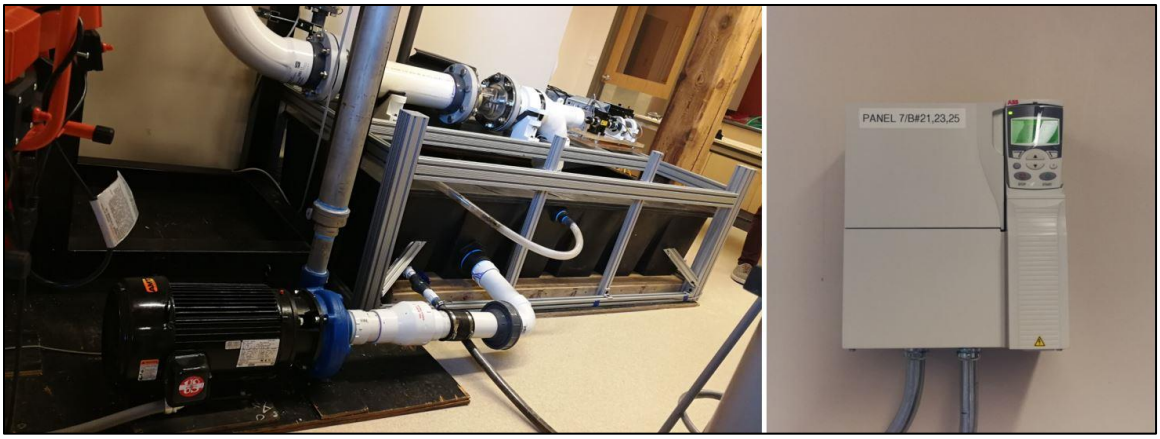

Figure 23: Pump-motor set and VSD

3.3.3.4 *FASTCAM Mini UX50*

Flow and cavitation can be captured using a high-speed camera that is capable of taking thousands of images in one second. The high-speed camera is considered a powerful tool, through image processing, in analyzing the different patterns of cavitation and physics, that can be seen in a slow-motion frame. The high-speed camera that was utilized in the experimentation, ISO 10,000 monochrome FASTCAM Mini UX50, is capable of capturing images up to 102,400 fps. The highest image resolution is 1280 x 1024 pixels which can be achieved with 2000 fps [108]. The camera can be connected to a computer to process and enhance the images captured through special software developed for the camera. The high-speed camera is shown in *Figure 24*.

Figure 24: High-speed camera

3.4 Results

3.4.1 Mesh Independent Study

It is important to have fine enough mesh around the hydrofoil to get accurate simulation results, due to the big amount of changes in the physical values near the hydrofoil wall. Before doing the mesh test, a new modified mesh was created with a volumetric control close to the hydrofoil to focus more on the phase changes close to the hydrofoil surface. *Figure 25* shows the new modified mesh scene for the whole system with the volumetric control close to the hydrofoil with (30%) from the original base size.

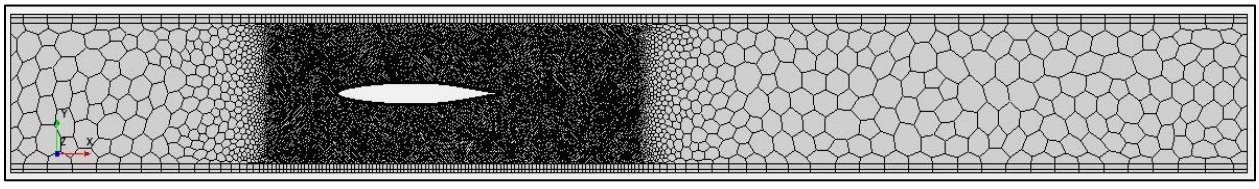

Figure 25: Mesh scene of the whole simulation domain

Mesh independent study involves analyzing the solution of the simulations based on changing the discretization criteria of the computational domain only. The size of the cell is changed, and

the solution time, as well as the accuracy, are monitored. Another way to analyze the mesh sizing is the y+ and the Courant number numbers.

y^+ is a dimensionless wall distance for a wall-bounded flow and is also known as the Law of the Wall. It was introduced by Theodore von Karman in 1930 and is defined in Eq. 11. It is a function of the shear velocity near the wall, the distance to the nearest wall, and the kinematic viscosity of the fluid. y^+ is used in turbulence models to indicate the effect of the influence of the Reynolds stress tensor [109]. The wall function approach is used to apply boundary conditions to a distance away from the wall, so the turbulence model equations are not solved close to the wall [110].

$$y^+ = \frac{u_\tau y}{\nu} \qquad \text{Eq. 11}$$

The Courant number, or mean of Convective Courant number, is a dimensionless number that is a function of the time step and the mesh size. It is defined in Eq. 12 [111].

$$C = \frac{u\Delta t}{\Delta L} \qquad \text{Eq. 12}$$

The Vapor Volume Fraction (VVF) can be a way to track the cavitation over a hydrofoil. Ranging from “0” to “1”, with “1” indicating 100% vapor bubbles, VVF can be useful to understand the location and quantify the phenomena.

Trials on different mesh sizes generated a range of results that were averaged to (VVF = 0.221) over the hydrofoil. Additionally, the computational time consumed for each case is monitored to investigate the impact of increasing the number of cells. Five kinds of polyhedral meshes were tested around the hydrofoil to find the effect of the mesh size. *Table 2* shows the five kinds of meshes with a different number of cells starting from coarse mesh 1.5 Million and up to very fine mesh with 6.3 million cells. With a 31% time saving compared to the 6.3 million cells, the 3.8 million cells are considered as the best number of cells to capture most of the changes around the

tested hydrofoil efficiently. *Figure 26* shows the mesh scene for the entire system at 3.8 million cells and twelve prism layers, while *Figure 27* shows the mesh scene around the hydrofoil at the same conditions.

Table 2: Mesh independent test results

Number of Cells (in millions)	**1.5**	**2.6**	**3.8**	**5.1**	**6.3**
VVF (Surface Average)	0.202	0.191	0.233	0.272	0.309
Percentage of VVF to overall Avg.	8.5%	13.6%	5.5%	22%	35.0%
Comp. Time	1.0x	1.5x	2.0x	2.5x	3.0x

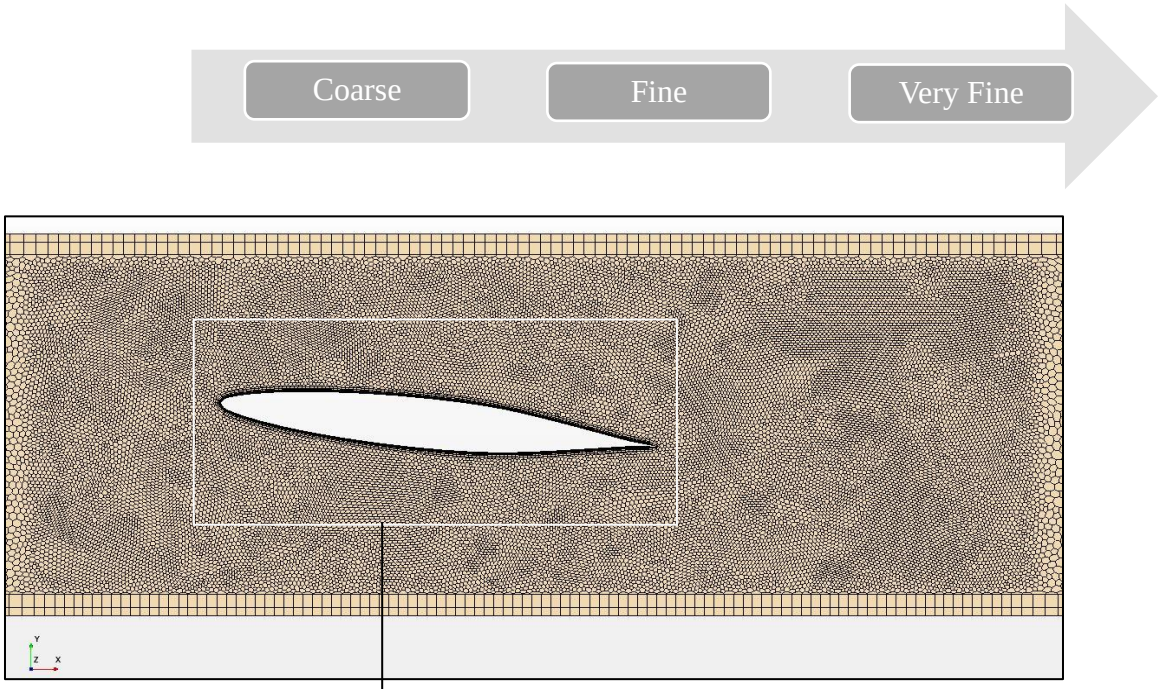

Figure 26: Mesh scene for the entire system at 3.8 million cells and 12 prism layers

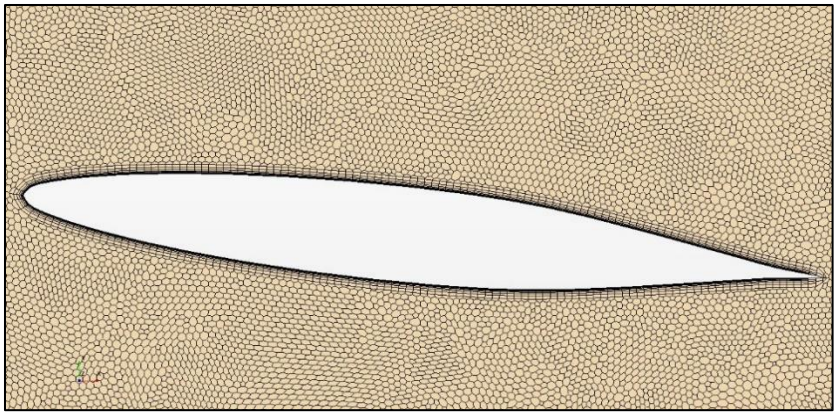

Figure 27: Mesh scene around the hydrofoil at 3.8 million cells and 12 prism layers

Moreover, and the confirming the validity of the results with the selected mesh size, an assessment for the time-averaged y^+ on the hydrofoil was checked to be found ($y^+ < 2$) as shown in *Figure 28*, where 12 prism layers were used. Finally, and though using unconditionally stable implicit time marching, the time-averaged convective Courant number was below 5 (see *Figure 29*) to validate the accuracy for the LES computation.

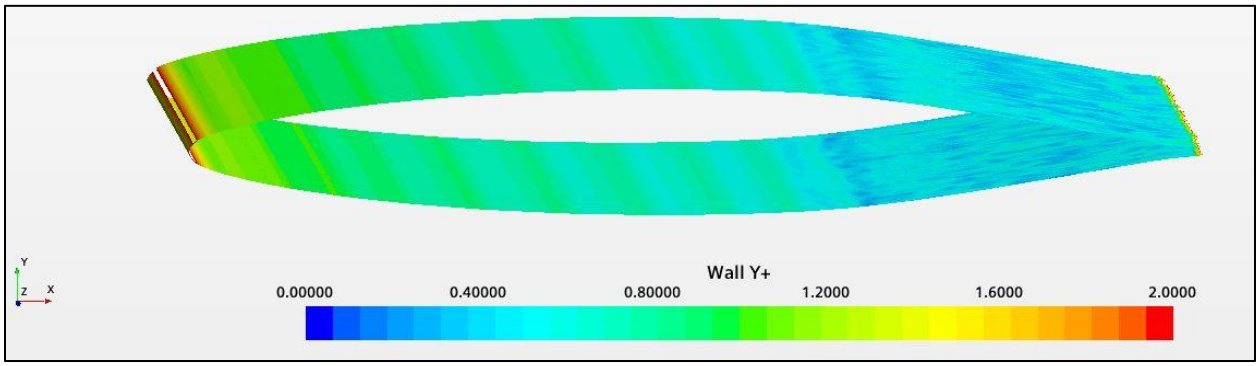

Figure 28: Mean of wall y+ values at the hydrofoil

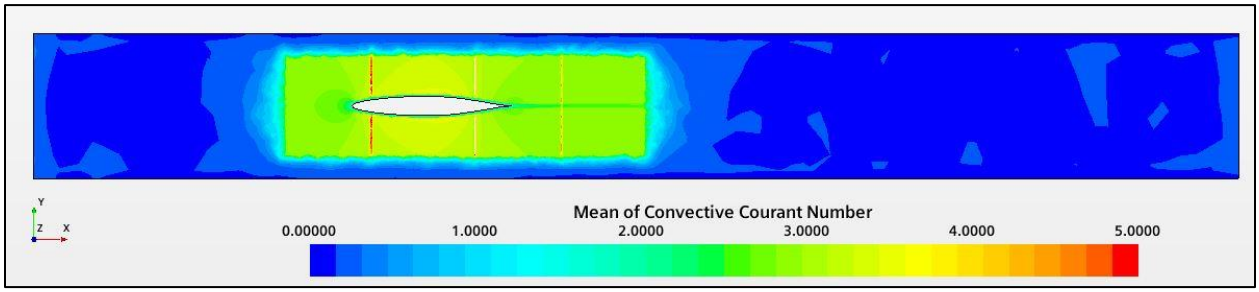

Figure 29: Mean of convective Courant number nearby the hydrofoil

3.4.2 CFD Validation

A comparison between the experimental data from Kermeen et al. [80] and the simulation results was made by taking into consideration changing the velocity, AoA, and the σ. As shown in *Figure 30* and *Figure 31*, both experimental and CFD data are following the same trend where the maximum average relative error reached 10% in the case of 9 degrees AoA. Due to the limitations in the CFD work, some components; as the fraction losses and the mass and the material of the hydrofoil, were not taken into consideration. Thus, these consistent results confirmed the ability of the CFD tool in predicting the cavitation process over the hydrofoils and contributed to saving time and cost.

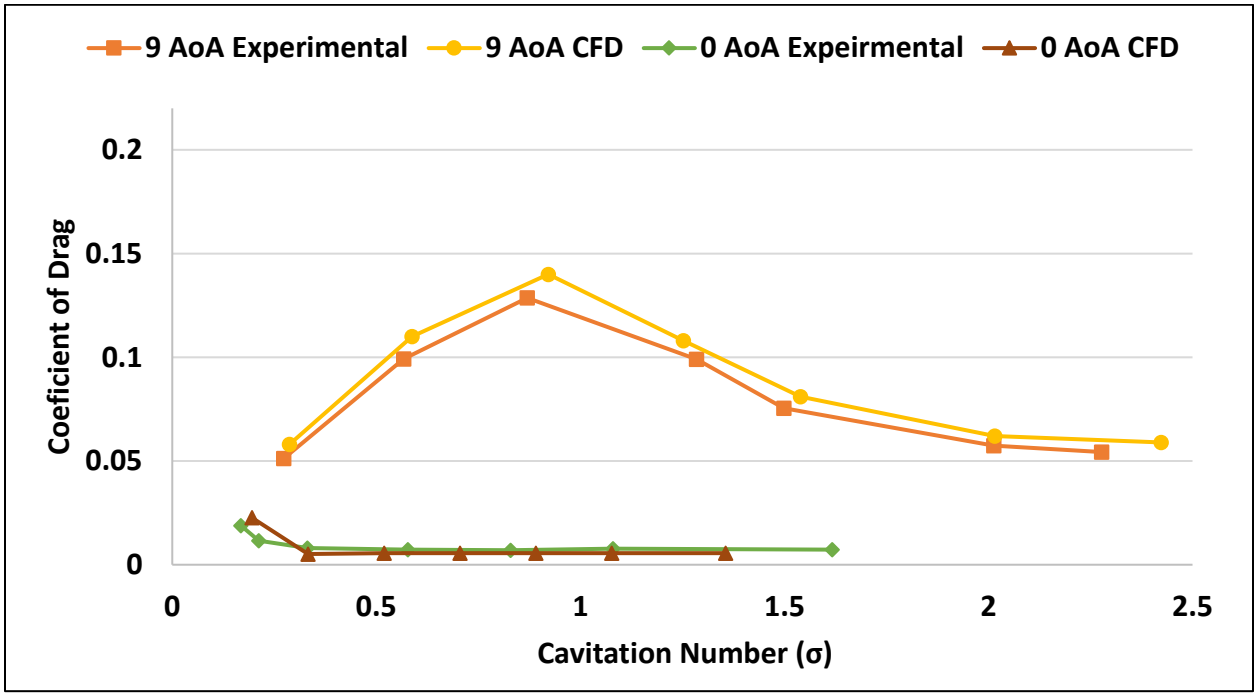

Figure 30: Comparison of coefficients of drag for 0 and 9 AoA

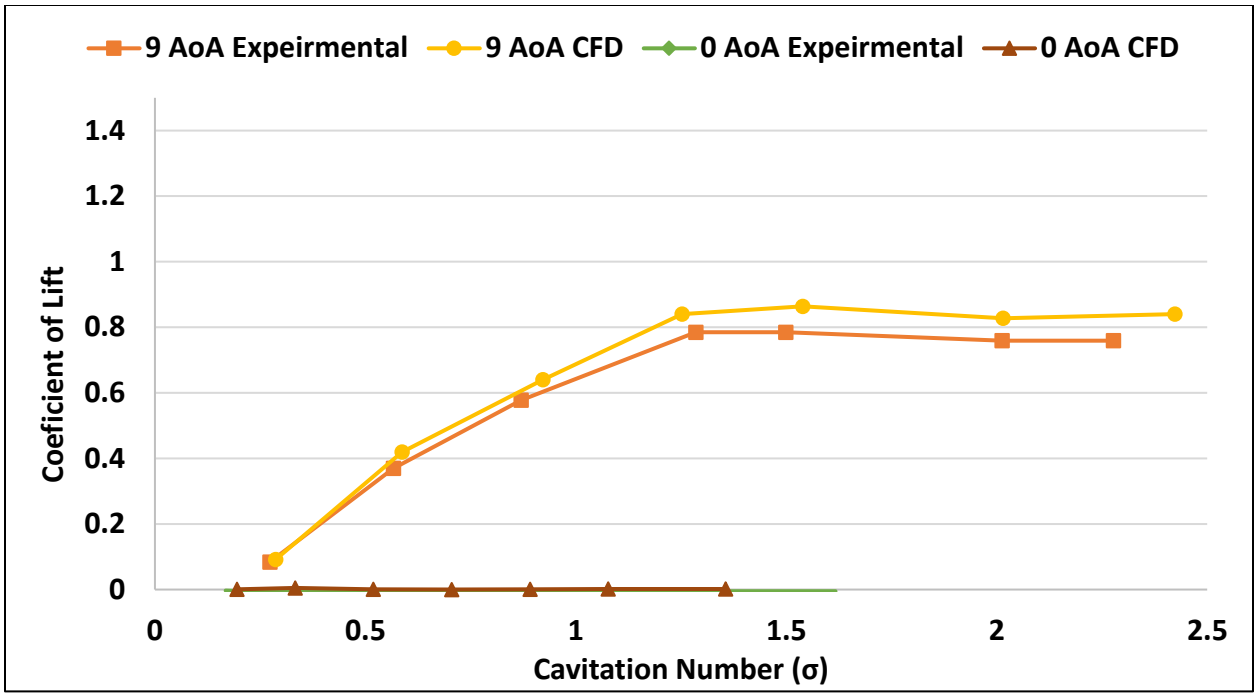

Figure 31: Comparison of coefficients of lift for 0 and 9 AoA

3.4.3 CFD – Experimental Validation Results

The results comparison and validation between the CFD and experimental work that was adhered to comprised of two parameters: CFD simulation results, and image processing. The first case that was investigated is the 9 AoA with no aeration having a water velocity of 18.2 m/s (60 ft/s) at the tunnel inlet. The images of the experimental testing captured via the high-speed camera were set along the time-averaged VVF scenes to compare the cavitation behavior. *Figure 32* illustrates an image of the experimental test and a CFD VVF scene of the 9 AoA case. The cavitation formation in the experimental testing, as shown in *Figure 32* (a), started at the hydrofoil leading edge before going downstream and merging with the cavitation cloud that formed in a similar approach at the middle of the hydrofoil. The CFD VVF scene, *Figure 32* (b), indicated the analogous trend of the cavitation formation at the hydrofoil and merging with the cavitation cloud downstream as represented in the colored formation.

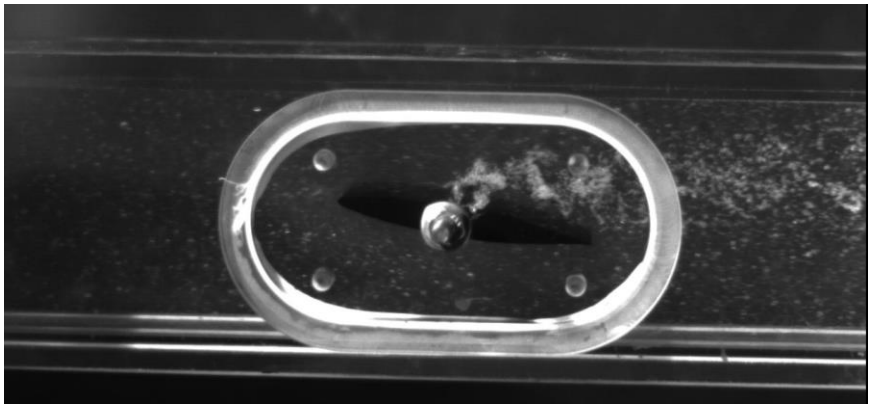

(a)

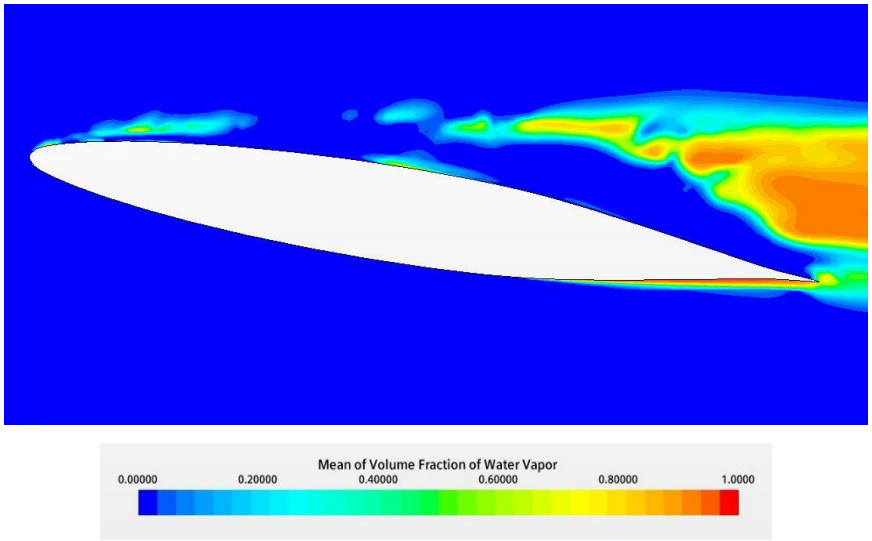

(b)

Figure 32: Visual comparison no aeration 9 AoA : (a) experimental (b) CFD VVF scene

The last step that was used in the validation of this case is image processing to estimate the percentage of the cavitation. This process incorporated cropping the CFD and experimental images to include the area around the hydrofoil, contrast enhancement, and converting them into binary images (0 = black and 1 = white) to differentiate the pixels. This process is illustrated in *Figure 33* and *Figure 34* for the experimental part and CFD VVF scene, respectively.

The selected colored areas, shown in *Figure 33* (b), indicated the cavitation areas whereas the not selected color is the no cavitation zone. The visual indication of this phenomenon led to the validation that cavitation started next to the leading edge of the hydrofoil, extended, and then

detached from the hydrofoil. The same cavitation behavior was observed in the CFD as shown in the grayscale image, *Figure 34* (b). In the CFD case, the cavitation was also generated next to the hydrofoil leading edge and detached later as it extended downstream of the runner. The white pixels in the binary image were added then divided on the total number of pixels including the white and black. The ratio obtained indicated the cavitation area percentage and this procedure was followed in both CFD and experimental images. The results showed a very close cavitation area percentage between the experimental image, 7%, versus 9% for the CFD scene.

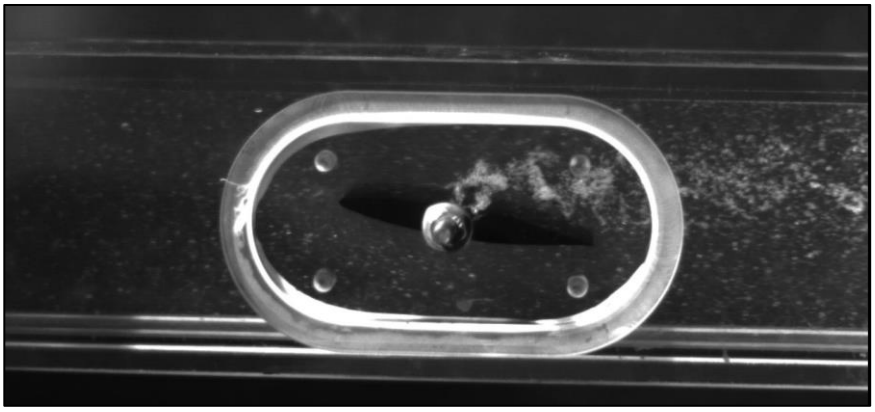

(a)

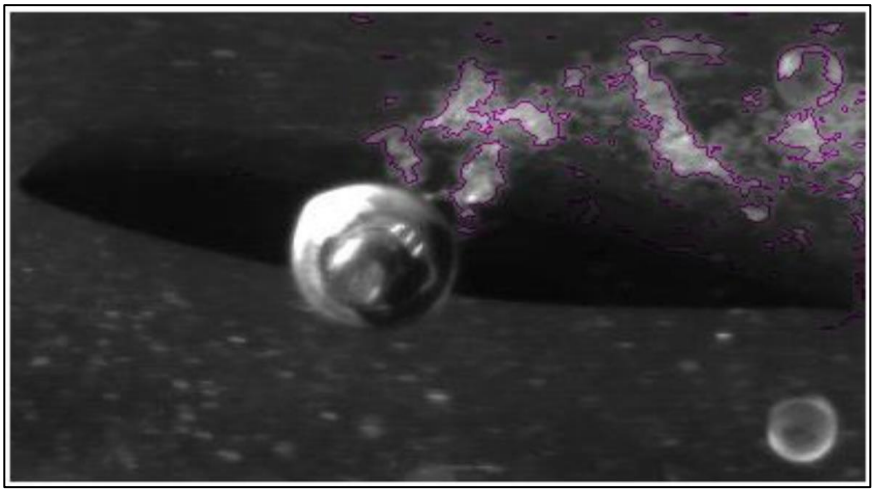

(b)

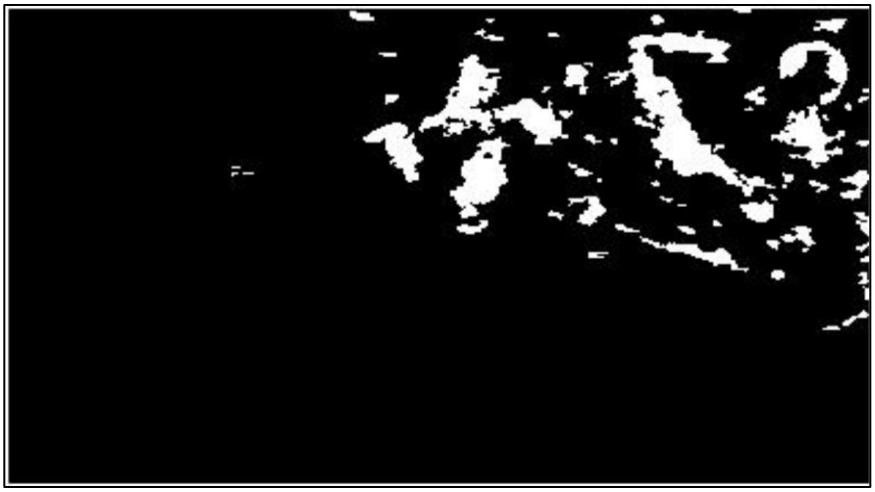

(c)

Figure 33: Experimental image processing for 9 AoA at 18.3 m/s water inlet velocity: (a) original image, (b) enhanced contrast, (c) binary converted image

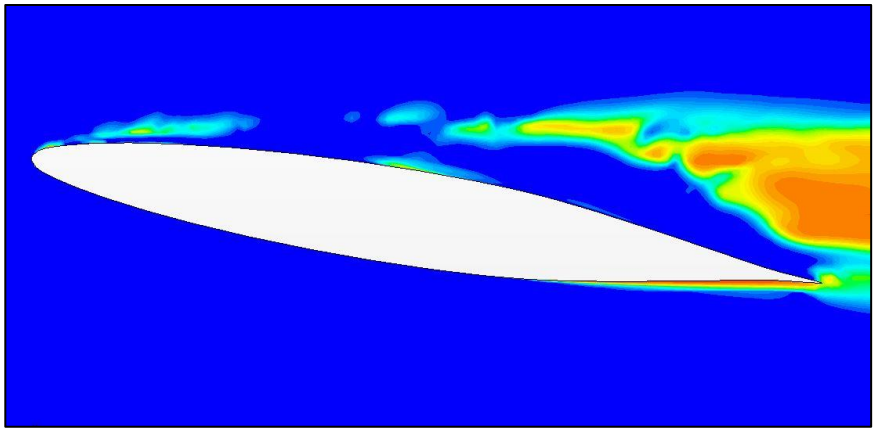

(a)

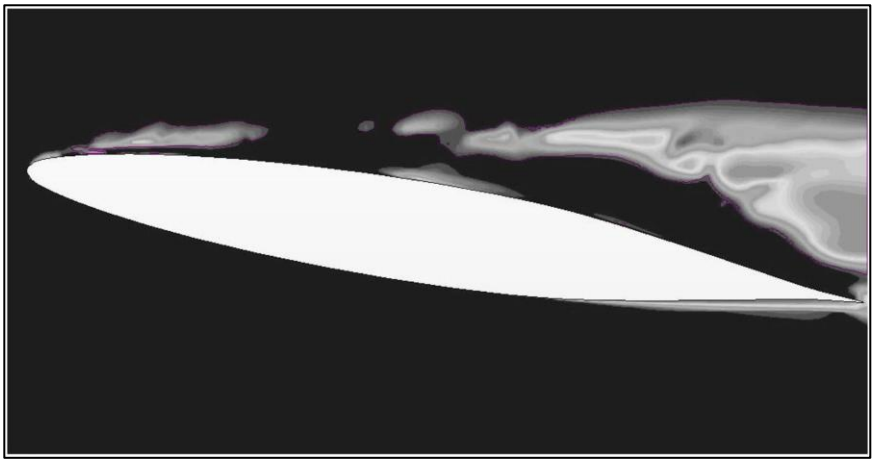

(b)

(c)

Figure 34: CFD image processing for 9 AoA at 18.3 m/s water inlet velocity: (a) original image, (b) grayscale converted image, (c) binary converted image

The approach detailed previously was adopted to the 12 AoA case as well. The water inlet velocity modeled in the CFD was 18.3 m/s (60 ft/s) to simulate the same flow parameters that were achieved in the experimental testing. As for the cavitation area percentage, the image processing of the CFD scene exhibited 11% whereas the experimental part indicated a 9% cavitation area. The image processing of the experimental part and CFD scene for the 12 AoA case is illustrated in *Figure 35*.

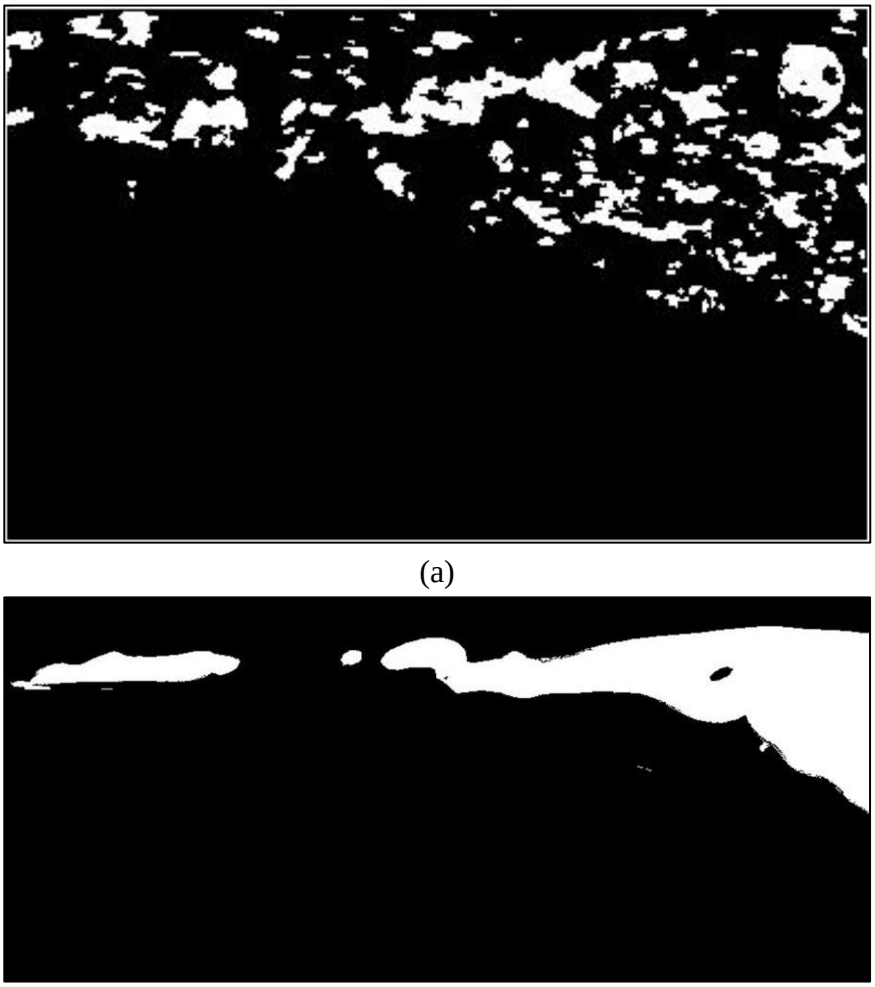

(a)

(b)

Figure 35: 12 AoA at 18.3 m/s water inlet velocity case image processing: (a) experimental binary image, (b) CFD binary image

3.4.4 Correlations of VVF and The Cavitation Number (σ)

The VVF distributions are time-averaged over the hydrofoil surface area to express a value for each case. Drag and lift coefficients were studied at different VVF values at different angles of attack (0, 6, 9, and 12 degrees).

Figure 36 shows how the VVF forms around the hydrofoil at different cavitation numbers at AoA of 6 degrees. At (σ = 1.36), a very small VVF was formed around the leading tip of the hydrofoil. As the cavitation number decreases at the same AoA, VVF starts getting higher in the value, and increasing until (σ = 0.3), where the VVF had reached the high values all over the hydrofoil from the leading tip to the trailing edge.

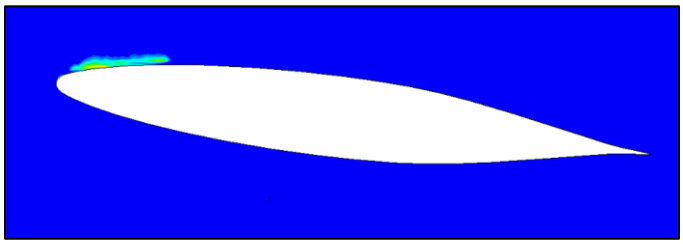

(a) σ = 1.36

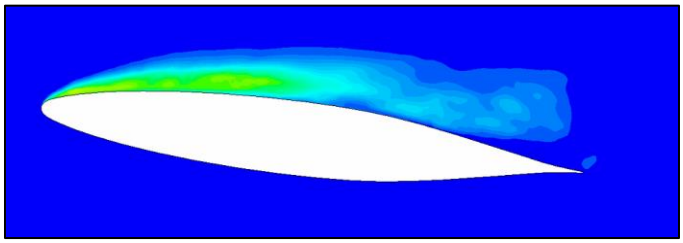

(b) σ = 0.91

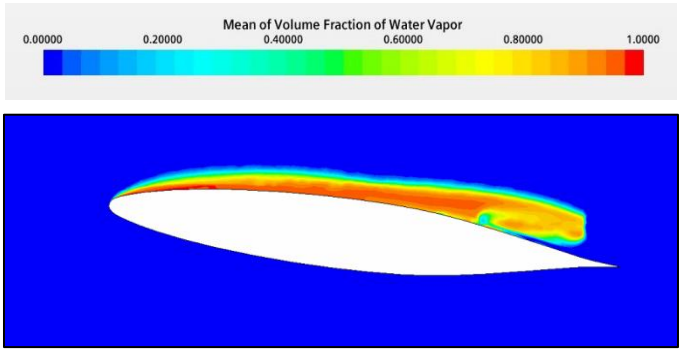

(c) σ = 0.53

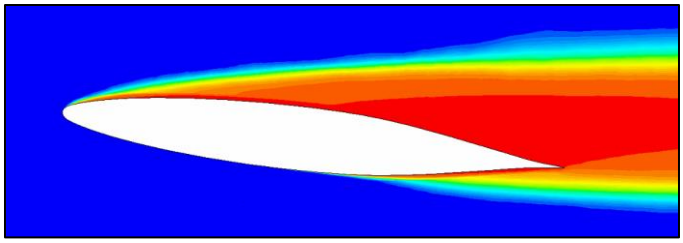

(d) σ = 0.30

Figure 36: VVF around hydrofoil at different cavitation number for 6 degrees AoA

As the σ decreases, the pressure drops below the vapor pressure leading to more cavitation. This increment in VVF can be explained by the pressure scenes in *Figure 37*. The absolute pressure around the hydrofoil tends to decrease as the σ decreases. The dark blue areas represent the areas where the absolute pressure is equal to or less than the water vapor pressure.

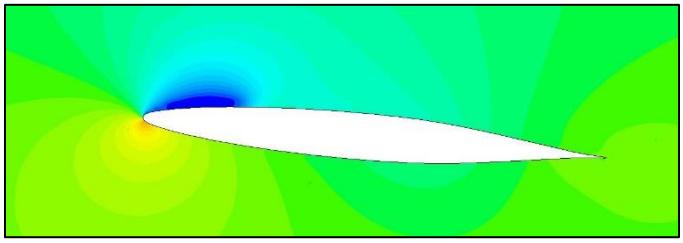

(a) σ = 1.36

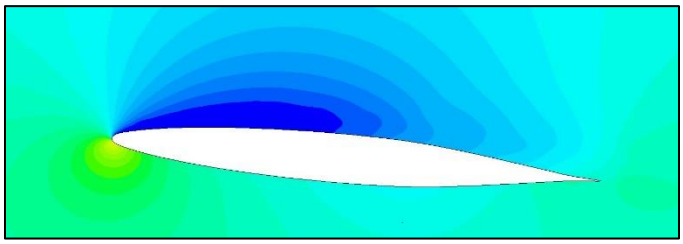

(b) σ = 0.91

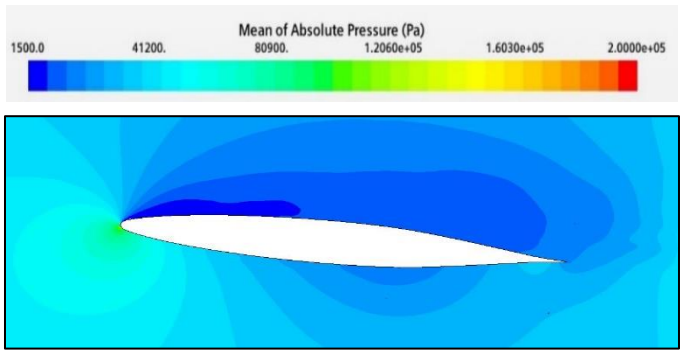

(c) σ = 0.53

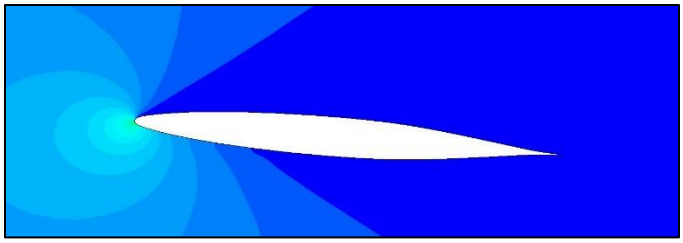

(d) σ = 0.30

Figure 37: Absolute pressure around hydrofoil at different cavitation number for 6 degrees AoA

At the same cavitation number of 0.3, velocity magnitude has been constructed at different angles of attack showing that the average velocity obtained for the fluid around the hydrofoil increases with the increase of the AoA for the same cavitation number, all that can be observed from *Figure 38*. Also, the separation spreads more over the hydrofoil surface by the increase of the AoA, and it extends towards the leading edge as seen in the cases of 9 and 12 degrees.

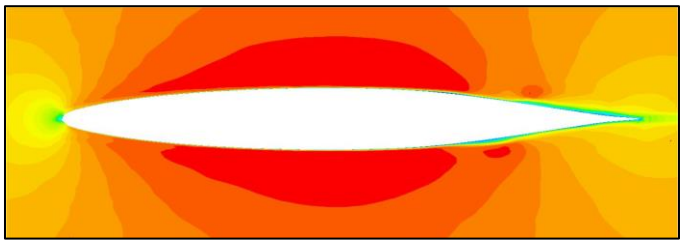

(a) 0 AoA

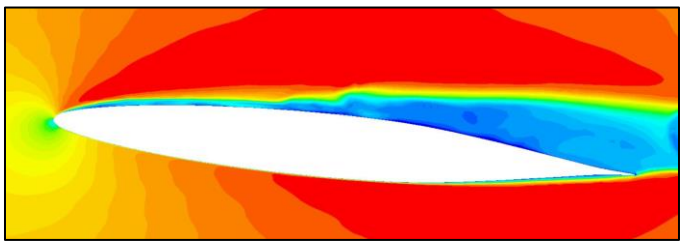

(b) 6 AoA

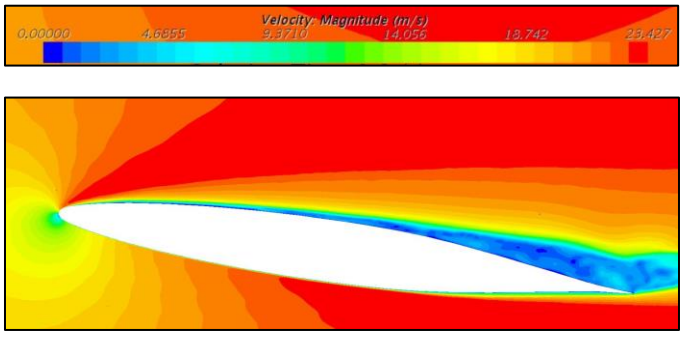

(c) 9 AoA

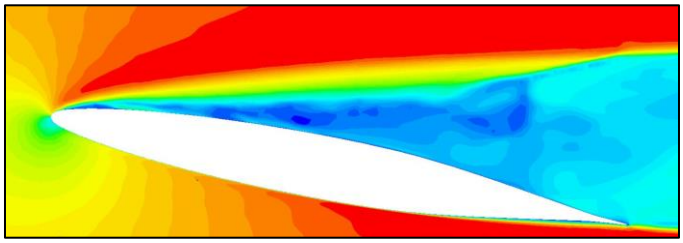

(d) 12 AoA

Figure 38: Velocity Magnitude around the hydrofoil at cavitation number of 0.3 for (0,6,9 & 12) degrees AoA

The cavitation could be initiated with an infinitesimal nucleus that withstands and starts the growth depending on some other factors like residence time, water temperature and quality, Reynolds number (Re), and the availability of solid boundaries and their roughness state. The Re at the water tunnel inlet for water is from 1.0 $x10^6$ to 2.0 x 10^6. The dependence of the cavitation number on the Reynolds number is evaluated and the critical cavitation number is different for each AoA, see *Figure 39*. The increase in the Re as the inlet water velocity increased led to an increment in the tendency for the cavitation to form over the hydrofoil. It was observed in all AoA cases, as indicated in *Figure 39*, that the σ decreased considerably with increasing the AoA. For instance, the σ at 9 AoA with was 1.1 at Re 1.9 x 10^6 whereas for 6 AoA is 0.7 at the same Re with which is almost a 35% increment.

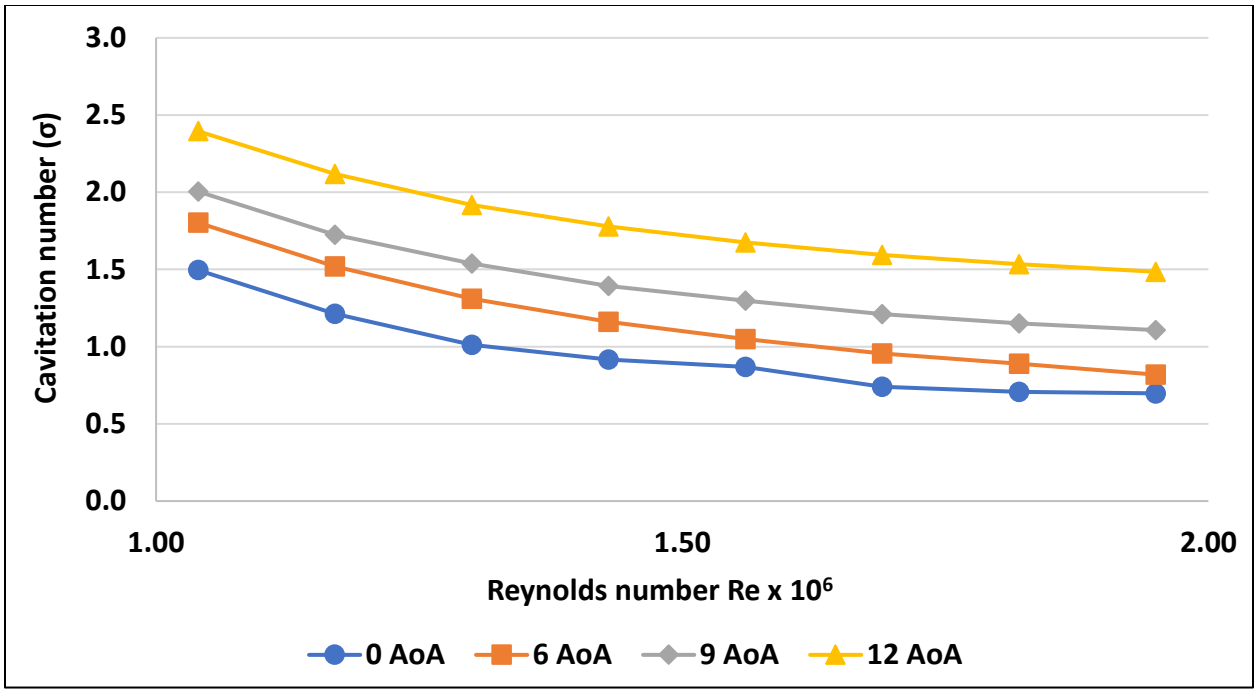

Figure 39: Dependence of cavitation number vs Reynolds number

With cavitation definition, and as shown in *Figure 40* that represents VVF at different cavitation numbers for different angles of attack (0, 6, 9, and 12 degrees), it can be noticed that, with the increase of the cavitation number, the VVF decreases in all cases of AoA. This phenomenon means the difference between the inlet pressure and the vapor pressure increases; thus, it supports the cavitation decrease for a higher σ number. For (9, 12) AoA where these angles are close to the stall angle, the cavitation is occurring at a higher σ, in our case less than (2.5). Also, for (0, 6) AoA, the cavitation formation starts at a lower σ less than (1.5).

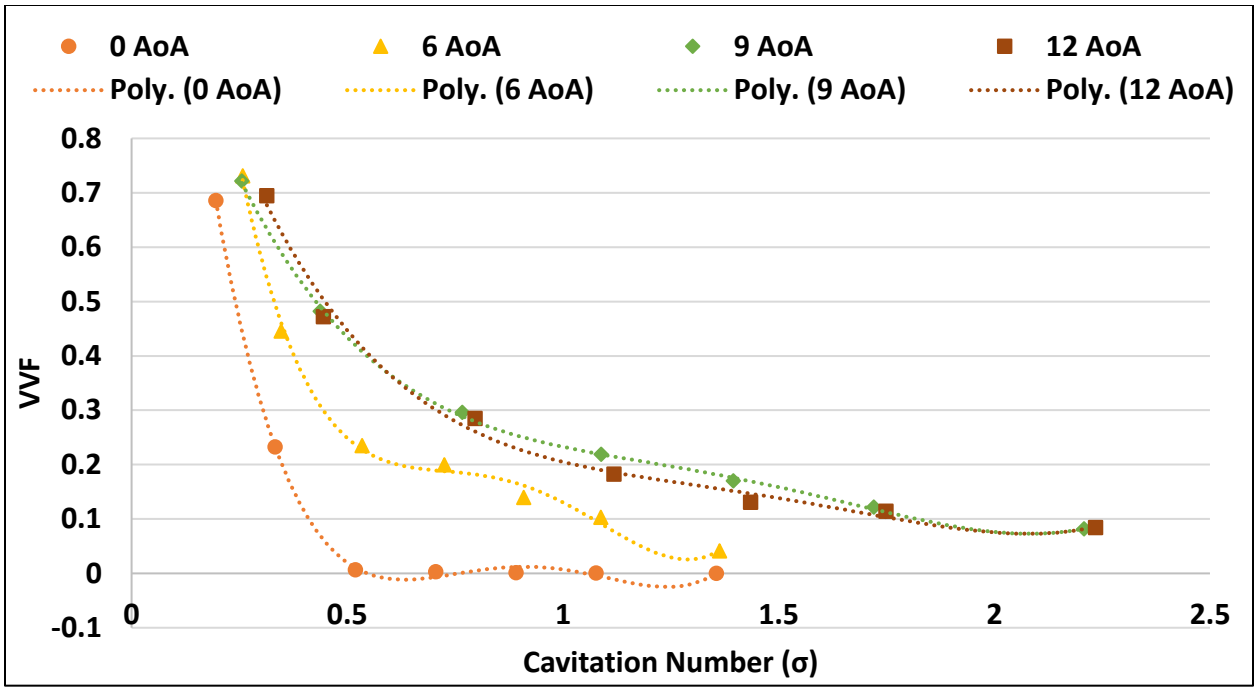

Figure 40: VVF at different cavitation number for (0, 6, 9 & 12) degrees AoA

The next observation from *Figure 40* is the higher the AoA, the higher the VVF value, and, thus, the tendency of cavitation goes up at any given cavitation number. When the AoA has the same inlet water velocity, 9 and 12 AoA have a similar pattern for all σ only with a slight difference in the lift coefficient values (see *Figure 42*). The cavitation behavior remains at the same level as long as the AoA is near the static stall angle of the hydrofoil. Figuring the correlation between the VVF and σ, the data points for each AoA are arranged in a way that a fourth-order curve could fit through them. The equations have a positive coefficient for (σ^4), while the other negative coefficients lead to the inverse correlation.

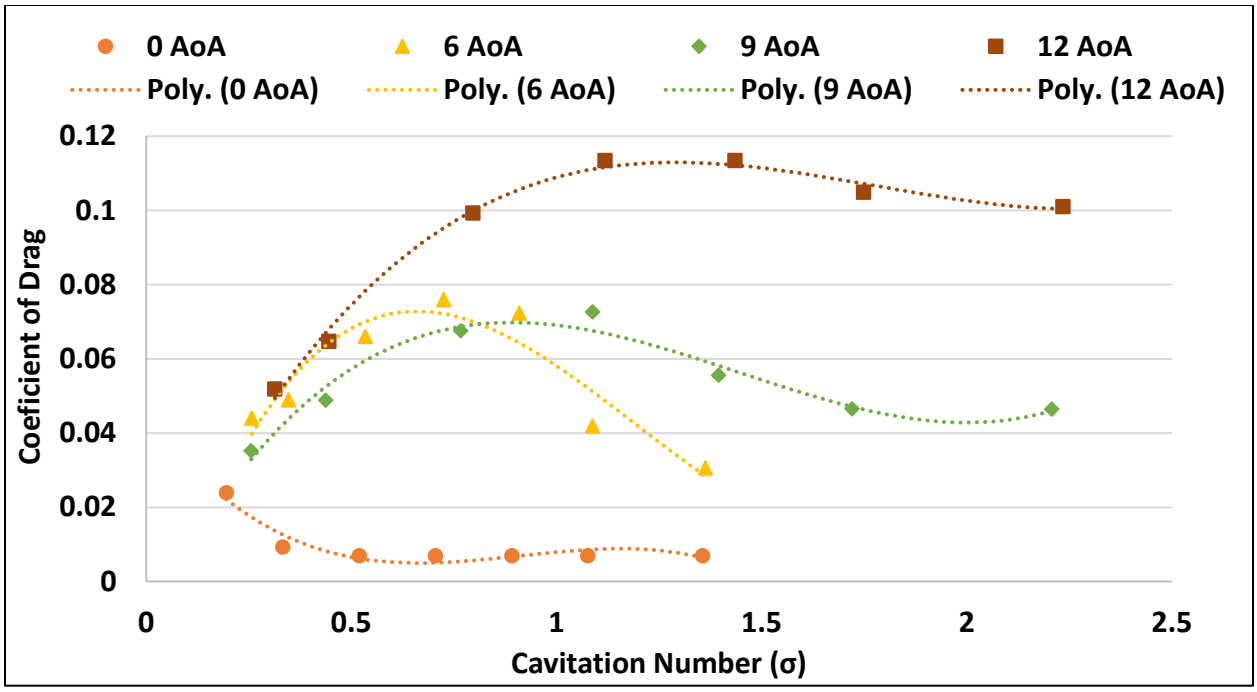

Figure 41: Drag coefficient variation for different (σ) values at different AoA

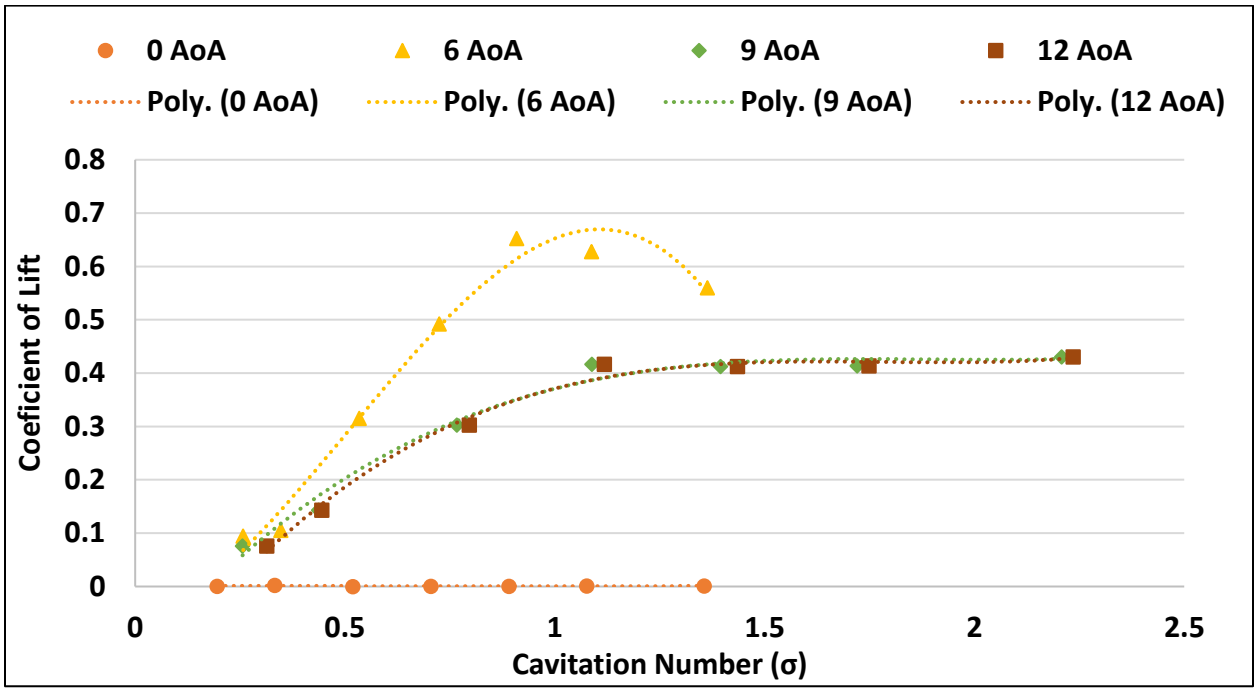

Figure 42: Lift coefficient variation for different (σ) values at different AoA

Cavitation number indicates the possibility of cavitation occurrence. In the current cases, a relation between drag and lift coefficients with the cavitation number was studied at different AoA.

It can be noticed from *Figure 41,* and *Figure 42* that at the same cavitation number, as the AoA increases, the drag and lift coefficients are quickly rising because of increased frontal area and the boundary layer thickness. The boundary layer around the hydrofoil is created by the water near the hydrofoil surface and the flow is reacting on the boundary layer as the physical surface of the hydrofoil. Due to increasing the AoA, this layer begins to separate from the surface and creates a different shape compared to the physical shape, which is called a stall, where both drag and lift forces become unsteady and difficult to predict. These two curves are separated into three zones; the first zone is the non-cavitating area where σ is higher than 1.5 this area. The drag and lift coefficients have almost constant values. The second zone is the sub-cavitating area with σ between 0.5-1.5, where the lift and drag coefficients hit the peak values. The third zone is the super-cavitating area where the σ is less than 0.5, and the drag and lift coefficients hit the minimum values. Around these values, the pressure over a substantial portion of the pressure side toward the trailing edge becomes quite low; causing a substantial loss of the lift and drag coefficients, as shown in *Figure 37*, *Figure 41,* and *Figure 42,* depicting the correlation of drag and lift coefficients with the cavitation number where third-order curves can fit most of the points.

Figure 43 shows how the drag coefficient tends to increase by the appearance of the vapor bubbles, which are described by the increase of the VVF values to reach its maximum of around 0.2 VVF. Then, the values of the drag coefficient go down by increasing the vapor bubbles over the hydrofoil. When the cavitation begins on the hydrofoil, the drag coefficient promptly increases and reaches the highest point when the cavitation is extended close to the trailing edge. Then, the drag coefficient decreases again as the cavitation number reduces (increase the VVF) further, as shown in *Figure 41* and *Figure 43*. The drag coefficient also increases when AoA increases at the same VVF as discussed before.

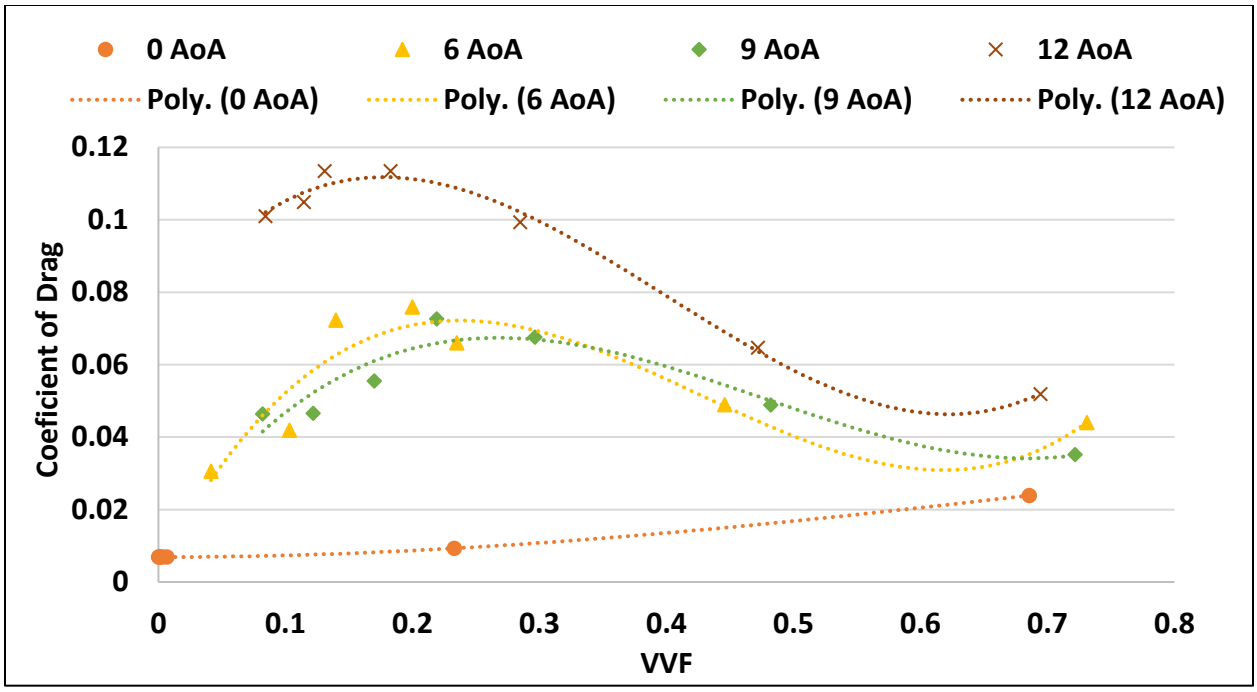

Figure 43: Drag coefficient variation for different VVF values at different AoA

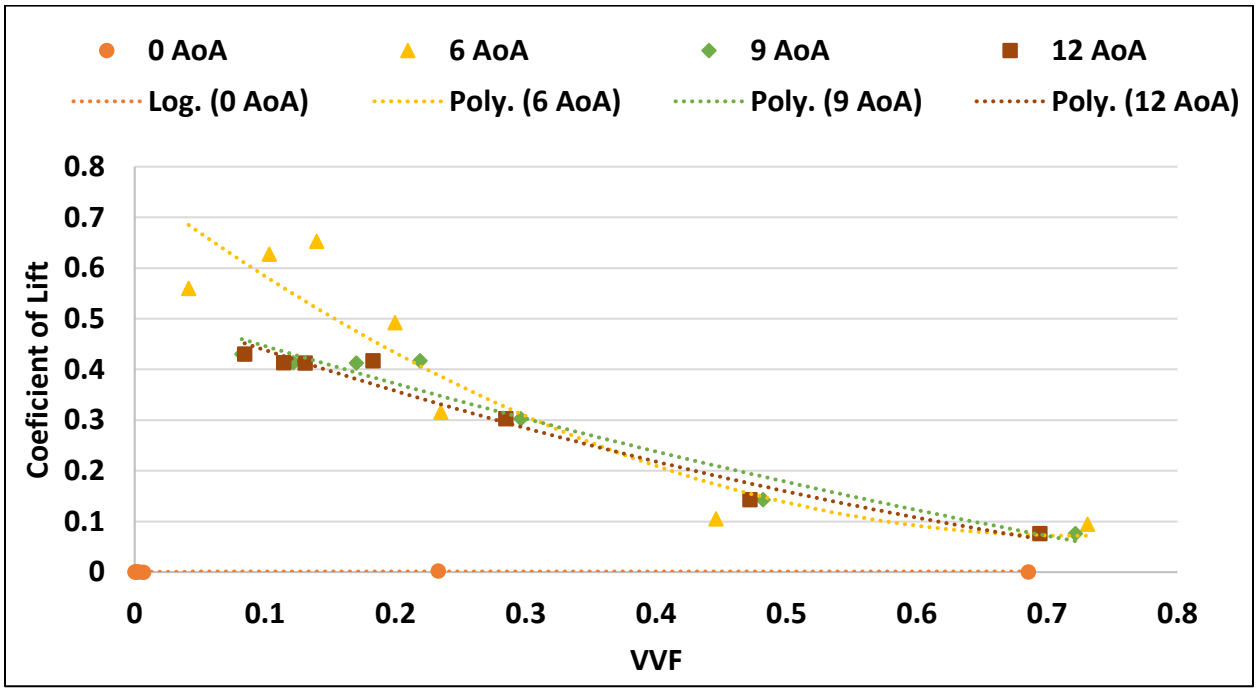

Figure 44: Lift coefficient variation for different VVF values at different AoA

As shown in *Figure 30* and *Figure 31* for 0 AoA, the drag and lift coefficients are almost zero for most of the cavitation numbers. This phenomenon is seen in most of the VVF values to be close to the low level in *Figure 43* and *Figure 44*.

For non-zero AoA, the lift coefficient starts decreasing with the increase of VVF, as can be noticed from *Figure 44*. At higher AoA, the lift coefficient starts falling with the increase of the vapor amount due to the loss of pressure difference on the pressure and suction sides of the hydrofoil. At high AoA, a small number of cavitation forms near the leading edge, which increases the lift and drag coefficients. It can be noticed that 6 AoA reaches a peak value at a smaller σ number than higher AoAs', and due to the higher velocity, this AoA was tested and simulated (see *Figure 42*).

The lift to drag ratio is one of the significant factors that affect the performance of the power in turbomachinery systems. Generally, the higher the lift to drag ratio, the better the efficiency of a turbomachine [112]. As shown in *Figure 45,* the relation between the cavitation number and the lift to drag ratio (L/D) was generated. L/D proportionally increases with the cavitation number, which shows the drop of the lift to drag ratio with the cavitation development; that is to say, the cavitation development is directly related to the performance of the turbomachines. Also, the case of 6 AoA seems to offer higher power production over the other cases of the AoA. Correlating the variables, L/D was found to be in a fourth-order correlation with the cavitation number at all the AoAs (except for the 0 AoA since there was no significant lift force generated).

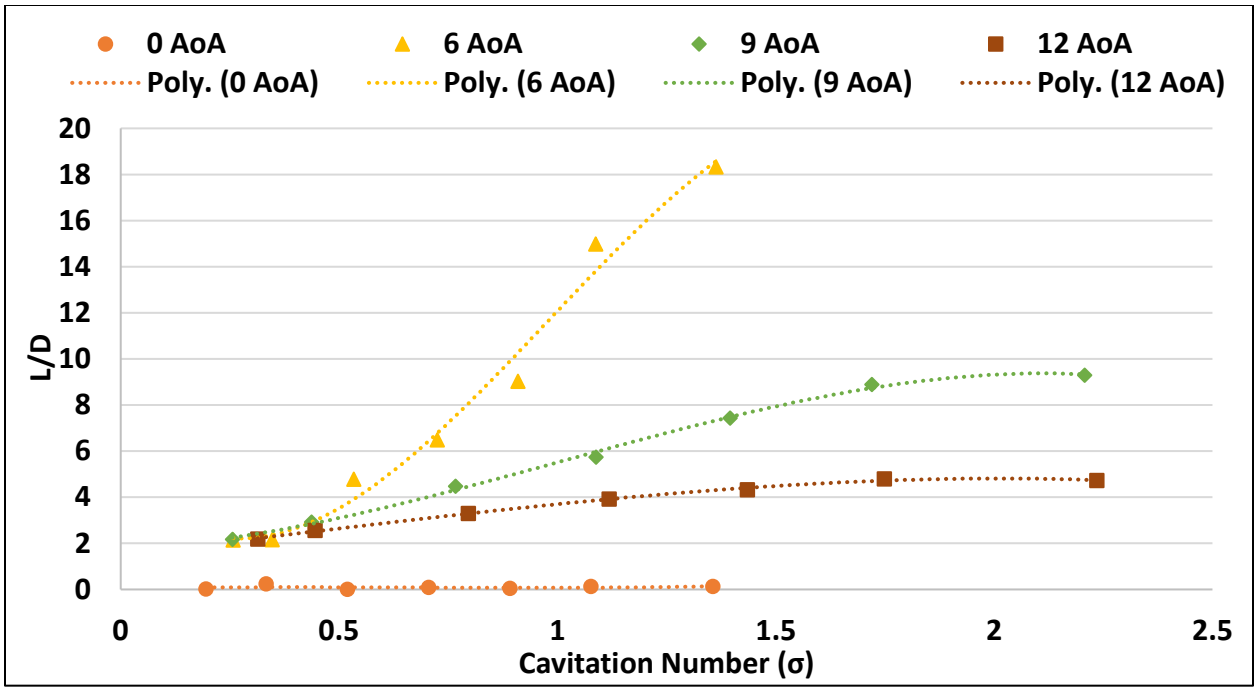

Figure 45: Lift to drag ratio at different cavitation number for (0, 6, 9 & 12) degrees AoA

3.5 Cavitation Treatment Simulations

The CFD models conducted in this study can be outlined as follows:

1. Initial simulations for each AoA at different inlet water velocities as a boundary condition without aeration.
2. Different water inlet velocity simulations with air injection at the same pressure.
3. Different air slots configuration for each AoA case at the same air injection pressure.

3.5.1 Modified New Hydrofoil Design

Based on previous results, a modified design for the hydrofoil has made with air slots on its upper surface to inject air close to the cavitation occurrence zones and study the opportunities of reducing the cavitation effect. In *Figure 46* below six air injection slots are added to the hydrofoil design. The slot width is considered as 5% of the Chord 0.42 cm (0.16 in), and the location of the slots was suggested based on the behavior of the cavitation in all four AoA cases.

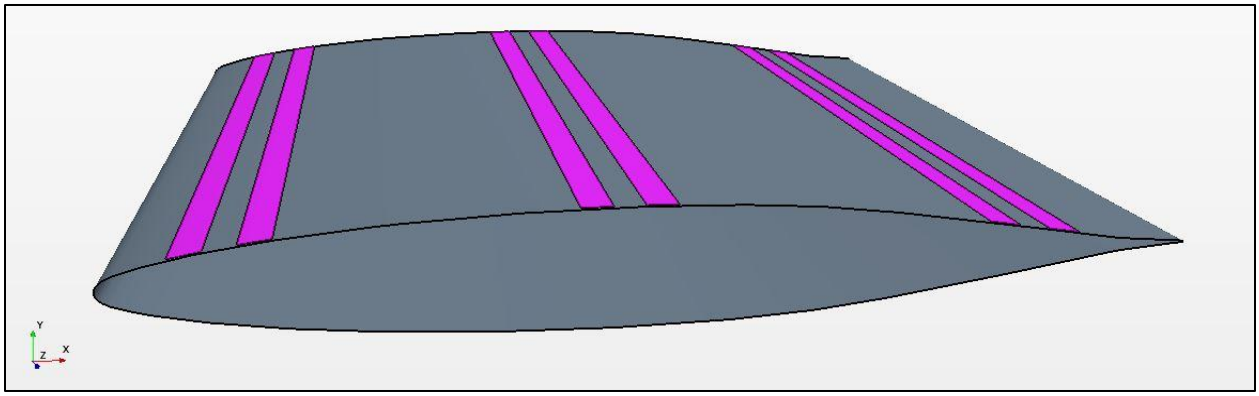

Figure 46: CAD model for modified NACA 661-012 hydrofoil with 6 air slots

3.5.2 Simulations Without Aeration

As mentioned before, constant water inlet water velocity was set as an inlet boundary condition in the first run of simulations and reduced gradually from 22.8 m/s (75 ft/s) to 12.2 m/s (40 ft/s). This approach was sought to induce and guarantee the presence of cavitation before air injection and calculate the cavitation number at each inlet water velocity. Although using an inlet constant water velocity as a boundary condition is not an erroneous method, however, velocity inlet is preferable for incompressible flows and the best way to control the cavitation phenomena at the current experimental setup. Velocity inlet boundary condition results in a better convergence and hence enhanced stability.

The outlet boundary conditions were maintained as atmospheric pressure and similar VOF conditions as in the inlet. The simulations were executed and the VVF along with the absolute pressure, and L/D were monitored.

It is also worth mentioning that the constant water inlet velocity boundary condition will ensure the study of aeration effect on the cavitation solely. The air injection will change the water velocity in a constant inlet pressure case since the velocity is not set as a constant input in the simulations. Thus, the cavitation pattern will be affected due to the fluctuation in the water velocity. However, the water velocity will not be altered in the constant water inlet velocity case

as the air is being introduced. Therefore, the cavitation pattern will only be affected by the air injection which is the aim of this research.

3.5.3 Air Injection Simulations

The air injection simulations are similar to the constant water velocity ones with the addition of aeration. Air is being introduced over the hydrofoil as shown in *Figure 46* with the magenta color. Air was injected at 0 psig gauge pressure for each AoA. The cavitation patterns, as well as the VVF, were monitored and compared with the no aeration simulations. Additionally, the L/D per each simulation was compared with the no aeration case to investigate the effect of aeration on the turbine performance.

3.5.4 CFD Results: Constant Water Inlet Velocity

3.5.4.1 *Case 1: No Aeration*

The first run of the CFD simulations was conducted without aeration to obtain the data of the cavitation. This case is considered as the "baseline" in which the data gathered were compared to the values generated by air injection models. *Figure 47* represents VVF scenes for all AoA (0 to 12 degrees). The VVF is represented on a scale of 0 – 1, where 1 indicates a 100% water vapor area and denoted in red color as can be seen in *Figure 47*.

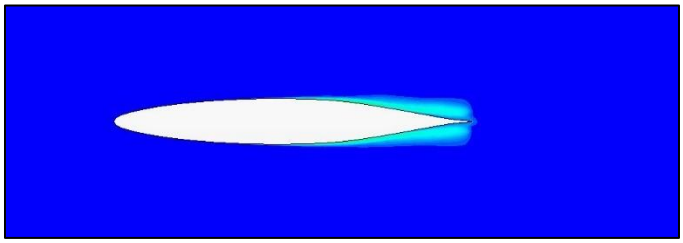

(a) 0 AoA

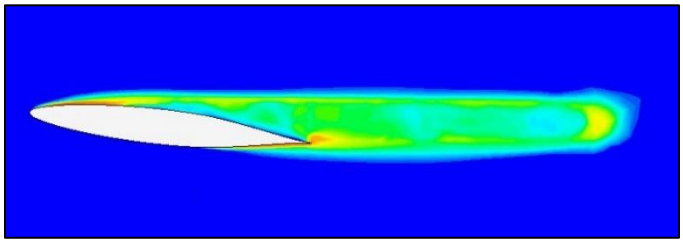

(b) 6 AoA

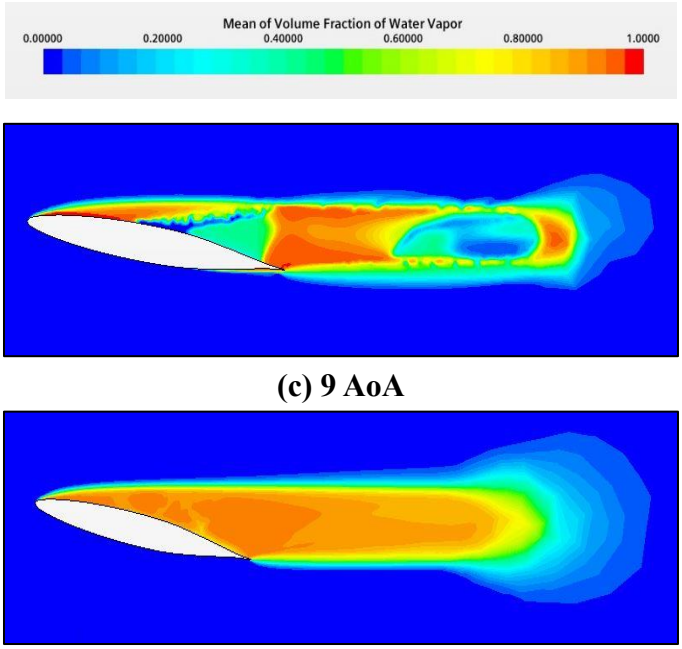

(c) 9 AoA

(d) 12 AoA

Figure 47: VVF around hydrofoil – no aeration case at 22.8 m/s water inlet velocity for (0, 6, 9 & 12) degrees AoA

The area representing the hydrofoil VVF increases with increasing the AoA as can be inferred from the VVF scenes. As the AoA increases, the pressure drops below the vapor pressure (see *Figure 48*) leading to more cavitation. Moreover, the cavitation cloud is being occurred near the leading edge of the hydrofoil as the AoA increases.

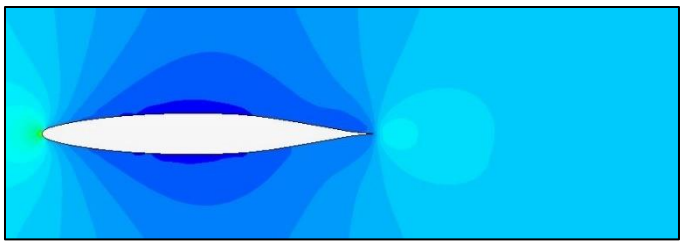

(a) 0 AoA

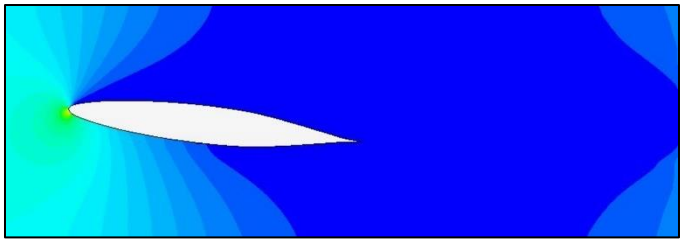

(b) 6 AoA

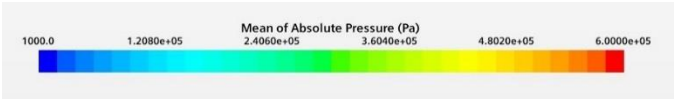

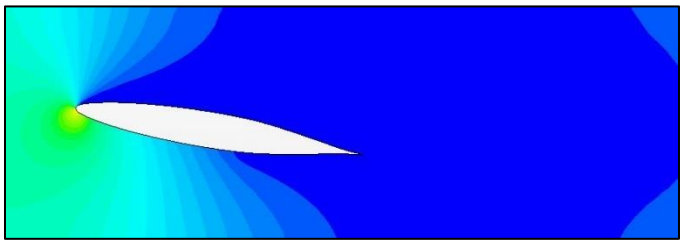

(c) 9 AoA

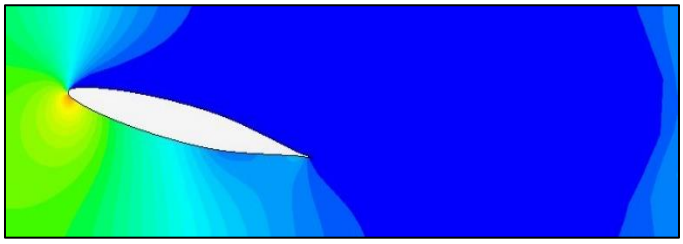

(d) 12 AoA

Figure 48: Absolute pressure CFD scenes – no aeration case at 22.8 m/s water inlet velocity for (0, 6, 9 & 12) degrees AoA

The results of the no aeration case are summarized in *Table 3*. As indicated previously, the VVF increased with the increasing the AoA and at the same AoA, the VVF increased with increasing the water inlet velocity. The lift to drag ratio for the hydrofoil increased as the water inlet velocity and VVF decreased for most AoA which means the best performance for the turbomachines.

Table 3: No aeration case summary of CFD results

0 AoA			
Water Inlet Velocity (m/s)	σ	VVF	L/D
22.86	0.501	2.36E-01	0.0422

21.34	0.521	4.95E-05	0.8303
19.81	0.591	1.71E-07	0.7240
18.29	0.680	5.36E-08	0.7203
16.76	0.793	6.45E-09	0.8767
15.24	0.942	0	0.5738
13.72	1.142	0	0.4377
12.19	1.421	0	0.5113
6 AoA			
22.86	0.656	4.41E-01	2.4204
21.34	0.659	4.07E-01	2.4197
19.81	0.688	3.15E-01	2.5250
18.29	0.811	2.26E-01	3.5820
16.76	0.946	1.85E-01	4.2521
15.24	1.086	1.75E-01	5.7932
13.72	1.280	1.70E-01	7.7306
12.19	1.501	1.05E-01	12.5195
9 AoA			
22.86	0.850	4.54E-01	2.5617
21.34	0.852	4.24E-01	2.5601
19.81	0.854	4.00E-01	2.5601
18.29	0.854	3.32E-01	2.5524
16.76	1.005	1.56E-01	3.1661
15.24	1.202	1.31E-01	3.8338
13.72	1.430	1.21E-01	4.1825
12.19	1.674	8.92E-02	5.4479
12 AoA			
22.86	1.198	4.62E-01	2.9509
21.34	1.214	4.52E-01	2.9528
19.81	1.204	4.50E-01	2.9052
18.29	1.210	4.05E-01	2.9079
16.76	1.222	2.04E-01	2.9176
15.24	1.299	1.10E-01	3.0293
13.72	1.608	1.02E-01	3.3773
12.19	1.886	7.09E-02	3.5666

3.5.4.2 *Case 2: 0 PSI with 6 Air Injection Slots*

The first aeration case was conducted with air injection at 0 psig from all of the 6 air slots to investigate the effect of adding a minimal amount of air all over the hydrofoil. It can be inferred from *Figure 49* that the areas representing the cavitation were reduced to the minimum in each AoA when compared with the no aeration case. The reduction in the VVF was more noticeable at

higher AoA (9 and 12 degrees). It can be justified from the absolute pressure scenes in *Figure 50* that indicated that the areas in which the absolute pressure is less or equal to the vapor pressure were reduced when compared to the no aeration case. Thus, it can be deduced that even a minimal air injection can lead to a high reduction in cavitation.

Table 4 lists the results of the hydrofoil VVF, σ, and the L/D of the 0 psig with 6 air injection slots case. The VVF showed an average reduction of 97.9% when compared to the no aeration case. The L/D was also reduced when compared to the no aeration case with an average reduction of 22.3%. The reduction in the L/D is due to introducing another substance, i.e. air, that caused reaction forces opposing the drag and lift forces acting on the hydrofoil. Thus, that caused the reduction in the L/D ratio in most cases.

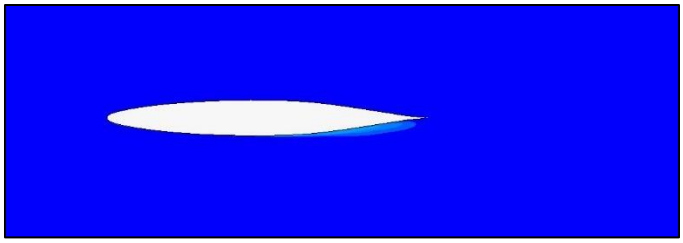

(a) 0 AoA

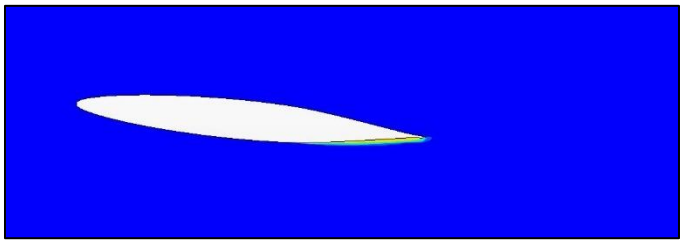

(b) 6 AoA

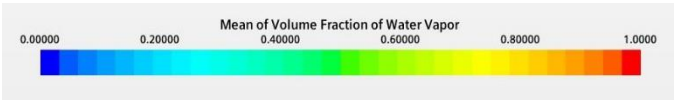

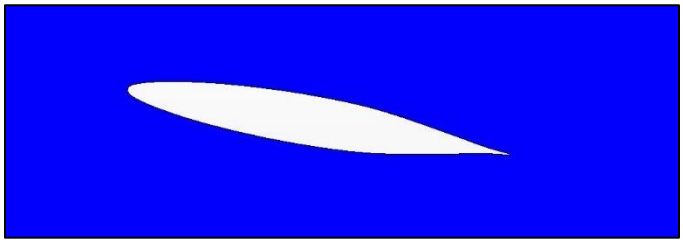

(c) 9 AoA

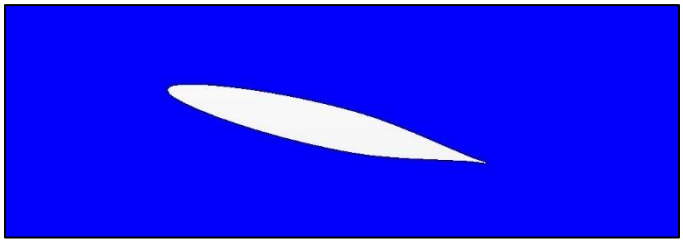

(d) 12 AoA

Figure 49: VVF around hydrofoil – 0 psi with 6 air slots case at 22.8 m/s water inlet velocity for (0, 6, 9 & 12) degrees AoA

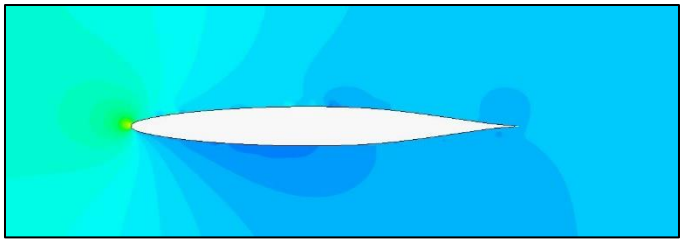

(a) 0 AoA

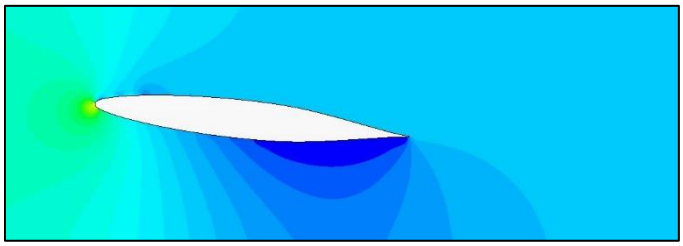

(b) 6 AoA

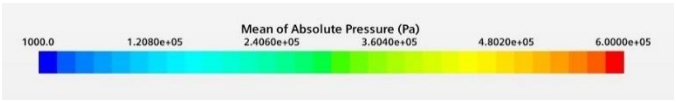

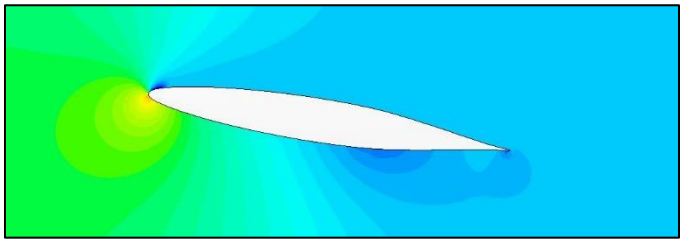

(c) 9 AoA

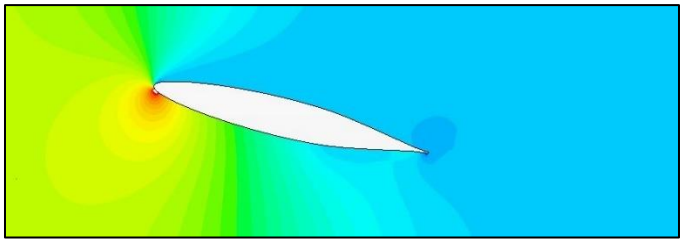

(d) 12 AoA

Figure 50: Absolute pressure CFD scenes – 0 psi with 6 air slots case at 22.8 m/s water inlet velocity for (0, 6, 9 & 12) degrees AoA

Table 4: 0 PSI with 6 air slots case summary of CFD results

0 AoA			
Water Inlet Velocity (m/s)	σ	VVF	L/D
22.86	0.708	4.83E-04	7.9116
21.34	0.698	5.45E-06	15.4946
19.81	0.741	2.00E-08	36.9806
18.29	0.916	6.40E-09	10.2650
16.76	0.868	7.10E-10	48.7770
15.24	1.012	0	49.8089
13.72	1.213	0	49.0457
12.19	1.496	0	49.2689
6 AoA			
22.86	0.819	3.61E-03	3.8679
21.34	0.890	3.22E-03	2.6851
19.81	0.956	7.50E-06	2.8553
18.29	1.049	3.27E-09	3.0456
16.76	1.161	2.15E-07	3.2048
15.24	1.310	1.02E-05	3.2650
13.72	1.519	8.42E-09	3.3570
12.19	1.803	7.06E-10	3.3342
9 AoA			
22.86	1.107	4.02E-03	2.0043
21.34	1.150	3.60E-03	1.9564
19.81	1.211	1.76E-03	1.8956
18.29	1.298	1.53E-03	1.9442
16.76	1.393	9.62E-04	1.9930
15.24	1.539	9.20E-04	2.0181
13.72	1.725	8.80E-04	2.1615
12.19	2.005	9.97E-04	2.2142
12 AoA			
22.86	1.485	9.18E-06	2.7100
21.34	1.533	8.69E-06	2.6911
19.81	1.594	6.72E-06	2.6556
18.29	1.675	3.38E-06	2.6048
16.76	1.778	3.15E-06	2.5633
15.24	1.918	9.61E-07	2.5226
13.72	2.118	3.78E-07	2.4988
12.19	2.395	1.53E-08	2.4991

3.5.4.3 *Effect of Air*

When air enters the system like a jet, it is affected by the two motion components: radially upward due to the pressurization, axial flow with the liquid water. The air content is added as a

factor in changing the shape of the vapor cloud over the hydrofoil. *Figure 51* displays the air and vapor volume fraction over the hydrofoil after reaching the steady state period. The domination of air over the hydrofoil diminishes the existence of vapor at the same place, which indicates the merit of air injection.

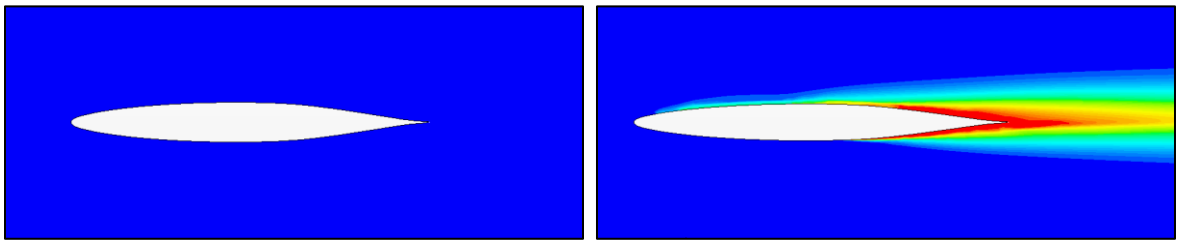

(a) 0 AoA

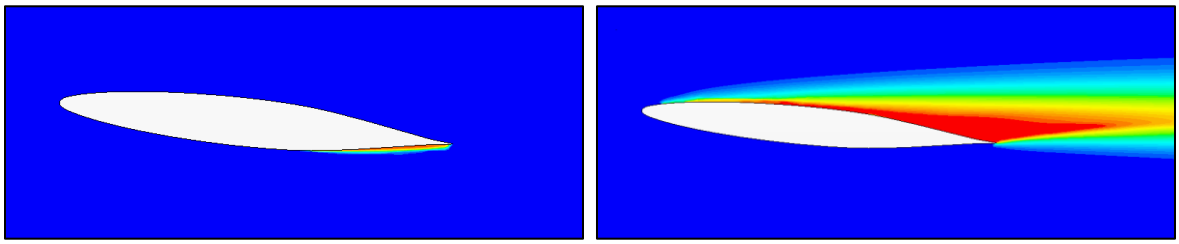

(b) 6 AoA

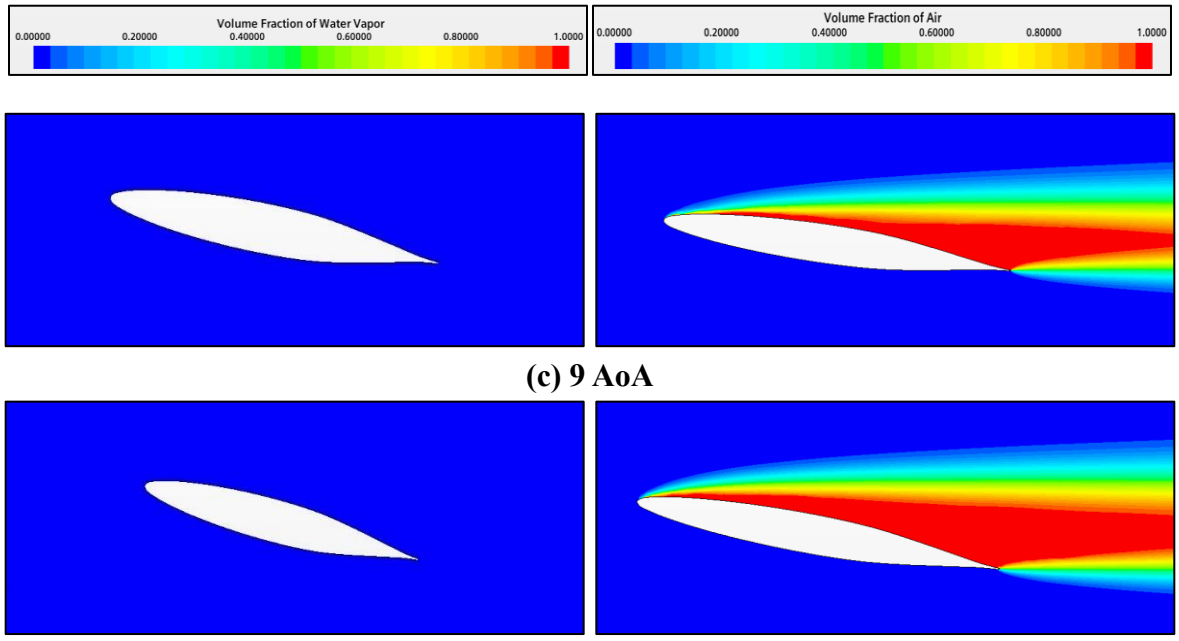

(c) 9 AoA

(d) 12 AoA

Figure 51: Volume fraction distribution for air (right scenes), and water vapor (left scenes) around hydrofoil after 0.2s– 0 psi with 6 air slots case at 22.8 m/s water inlet velocity for (0, 6, 9 & 12) degrees AoA

3.5.4.4 *Case 3: 0 PSI with 3 Air Injection Slots*

To study the air configuration effect on the cavitation, the air injection pressure and the water inlet velocity were fixed at 0 psig, and 22.86 m/s (75 ft/s) respectively. Air Injection slots were decreased in the second case of aeration to 3 air slots as shown in *Figure 52*. The cavitation pattern did not change from case 2 previously discussed and showed almost the same results.

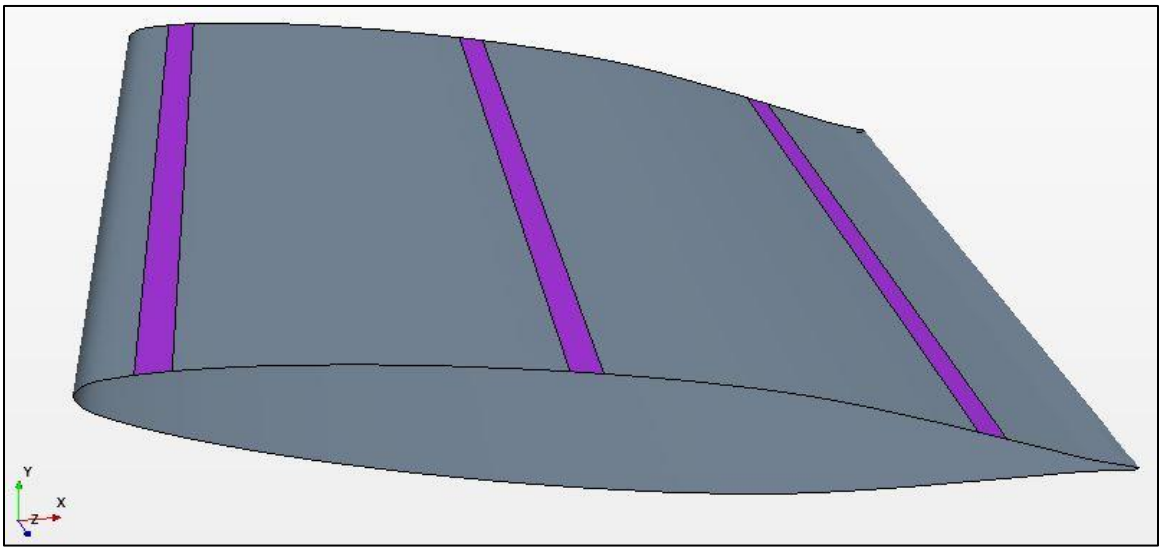

Figure 52: CAD model for modified NACA 661-012 hydrofoil with 3 air slots

The average reduction in the VVF is 93% in comparison to the no aeration case. The L/D ratio was also reduced when compared to the no aeration case with an average reduction of 14.3%. The results of the 3 air injection slots case are summarized in *Table 5*.

Table 5: 0 PSI with 3 air slots case summary of CFD results

0 AoA			
Water Inlet Velocity (m/s)	σ	VVF	L/D
22.86	0.645	1.30E-01	11.6493
6 AoA			
22.86	0.785	1.71E-01	3.6042
9 AoA			
22.86	1.092	5.44E-04	2.0406
12 AoA			
22.86	1.471	1.13E-05	2.7073

3.5.5 Results Comparison

It can be inferred from *Table 4* and *Table 5* that the VVF values were reduced while increasing the air injection slots over the hydrofoil. The highest reduction achieved is at 6 air slots case. Thus, it can be concluded that increasing the air injection slots leads to more treatment of cavitation and improved performance of the turbine in the long run. However, it should be noted that air slots were opened over the hydrofoil and it might affect the strengthening of the material, and the more air slots introduced, the more the hydrofoil might be weak. Hence, it will be an expensive approach to treat cavitation in hydro turbines. Also, introducing the air might lead to air entrainment which also impacts the components of the hydro turbine system. Therefore, it is worth investigating the impact and the feasibility of increasing the air slot injection.

To have a better understanding of the correlation between the cavitation and injecting air at different AoA, the hydrofoil average pressure scenes at the same water inlet velocity were examined more thoroughly. *Figure 53* shows the hydrofoil absolute pressure scenes of the four AoA cases at no aeration at the left-side scenes and with 3 slots air injection at 0 psig air pressure at the right-side scenes. The figure indicates that with minimum air pressure 0 psig, the pressure over the hydrofoil raised to more than the water vapor pressure and treat the cavitation. Furthermore, as the AoA increased the pressure over the hydrofoil raised to higher values leading to more cavitation treatment. This is more distinguished when looking at the 9 and 12 AoA scenes.

The air injection effect is even more obvious when looking at the VVF against the water inlet velocity presented in *Figure 54* and *Figure 55*. The first figure representing the no aeration case, which is the baseline case, had the highest VVF reaching up to 0.46 at 22.8 m/s for 12 degrees AoA. As air is being introduced with 0 psig, it can be shown clearly in the second figure how the air is effectively treating the cavitation phenomenon for all AoA and at all water velocity values.

Even with the smallest amount of air being injected 0 psig, can help in reducing the cavitation with a huge amount reaching up to 99% for 12 degrees AoA. The behavior of the cavitation treatment in the 0, 6, & 9 degrees AoA cases are almost similar whereas in the 12 degrees AoA case the reduction was larger, as shown in the graph. This is due to the remarkable increase of the absolute pressure in the system at the 12 degrees AoA case as seen in the pressure scenes, leading to better treatment of cavitation. As the AoA increased, the VVF reduction became larger since the cavitation increases at higher AoA. The reduction of the VVF at the 6 degrees AoA was 93% while maximizing at 99% in the 12 degrees AoA case.

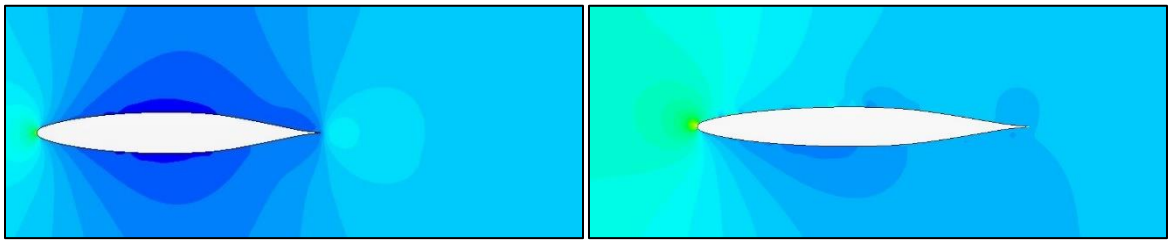

(a) 0 AoA

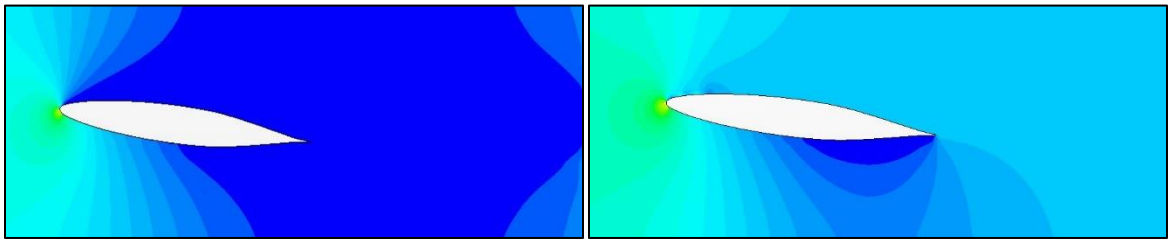

(b) 6 AoA

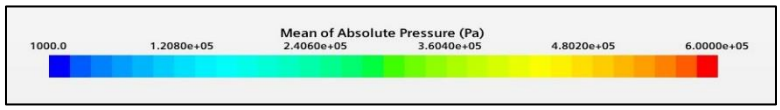

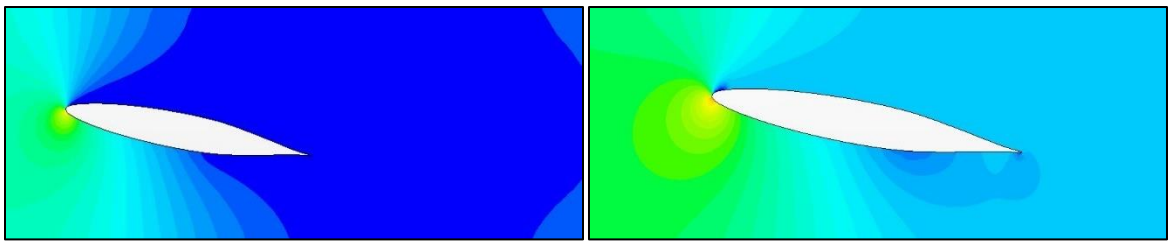

(c) 9 AoA

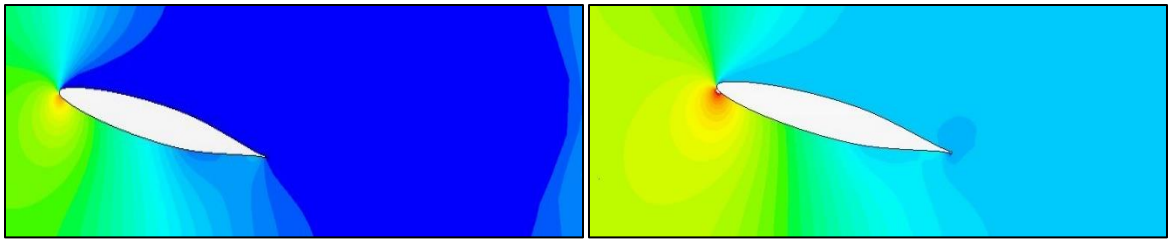

(d) 12 AoA

Figure 53: Absolute pressure – with aeration (on right) and without aeration (on left) cases at 22.8 m/s water inlet velocity for (0, 6, 9 & 12) degrees AoA

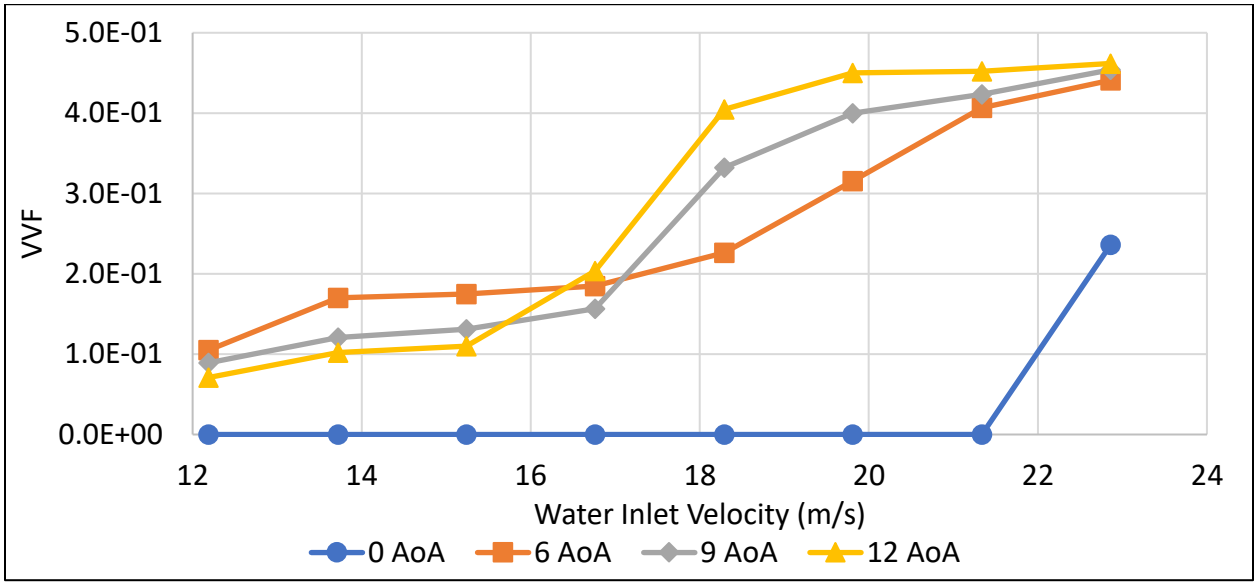

Figure 54: No aeration - VVF at different water velocity for (0, 6, 9 & 12) degrees AoA

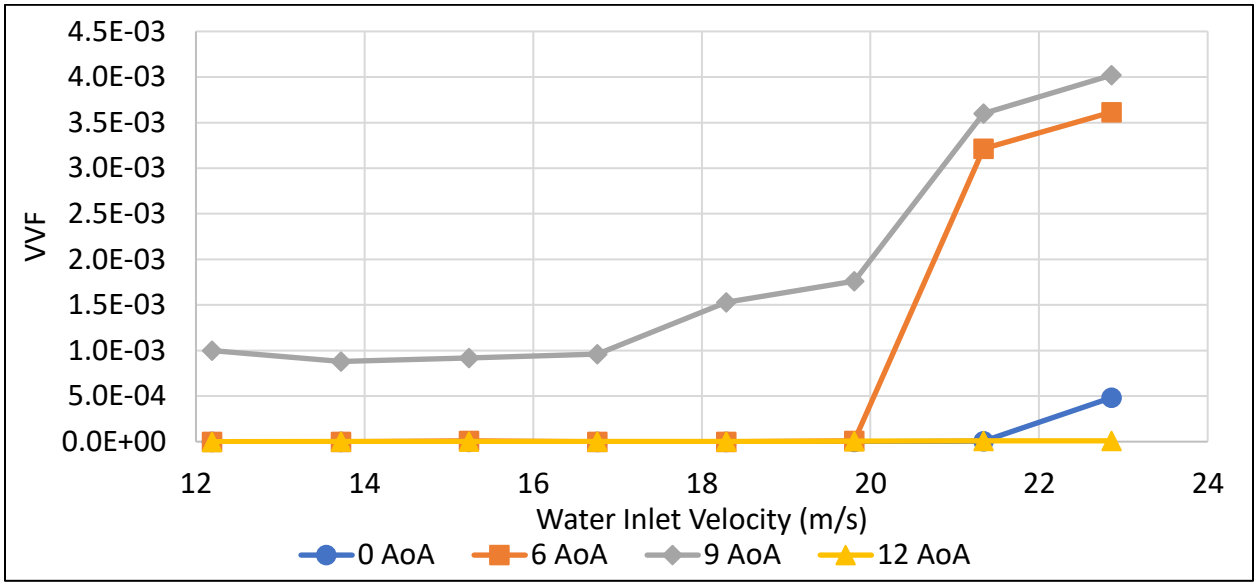

Figure 55: 0 PSI - VVF at different water velocity for (0, 6, 9 & 12) degrees AoA

The increase in the σ as the air is injected over the hydrofoil led to a decrease in the tendency for the cavitation to form and thus reducing the cavitation. It was observed in all AoA cases, as indicated in the difference between *Figure 56* and *Figure 57*, that the σ increased considerably with increasing the AoA. For instance, the σ at 6 AoA with no aeration case was 0.656 at 22.8 m/s whereas 0.819 at the same water velocity with 0 psig air pressure case which is almost a 25% increment.

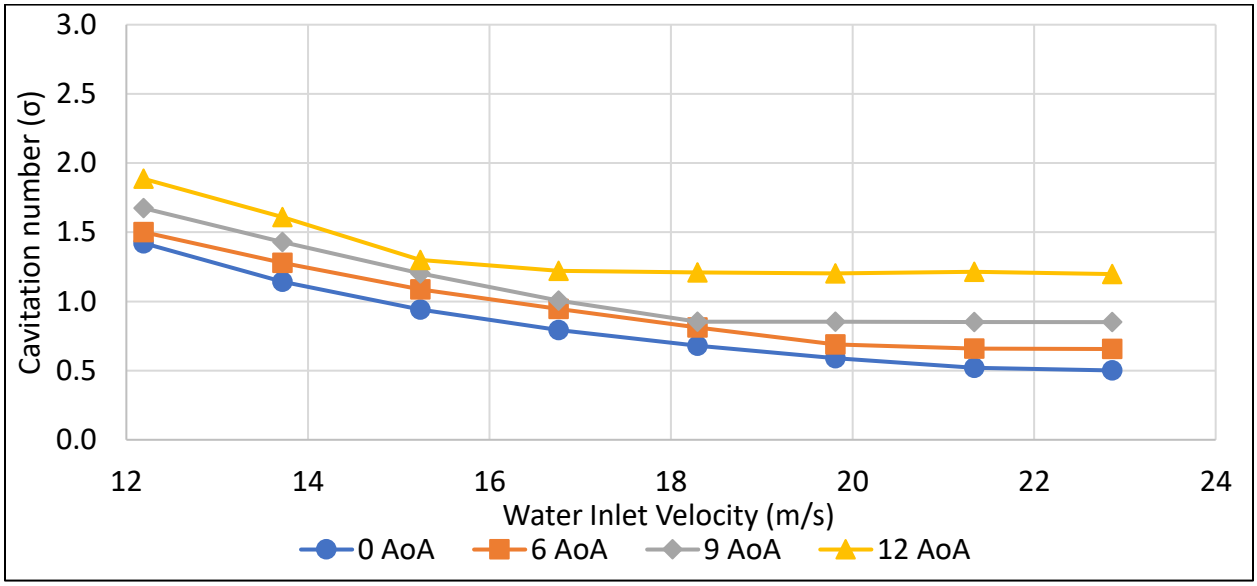

Figure 56: No aeration - Cavitation number at different water velocity for (0, 6, 9 & 12) degrees AoA

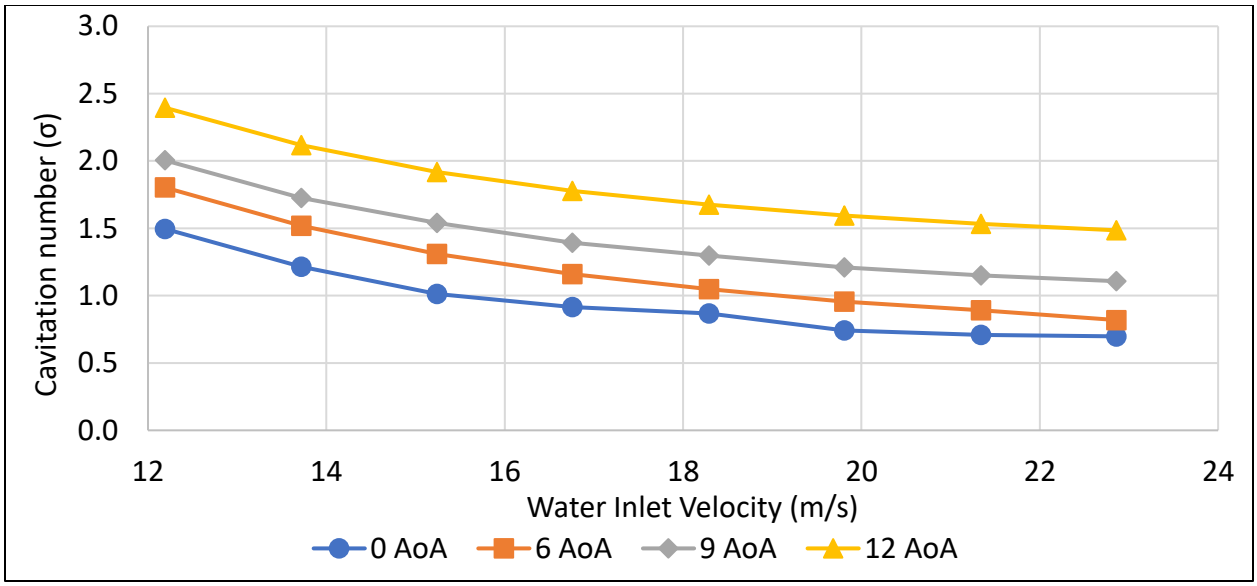

Figure 57: 0 PSI - Cavitation number at different water velocity for (0, 6, 9 & 12) degrees AoA

Chapter 4: Optimization of Hybrid Systems in Remote Areas

4.1 Introduction

A hybrid RE system consists of several renewable sources used together to produce an increased system efficiency with greater balance in the energy supply. Stand-alone systems in remote areas can include a secondary non-renewable source to act as backup. *Figure 58* represents a common arrangement of a stand-alone residential PV-Wind hybrid energy system.

For this study, the hybrid system will include the use of PV solar panels and wind turbines as renewable sources of energy, while using a diesel generator as a secondary non-renewable standby source (see *Figure 58*).

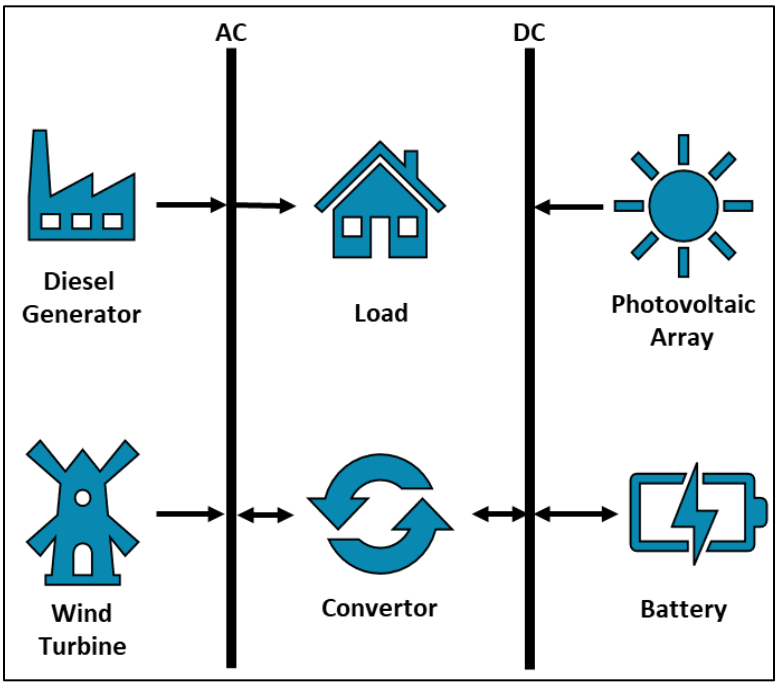

Figure 58: General scheme of a residential PV-Wind hybrid energy system

4.2 HOMER Software

The economic viability of this stand-alone hybrid system is to be analyzed on a life-cycle cost basis, and complete system optimization is conducted with the aid of the HOMER software.

HOMER is a computerized application developed by the National Renewable Energy Laboratory (NREL) in the United States [113]. This software is used to design and evaluate technically and financially the options for off-grid and on-grid power systems for remote, stand-alone, and distributed generation applications. It allows users to consider many technology options to account for energy resource availability and other variables.

On the other hand, HOMER simulates the operation of any system by making energy balance calculations for each of the 8,760 hours in a year. For each hour, HOMER compares the electric and thermal loads in the hour to the energy that the system can supply in that hour. For systems that include batteries or fuel-powered generators, HOMER also decides for each hour how to operate the generators and whether to charge or discharge the batteries. If the system meets the loads for the entire year, HOMER estimates the lifecycle cost of the system, accounting for the capital, replacement, operation and maintenance, fuel, and interest costs [114].

4.3 Sites Overview

The proposed project takes place in all states in the U.S. to have a library about the cost of installing the system in any location around the states. Being a huge country and a range of geographic features, including mountains and deserts, the U.S. has a wide variety of climates with cold winters and hot summers, with a different season duration depending on latitude and distance from the sea. The U.S terrain has a vast central plain, interior highlands and low mountains in Midwest, mountains, and valleys in the mid-south, coastal flatland near the Gulf and Atlantic coasts, complete with mangrove forests and temperate, subtropical, and tropical laurel forest and jungle, canyons, basins, plateaus, and mountains in west, hills and low mountains in the east (see *Figure 59*) [115].

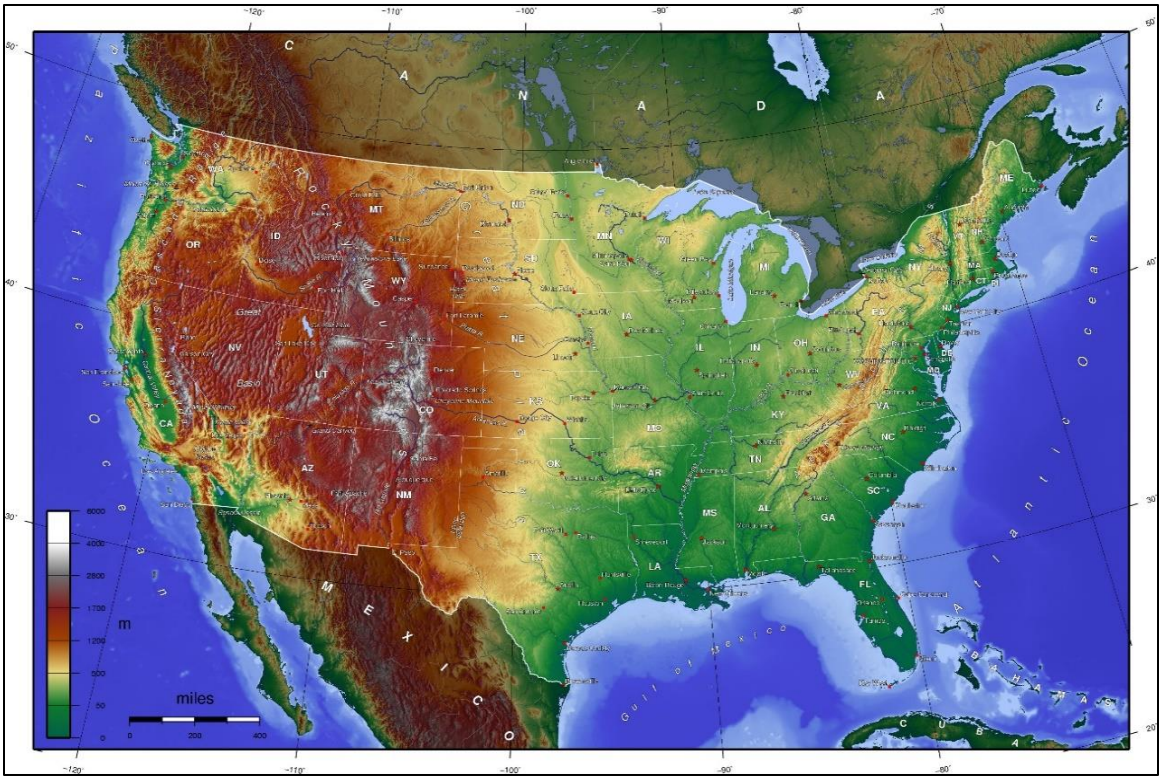

Figure 59: Topographic map of the United States [116]

4.3.1 Load Profile

Load profiling is to be used to understand the variation in the electrical load with the time of the day and year-round. Typical day energy consumption for a residential building will be higher in the morning and evening hours. While on the other hand, the winter months will show an elevated power demand in comparison with the summer months. On average, the typical American house uses 41% of its energy on heating, and 35% on appliances, electronics, and lighting. However, not all states within the U.S. consume energy in the same way. *Figure 60* shows the average electricity consumption for a typical home per day for each state. On average, residents in the East South-Central region of the U.S., including Alabama, Kentucky, Mississippi, and Tennessee, use the most electricity. While aside from Alaska and Hawaii, homes in New England use the least amount of electricity. The average electricity load for all states is 30.25 kWh/day and a peak load of 5.34 kW.

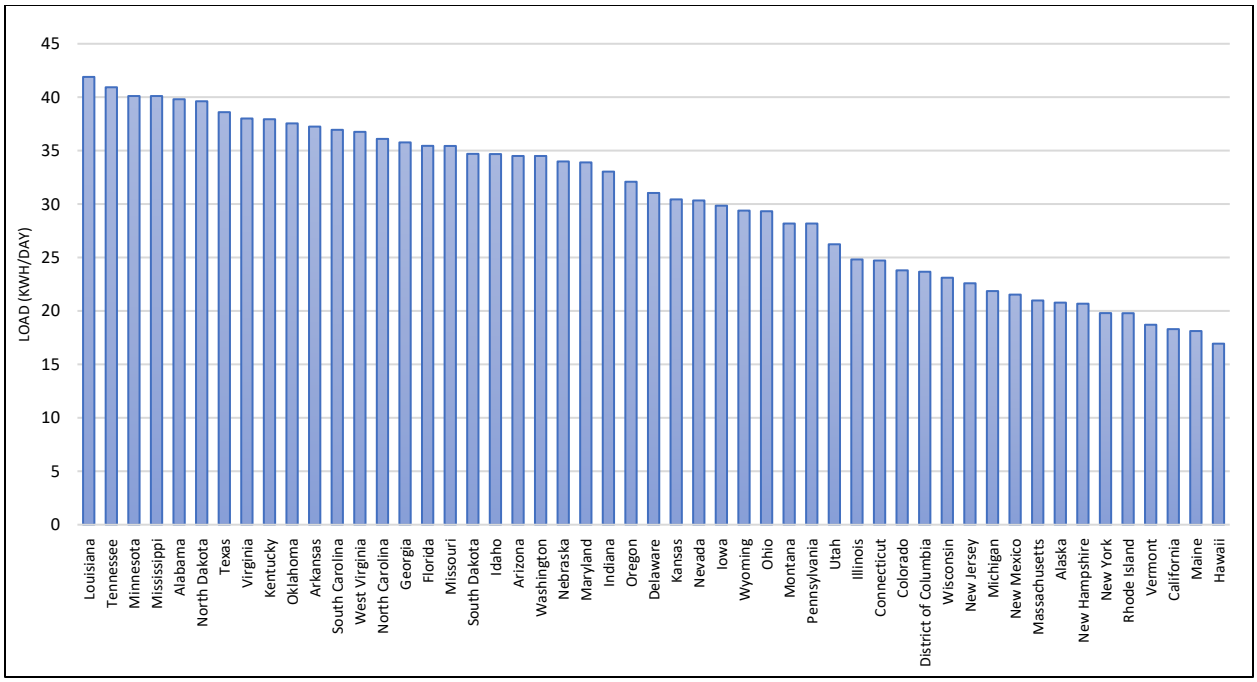

Figure 60: Average electricity load for a typical home in each state [117]

Two more applications are to be studied to understand the effect of the load profile on the system configuration selection. The main energy consumption for an ordinary commercial building would be from 8:00 AM to 5:00 PM as shown in *Figure 61*, varying slightly for some buildings. Accordingly, the average electrical load is 2,424 kWh/day with a peak load of 348 kW and a 0.29 load factor.

The nature of industrial facilities' power consumption can be continuously fluctuating to accommodate the production scheme. Generally, and in order to standardize such load profiles, the most common scenario of energy consumption shall be discussed in detail with the concerned parties. *Figure 62* belongs to a typical industrial facility that is considered for this study. The average electrical load is 24,000 kWh/day with a peak load of 1,000 kW and a 0.55 load factor.

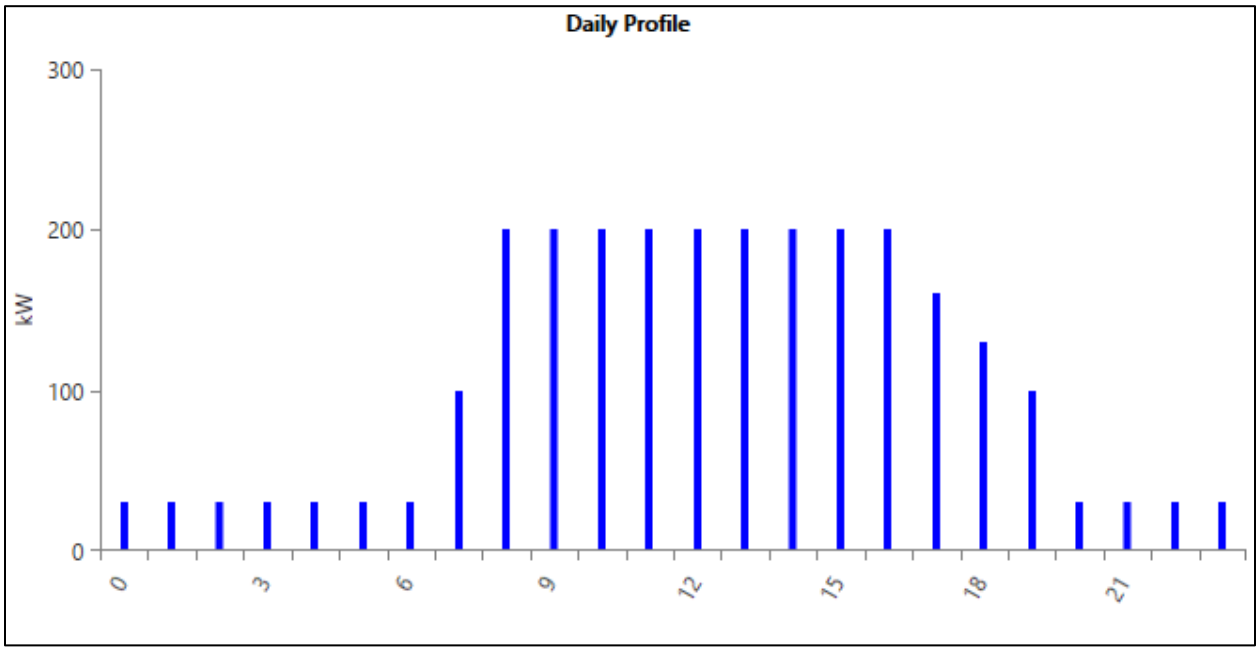

Figure 61: Average daily load profile for a typical Commercial building in a Whole Year

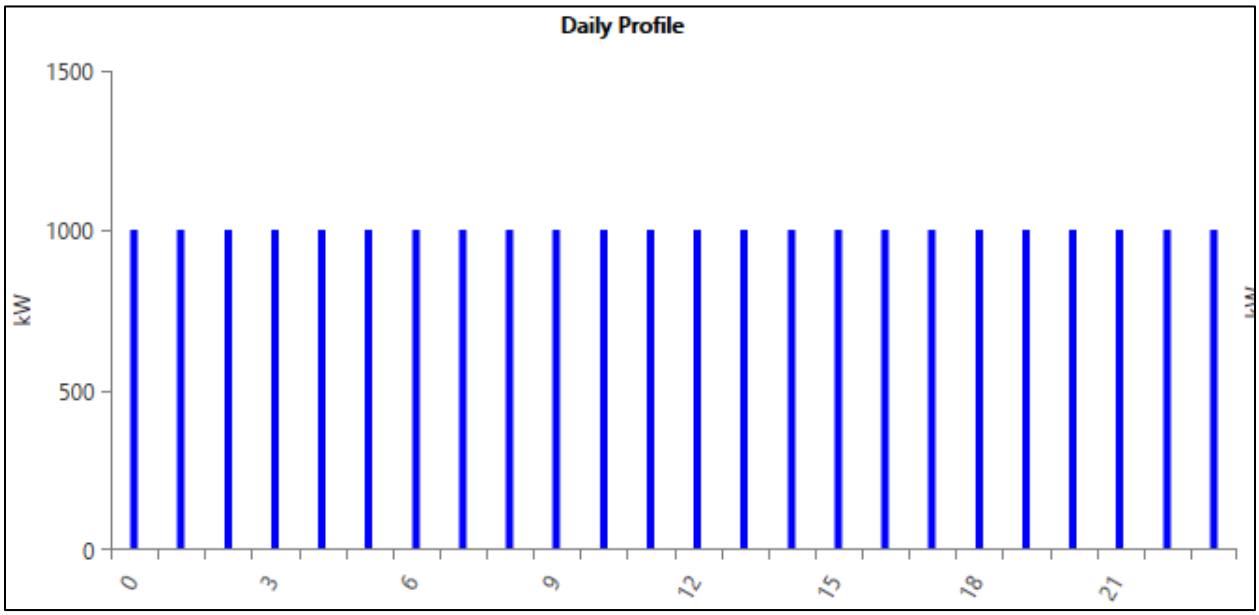

Figure 62: Average daily load profile for a typical Industrial facility in a Whole Year

4.3.2 Solar Irradiation

The annual average Global Horizontal Solar Irradiance (GHI) data for each state for the year 2017 from NREL considered and analyzed using HOMER (see *Figure 63*). As indicated in *Figure*

63 and Appendix A, the solar radiation ranges from 2.70 kWh/m^2/day in Alaska to the highest value in Hawaii with an average of 5.77 kWh/m^2/day. The average solar radiation in the U.S. is 4.14 kWh/m^2/day.

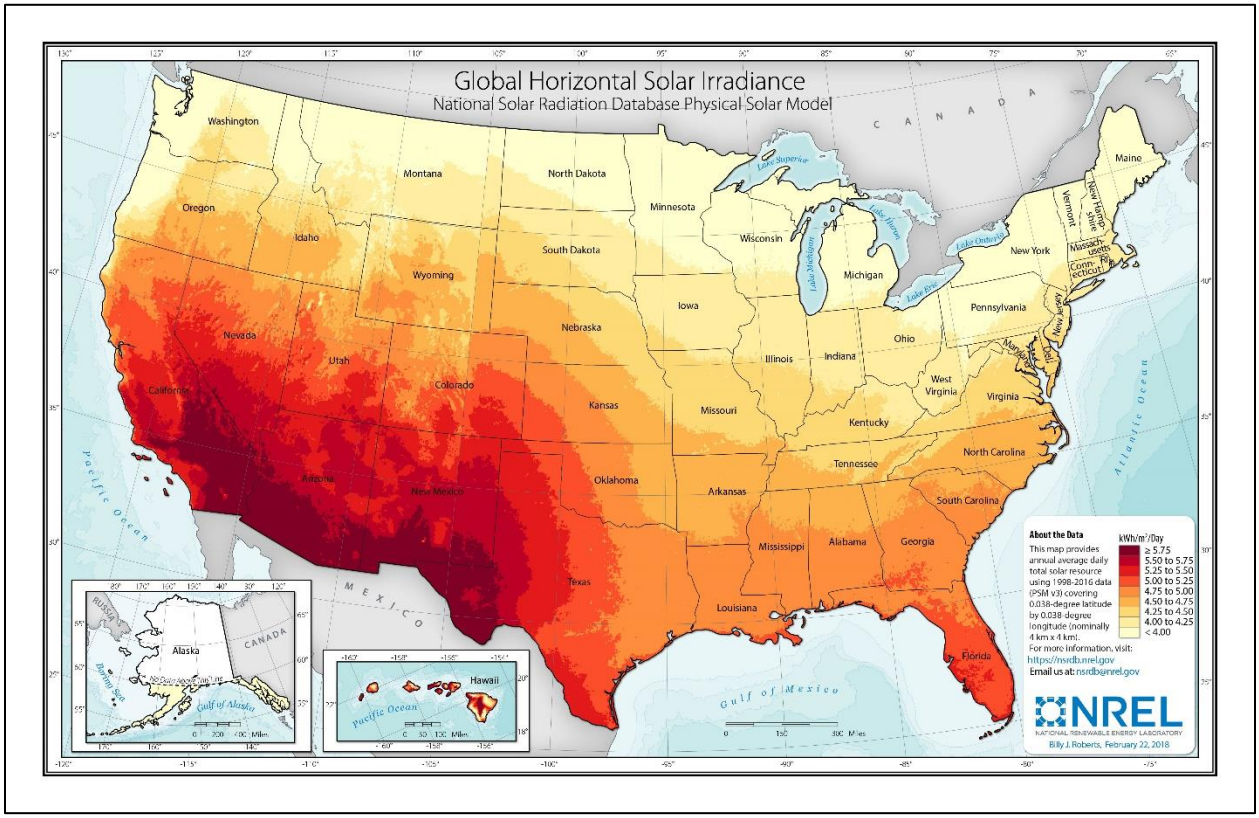

Figure 63: U.S. annual average solar GHI for 2017 [118]

4.3.3 Wind Speed

The wind is not distributed equally among all 50 states. The average wind speed for each state as per the end of the year 2017 is summarized in *Figure 64* and *Appendix A*. It can be noticed from the figure that the windiest weather tends to occur in the Plains as in Kansas and Colorado, while the least windy weather occurs in the Southeast as in Georgia, Alabama, and Mississippi. The average wind speed in the U.S. is 5.17 m/s.

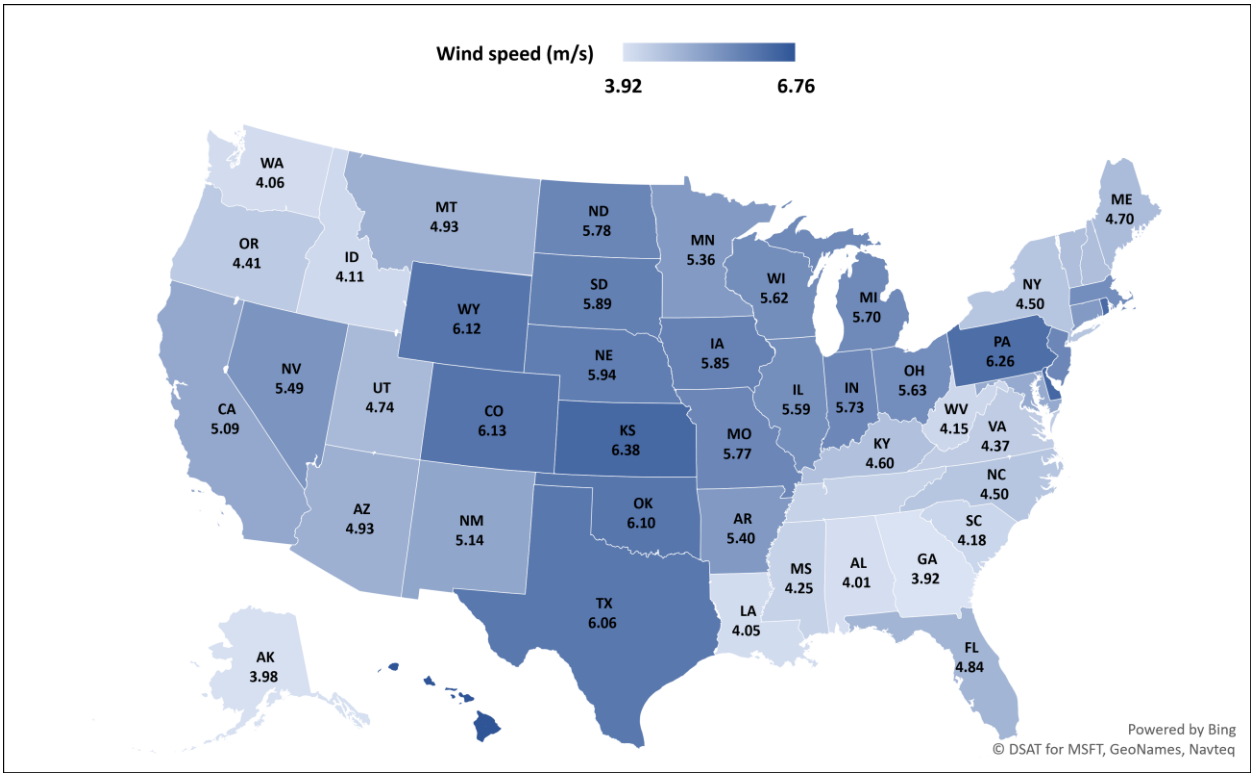

Figure 64: U.S. Average wind speed per state for 2017 [119]

4.4 Hybrid System Components

Due to the non-availability of RE resources all the time throughout the year, more hybrid RE systems were constructed, combining diverse types of alternative energy solutions along with conventional sources of energy, which helped to overcome any shortage in energy supply upon demand.

Many elements such as cost, number of units to be used, and operating hours need to be specified in HOMER for each of this equipment. The software then optimizes all inputs, and proper consideration of various options will be ensured. In this section, a detailed description of each of these components and their inputs is illustrated.

4.4.1 Diesel Generator

Diesel generating sets are often used in places without connection to a power grid, or as an emergency power supply if the grid fails, as well as for more complex applications such as peak-lopping, grid support, and export to the power grid. The diesel generator market is attracting considerable interest, and it has been segmented based on various parameters such as power rating, end-user, application, and region. Generally, the capital cost for diesel generators is lower than other alternatives of energy technologies. However, the diesel cost in the local market is affected by the unstable fossil-fuel prices internationally, which is gaining more interest when it is related to the operating costs of other energy generation systems. With a fuel rise percentage of around 15%, the COE was estimated to be increased by 40% [120].

The cost of the currently available diesel gen-sets in the global market may vary considerably from $500/kW to $1,200/kW according to Distributed Generation Forum, a group of utilities, industry associations, and government agencies. The cost per kW for large units is necessarily lower than smaller units. For this study, the diesel generator cost is taken as $900/kW, with replacement and maintenance costs of $700/kW and $0.050/hour, respectively.

The sizing of a diesel generator depends solely on the maximum demand of power to be supplied, along with few other factors such as the efficiency of the gen-set and the possibility of future loads to be added. HOMER software can auto-size the generator and select the most suitable size that meets the maximum annual capacity shortage including a zero size to enable HOMER to consider options where no generators are used.

The main source of cost for the gen-set is diesel fuel, and due to the cyclic nature of oil prices worldwide, fuel expenses are gaining more and more concern when it comes to operational costs of any energy system. To ensure the proper credit of this study, different diesel prices were

considered through analysis of output different feasibility scenarios. Three discrete price values were used; the 2018 U.S market prices (see *Figure 65* and *Appendix A*), $0.5/L, and $1.5/L [121].

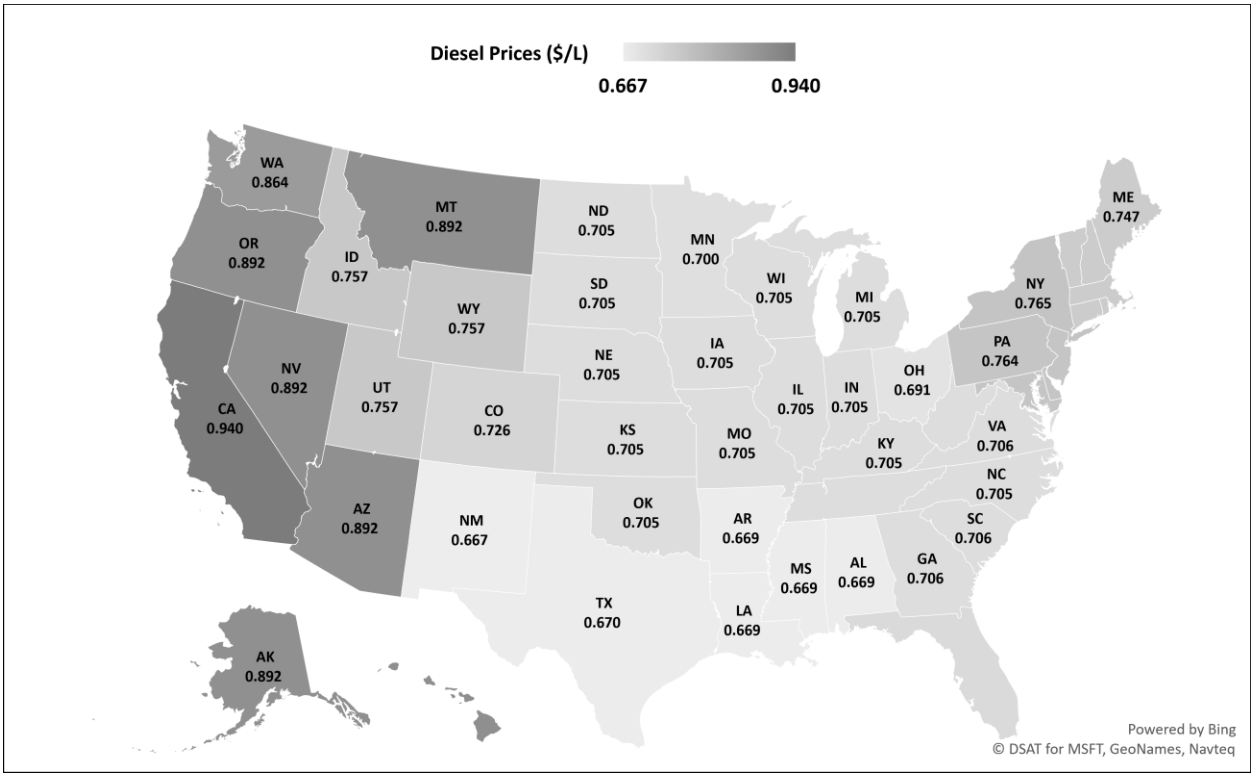

Figure 65: U.S. Average diesel price per state for 2018 [121]

4.4.2 Photovoltaic Array

The vast majority of market solar cells are made of crystalline silicon. Mono-crystalline cells are the most efficient. However, cheaper Poly-crystalline cells are also popular. The cheapest would be amorphous silicon cells which are also available and used widely for small consumer products but rarely used for power systems. Several aspects characterize the selection of a solar panel type, which can be summarized as follows [122]:

1. Cell's Type: In most situations, the use of a quality poly-crystalline solar panel is recommended for solar power systems.

2. Size and Watts: The size or output (in Watts) of the solar panel directly affects the cost, as solar panels are usually priced and compared in dollars per Watt, and the physical size.

3. Durability/Longevity/Warranty: Reputable solar panels have a warranty period of at least 10 years of artistry, and 25 years of output.

4. Cost: The cost of a solar panel is determined in part by the size (in Watts), the physical size, the brand, the durability/longevity (or warranty period), and any certifications the solar panel might have.

To decide whether to use poly-crystalline or mono-crystalline modules is not easy, it requires weighing costs against efficiencies, and since the cost has a higher importance in the configuration of this system due to a large number of modules expected to be needed in some cases, poly-crystalline modules are more likely to be selected, bearing in mind that its efficiency also has to be considerably high.

For the proposed system, a large variety of PV panel options were studied in terms of their type, power, cost, and warranty. Capital and replacement costs of a PV system include PV panels, mounting hardware, wiring, and installation. The baseline capital cost of installing the PV system in this study will be taken based on each state with a range from $2,500/kW in North Dakota up to $3,800/kW in Oregon with the same estimation for the replacement costs were considered as while the operation and maintenance costs will be set to $10/year [122].

Sizing of the PV system in HOMER includes the load to be considered as the software searches for the optimal PV system for each case. The proposed PV panels' outputs to be optimized is range from zero sizes where HOMER considers a hybrid system without PV panels, and 11 kW as the maximum size to be optimized.

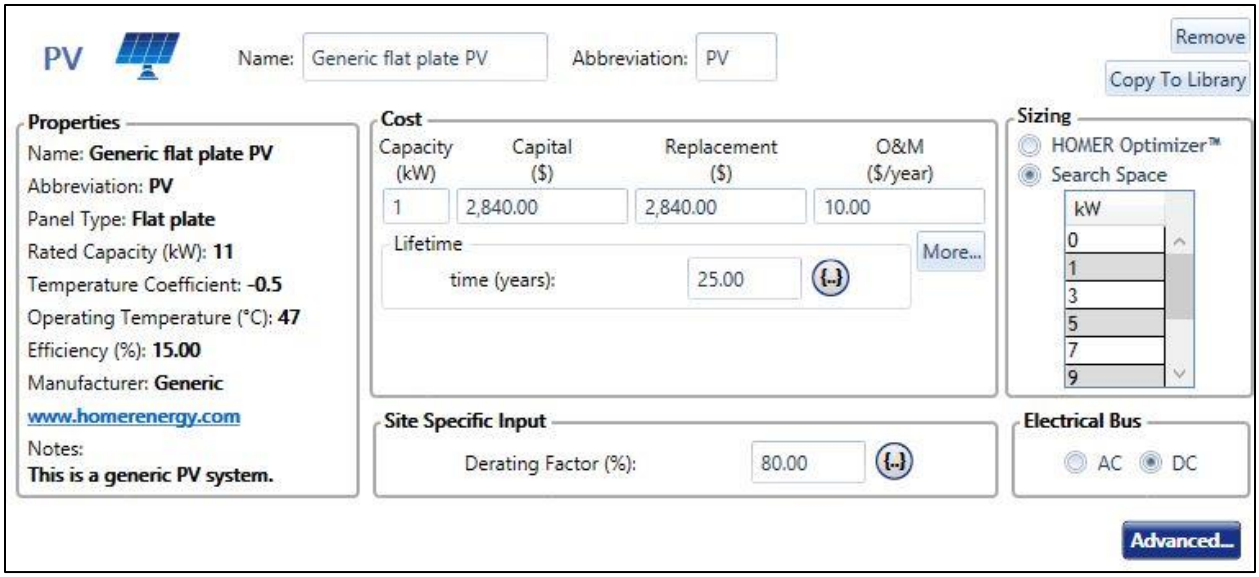

Figure 66: PV's input window in HOMER

Various elements to be inputted in *Figure 66*, which can be explained as follows:

- Electric bus: All PV cells produce DC electricity, but some PV arrays have built-in inverters to convert to AC. In this study, PV panels produce non-inverted DC electricity.
- Lifetime: The number of years the PV panels will last and was taken as 25 years.
- PV derating factor: It is a scaling factor that HOMER applies to the PV array power output to account for reduced output in real-world operating conditions, compared to the conditions under which the PV panel was rated. Such conditions include the soiling of the panels, wiring losses, shading, snow cover, and aging. For this study, it was assumed to be 80% [123].
- PV slope: The slope (also called tilt) is the angle at which the panels are mounted relative to the horizontal, as shown in *Figure 67*. In this study, a fixed-slope system was considered where HOMER set the default angle for each state.
- PV Azimuth: The azimuth is the direction towards which the PV panels face. Due south is 0°, due east is -90°, due west is 90°, and due north is 180°. With fixed-azimuth systems,

the panels are almost always oriented towards the equator (0° azimuth in the northern hemisphere, 180 ° azimuths in the southern hemisphere). *Figure 67* illustrates the Azimuth angle, which is selected by HOMER as per the location for each state.

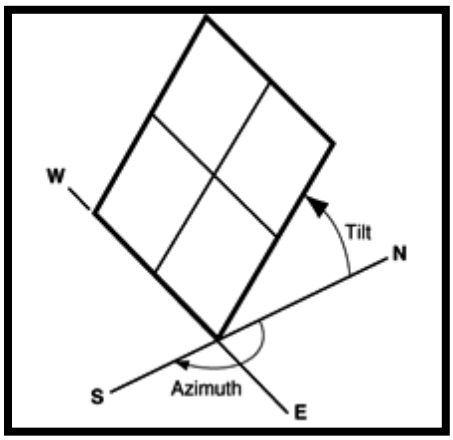

Figure 67: PV's azimuth and slope angles

- Ground reflectance: The ground reflectance (also called albedo) is the fraction of solar radiation incident on the ground that is reflected. A typical value for grass-covered areas is 20%. Snow-covered areas may have a reflectance as high as 70%. This value is used in calculating the radiation incident on the tilted PV panels, but it has only a modest effect [124]. In this study, albedo is taken as 20%.
- PV tracking system: Determines the type of tracking system used to direct the PV panels towards the sun. Non-tracking PV system to be considered here.
- Temperature effects on power: This indicates how strongly the PV array power output depends on the surface temperature of the PV array. It is a negative number because power output decreases with increasing cell temperature. Manufacturers of PV modules usually provide this coefficient in their product brochures, often labeled either as "temperature coefficient of power", "power temperature coefficient", or "max. Power temperature coefficient". This value will be taken as -0.5%/°C for the proposed system.

- PV nominal operating cell temperature (NOCT): It is the surface temperature that the PV array would reach if it were exposed to 0.8 kW/m^2 of solar radiation, an ambient temperature of 20°C, and a wind speed of 1 m/s. Which provides a measure of how the PV cell temperature (the surface temperature of the PV array) varies with the ambient temperature and the solar radiation [113]. NOCT will be set to 47°C in this study.
- PV efficiency at standard test conditions: The efficiency at which the PV array converts sunlight into electricity with its maximum power point under standard test conditions, and it is usually around 15%.
- Additional Note: HOMER assumes the output of the PV array is linearly related to the solar radiation incident on the PV array, and independent of the DC bus voltage. That means HOMER assumes the PV array has a maximum power point tracker.

4.4.3 Wind Turbine

This section describes the basic components of small wind turbines mainly by contrast to those of the better-known large turbines. However, there are aspects of turbine operation that are common to turbines of all sizes. The main operating parameter is the tip speed ratio (TSR), defined as the circumferential velocity of the blade tips divided by the wind speed. The TSR controls the blade aerodynamics, in particular the angle of attack of the airflow over the blades. This, in turn, sets the L/D ratio and therefore the power output [125]. Most turbines operate with a TSR between 5 and 10, with the lower values typical of three or more blades and the higher values of two blades [126].

It can be a challenging control problem to maintain the optimum TSR as the wind speed varies in the absence of an anemometer–these are usually too expensive for small turbines. Part of a typical power curve (power output versus wind speed) is shown in *Figure 68*. The major

differences between large and small turbines usually occur near the ‘cut-in’ wind speed, the lowest at which power is produced, and at the top end where small turbines tend to have a lower ‘rated’ wind speed and the differences in safety mechanisms become important.

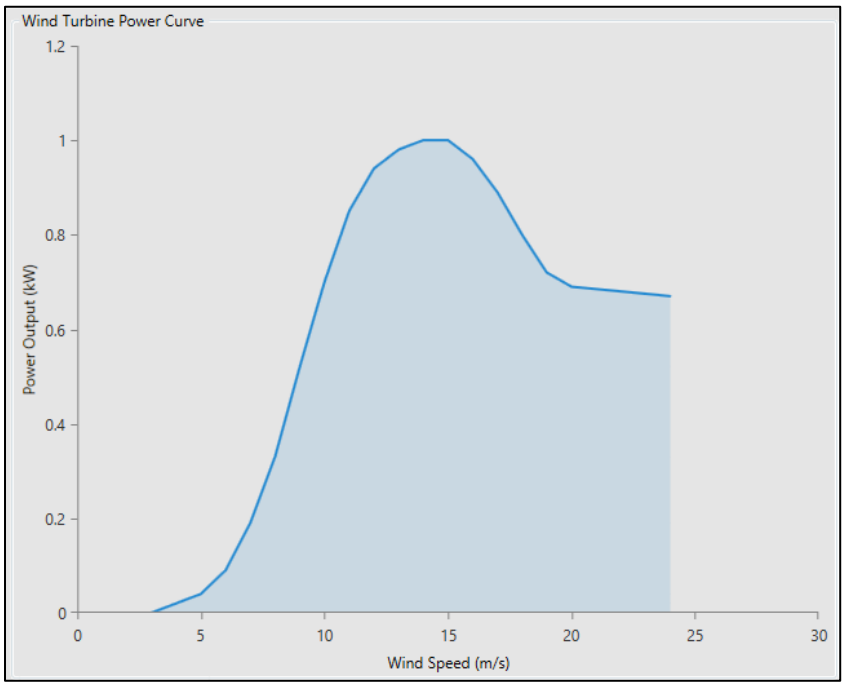

Figure 68: Proposed wind turbine power curve [127]

The rated power of the selected wind-turbine(s) depends on the system electricity demand, the available wind potential, and the operational characteristics of the machine. The cost of a wind turbine varies depending on the type of technology, performance, auxiliary equipment, installation location, and power converters. At present, market-available wind turbine installation prices are in the range of $3,000 to $6,000/kW [128].

Considering these factors, the capital, replacement, and operational costs are taken as $5,000, $4,000, and $70/year respectively for a 1 kW system. The high capital installation cost of the wind turbine has been the major issue of not utilizing this technology in hybrid systems. By developing wind turbine manufacturing technologies, the cost of installing a small wind turbine in a hybrid

system is expected to be reduced in the future. In this study, various two cost multiplying factors for a wind turbine was considered: 0.5 and 1.0.

According to the discussed loads for each of the proposed cases, the wind turbine sizes are increasing by 1 kW step from 0 to 5 kW for HOMER software to consider as it searches for the optimal system of each case, including the zero sizes for considering systems without wind turbine.

4.4.4 Battery

Storing the produced electrical energy has very high importance for any off-grid system design. Even though many battery technologies are commercially available, relatively few are found in PV and wind systems. That would be because, unlike regular batteries, solar cells, and wind turbine development demand a vast discharge and charge ratio, with a high capacity range to meet the desired electrical demand. Several factors may be affecting the performance of batteries for an off-grid PV-wind system, namely; temperature, age, discharge rate, and Depth of Discharge (DOD) [129].

Batteries used in home energy storage typically are made with one of three chemical compositions: lead-acid, Lithium-Ion (Li-Ion), and saltwater (see *Figure 69*). In most cases, Li-Ion batteries are the best option for a solar panel system, though other battery types can be more affordable. Li-Ion batteries are lighter and more compact than lead-acid batteries. They also have a higher DoD and longer lifespan when compared to lead-acid batteries [130].

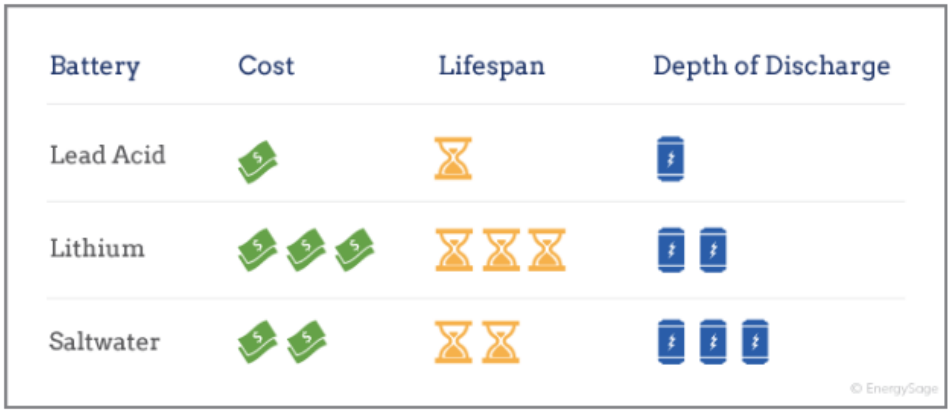

Figure 69: Comparison between hybrid system batteries [130]

After going through many types of batteries while keeping in mind the factors listed before, 1 kWh Li-Ion battery type seemed to be a promising choice. The 6 V series battery with a 1 kWh rated capacity of 167 Ah (Ampere Hour) was selected. The estimated capital cost of one battery is $550, with a replacement cost of $550 and operational and maintenance costs of $10/year. To search for the optimal system components, HOMER Optimizer was selected to choose the number of batteries depending on the load profile and that includes a zero-value for the software to consider systems without batteries.

It is to be noted that HOMER allows input numbers for either batteries or strings of batteries, where a battery string is a group of batteries connected in series together via DC bus. HOMER shows the DC bus voltage in parentheses next to the number of batteries per string. The bus voltage is the battery's nominal voltage multiplied by the number of batteries per string. In this study, two batteries are to be connected in series to form a string, and all strings are connected in parallel to form a battery bank.

4.4.5 Converter

Any system involving AC and DC elements, such as the proposed hybrid structure, requires a converter. The AC power generated by the generator can be converted to DC power stored in

battery banks by a convertor. Also, It can convert the DC PV panels or wind turbine power into AC power to be used by the load. Nowadays, there is a massive range of converter sizes in the market; each customer can choose depending on where it will be used. Large-sized converters or a group of converters are used in large network systems, medium-sized converters are used for residential and commercial buildings, and small-sized converters are used in small homes [131].

The available converters in the market have a capital cost ranges from $200/kW to $400/kW; an average cost of 300/kW is taken in this study. With the same cost for the replacement and $20/year for the operational costs per kW. Based on the load profile for each case, the suggested converter sizes inserted into HOMER ranges from zero up to 7 kW capacity.

4.4.6 Economical Aspects and Constraints

HOMER software uses some economic aspects and operational constraints within its simulations. Before proceeding to simulations, these aspects and constraints are defined as follows:

- Nominal discount rate: interest rate which is used for converting between annualized costs and one-time costs without accounting for the inflation effect. This rate is used in HOMER to calculate annual costs and discount factors based on the "net present costs" (NPC). For RE projects in the U.S., this rate is averaged at 8.0 percent. Thus, the actual discount rate that accounts for the inflation effect was calculated in this study as 5.9 percent [132], using 1.983% as an expected annual inflation rate.
- Project Lifetime: 25 years was taken as the project lifetime, which is the period at which the project is expected to be in operation.
- Operating Reserve: It is the generating amount reserved in the system a spare to conquer any sudden lack in electricity supply. This shortage could be resulted from a spike in the

load or by renewable energy source intermittency. Operating reserve ensures the reliability of the hybrid system regardless of any disruption in meeting the required load.

In HOMER software, operating reserve value is defined using two main categories: two sub-inputs are under each category. The main categories are correlated to the load profile irregularity and the variability of RE power, as shown in *Figure 70*. The total required operating reserve is the sum of the four values resulting from these four inputs. The value of the required reserve is calculated by adding the resulted four values from these inputs together. The hybrid power system is run during the HOMER simulation while keeping the reserve greater than or equal to the required reserve value.

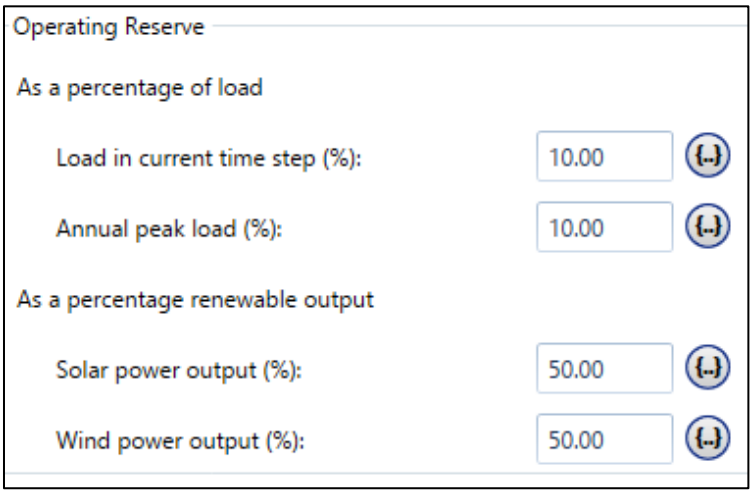

Figure 70: Operating reserve's input window in HOMER

Any power supply deficiency is recorded as a shortage in capacity. Inputs listed in *Figure 70* can be explained as follows:

- As a percent of the current load: In the current time step, the AC and DC percentages of primary load are added to the operating reserve required in each time step. In this study, 10% was used for this value. In other words, the system will have a surplus capacity to cover a 10% sudden load increase.

- As a percent of annual peak load: HOMER adds this percentage of the peak primary load (AC and DC separately) to the required operating reserve in each time step. It, therefore, defines a constant amount of operating reserve. For example, if the peak AC primary load is 40 kW and the user wants to ensure at least 8 kW of operating reserve on the AC bus at all times (maybe to cover a 4 kW motor starting load), this input is set to 10%.
- As a percent of solar and wind power outputs: This percentage of the PV and wind power capacities is added to the required reserve every time step. In this study, 50% was used for this input. In other words, the system must have a surplus capacity to cover a 50% sudden output power decrease in the PV or wind systems.

4.4.7 Summary

As discussed previously, *Table 6* summarizes all inputted data in HOMER for each system component:

Table 6: Summarized input data

Data Input		Diesel Generator	PV	Wind Turbine	Battery	Convertor
Cost	Size	1 kW	1 kW	1 kW	1 kWh	1 kW
	Capital	$900/kW	As per the state	$5,000/kW	$550	$300/kW
	Replacement	$700/kW	As per the state	$4,000/kW	$550	$300/kW
	O&M	$0.050/hour	$10/year	$70/year	$10/year	$20/year
Properties	Output current	AC	DC	AC	DC	AC/DC
	Lifetime	15,000 hours	25 years	20 years	15 years	15 years
	Min. load ratio	25 %	-	-	-	-
	PV Derating Factor	-	80 %	-	-	-
	PV Slope	-	As per the state	-	-	-
	PV Azimuth	-	As per the state	-	-	-
	Ground Reflectance	-	20 %	-	-	-
	Efficiency	-	15 %	-	90 %	95 % (Inv.) 95 % (Rec.)

	Hub Height	-	-	17.0 m	-	-
	Batteries per string	-	-	-	2 (16 V)	-
Diesel Prices		\$0.5/L, 2018 price for each state, \$1.5/L				
Cost multiplying factors for wind turbine		0.5, 1.0				
Cost multiplying factors for solar panels		0.5, 1.0				
Real Discount Rate		5.9 %				
Project Lifetime		25 years				
Operating reserve as a percent of annual peak load		10 %				
Operating reserve as a percent of solar and wind power outputs		50 %				

4.5 Optimization Results

HOMER software used all element inputs in the optimization process to find the best configuration systems by combining all components; it rejects all impractical configuration systems from the successful results, which are the failed configurations do not satisfactorily meet the available RE resource or the stated constraints. 12 scenarios (including three diesel prices, two wind turbine multipliers, and two solar panels capital cost multipliers) were checked for each system configuration on a 2.4 GHz Intel Core i7 computer. Systems were modeled with all 127,000 alternatives examined, and more than 6.4 Million solutions for all states were found with 75% feasible solutions [133].

4.5.1 System Configuration

In the table of the total optimization outcomes, HOMER shows a list of all feasible configuration hybrid systems. Feasible configurations are listed based on the configuration's NPC, starting from the configuration of the lowest NPC to the configuration of the highest NPC (see *Figure 71*). A component's net present value is calculated by discounting all types of costs from

all revenues throughout the project after returning them to the current time. HOMER calculates the NPC of the whole system as well as the NPC of each system component. The optimization outcomes from HOMER can be classified for fixed sensitivity boundaries. The diesel price for each state is fixed at 2018 prices, PV cost multiplier at 1.0, and 1.0 wind turbine cost multiplier were considered as the sensitivity parameters.

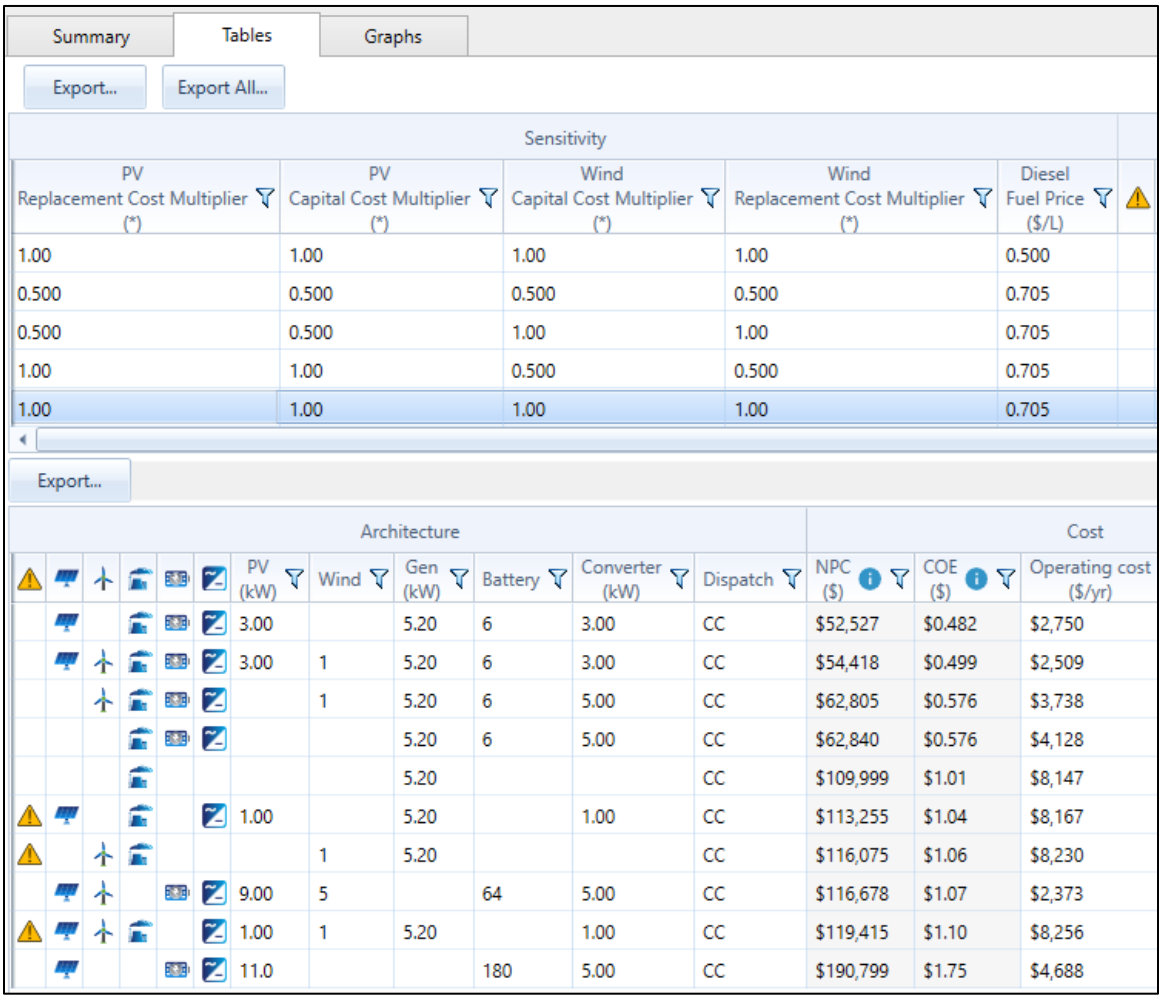

Figure 71: Optimization results for the Wisconsin state case study

In all states and for a typical residential building, PV panels, diesel generators, and battery systems were observed as the best solution for most cases. *Table 7* shows the system architecture

of the most suitable configuration for each state according to sensitivity analysis using a diesel price at 2018 prices, PV cost multiplier at 1.0, and 1.0 wind turbine cost multiplier.

Table 7: System architecture for 2018 diesel price, 1.0 PV cost multiplier, and 1.0 wind turbine cost multiplier

State	PV Array (kW)	Wind Turbine (1.0 kW)	Diesel Gen. (kW)	Battery (Strings)	Converter (kW)	Total NPC ($)	COE ($/kW)	Annual Operating cost ($/year)
NM	5.0	0.0	4.8	18.0	3.0	43,880	0.432	1,134
TX	9.0	0.0	8.7	32.0	5.0	79,421	0.436	2,264
UT	5.0	0.0	5.9	20.0	3.0	54,418	0.440	1,822
CO	5.0	0.0	5.4	20.0	3.0	49,756	0.443	1,496
WY	5.0	0.0	6.6	20.0	3.0	62,118	0.448	2,435
NV	5.0	0.0	6.8	18.0	3.0	64,504	0.450	2,590
AZ	7.0	0.0	7.7	30.0	5.0	73,565	0.452	2,284
AL	5.0	0.0	8.9	12.0	7.0	85,169	0.453	4,255
MS	5.0	0.0	9.0	12.0	7.0	86,537	0.457	4,339
KS	5.0	0.0	6.8	20.0	3.0	65,773	0.458	2,638
LA	5.0	0.0	9.4	12.0	7.0	90,977	0.460	4,635
NE	5.0	0.0	7.6	8.0	5.0	73,937	0.461	3,721
FL	5.0	0.0	7.9	8.0	5.0	77,218	0.462	3,923
OK	5.0	0.0	8.4	12.0	7.0	81,866	0.462	4,062
AR	5.0	0.0	8.3	10.0	7.0	81,379	0.463	4,054
ID	7.0	0.0	7.8	32.0	5.0	75,823	0.463	2,339
IA	5.0	0.0	6.7	20.0	3.0	65,354	0.464	2,655
SD	5.0	0.0	7.8	8.0	5.0	76,071	0.465	3,895
NC	5.0	0.0	8.1	10.0	7.0	79,310	0.466	3,970
ND	5.0	0.0	8.9	12.0	7.0	87,186	0.466	4,462
HI	5.0	0.0	3.8	16.0	3.0	37,336	0.467	798
MO	5.0	0.0	7.9	10.0	7.0	78,088	0.467	3,889
VA	5.0	0.0	8.5	12.0	7.0	83,755	0.467	4,201
GA	5.0	0.0	8.0	10.0	7.0	78,969	0.468	3,888
SC	5.0	0.0	8.3	10.0	7.0	81,605	0.468	4,056
CA	5.0	0.0	4.1	16.0	3.0	40,594	0.470	1,029
MN	5.0	0.0	9.0	12.0	7.0	88,999	0.470	4,548
TN	5.0	0.0	9.2	12.0	7.0	90,809	0.470	4,674
IL	5.0	0.0	5.6	18.0	3.0	55,883	0.477	2,022
MT	5.0	0.0	6.3	22.0	3.0	63,396	0.477	2,446
DE	5.0	1.0	7.0	18.0	3.0	70,000	0.478	2,630
KY	5.0	0.0	8.5	12.0	7.0	85,736	0.479	4,311
WV	5.0	0.0	8.2	10.0	7.0	83,003	0.479	4,272

IN	5.0	0.0	7.4	8.0	5.0	74,874	0.480	3,764
OH	5.0	0.0	6.6	20.0	3.0	66,716	0.482	2,725
WI	3.0	0.0	5.2	6.0	3.0	52,527	0.482	2,750
MI	3.0	0.0	4.9	6.0	5.0	50,006	0.485	2,548
DC	5.0	0.0	5.3	20.0	3.0	54,427	0.487	1,845
MD	5.0	0.0	7.6	8.0	5.0	77,895	0.487	4,027
PA	5.0	1.0	6.3	18.0	3.0	64,778	0.487	2,337
CT	5.0	0.0	5.6	16.0	3.0	57,309	0.491	2,194
MA	3.0	0.0	4.7	6.0	3.0	48,801	0.493	2,468
RI	3.0	0.0	4.5	10.0	3.0	46,171	0.494	2,106
ME	3.0	0.0	4.1	6.0	3.0	42,372	0.496	2,059
VT	3.0	0.0	4.2	10.0	3.0	43,981	0.498	2,007
NJ	3.0	0.0	5.1	6.0	5.0	53,389	0.501	2,749
NH	3.0	0.0	4.7	6.0	3.0	49,171	0.504	2,518
NY	3.0	0.0	4.5	6.0	3.0	47,612	0.510	2,390
WA	5.0	0.0	7.7	8.0	5.0	83,691	0.514	4,468
OR	5.0	0.0	7.2	20.0	3.0	78,344	0.517	3,176
AK	3.0	0.0	4.7	6.0	5.0	55,629	0.567	2,946

This study compares states according to their Levelized Cost of Energy (COE) where HOMER defines it as the average power generated cost for each kWh of the electrical energy generated by the hybrid system. *Figure 72* shows the COE for each state. It can be noticed from the figure that Alaska has the highest COE value of around $0.567/kWh, and the lowest COE value is in New Mexico, with approximately $0.432/kWh. The average COE for all states was found to be around $0.475/kWh; these results are discussed in the following sections.

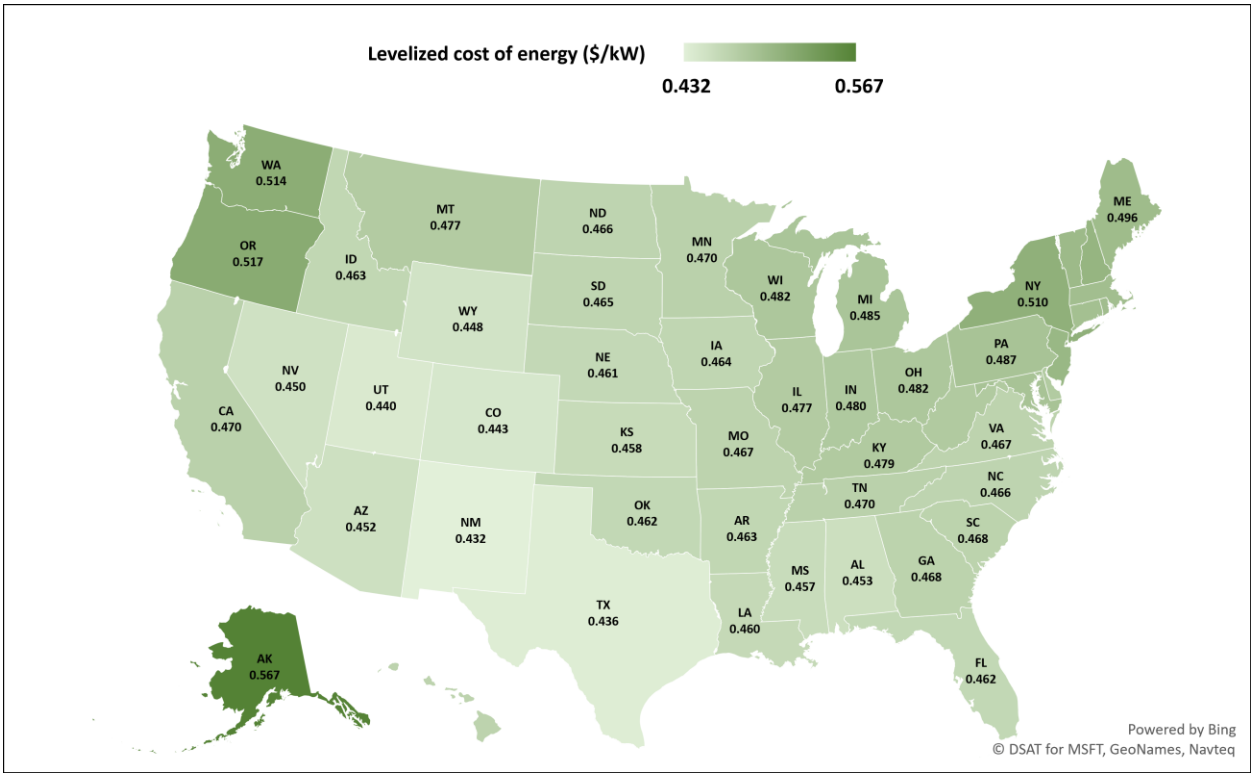

Figure 72: U.S. Average COE per state at 2018 diesel price, 1.0 PV cost multiplier, and 1.0 wind turbine cost multiplier for a typical Home

4.5.2 Cost Summary

Figure 73 shows the cost summary, which presents the cash flow value as a percentage or as a yearly cost in the simulation results window. Outcomes are categorized by the type of cost or by component. For the residential building case study and compared to other hybrid components, it can be observed from the outcomes that the higher NPC values are for the battery and the diesel generator for all states. That can be anticipated to the residential building load profile and the high electricity demand during the night, where the electricity should be stored to electrify the building at night (from 6:00 PM to 11:00 PM).

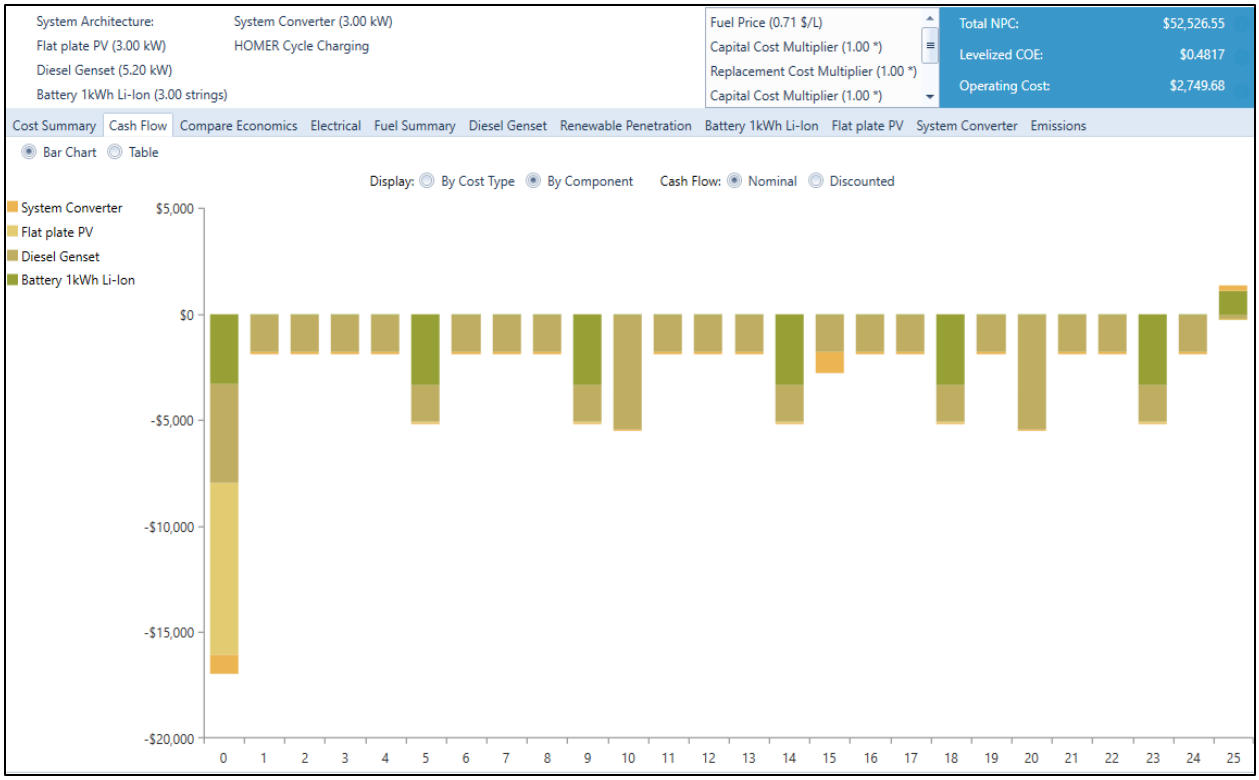

Figure 73: Cost summary window for Wisconsin case study

The cash flow graph resulted from the simulated system is shown in *Figure 73*. In this graph, the total outflow cash at the negative side of the total inflow cash at the positive side of the graph is represented as bars for each component. Outflow values could represent diesel expenses, equipment replacement costs or operation and maintenance (O&M) costs. Inflow cash could represent revenue from selling the generated electricity or selling a piece of equipment at the end of its useful lifecycle. HOMER represents cash flows by a filled bar for each component in different colors. The color for each bar represents capital cost, O&M cost, replacement cost, salvage cost, and diesel price, where the salvage cost is the positive value by the end of the project lifetime.

4.5.3 Electrical Aspects

The total electricity produced by the proposed hybrid system is the summation of the generated electricity by each component in a single year. The outcomes present the total annual

power output from every electricity-producing element of the hybrid energy system. The load profile for each state has a significant effect on the system generating electricity.

It can be spotted from *Figure 74* that, for the residential case study in Wisconsin, in winter, the generator has the longest run time. Some of the produced energy cannot be utilized in charging batteries nor contributed to meeting the electricity load. This portion of the generated power is called the surplus, which is dumped into the grid. A surplus occurs when either the diesel generator or a renewable energy source generates electricity exceeding the required load. The batteries are fully charged and cannot absorb more electricity.

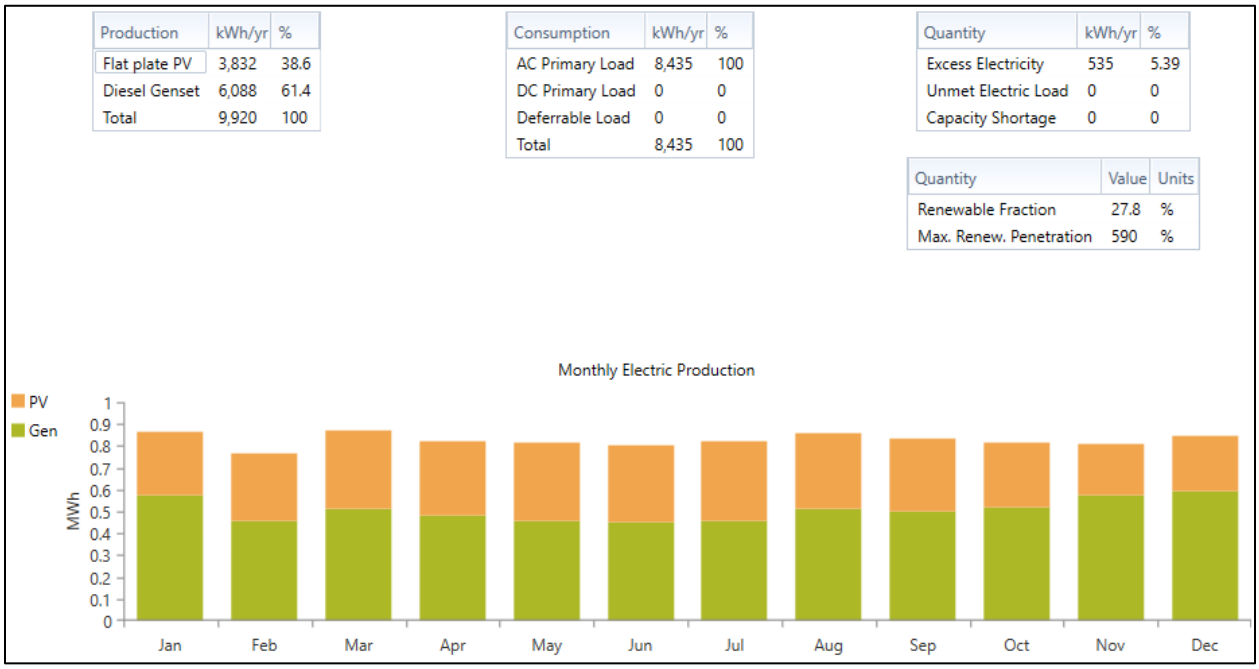

Figure 74: Monthly averaged electrical energy production for Wisconsin case study

4.5.4 Results Comparison

A comparison for three different cases from the high, average, and low COE was performed. The comparison *Table 12* for the three states (Texas, Wisconsin, and Oregon) shows the component sizes, capital cost, NPC, COE, the daily radiation, and the diesel prices. It can be noticed that Oregon has a higher COE than Wisconsin, although Wisconsin has lower daily

radiation, and that can be related to the high diesel rate in Oregon. The Texas case study has the lowest diesel price with the highest daily radiation rate, which resulted in having the lowest COE among the three cases.

Table 8: Comparison of three stats at 2018 diesel price, 1.0 PV cost multiplier and 1.0 wind turbine cost multiplier

Component	Texas	Wisconsin	Oregon
PV Array (kW)	9.0	3.0	5.0
Diesel Gen. (kW)	8.7	5.2	7.2
Battery (1 kWh Li-Ion)	32	6	20
Converter (kW)	5.0	3.0	3.0
Total net present cost ($)	79,421	52,527	78,344
Annual Operating cost ($)	2,264	2,750	3,176
COE ($/kWh)	0.436	0.482	0.517
Daily Radiation (kWh/m^2/day)	4.93	3.73	4.48
Diesel Prices ($/L)	0.670	0.705	0.892

Based on the results of the COE for each state, the correlation between the COE, diesel prices, and daily radiation is presented in *Figure 75* for all states. The gray line represents the diesel prices. In most cases, the cost of generating power from the system increased as the diesel prices increased and increased COE. On the other side, the COE has been affected adversely by the daily radiation. The power generated by the solar panels was increased at the higher daily radiation rates, which reduced the price of the generated power, and that was responsible for lowering the COE.

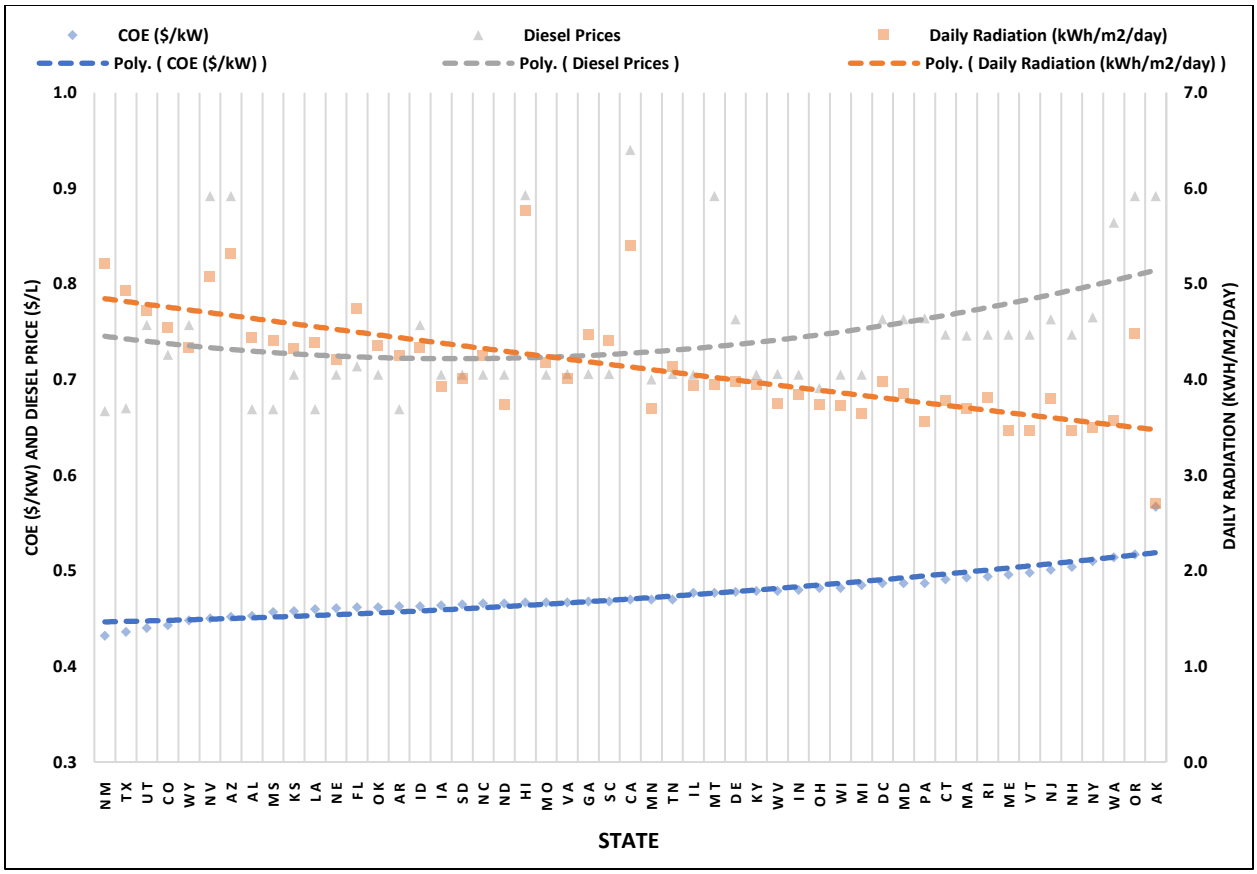

Figure 75: COE, diesel price, and daily radiation for each state

The diesel price and the daily radiation for each state substantially affect how the system will produce electric power. *Table 9* displays the annual energy production from each electricity-producing system of the hybrid power system, along with the total electrical production. Wisconsin's low daily radiation rate led to only 38.6% of the generated power to be generated from the PV panels compared to 56.4% and 75.7% for Oregon and Texas, respectively. The diesel prices have a lower effect than the daily radiation on energy production, as in Oregon, where it has the highest diesel rate in 2018 among the three cases. However, diesel generators contributed to 61.4% of the total energy production in Wisconsin compared to only 43.6% in the Oregon case.

Table 9: Electrical production for three stats at 2018 diesel price, 1.0 PV cost multiplier, and 1.0 wind turbine cost multiplier Home application

Component	Texas		Wisconsin		Oregon	
	Production (kWh/year)	Fraction	Production (kWh/year)	Fraction	Production (kWh/year)	Fraction
PV	13,456	75.7%	3,832	38.6%	7,671	56.4%
Diesel Gen.	4,324	24.3%	6,088	61.4%	5,927	43.6%
Total	**17,780**	**100%**	**9,920**	**100%**	**13,597**	**100%**

4.5.5 CO_2 Emission

The impact of the high greenhouse gas (GHG) concentrations impact would take quite some time to be notable as one of the deep-rooted characteristics of the interrelating climate, environmental, and social-economic stability [134]. Nonetheless, stable CO_2 concentration in the atmosphere does not necessarily mean the global warming and sea level would not remain to occur and rise in the future since the natural climate cycles would still happen, due to multiple irretrievable climate changes that had happened in the past.

The operation of renewable energy resources in the proposed system in this study does not affect increasing GHG emissions. It also does not emit other substances that might be non-environmentally friendly. Replacing the conventional resources with renewable energy resources for generating electricity will result in a substantial GHG emissions reduction. However, the only source of GHG emissions is the fossil fuel generator as a part of a stand-alone hybrid system. Therefore, *Table 10*, presents the total output of emissions for the three states (Texas, Wisconsin, and Oregon), which shows the annual amount in kg (kg/year) for each pollutant formed by the proposed power system. Nevertheless, it is worth mentioning that hybrid systems generally have 45% – 75% fewer emissions values than diesel generator systems for a similar case.

Table 10: Emissions outputs for three stats at 2018 diesel price, 1.0 PV cost multiplier and 1.0 wind turbine cost multiplier

Pollutant	Texas		Wisconsin		Oregon	
	Hybrid System	Diesel System	Hybrid System	Diesel System	Hybrid System	Diesel System
Carbon dioxide (kg/year)	**3,474**	**12,555**	**4,941**	**7,539**	**5,055**	**10,552**
Carbon monoxide (kg/year)	21.90	79.10	31.10	47.50	31.9	66.50
Unburned hydrocarbons (kg/year)	0.96	3.45	1.36	2.07	1.39	2.90
Particulate matter (kg/year)	0.13	0.48	0.19	0.29	0.193	0.40
Sulfur dioxide (kg/year)	8.51	30.70	12.10	18.50	12.4	25.80
Nitrogen oxides (kg/year)	20.60	74.30	29.30	44.60	29.9	62.50

4.6 Different Scenarios

4.6.1 Sensitivity Analysis

The PV cost, wind turbine cost, and diesel price are the three scenarios' variables to be considered in this study. Also, different alternatives are introduced as listed in the previous section to find the optimum system configuration presented by the technologies combination and the number and size of each component.

For each of the different scenarios' values, HOMER simulates all systems in their respective search space. An hourly time-series simulation for every possible system type and configuration is done for one year. The optimization results in a graphical form are shown in the below figures. In these figures, various Optimal System Types (OST) are displayed as functions of different scenario parameters. These plots are given in terms of diesel price and wind turbine price multiplier.

When it comes to the Wisconsin case study, and with the PV cost multiplier set at 1.0 in *Figure 76*, a generator/PV/battery hybrid system is found to be the most suitable for stand-alone loads. However, if the wind turbine price reduced shortly to 10% of its current price, the system

of generator/PV/wind/battery appears to be the best choice for the high diesel price rates, and at less wind turbine cost multipliers this configuration starts to appear at lower diesel rates. On the other hand, when the PV cost multiplier is reduced to 0.5 in *Figure 77*, the OST for the Wisconsin case changed as shown; it resulted that the generator/PV/wind/battery appears after reducing the wind cost by 70% of the current cost with slightly reduced COE values.

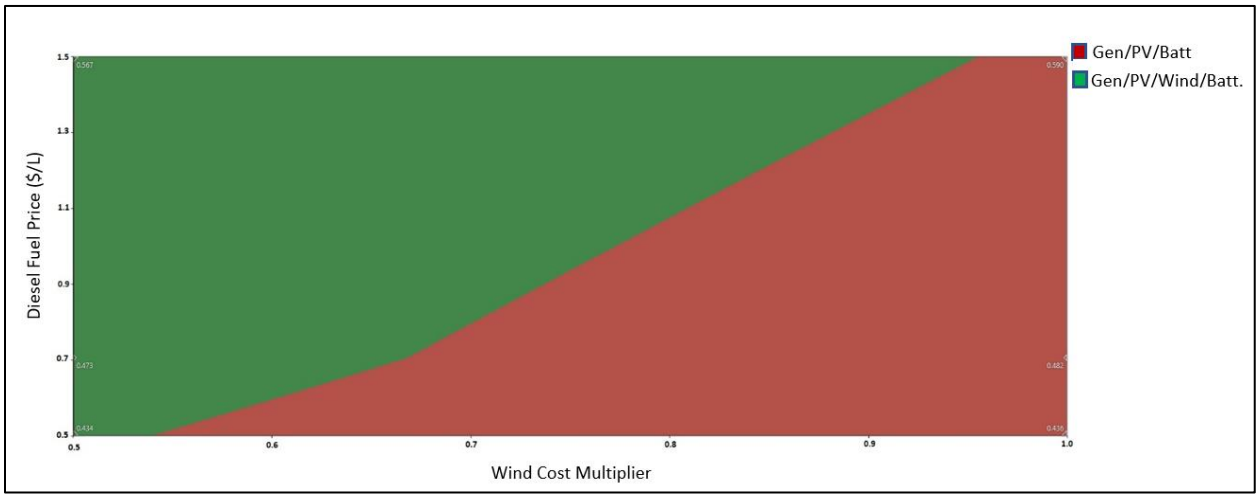

Figure 76: OST with 1.0 PV cost multiplier for Wisconsin case study

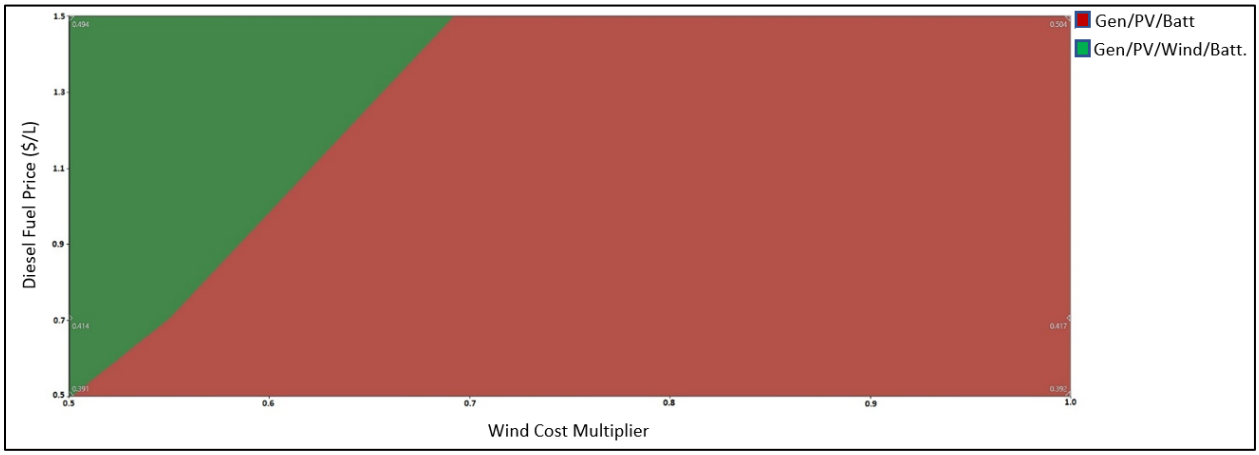

Figure 77: OST with 0.5 PV cost multiplier for Wisconsin case study

For the Oregon case study, considering a PV cost multiplier 1.0 in, a PV/Generator/battery hybrid system is suitable for stand-alone loads, even with the diesel price increased to $1.5/L or decreased to $0.5/L as indicated in *Figure 78*. Therefore, while expecting the wind turbine costs to reduce shortly to reach 50% from its price, the PV/Generator/battery system would still be the

best configuration. *Figure 79* represents a scenario where the PV cos multiplier is reduced to 0.5, noting that there are no changes on the graph except for the reduction in the COE values.

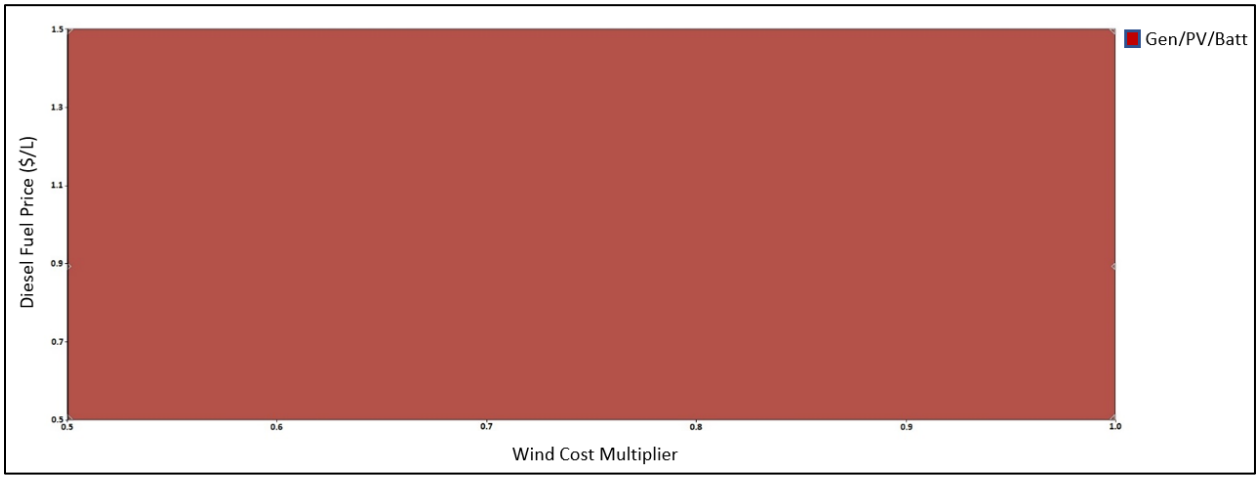

Figure 78: OST with 1.0 PV cost multiplier for the Oregon case study

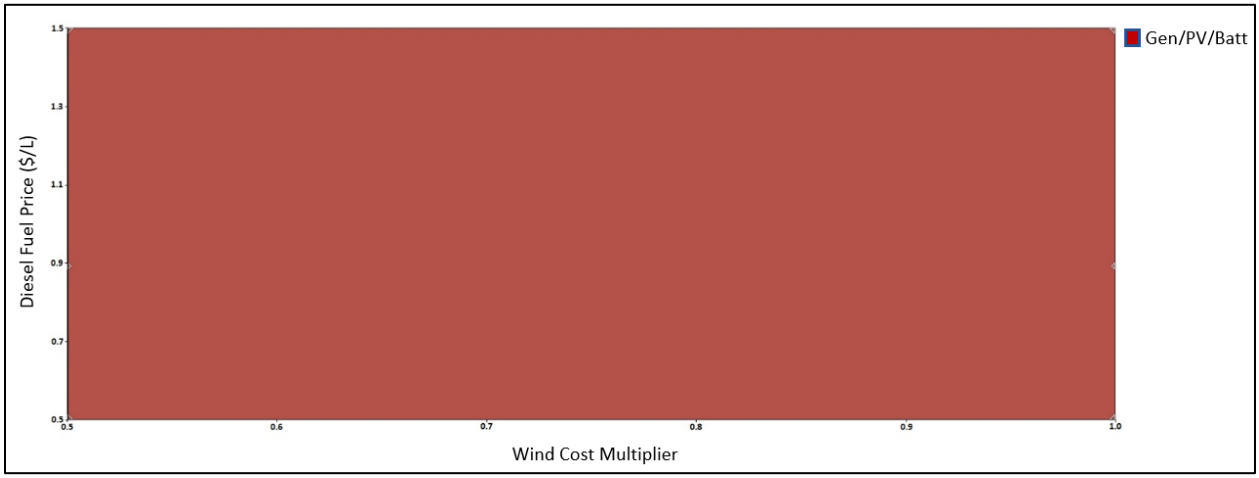

Figure 79: OST with 0.5 PV cost multiplier for the Oregon case study

OST was investigated for the Texas case study in *Figure 80*, where a 1.0 PV cost multiplier was considered. Diesel price and wind turbine cost multiplier values were taken as the different scenario parameters. Irrespective of diesel price, a generator/PV/battery hybrid system would be feasible unless the wind turbine is reduced by less than 0.85 of its current cost. *Figure 81* shows the OST for an 0.5 PV cost multiplier. This figure stresses the fact that, if the wind turbine becomes below 0.65 of it is current cost, the generator/PV/wind/battery configuration would probably be the feasible solution.

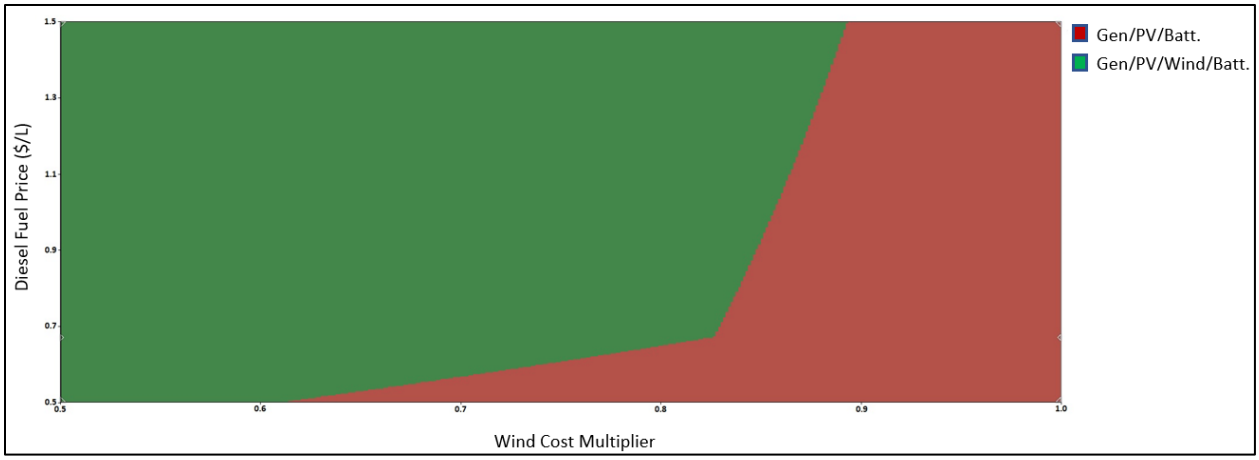

Figure 80: OST with 1.0 PV cost multiplier for Texas case study

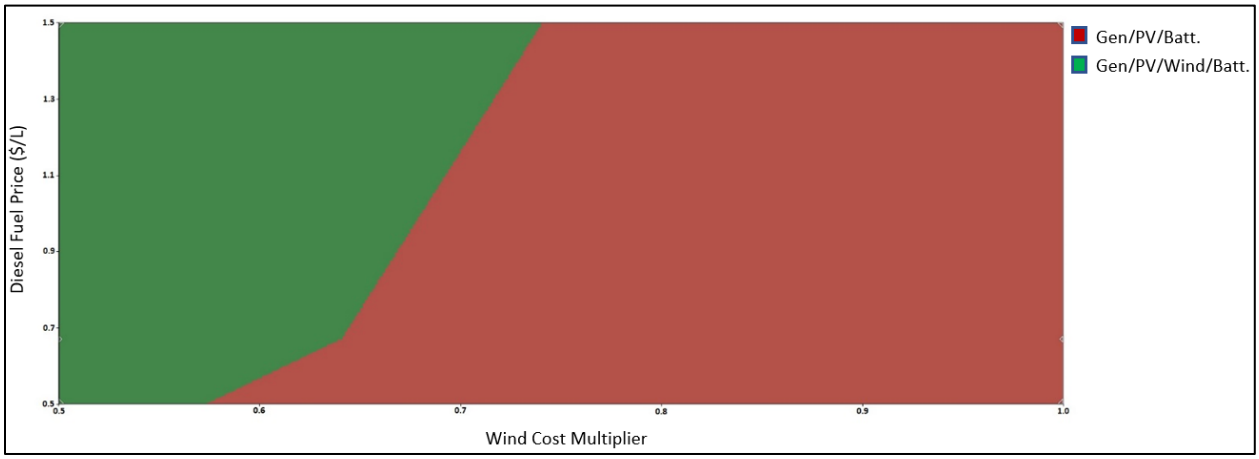

Figure 81: OST with 0.5 PV cost multiplier for Texas case study

4.6.2 Different Applications

The simulation procedure has been repeated for both commercial and industrial applications to understand the effect of having a different load profile on the system configuration selection for each case. *Figure 82* and *Figure 83* shows the COE for each state for commercial building and industrial facility, respectively. After comparing these results of the three applications, it has been noticed that the size of the system affects the COE values, where the higher the system size the lower the COE for the system. For example, in Wisconsin, the COE for the home case study is 0.482, and it becomes 0.403 and 0.379 for the commercial building and industrial facility, respectively.

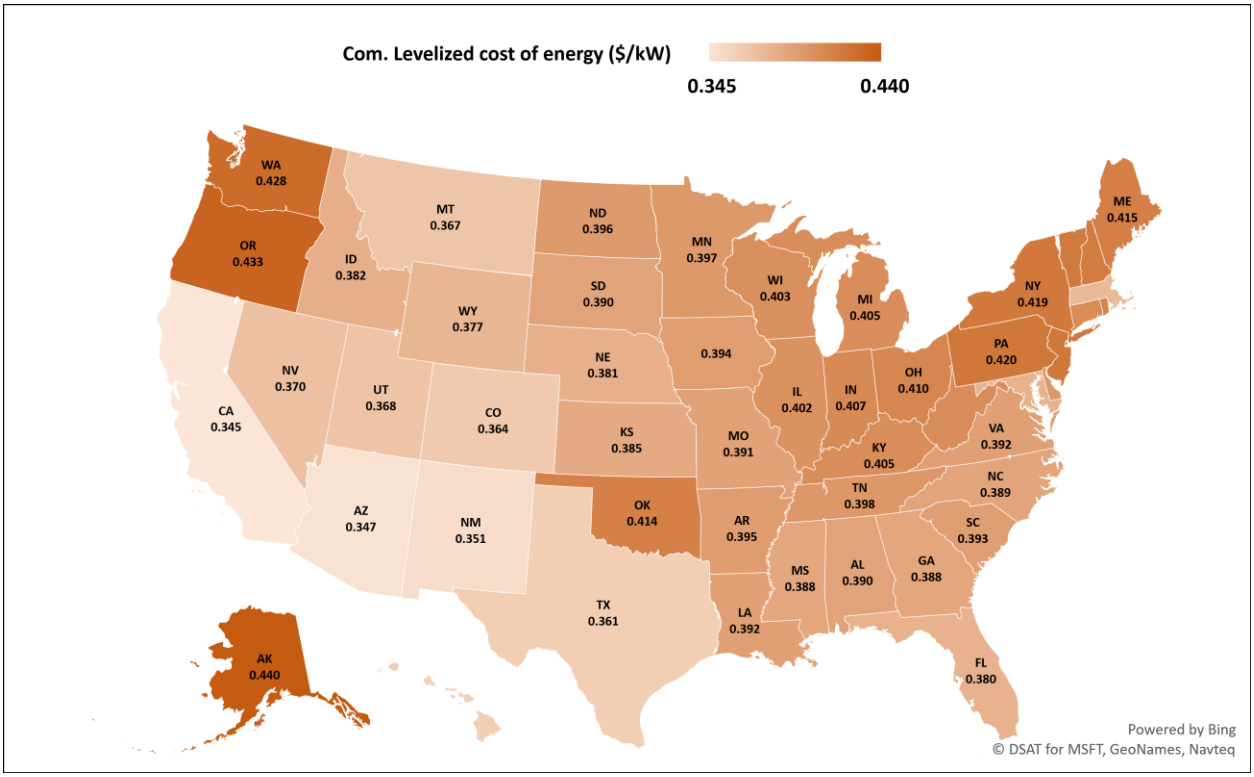

Figure 82: U.S. Average COE per state at 2018 diesel price, 1.0 PV cost multiplier, and 1.0 wind turbine cost multiplier for a typical Commercial building

Figure 84, *Figure 86*, and *Figure 85* display the cash flow summary for all case studies for Wisconsin state broken down by component and by cost type. For the Home case study, it can be noticed from the chart in

Figure 84 that the battery and the diesel generator are having higher NPC values than the other components, this is due to the need to store energy and power the building at night (from 6:00 PM to 11:00 PM), which has the highest power demand during the day.

For the Commercial building case study and from the chart in *Figure 85*, it is obvious that the PV is having a larger amount of NPC than the home case study; this can be explained according to its load profile, which has higher power demand during daylight (from 8:00 AM to 5:00 PM).

From the Industrial facility case cash flow summary in *Figure 86*, the diesel generator component appears as the maximum NPC value due to the variation of load demand during the day.

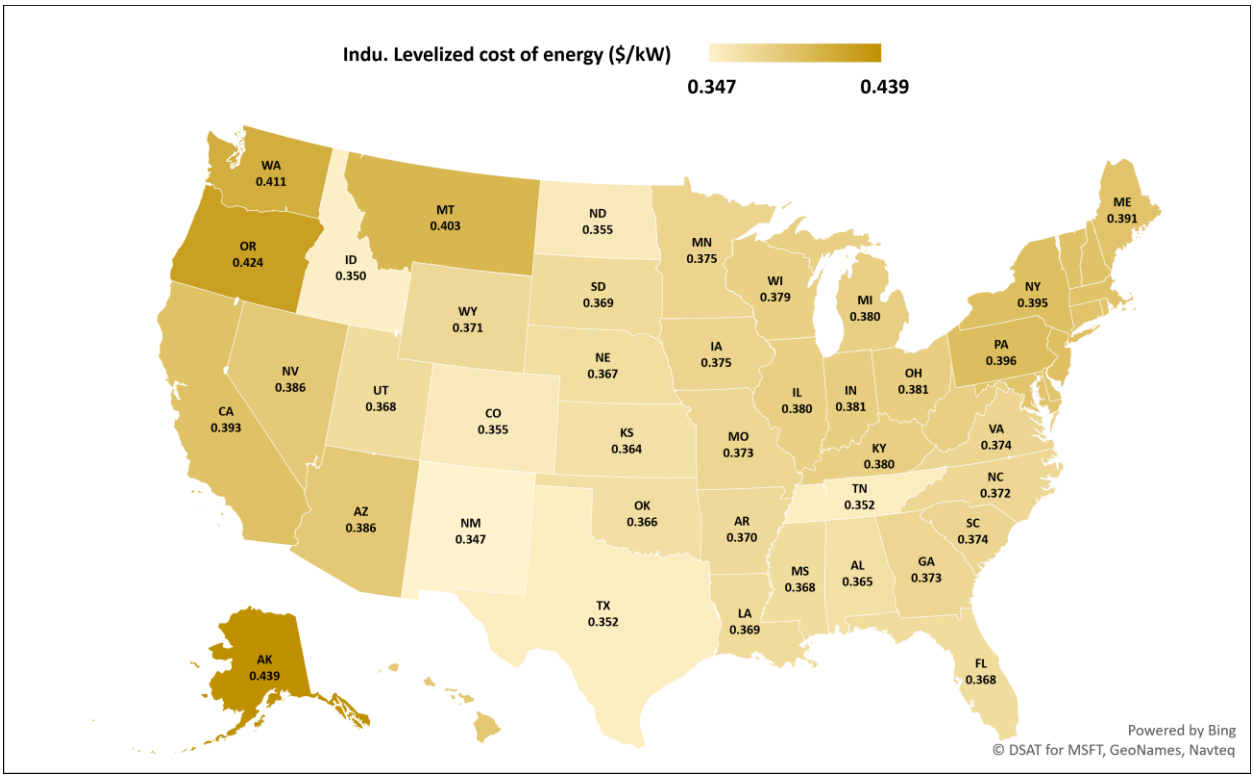

Figure 83: U.S. Average COE per state at 2018 diesel price, 1.0 PV cost multiplier, and 1.0 wind turbine cost multiplier for a typical Industrial facility

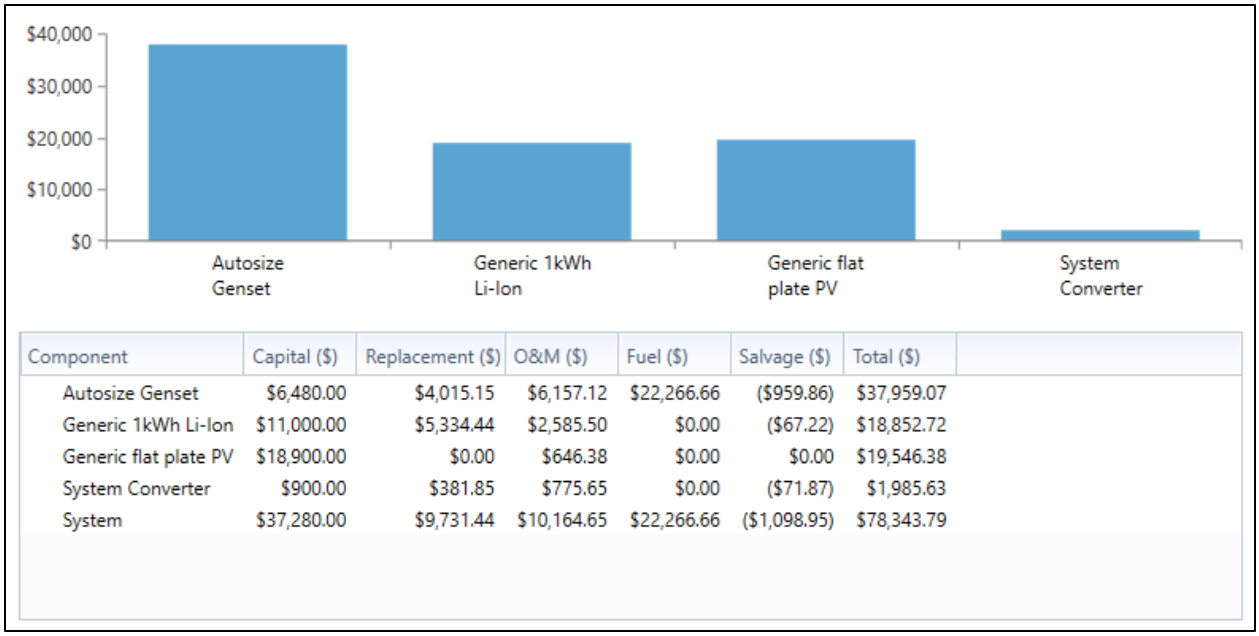

Component	Capital ($)	Replacement ($)	O&M ($)	Fuel ($)	Salvage ($)	Total ($)
Autosize Genset	$6,480.00	$4,015.15	$6,157.12	$22,266.66	($959.86)	$37,959.07
Generic 1kWh Li-Ion	$11,000.00	$5,334.44	$2,585.50	$0.00	($67.22)	$18,852.72
Generic flat plate PV	$18,900.00	$0.00	$646.38	$0.00	$0.00	$19,546.38
System Converter	$900.00	$381.85	$775.65	$0.00	($71.87)	$1,985.63
System	$37,280.00	$9,731.44	$10,164.65	$22,266.66	($1,098.95)	$78,343.79

Figure 84: Cash flow summary for a Home case study for Wisconsin state

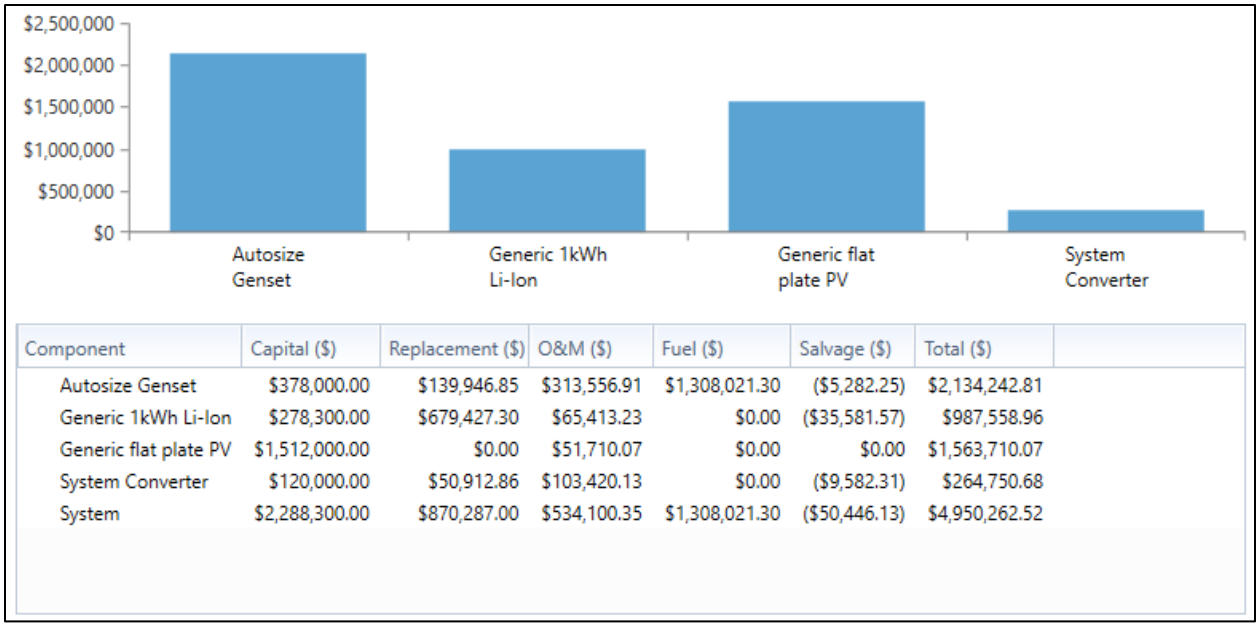

Component	Capital ($)	Replacement ($)	O&M ($)	Fuel ($)	Salvage ($)	Total ($)
Autosize Genset	$378,000.00	$139,946.85	$313,556.91	$1,308,021.30	($5,282.25)	$2,134,242.81
Generic 1kWh Li-Ion	$278,300.00	$679,427.30	$65,413.23	$0.00	($35,581.57)	$987,558.96
Generic flat plate PV	$1,512,000.00	$0.00	$51,710.07	$0.00	$0.00	$1,563,710.07
System Converter	$120,000.00	$50,912.86	$103,420.13	$0.00	($9,582.31)	$264,750.68
System	$2,288,300.00	$870,287.00	$534,100.35	$1,308,021.30	($50,446.13)	$4,950,262.52

Figure 85: Cash flow summary for Commercial building case study for Wisconsin state

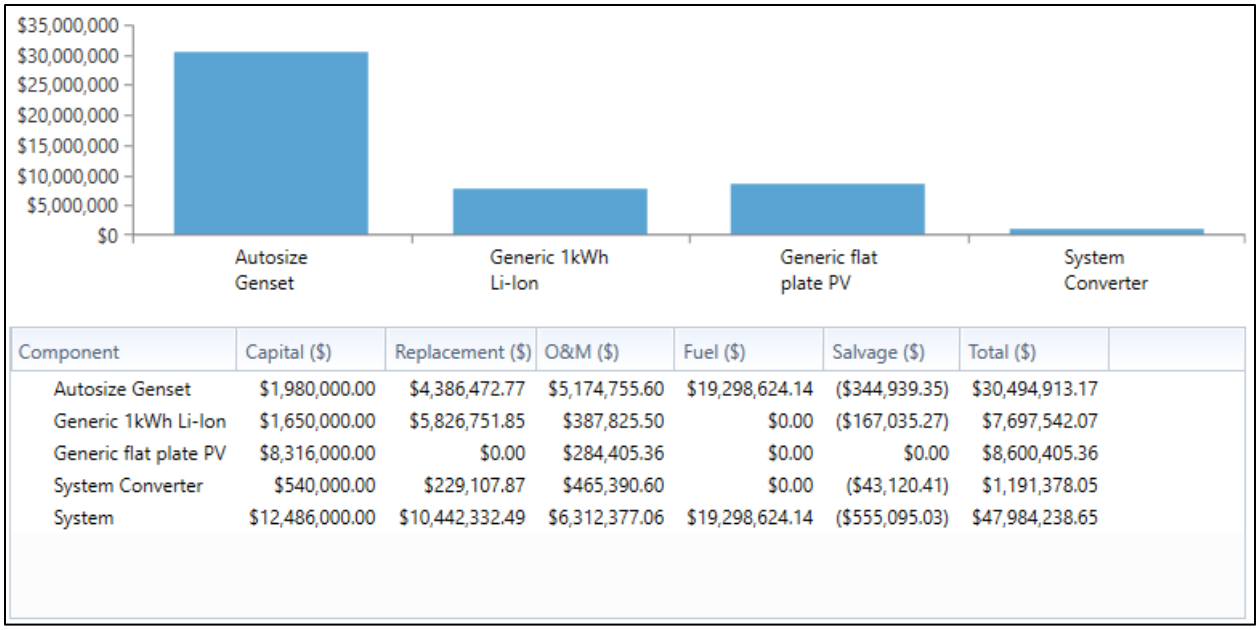

Component	Capital ($)	Replacement ($)	O&M ($)	Fuel ($)	Salvage ($)	Total ($)
Autosize Genset	$1,980,000.00	$4,386,472.77	$5,174,755.60	$19,298,624.14	($344,939.35)	$30,494,913.17
Generic 1kWh Li-Ion	$1,650,000.00	$5,826,751.85	$387,825.50	$0.00	($167,035.27)	$7,697,542.07
Generic flat plate PV	$8,316,000.00	$0.00	$284,405.36	$0.00	$0.00	$8,600,405.36
System Converter	$540,000.00	$229,107.87	$465,390.60	$0.00	($43,120.41)	$1,191,378.05
System	$12,486,000.00	$10,442,332.49	$6,312,377.06	$19,298,624.14	($555,095.03)	$47,984,238.65

Figure 86: Cash flow summary for Industrial facility case study for Wisconsin state

Table 11 displays the total annual energy output from each electrical energy-producing component of the power system, along with the total electrical production. The table is an electrical production comparison between three stats for the three application case studies. The load profile for each case has a strong effect on how the system will produce electric power. It can be spotted that, for the Home case, the PV panels have a high contribution in producing electricity in states with high solar irradiation values as in Oregon and Texas with more than 50% of the total electricity production, and a lower percentage for states with low solar irradiation values as Wisconsin. However, for the Commercial building case, the PV panels have the highest electricity production percentage at most states with more than 50% despite its solar irradiation and that due to the load profile for this application throughout the year.

Table 11: Electrical production for three stats at 2018 diesel price, 1.0 PV cost multiplier, and 1.0 wind turbine cost multiplier for different applications

State	Application	Component	PV	Diesel Gen.	Total
Texas	Home	Production (kWh/year)	13,456	4,324	**17,780**
		Fraction	***75.7%***	***24.3%***	**100%**
	Commercial building	Production (kWh/year)	747,558	381,753	**1,129,311**
		Fraction	***66.2%***	***33.8%***	**100%**
	Industrial facility	Production (kWh/year)	3,588,278	6,346,098	**9,934,376**
		Fraction	***36.1%***	***63.9%***	**100%**
Wisconsin	Home	Production (kWh/year)	3,832	6,088	**9,920**
		Fraction	***38.6%***	***61.4%***	**100%**
	Commercial building	Production (kWh/year)	638,690	451,500	**1,090,190**
		Fraction	***58.6%***	***41.4%***	**100%**
	Industrial facility	Production (kWh/year)	3,065,713	6,777,772	**9,843,485**
		Fraction	***31.1%***	***68.9%***	**100%**
Oregon	Home	Production (kWh/year)	7,671	5,927	**13,597**
		Fraction	***56.4%***	***43.6%***	**100%**
	Commercial building	Production (kWh/year)	613,667	443,382	**1,057,049**
		Fraction	***58.1%***	***41.9%***	**100%**
	Industrial facility	Production (kWh/year)	3,201,942	6,593,042	**9,794,984**
		Fraction	***32.7%***	***67.3%***	**100%**

In the case study of an industrial facility, the diesel generator has the highest electricity production percentage due to the long working hours (24 hours a day) for industrial applications in all three states. *Appendix D* and *Appendix F* shows the electrical production for all states for the Commercial, and Industrial application, respectively.

The data map (DMap) in *Figure 87*, is a type of graph showing one year of time series data. With the time of day on one axis and day of the year on the other, each time step of the year is represented by a rectangle which is colored according to the data value for that hour, *Figure 87* show the power output of the generator in each hour of the year for the three applications in Wisconsin case study.

For the Home case study, the concentrated area, which is denoted by the colored stripes representing the use of a diesel generator, lies in the early and late hours of the day. On the other hand, there would be a minor use of the diesel generator throughout the year for the commercial building case study. That is due to the loaded nature and working hours of the building, which is normally around midday. In the last case of an industrial facility, the map illustrates a major need for the diesel generator, especially at the beginning and end of daylight hours, which is due to the absence of sunlight and the need for a high electrical energy supply.

Noting from *Appendix E* and *Appendix G* that the emission values for hybrid systems are between 45-75% less than emission values for diesel systems for the same case study at all applications.

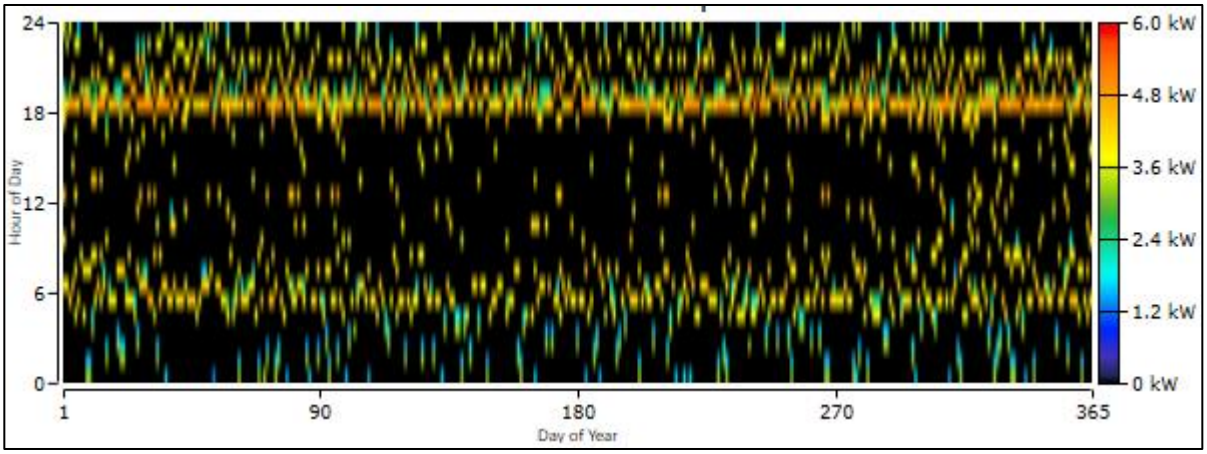

a) Home

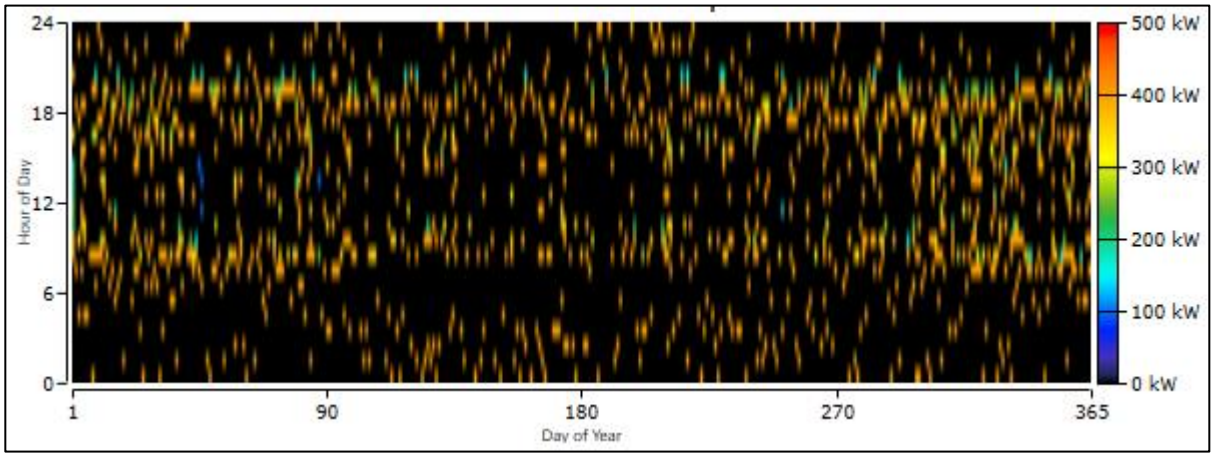

b) Commercial building

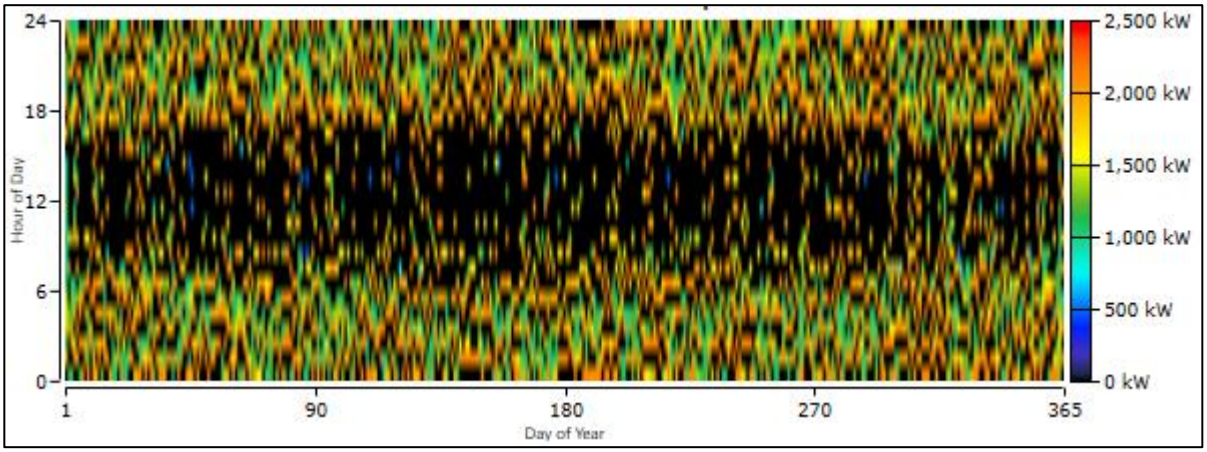

c) Industrial facility

Figure 87: DMap of the Generator for three applications in Wisconsin case study: a) Home b) Commercial building c) Industrial facility

4.6.3 Fuels of the Generator

Generating power by using a natural gas generator is widely used. Natural gas can be used to power both emergency and portable generators and it is considered one of the most affordable, clean, and effective fuels among fossil fuels nowadays [135]. The liquid form of the natural gas can be transported and then converted into its gaseous form to be used in the generators.

This study considered diesel as the fuel for the generator. The simulation then repeated using the natural gas as the fuel, to compare between both fuels. *Table 12* shows a comparison between the use of a diesel generator and natural gas one for residential building application in three different states (Texas, Wisconsin & Oregon). It can be noticed that considering the natural gas generator which has lower installation and running cost than the diesel generator, reduces the net present cost, the COE, PV size, and the number of batteries at all states.

Table 12: Comparison of three stats at 2018 fuel prices, 1.0 PV cost multiplier and 1.0 wind turbine cost multiplier for home application

Component	**Texas**		**Wisconsin**		**Oregon**	
Fuel type	Diesel	Natural Gas	Diesel	Natural Gas	Diesel	Natural Gas
PV Array (kW)	9.0	5.0	3.0	3.0	5.0	3.0
Gen. (kW)	8.7	8.7	5.2	5.2	7.2	7.2
Battery (1 kWh Li-Ion)	32	8	6	4	20	8
Converter (kW)	5.0	5.0	3.0	3.0	3.0	5.0
Total net present cost ($)	79,421	58,911	52,527	35,819	78,344	51,542
Annual Operating cost ($)	2,264	2,901	2,750	1,784	3,176	2,486
COE ($/kWh)	**0.436**	**0.323**	**0.482**	**0.328**	**0.517**	**0.340**
Daily Radiation (kWh/m^2/day)	4.93	4.93	3.73	3.73	4.48	4.48
Fuel Price	0.670 $/L	0.300 $/m^3	0.705 $/L	0.220 $/m^3	0.892 $/L	0.280 $/m^3
Gen. working hours	631	1,519	1,552	1,899	1,323	1,448
Production (kWh)	4,324	9,478	6,088	6,180	5,927	8,722
Gen. production fraction	24.3%	55.9%	61.4%	61.7%	43.6%	65.5%

Chapter 5: Conclusions and Future Work Recommendations

5.1 Research Conclusions

5.1.1 Conclusions of the Cavitation Characteristics

In this study, the relation between the cavitation number and the lift to drag ratio was investigated. The simulation for the hydrofoil in the water tunnel was done for four different AoA at two water flow velocities (9.1 m/s and 12.2 m/s). The validation of using the CFD software has been done by comparing the simulation results with published experimental data and by showing that both effects have the same trend with a maximum average relative error of 10%, which is estimated in the acceptable range of accuracy for CFD software.

The designed hydrofoil was 3D printed along with other parts, such as the water straightener, and was used in building the experimental setup for testing. The experimental setup had two reservoirs; an elevated tank upstream of the turbine and a downstream sink with a circulating pump in between. The hydrofoil was installed in a clear water tunnel to capture the cavitation by a high-speed camera. The images captured by the high-speed camera were used in the validation and comparison process.

The validation and comparison were accomplished through three steps: visual validation, CFD simulation results, and image processing. The VVF scenes and high-speed camera images were compared and validated, visually, the cavitation behavior and pattern. The image processing confirmed the percentages of the cavitation area, numerically and experimentally, with almost matching values.

It was found that the amount of the generated vapor over the NACA 66-012 hydrofoil strongly affects the lift and drag coefficients and the turbomachines' performance. With the 3rd order curves, where most of the points were fit on the graphs between the VVF and lift/drag coefficients, the

more bubbles generated over the hydrofoil, the drag coefficient tends to increase to a specific limit; it starts to decrease in most AoA cases. The lift coefficient, however, decreases by increasing the VVF values in all cases. The drag and lift coefficients tend to increase when increasing the AoA at the same cavitation number due to degradation of the average flow velocity over the hydrofoil. For a given cavitation number, the higher the AoA, the VVF value becomes higher, and, thus, the possibility of occurring cavitation increases. The correlation between the VVF and the cavitation number for each AoA was found to give a 4^{th} order curve that could fit through them.

Finally, what one also notices is that, for the same AoA, when the cavitation number starts to decrease, the VVF starts to form. Thus, more cavitation occurs. At high cavitation numbers, the cavitation formed only on the leading-edge tip of the hydrofoil, while when the cavitation number decrease, the cavitation formed all over the hydrofoil. The lift to drag ratio decreases with the formation of the cavitation over the hydrofoil, which leads to the fact that the cavitation is dropping the efficiency of the turbomachines.

5.1.2 Conclusions of the Cavitation Treatment Simulations

In this study, a method to treat the cavitation phenomenon over a hydrofoil was introduced. The cavitation treatment via air injection was investigated numerically. The CFD simulations monitored the VVF scenes to study cavitation behavior. With eight water inlet velocities per each AoA case, all cases were simulated including no aeration and air injection cases at 0 psig air pressure. The first group was simulated without air injection to provide baseline data for the comparison process. Then, the air was introduced at 0 psig to examine the effect of injecting air. The air was injected via 6 and 3 air slots over the hydrofoil.

As a result, the following can be concluded:

- The air injection showed an increase in the absolute pressure in the system offsetting most zones' pressure above the water vapor pressure.
- Air injection at 0 psig and 6 air slots showed an average VVF reduction of 97.9% when compared to no aeration case.
- Air injection at 0 psig and 3 air slots showed an average VVF reduction of 93% when compared to no aeration case.
- The cavitation was further reduced while increasing the air injection slots.
- The cavitation reduction was substantial and reached 99% in some cases.
- The air injection exhibited an effective method in the mitigation and treatment of the cavitation phenomenon in hydro turbines.

5.1.3 Conclusion of the Hybrid Systems Optimization in Remote Areas

Whether generation systems are off-grid or on-grid, currently, hybrid renewable energy systems are still less feasible than conventional fossil-fuel-based power resources. Yet, the continuous need for cleaner energy and increased demand for alternative energy resources involves ample opportunity for utilizing such systems.

Several renewable (i.e., solar and wind) and non-renewable (i.e., fossil-fuel-based) energy resources with a storage system (battery) were presented in the current study. An optimization software tool by NREL called HOMER was utilized to detect the possible hybrid energy systems' configurations with taking applicability and feasibility into consideration. Subsequently, and based on the analysis presented, below are the main findings and conclusions of this research:

- The most proper combination for a residential building in most states is the PV-diesel generator system equipped with battery storage. Such a system can deliver 30 kWh/day on average with a peak of 5.3 kW with an energy cost of $0.43/kWh to $0.57/kWh.

- The most impactful variables on selecting the best combination for each state and COE values are the daily radiation and the diesel price.
- Hybrid systems can have 45-75% less GHG emissions than conventional generation systems.
- The relatively low cost of wind turbines makes the generator-PV-wind-battery system combination the optimum option in some cases.
- The selection process of the best suitable configuration in most states largely depends on diesel prices.
- The size of the system (Home, commercial, and facility) affects the COE values, where the higher the system size the lower the COE for the system for the same state. Also, it affects the power generated by the hybrid system, where the working hours for each application changing the hybrid system performance.
- The natural gas generator has a lower installation and running cost than the diesel generator, reduces the net present cost, the COE, PV size, and the number of batteries at all states.

For more feasible and cost-competitive hybrid systems, multiple and more extensive systems are recommended over single stand-alone units. The economies of scale can reduce that energy cost to be comparable with the current average utility electricity prices. Also, to take hybrid systems to a commercial scale with acceptable feasibility, substantial research and development are highly recommended.

5.2 Future Work Recommendations

5.2.1 Recommendation for the Cavitation Treatment

The work that was completed during this study is promising and can lead to a breakthrough in cavitation treatment technologies, extending the lifespan of the hydro turbines, and enhancing their performance over time. Therefore, the following can be investigated in the future on the same setup to expand on this study:

- Examine the effect of changing the air injection slots' size and location.
- Expand the experimental setup by developing the water tunnel to enable running it as a professional water tunnel and controlling the cavitation number over the hydrofoils.
- Testing more hydrofoils at the experimental setup.
- Further investigation for optimizing the air injection design and location experimentally, some parameters were not evaluated in this study and some of these are more hydrofoils AoA and the effect of the air slots openings on the hydrofoil construction.

5.2.2 Recommendation for the Hybrid System

Based on the findings of the study in hand, future work is recommended as below:

- More optimization regarding the effects of including one more energy storage type, by produce hydrogen, using electrolyzer during and supply the hydrogen into a fuel cell to generate electricity.

The Fuel Cell (FC), schematically shown in *Figure 88*, is an electrochemical device that produces electricity through the reaction of hydrogen and oxygen in the presence of an electrolyte. Most of the fuel cells made have three components: the anode, the cathode, and the electrolyte. After the chemical reactions occur between these components with consuming the hydrogen fuel

through it, the results are water or carbon dioxide and generate electric current. The current generated is used to power an electrical load.

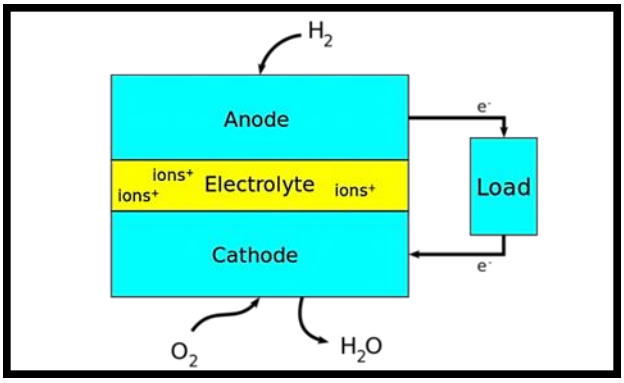

Figure 88: Fuel Cell block diagram [136]

Electrolysis is using the electric current to break down the water (H_2O) into oxygen (O_2) and hydrogen gas (H_2). As per *Figure 89*, an electrical power source is connected to two electrodes or two plates that are placed in water. Hydrogen appears at the cathode and oxygen appears at the anode (the positively charged electrode).

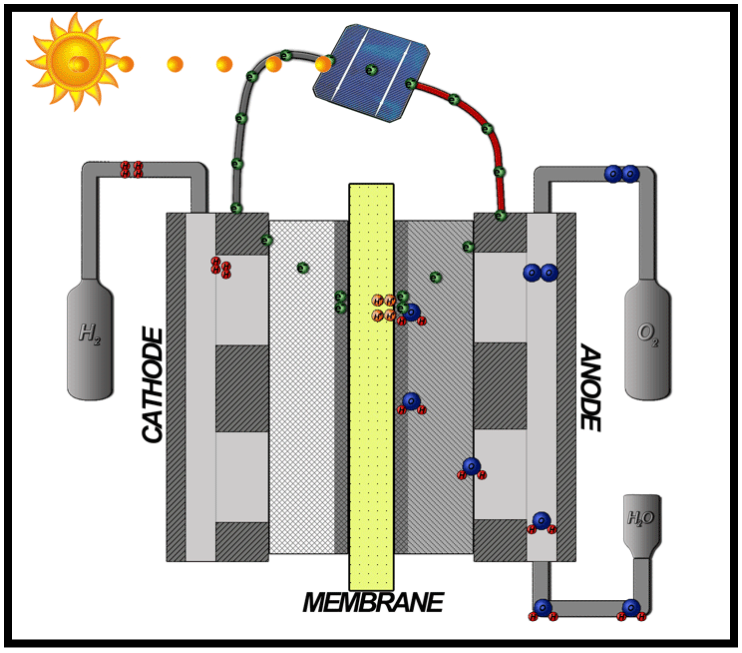

Figure 89: Diagram of an Electrolyzer cell and the basic principle of operation [137]

References

[1] K. Vincent Wong, “Engineering Solutions to the Greenhouse Gases Generated by Hydroelectric Plants,” *J. Energy Resour. Technol.*, vol. 136, no. 2, p. 024701, Apr. 2014, doi: 10.1115/1.4027260.

[2] B. G. S. Prasad, “Energy efficiency, sources and sustainability,” *J. Energy Resour. Technol. Trans. ASME*, vol. 132, no. 2, pp. 1–2, 2010, doi: 10.1115/1.4001684.

[3] REN21 Secretariat, “Renewable Energy Policy Network for the 21st Century, 2019, Renewables 2019 Global Status Report,” Paris, France, 2019.

[4] “Solar explained - U.S. Energy Information Administration (EIA).” https://www.eia.gov/energyexplained/solar/ (accessed May 11, 2020).

[5] U. Rau and H. W. Schock, “Chapter 6: $Cu(In,Ga)Se_2$ and related solar cells,” in *Series on Photoconversion of Solar Energy - Vol 4: Clean Electricity From Photovoltaics, Second Edition*, 2015.

[6] V. V. Tyagi, N. A. A. Rahim, N. A. Rahim, and J. A. L. Selvaraj, “Progress in solar PV technology: Research and achievement,” *Renewable and Sustainable Energy Reviews*, vol. 20. Elsevier Ltd, pp. 443–461, Apr. 01, 2013, doi: 10.1016/j.rser.2012.09.028.

[7] REN 21 Renewables Now, *Renewables Global Status Report 2019*. 2019.

[8] J. K. Kaldellis, *Stand-Alone and Hybrid Wind Energy Systems - Technology, Energy Storage and Applications - Knovel*. Woodhead Publishing, 2010.

[9] Energy Information Administration, “Wind explained - U.S. Energy Information Administration (EIA).” https://www.eia.gov/energyexplained/wind/ (accessed May 11, 2020).

[10] A. I. Abbas, M. D. Qandil, M. R. Al-Haddad, M. S. Saravani, and R. S. Amano, “Utilization

of Hydroturbines in Wastewater Treatment Plants," *J. Energy Resour. Technol. Trans. ASME*, vol. 141, no. 6, Jun. 2019, doi: 10.1115/1.4042969.

[11] A. I. Abbas, M. D. Qandil, M. R. Al-Haddad, M. S. Saravani, and R. S. Amano, "Utilization of hydro-turbines in wastewater treatment plants (WWTPS)," in *ASME 2018 12th International Conference on Energy Sustainability, ES 2018, collocated with the ASME 2018 Power Conference and the ASME 2018 Nuclear Forum*, Oct. 2018, doi: 10.1115/es2018-7349.

[12] A. I. Abbas, M. D. Qandil, M. R. Al-Haddad, and R. S. Amano, "Performance investigation of very-low-head kaplan hydro-turbines," in *AIAA Scitech 2019 Forum*, 2019, doi: 10.2514/6.2019-0241.

[13] "Total Energy Annual Data - U.S. Energy Information Administration (EIA)," 2019. https://www.eia.gov/totalenergy/data/annual/index.php.

[14] T. Rosado, "How a Hydrofoil Works," 1999. Accessed: May 12, 2020. [Online]. Available: http://web.mit.edu/2.972/www/reports/hydrofoil/hydrofoil.html.

[15] M. D. Qandil, T. Elgammal, A. I. Abbas, A. I. Abdelhadi, and R. S. Amano, "Predicting the cavitation phenomena over the hydrofoil: CFD validation," in *AIAA Scitech 2019 Forum*, 2019, doi: 10.2514/6.2019-0783.

[16] "Polymeric Solution for Pumps Suffering from Cavitation | Pumps & Systems." https://www.pumpsandsystems.com/polymeric-solution-pumps-suffering-cavitation (accessed May 13, 2020).

[17] C. Brennen, "An Introduction to Cavitation Fundamentals," in *WIMRC FORUM*, 2011, pp. 1–17, Accessed: May 13, 2020. [Online]. Available: https://www.researchgate.net/publication/279685077_An_Introduction_to_Cavitation_Fu

ndamentals.

[18] Y. Liu, A. Zhang, and Z. Tian, “Approximation of underwater explosion bubble by singularities based on BEM,” *Ocean Eng.*, vol. 75, pp. 46–52, Jan. 2014, doi: 10.1016/j.oceaneng.2013.11.008.

[19] C. E. (Christopher E. Brennen, *Cavitation and bubble dynamics*. 2013.

[20] “Cavitation vs. Air Entrainment | Pumps & Systems.” https://www.pumpsandsystems.com/cavitation-vs-air-entrainment (accessed May 13, 2020).

[21] R. Yakushiji, “MECHANISM OF TIP VORTEX CAVITATION SUPPRESSION BY POLYMER AND WATER INJECTION,” 2009.

[22] P. Kumar and R. P. Saini, “Study of cavitation in hydro turbines-A review,” *Renewable and Sustainable Energy Reviews*. 2010, doi: 10.1016/j.rser.2009.07.024.

[23] A. Kubota, H. Kato, and H. Yamaguchi, “A new modelling of cavitating flows: A numerical study of unsteady cavitation on a hydrofoil section,” *J. Fluid Mech.*, 1992, doi: 10.1017/S002211209200003X.

[24] J. Amano, R.S., Lequesne, B., and Millevolte, “Very Low-Head Hydro Turbine Research,” 2017.

[25] R. W. Kermeen, “NACA 4412 AND WALCHNER PROFILE 7 HYDROFOILS IN NONCAVITATINC AND CAVITATING FLOWS,” *Aging (Albany. NY).*, 2015, doi: 10.1017/CBO9781107415324.004.

[26] “SDG7: Data and Projections – Analysis - IEA.” https://www.iea.org/reports/sdg7-data-and-projections (accessed May 12, 2020).

[27] International Energy Agency, “World Energy Model Documentation,” 2019.

[28] U. C. Bureau, “New Census Data Show Differences Between Urban and Rural Populations,” 2016. Accessed: May 14, 2020. [Online]. Available: https://www.census.gov/newsroom/press-releases/2016/cb16-210.html.

[29] L. Zhang and B. C. Khoo, “Dynamics of unsteady cavitating flow in compressible two-phase fluid,” *Ocean Eng.*, vol. 87, pp. 174–184, Sep. 2014, doi: 10.1016/j.oceaneng.2014.06.005.

[30] Q. Wu, B. Huang, G. Wang, and Y. Gao, “Experimental and numerical investigation of hydroelastic response of a flexible hydrofoil in cavitating flow,” *Int. J. Multiph. Flow*, vol. 74, pp. 19–33, Sep. 2015, doi: 10.1016/j.ijmultiphaseflow.2015.03.023.

[31] J.-B. Leroux, J. A. Astolfi, and J. Y. Billard, “An experimental study of unsteady partial cavitation,” *asmedigitalcollection.asme.org*, vol. 126, no. 1, pp. 94–101, Jan. 2004, doi: 10.1115/1.1627835.

[32] A. I. Abbas, M. D. Qandil, M. R. Al-Haddad, and R. S. Amano, “Performance investigation of very-low-head kaplan hydro-turbines,” in *AIAA Scitech 2019 Forum*, 2019, doi: 10.2514/6.2019-0241.

[33] A. Y. Kravtsova, D. M. Markovich, K. S. Pervunin, M. V. Timoshevskiy, and K. Hanjalić, “High-speed visualization and PIV measurements of cavitating flows around a semi-circular leading-edge flat plate and NACA0015 hydrofoil,” *Int. J. Multiph. Flow*, vol. 60, pp. 119–134, Apr. 2014, doi: 10.1016/j.ijmultiphaseflow.2013.12.004.

[34] M. Kjeldsen, R. E. A. Arndt, and M. Effertz, “Spectral characteristics of sheet/cloud cavitation,” *J. Fluids Eng. Trans. ASME*, vol. 122, no. 3, pp. 481–487, 2000, doi: 10.1115/1.1287854.

[35] D. F. De Lange and G. J. De Bruin, “Sheet cavitation and cloud cavitation, re-entrant jet

and three-dimensionality," *Appl. Sci. Res. (The Hague)*, vol. 58, no. 1–4, pp. 91–114, 1997, doi: 10.1023/A:1000763130780.

[36] Y. Yang *et al.*, "Experimental Study of a Lift-Type Wave Energy Converter Rotor in a Freewheeling Mode," *asmedigitalcollection.asme.org*, vol. 142, no. 3, Mar. 2019, doi: 10.1115/1.4044550.

[37] K. R. Laberteaux and S. L. Ceccio, "Partial cavity flows. Part 2. Cavities forming on test objects with spanwise variation," *J. Fluid Mech.*, vol. 431, pp. 43–63, Mar. 2001, doi: 10.1017/S0022112000002937.

[38] E. J. Foeth, C. W. H. Van Doorne, T. Van Terwisga, and B. Wieneke, "Time resolved PIV and flow visualization of 3D sheet cavitation," *Exp. Fluids*, vol. 40, no. 4, pp. 503–513, Apr. 2006, doi: 10.1007/s00348-005-0082-9.

[39] E. Foeth, … T. van T.-J. of F., and undefined 2008, "On the collapse structure of an attached cavity on a three-dimensional hydrofoil," *asmedigitalcollection.asme.org*, Accessed: May 17, 2020. [Online]. Available: https://asmedigitalcollection.asme.org/fluidsengineering/article-abstract/130/7/071303/444688.

[40] R. Kermeen, "Water tunnel tests of NACA 4412 and Walchner Profile 7 hydrofoils in noncavitating and cavitating flows," 1956. Accessed: May 17, 2020. [Online]. Available: https://authors.library.caltech.edu/6014/.

[41] Y. Kawanami, H. Kato, H. Yamaguchi, M. Tanimura, and Y. Tagaya, "Mechanism and control of cloud cavitation," *J. Fluids Eng. Trans. ASME*, vol. 119, no. 4, pp. 788–794, 1997, doi: 10.1115/1.2819499.

[42] R. Arndt, C. Song, M. Kjeldsen, J. He, and A. Keller, "Instability of partial cavitation: a

numerical/experimental approach," 2000. Accessed: May 17, 2020. [Online]. Available: https://conservancy.umn.edu/handle/11299/49781.

[43] S.-E. Kim, "A Numerical Study of Unsteady Cavitation on A Hydrofoil," 2009. Accessed: May 17, 2020. [Online]. Available: https://deepblue.lib.umich.edu/handle/2027.42/84252.

[44] Z. Li and T. Van Terwisga, "On the Capability of Multiphase RANS Codes to Predict Cavitation Erosion," 2011. Accessed: May 17, 2020. [Online]. Available: http://www.marinepropulsors.com/smp/files/downloads/smp11/Paper/TB3-1_Li.pdf.

[45] J. Decaix and E. Goncalvès, "Investigation of three-dimensional effects on a cavitating Venturi flow," *Int. J. Heat Fluid Flow*, vol. 44, pp. 576–595, Dec. 2013, doi: 10.1016/j.ijheatfluidflow.2013.08.013.

[46] A. Abbas, … M. Q.-J. of E., and undefined 2020, "Investigation of Horizontal Micro Kaplan Hydro Turbine Performance Using Multi-Disciplinary Design Optimization," *asmedigitalcollection.asme.org*, Accessed: May 17, 2020. [Online]. Available: https://asmedigitalcollection.asme.org/energyresources/article-abstract/142/5/052101/1072203?casa_token=02-lvtes2YAAAAAA:WI5ofnhT1iMc0apodQUXWbt95q8CEhZCfGR7M_6Kxm59vu5F_kpoSJLoLMi7DnVVSGmK373jxA.

[47] X. C. Wu, Y. W. Wang, and C. G. Huang, "Effect of mesh resolution on large eddy simulation of cloud cavitating flow around a three dimensional twisted hydrofoil," *Eur. J. Mech. B/Fluids*, vol. 55, pp. 229–240, Jan. 2016, doi: 10.1016/j.euromechflu.2015.09.011.

[48] P. J. Hartman, P. Luetjen, and D. Mandel, "RELIABILITY ANALYSIS OF TOTAL SYSTEMS USING COMPONENT FAILURE DATA.," *J. Energy Resour. Technol. Trans. ASME*, vol. 105, no. 2, pp. 217–221, 1983, doi: 10.1115/1.3230906.

[49] N. Tabatabaei, S. Gantasala, and M. J. Cervantes, “Wind Turbine Aerodynamic Modeling in Icing Condition: Three-Dimensional RANS-CFD Versus Blade Element Momentum Method,” *J. Energy Resour. Technol. Trans. ASME*, vol. 141, no. 7, Jul. 2019, doi: 10.1115/1.4042713.

[50] S. Huang, M. He, C. Wang, and X. Chang, “Simulation of Cavitating Flow around a 2-D Hydrofoil,” *J. Mar. Sci. Appl*, vol. 9, no. 1, pp. 63–68, Mar. 2010, doi: 10.1007/s11804-010-8090-4.

[51] S. Schroeder, S.-E. Kim, and H. Jasak, “Toward Predicting Performance of an Axial Flow Waterjet Including the Effects of Cavitation and Thrust Breakdown,” in *Citeseer*, 2009, Accessed: May 17, 2020. [Online]. Available: http://citeseerx.ist.psu.edu/viewdoc/download?doi=10.1.1.538.8738&rep=rep1&type=pdf.

[52] M. Wosnik and I. Nedyalkov, “Cavitation Investigation of Hydrofoils for Marine Hydrokinetic Turbines FEDSM2013-16576 CAVITATION INVESTIGATION OF HYDROFOILS FOR MARINE HYDROKINETIC TURBINES,” in *asmedigitalcollection.asme.org*, doi: 10.1115/FEDSM2013-16576.

[53] R. E. Bensow and G. Bark, “Implicit LES predictions of the cavitating flow on a propeller,” *J. Fluids Eng. Trans. ASME*, vol. 132, no. 4, pp. 0413021–04130210, Apr. 2010, doi: 10.1115/1.4001342.

[54] Y. Wang *et al.*, “A study on the collapse of cavitation bubbles surrounding the underwater-launched projectile and its fluid-structure coupling effects,” *Ocean Eng.*, vol. 84, pp. 228–236, Jul. 2014, doi: 10.1016/j.oceaneng.2014.04.014.

[55] A. I. Abbas, R. S. Amano, M. S. Saravani, M. D. Qandil, and T. Sakamoto, “Optimization of Kaplan Hydroturbine at Very Low Head with Rim-Driven Generator,” *J. Energy Resour.*

Technol. Trans. ASME, vol. 141, no. 11, Nov. 2019, doi: 10.1115/1.4043710.

[56] R. E. A. Arndt, C. R. Ellis, and S. Paul, "Preliminary investigation of the use of air injection to mitigate cavitation erosion," *J. Fluids Eng. Trans. ASME*, vol. 117, no. 3, pp. 498–504, Sep. 1995, doi: 10.1115/1.2817290.

[57] P. Tomov, S. Khelladi, F. Ravelet, C. Sarraf, F. Bakir, and P. Vertenoeuil, "Experimental study of aerated cavitation in a horizontal venturi nozzle," *Exp. Therm. Fluid Sci.*, vol. 70, pp. 85–95, 2016, doi: 10.1016/j.expthermflusci.2015.08.018ï.

[58] T. Elgammal, O. Elsayed, and R. S. Amano, "Numerical simulation of a cavitation treatment in kaplan hydro-turbine," in *AIAA Propulsion and Energy Forum and Exposition, 2019*, 2019, doi: 10.2514/6.2019-4408.

[59] T. ElGammal, T. Sakamoto, and R. S. Amano, "Cavitation modelling in different designs of micro Kaplan hydroturbine," in *American Society of Mechanical Engineers, Power Division (Publication) POWER*, Oct. 2018, vol. 1, doi: 10.1115/POWER2018-7109.

[60] M. D. Qandil, A. I. Abbas, H. D. Qandil, M. R. Al-Haddad, and R. S. Amano, "A Stand-Alone Hybrid Photovoltaic, Fuel Cell, and Battery System: Case Studies in Jordan," *J. Energy Resour. Technol. Trans. ASME*, vol. 141, no. 11, Nov. 2019, doi: 10.1115/1.4043656.

[61] E. M. Nfah and J. M. Ngundam, "Modelling of wind/Diesel/battery hybrid power systems for far North Cameroon," *Energy Convers. Manag.*, vol. 49, no. 6, pp. 1295–1301, Jun. 2008, doi: 10.1016/j.enconman.2008.01.007.

[62] S. Shaahid and I. El-Amin, "Techno-economic evaluation of off-grid hybrid photovoltaic–diesel–battery power systems for rural electrification in Saudi Arabia—A way forward for sustainable development," *Renew. Sustain. Energy Rev.*, vol. 13, no. 3, pp. 625–633, Apr.

2009, doi: 10.1016/j.rser.2007.11.017.

[63] S. K. Singal, Varun, and R. P. Singh, “Rural electrification of a remote island by renewable energy sources,” *Renew. Energy*, vol. 32, no. 15, pp. 2491–2501, Dec. 2007, doi: 10.1016/j.renene.2006.12.013.

[64] K. Q. Nguyen, “Internalizing externalities into capacity expansion planning: The case of electricity in Vietnam,” *Energy*, vol. 33, no. 5, pp. 740–746, May 2008, doi: 10.1016/j.energy.2008.01.014.

[65] M. R. Nouni, S. C. Mullick, and T. C. Kandpal, “Providing electricity access to remote areas in India: An approach towards identifying potential areas for decentralized electricity supply,” *Renew. Sustain. Energy Rev.*, vol. 12, no. 5, pp. 1187–1220, 2008.

[66] R. Hunter and G. Elliot, “Wind-diesel systems: a guide to the technology and its implementation,” 1994.

[67] O. Badran, “Wind turbine utilization for water pumping in Jordan,” *J. Wind Eng. Ind. Aerodyn.*, vol. 91, no. 10, pp. 1203–1214, Oct. 2003, doi: 10.1016/S0167-6105(03)00073-4.

[68] E. S. Hrayshat and M. S. Al-Soud, “Potential of solar energy development for water pumping in Jordan,” *Renew. Energy*, vol. 29, no. 8, pp. 1393–1399, Jul. 2004, doi: 10.1016/j.renene.2003.12.016.

[69] H. Abatcha, A. Jumba, L. M.-C. J. of E. Sciences, and undefined 2011, “Design and simulation of a hybrid PV/fuel cell energy system.”

[70] B. Kalappan and V. Ponnudsamy, “Modeling, Simulation and Optimization of Hybrid Renewable Power System for Daily Load demand of Metropolitan Cities in India,” *Am. J. Eng. Res.*, vol. 02, no. 11, pp. 174–184, 2013, Accessed: May 19, 2020. [Online]. Available:

www.ajer.org.

[71] A. Shiroudi, S. R. H. Taklimi, S. A. Mousavifar, and P. Taghipour, “Stand-alone PV-hydrogen energy system in Taleghan-Iran using HOMER software: Optimization and techno-economic analysis,” *Environ. Dev. Sustain.*, vol. 15, no. 5, pp. 1389–1402, Oct. 2013, doi: 10.1007/s10668-013-9443-3.

[72] J. O. Jaber, Q. M. Jaber, S. A. Sawalha, and M. S. Mohsen, “Evaluation of conventional and renewable energy sources for space heating in the household sector,” *Renew. Sustain. Energy Rev.*, vol. 12, no. 1, pp. 278–289, Jan. 2008, doi: 10.1016/j.rser.2006.05.004.

[73] H. Ge, L. Ni, and S. Asgarpoor, “Reliability-based Stand-alone Photovoltaic System Sizing Design-Reliability-based Stand-alone Photovoltaic System Sizing Design-A Case Study A Case Study,” 2008. Accessed: May 19, 2020. [Online]. Available: https://digitalcommons.unl.edu/electricalengineeringfacpub/141.

[74] J. Lagorse, M. G. Simões, A. Miraoui, and P. Costerg, “Energy cost analysis of a solar-hydrogen hybrid energy system for stand-alone applications,” *Int. J. Hydrogen Energy*, vol. 33, no. 12, pp. 2871–2879, Jun. 2008, doi: 10.1016/j.ijhydene.2008.03.054.

[75] J. Kaldellis, D. Zafirakis, K. Kavadias, and E. Kondili, “Optimum PV-diesel hybrid systems for remote consumers of the Greek territory,” *Appl. Energy*, vol. 97, pp. 61–67, Sep. 2012, doi: 10.1016/j.apenergy.2011.12.010.

[76] I. Kyriakidis, “Optimal Sizing and Operation of Battery Storages in StandAlone Hybrid Power Systems,” Denmark, 2012.

[77] S. B. Silva, M. M. Severino, and M. A. G. De Oliveira, “A stand-alone hybrid photovoltaic, fuel cell and battery system: A case study of Tocantins, Brazil,” *Renew. Energy*, vol. 57, pp. 384–389, Sep. 2013, doi: 10.1016/j.renene.2013.02.004.

[78] M. D. Qandil, A. I. Abbas, T. Elgammal, A. I. Abdelhadi, and R. S. Amano, “Water Energy Resource Innovation on the Cavitation Characteristics,” *J. Energy Resour. Technol. Trans. ASME*, vol. 143, no. 2, Feb. 2021, doi: 10.1115/1.4047885.

[79] M. D. Qandil, T. Elgammal, A. I. Abbas, A. I. Abdelhadi, and R. S. Amano, “Predicting the cavitation phenomena over the hydrofoil: CFD validation,” in *AIAA Scitech 2019 Forum*, 2019, doi: 10.2514/6.2019-0783.

[80] R. W. Kermeen, “Water Tunnel Tests of the NACA 66-012 Hydrofoil in Non-Cavitating and Cavitating Flows,” 1956.

[81] W. F. Noh, P. Woodward, A. van de Vooren, and P. Zandbergen, *Proceedings of the Fifth International Conference on Numerical Methods in Fluid Dynamics June 28 – July 2, 1976 Twente University, Enschede*, vol. 59. Berlin, Heidelberg: Springer Berlin Heidelberg, 1976.

[82] C. . Hirt and B. . Nichols, “Volume of fluid (VOF) method for the dynamics of free boundaries,” *J. Comput. Phys.*, vol. 39, no. 1, pp. 201–225, Jan. 1981, doi: 10.1016/0021-9991(81)90145-5.

[83] S. Beyhaghi and R. S. Amano, “Improvement of Aerodynamic Performance of Cambered Airfoils Using Leading-Edge Slots,” *J. Energy Resour. Technol.*, vol. 139, no. 5, Sep. 2017, doi: 10.1115/1.4036047.

[84] D. Simms, S. Schreck, M. Hand, and L. J. Fingersh, “NREL Unsteady Aerodynamics Experiment in the NASA-Ames Wind Tunnel: A Comparison of Predictions to Measurements,” 2001. Accessed: Apr. 04, 2021. [Online]. Available: http://www.doe.gov/bridge.

[85] W. J. Mccroskey, “A Critical Assessment of Wind Tunnel Results for the NACA < 0012

Airfoil," 1987. Accessed: Apr. 04, 2021. [Online]. Available: https://apps.dtic.mil/sti/citations/ADA193182.

[86] E. L.-A. and and undefined 1957, "BASE PRESSURE. AT SUPERSONIC SPEEDS'ON TWO-DIMENSIONAL," *core.ac.uk*, Accessed: Apr. 04, 2021. [Online]. Available: https://core.ac.uk/download/pdf/42801626.pdf.

[87] S. R. Risti´c and S. Ristić, "A-A VIEW IN THE INVISIBLE," * * *Theor. Appl. Mech. Ser. Spec. Issue-Address to Mech.*, vol. 40, no. 1, pp. 87–119, 2013, doi: 10.2298/TAM1301087R.

[88] W. C.-J. of S. Research and undefined 1966, "A critical re-evaluation of hydrodynamic theories and experiments in subcavitating hydrofoil flutter," *onepetro.org*, Accessed: Apr. 04, 2021. [Online]. Available: https://onepetro.org/JSR/article-abstract/10/02/122/174509.

[89] I. Nedyalkov, "Design of Contraction, Test Section, and Diffuser for a High-Speed Water Tunnel," 2012. Accessed: Apr. 04, 2021. [Online]. Available: https://odr.chalmers.se/handle/20.500.12380/174857.

[90] R. Etter, M. W.-M. Engineering, and undefined 1993, "Testing ship designs in a water tunnel," *search.proquest.com*, Accessed: Apr. 04, 2021. [Online]. Available: https://search.proquest.com/openview/5a60dd628d103504309f7fe4a3e47d1c/1.pdf?pq-origsite=gscholar&cbl=40505.

[91] M. Wosnik and R. Arndt, "Testing of a 1:6 Scale Physical Model of the Large, Low-Noise Cavitation Tunnel (LOCAT)," 2006. Accessed: Apr. 04, 2021. [Online]. Available: https://conservancy.umn.edu/handle/11299/113693.

[92] R. Sato, M. Nishimura, and K. Nakagawa, "CONCEPTUAL DESIGN OF THE FLOW NOISE SIMULATOR," 2003. Accessed: Apr. 04, 2021. [Online]. Available:

https://proceedings.asmedigitalcollection.asme.org.

[93] J. Wetzel and R. Arndt, “Hydrodynamic design considerations for hydroacoustic facilities: part I—flow quality,” 1994, Accessed: Apr. 04, 2021. [Online]. Available: https://asmedigitalcollection.asme.org/fluidsengineering/article-abstract/116/2/324/411151.

[94] P. A. Brandner, Y. Lecoffre, and G. J. Walker, “Design Considerations in the Development of a Modern Cavitation Tunnel,” 2007. Accessed: Apr. 04, 2021. [Online]. Available: https://eprints.utas.edu.au/6301/1/16AFMC_Brandner_Lecoffre_Walker_2007_F1.pdf.

[95] E. W.-O. Engineering and undefined 1981, “Cavitation phenomena, propeller excited hull pressure amplitudes and cavitation scale effect,” *Elsevier*, Accessed: Apr. 04, 2021. [Online]. Available: https://www.sciencedirect.com/science/article/pii/0029801881900172.

[96] L. Daniel, “DESIGN AND INSTALLATION OF A HIGH REYNOLDS NUMBER RECIRUCLATING WATER TUNNEL,” Oklahoma State University, Jul. 2014. Accessed: Apr. 04, 2021. [Online]. Available: https://shareok.org/handle/11244/14791.

[97] A. Fontaine, J. Crafton, S. Fonov, E. G. Jones, and L. Goss, “PLEASE DO NOT RETURN YOUR FORM TO THE ABOVE ADDRESS. 1. REPORT DATE (DD-MM-YYYY) 2. REPORT TYPE 3. DATES COVERED (From-To) Evaluation of the ISSI S3F Film for Distributed Measurements of Pressure,” 2006, Accessed: Apr. 04, 2021. [Online]. Available: https://apps.dtic.mil/sti/citations/ADA455976.

[98] M. Oyeyemi, “The design and qualification of the UGA water tunnel,” 2018, Accessed: Apr. 04, 2021. [Online]. Available: http://athenaeum.libs.uga.edu/handle/10724/38344.

[99] L. Daniel, S. Mohagheghian, D. Dunlap, E. Ruhlmann, and B. R. Elbing, “Design of a

recirculating water tunnel for the study of highreynolds number turbulent boundary layers," in *ASME International Mechanical Engineering Congress and Exposition, Proceedings (IMECE)*, Mar. 2015, vol. 7B-2015, doi: 10.1115/IMECE2015-52030.

[100] R. E. A. Arndt, R. E. A. Arndt,', V. H. Arakeriz, and H. Higuch13, "Some observations of tip-vortex cavitation Cavitation and Bubbly Flows View project Some observations of tip-vortex cavitation," *Artic. J. Fluid Mech.*, vol. 229, pp. 26–289, 1991, doi: 10.1017/S0022112091003026.

[101] J. B. Leroux, J. A. Astolfi, and J. Y. Billard, "An experimental study of unsteady partial cavitation," *J. Fluids Eng. Trans. ASME*, vol. 126, no. 1, pp. 94–101, Jan. 2004, doi: 10.1115/1.1627835.

[102] L. Preserve and S. C. Ko, "Design and construction of a water tunnel, January 1971," 1971. Accessed: Apr. 04, 2021. [Online]. Available: http://preserve.lehigh.edu/engr-civil-environmental-fritz-lab-reports/1906.

[103] "Eastman | Amphora - 3D Polymer AM3300." https://www.eastman.com/Pages/ProductHome.aspx?product=71104597&pn=Amphora+-+3D+Polymer+AM3300 (accessed Apr. 28, 2021).

[104] "Ultimaker 2+ Connect: Start 3D printing the Ultimaker way." https://ultimaker.com/3d-printers/ultimaker-2-plus-connect (accessed Apr. 28, 2021).

[105] "Badger Meter M2000 Electromagnetic Flow Meter | Magmeters | Instrumart." https://www.instrumart.com/products/33603/badger-meter-m2000-electromagnetic-flow-meter?gclid=CjwKCAjwj6SEBhAOEiwAvFRuKHuYvfSJSlsrCOC7L6d-UMHa2zRAgKIgZ-q015GMTDSJsu33Z26OshoCoDAQAvD_BwE (accessed Apr. 28, 2021).

[106] “ATM 10 HP pump.” .

[107] “ABB ACS310 VSD.” .

[108] “FASTCAM MINI UX – Photron.” https://photron.com/fastcam-mini-ux/ (accessed Apr. 28, 2021).

[109] S. B. Pope, “Simple models of turbulent flows,” *Phys. Fluids*, vol. 23, no. 1, Jan. 2011, doi: 10.1063/1.3531744.

[110] B. E. Launder and D. B. Spalding, *Lectures in Mathematical Models of Turbulence*. 1972.

[111] D. Anderson, J. C. Tannehill, and R. H. Pletcher, *Computational fluid mechanics and heat transfer, Third edition*. 2016.

[112] S. L. Dixon and C. A. Hall, *Fluid mechanics and thermodynamics of turbomachinery, 7th edition*. Elsevier Inc., 2013.

[113] “HOMER Pro - Microgrid Software for Designing Optimized Hybrid Microgrids.” https://www.homerenergy.com/products/pro/index.html (accessed Jun. 05, 2020).

[114] T. Lambert, T. Lambert, M. E. Inc, P. Gilman, and P. Lilienthal, “Chapter 15: Micropower System Modeling with Homer”, in Integration of Alternative Sources of Energy by Felix A. Farret and M. Godoy Simoes,” 2006, Accessed: Jun. 05, 2020. [Online]. Available: http://citeseerx.ist.psu.edu/viewdoc/summary?doi=10.1.1.508.356.

[115] “North America :: United States — The World Factbook - Central Intelligence Agency.” https://www.cia.gov/library/publications/the-world-factbook/geos/us.html (accessed Jun. 06, 2020).

[116] “File:USA topo en.jpg - Wikimedia Commons.” https://commons.wikimedia.org/wiki/File:USA_topo_en.jpg (accessed Jun. 05, 2020).

[117] “How Much Electricity Do Homes in Your State Use?”

https://www.electricchoice.com/blog/electricity-on-average-do-homes/ (accessed Jun. 06, 2020).

[118] "Solar Resource Data, Tools, and Maps | Geospatial Data Science | NREL." https://www.nrel.gov/gis/solar.html (accessed Jun. 06, 2020).

[119] "U.S. Average Wind Speed State Rank." http://www.usa.com/rank/us--average-wind-speed--state-rank.htm (accessed Jun. 06, 2020).

[120] B. Mainali and R. Dhital, "Isolated and Mini-Grid Solar PV Systems: An Alternative Solution for Providing Electricity Access in Remote Areas (Case Study from Nepal)," in *Solar Energy Storage*, Elsevier Inc., 2015, pp. 359–374.

[121] "Gasoline and Diesel Fuel Update - U.S. Energy Information Administration (EIA)." https://www.eia.gov/petroleum/gasdiesel/ (accessed Jun. 07, 2020).

[122] "Solar Energy: Mapping the Road Ahead," Paris, 2019. Accessed: Jun. 07, 2020. [Online]. Available: https://www.iea.org/reports/solar-energy-mapping-the-road-ahead.

[123] F. Brihmat and S. Mekhtoub, "PV Cell Temperature/ PV Power Output Relationships Homer Methodology Calculation," Tunisie-Sousse, 2013. Accessed: May 22, 2021. [Online]. Available: https://library.crti.dz/jr218.

[124] S. B. Silva, M. M. Severino, and M. A. G. De Oliveira, "A stand-alone hybrid photovoltaic, fuel cell and battery system: A case study of Tocantins, Brazil," *Renew. Energy*, vol. 57, pp. 384–389, Sep. 2013, doi: 10.1016/j.renene.2013.02.004.

[125] T. Burton, N. Jenkins, D. Sharpe, and E. Bossanyi, *Wind Energy Handbook, Second Edition*. John Wiley and Sons, 2011.

[126] A. S. Hasan, "Comparative study of the inline configuration wind farms," in *AEE World Energy Engineering Congress 2019*, Jun. 2019, vol. 142, no. 6, pp. 4870–4878, doi:

10.1115/1.4045463.

[127] “HOMER Pro - Microgrid Software for Designing Optimized Hybrid Microgrids.” https://www.homerenergy.com/products/pro/index.html (accessed May 22, 2021).

[128] “Small Wind Turbines: Are They Right For You? | EnergySage.” https://news.energysage.com/small-wind-turbines-overview/ (accessed Jun. 08, 2020).

[129] Concorde Battery Co., “Battery sizing tips for stand-alone PV systems - Handbook,” 2009. http://concordebattery.com/otherpdf/sunextenderbatterysizingtips.pdf (accessed Jun. 08, 2020).

[130] “What is the Best Battery for Solar Storage in 2019? | EnergySage.” https://www.energysage.com/solar/solar-energy-storage/what-are-the-best-batteries-for-solar-panels/ (accessed Jun. 09, 2020).

[131] M. S. Y. Ebaid, H. Qandil, and M. Hammad, “A unified approach for designing a photovoltaic solar system for the underground water pumping well-34 at Disi aquifer,” *Energy Convers. Manag.*, vol. 75, pp. 780–795, Nov. 2013, doi: 10.1016/j.enconman.2013.07.083.

[132] D. Feldman and P. Schwabe, “Terms, Trends, and Insights on PV Project Finance in the United States, 2018,” 2018. Accessed: Jun. 10, 2020. [Online]. Available: https://www.nrel.gov/docs/fy19osti/72037.pdf.

[133] M. Qandil, A. Abbas, S. Al Hamad, W. Saadeh, and R. S. Amano, “Performance of Hybrid Renewable Energy Power System for A Residential Building,” *J. Energy Resour. Technol.*, pp. 1–42, Jun. 2021, doi: 10.1115/1.4051541.

[134] M. D. Qandil, A. I. Abbas, A. I. Abdelhadi, A. R. Salem, and R. S. Amano, “Energy analysis: ways to save energy and reduce the emissions in wastewater treatment plants,” *Int.*

J. Energy a Clean Environ., vol. 22, no. 1, pp. 91–112, 2021, doi: 10.1615/INTERJENERCLEANENV.2020035138.

[135] C. Ghenai and M. Bettayeb, "Modelling and performance analysis of a stand-alone hybrid solar PV/Fuel Cell/Diesel Generator power system for university building," *Energy*, vol. 171, pp. 180–189, Mar. 2019, doi: 10.1016/j.energy.2019.01.019.

[136] "File:Fuel Cell Block Diagram.svg - Wikipedia." https://en.wikipedia.org/wiki/File:Fuel_Cell_Block_Diagram.svg (accessed Jun. 15, 2020).

[137] M. Carmo, D. L. Fritz, J. Mergel, and D. Stolten, "A comprehensive review on PEM water electrolysis," *International Journal of Hydrogen Energy*, vol. 38, no. 12. pp. 4901–4934, Apr. 22, 2013, doi: 10.1016/j.ijhydene.2013.01.151.

Appendices

Appendix A: Sites Data

State	Diesel Prices ($/L)	Wind speed (m/s)	Daily Radiation (kWh/m^2/day)
Louisiana	0.669	4.05	4.39
Tennessee	0.706	4.26	4.14
Minnesota	0.700	5.36	3.69
Mississippi	0.669	4.25	4.41
Alabama	0.669	4.01	4.44
North Dakota	0.705	5.78	3.74
Texas	0.670	6.06	4.93
Virginia	0.706	4.37	4.01
Kentucky	0.705	4.60	3.94
Oklahoma	0.705	6.10	4.35
Arkansas	0.669	5.40	4.25
South Carolina	0.706	4.18	4.41
West Virginia	0.706	4.15	3.75
North Carolina	0.705	4.50	4.25
Georgia	0.706	3.92	4.47
Florida	0.714	4.84	4.74
Missouri	0.705	5.77	4.18
South Dakota	0.705	5.89	4.01
Idaho	0.757	4.11	4.33
Arizona	0.892	4.93	5.32
Washington	0.864	4.06	3.57
Nebraska	0.705	5.94	4.21
Maryland	0.763	5.06	3.85
Indiana	0.705	5.73	3.84
Oregon	0.892	4.41	4.48
Delaware	0.763	6.39	3.98
Kansas	0.705	6.38	4.32
Nevada	0.892	5.49	5.08
Iowa	0.705	5.85	3.92
Wyoming	0.757	6.12	4.33
Ohio	0.691	5.63	3.74
Montana	0.892	4.93	3.95
Pennsylvania	0.764	6.26	3.56
Utah	0.757	4.74	4.72
Illinois	0.705	5.59	3.93
Connecticut	0.747	5.38	3.78

Colorado	0.726	6.13	4.54
District of Columbia	0.763	4.55	3.98
Wisconsin	0.705	5.62	3.73
New Jersey	0.763	5.77	3.80
Michigan	0.705	5.70	3.64
New Mexico	0.667	5.14	5.21
Massachusetts	0.746	5.63	3.70
Alaska	0.892	3.98	2.70
New Hampshire	0.747	4.65	3.47
New York	0.765	4.50	3.50
Rhode Island	0.747	6.33	3.81
Vermont	0.747	4.65	3.47
California	0.940	5.09	5.40
Maine	0.747	4.70	3.47
Hawaii	0.893	6.76	5.77

Appendix B: Electrical production for each stat at 2018 diesel price, 1.0 PV cost multiplier, and 1.0 wind turbine cost multiplier for Home application

State		PV	Diesel Gen.	Wind Turbine	Total
Louisiana	**Production (kWh/year)**	6,528	11,208	-	17,736
	Fraction	36.8%	63.2%	-	100%
Tennessee	**Production (kWh/year)**	6,416	11,040	-	17,457
	Fraction	36.8%	63.2%	-	100%
Minnesota	**Production (kWh/year)**	6,632	10,703	-	17,335
	Fraction	38.3%	61.7%	-	100%
Mississippi	**Production (kWh/year)**	6,627	10,471	-	17,099
	Fraction	38.8%	61.2%	-	100%
Alabama	**Production (kWh/year)**	6,686	10,284	-	16,970
	Fraction	39.4%	60.6%	-	100%
North Dakota	**Production (kWh/year)**	6,731	10,412	-	17,143
	Fraction	39.3%	60.7%	-	100%
Texas	**Production (kWh/year)**	13,456	4,324	-	17,780
	Fraction	75.7%	24.3%	-	100%
Virginia	**Production (kWh/year)**	6,566	9,817	-	16,383
	Fraction	40.1%	59.9%	-	100%
Kentucky	**Production (kWh/year)**	6,215	10,081	-	16,295
	Fraction	38.1%	61.9%	-	100%
Oklahoma	**Production (kWh/year)**	6,836	9,453	-	16,289
	Fraction	42%	58%	-	100%
Arkansas	**Production (kWh/year)**	6,550	9,702	-	16,252
	Fraction	40.3%	59.7%	-	100%
South Carolina	**Production (kWh/year)**	6,776	9,432	-	16,208
	Fraction	41.8%	58.2%	-	100%
West Virginia	**Production (kWh/year)**	6,002	9,965	-	15,967
	Fraction	37.6%	62.4%	-	100%
North Carolina	**Production**	6,673	9,249	-	15,922

	(kWh/year)				
	Fraction	41.9%	58.1%	-	100%
Georgia	**Production (kWh/year)**	6,740	9,031	-	15,771
	Fraction	42.7%	57.3%	-	100%
Florida	**Production (kWh/year)**	6,786	8,813	-	15,599
	Fraction	43.5%	56.5%	-	100%
Missouri	**Production (kWh/year)**	6,602	9,050	-	15,652
	Fraction	42.2%	57.8%	-	100%
South Dakota	**Production (kWh/year)**	6,887	8,815	-	15,702
	Fraction	43.9%	56.1%	-	100%
Idaho	**Production (kWh/year)**	10,783	4,443	-	15,226
	Fraction	70.8%	29.2%	-	100%
Arizona	**Production (kWh/year)**	11,574	3,850	-	15,424
	Fraction	75%	25%	-	100%
Washington	**Production (kWh/year)**	6,199	9,175	-	15,375
	Fraction	40.3%	59.7%	-	100%
Nebraska	**Production (kWh/year)**	7,082	8,473	-	15,554
	Fraction	45.5%	54.5%	-	100%
Maryland	**Production (kWh/year)**	6,189	8,851	-	15,040
	Fraction	41.1%	58.9%	-	100%
Indiana	**Production (kWh/year)**	6,179	8,597	-	14,776
	Fraction	41.8%	58.2%	-	100%
Oregon	**Production (kWh/year)**	7,671	5,927	-	13,597
	Fraction	56.4%	43.6%	-	100%
Delaware	**Production (kWh/year)**	6,397	5,192	1,587	13,176
	Fraction	48.5%	39.4%	12%	100%
Kansas	**Production (kWh/year)**	7,035	5,689	-	12,724
	Fraction	55.3%	44.7%	-	100%
Nevada	**Production (kWh/year)**	8,474	4,751	-	13,225
	Fraction	64.1%	35.9%	-	100%
Iowa	**Production**	6,543	5,869	-	12,412

	(kWh/year)				
	Fraction	52.7%	47.3%	-	100%
Wyoming	**Production (kWh/year)**	7,500	5,010	-	12,509
	Fraction	60%	40%	-	100%
Ohio	**Production (kWh/year)**	6,013	6,130	-	12,143
	Fraction	49.5%	50.5%	-	100%
Montana	**Production (kWh/year)**	7,145	4,720	-	11,865
	Fraction	60.2%	39.8%	-	100%
Pennsylvania	**Production (kWh/year)**	5,874	4,702	1,473	12,049
	Fraction	48.7%	39%	12.2%	100%
Utah	**Production (kWh/year)**	7,916	3,575	-	11,491
	Fraction	68.9%	31.1%	-	100%
Illinois	**Production (kWh/year)**	6,374	4,452	-	10,825
	Fraction	58.9%	41.1%	-	100%
Connecticut	**Production (kWh/year)**	6,303	4,667	-	10,971
	Fraction	57.5%	42.5%	-	100%
Colorado	**Production (kWh/year)**	7,858	2,927	-	10,785
	Fraction	72.9%	27.1%	-	100%
District of Columbia	**Production (kWh/year)**	6,438	3,851	-	10,289
	Fraction	62.6%	37.4%	-	100%
Wisconsin	**Production (kWh/year)**	3,832	6,088	-	9,920
	Fraction	38.6%	61.4%	-	100%
New Jersey	**Production (kWh/year)**	3,720	6,118	-	9,838
	Fraction	37.8%	62.2%	-	100%
Michigan	**Production (kWh/year)**	3,699	5,881	-	9,580
	Fraction	38.6%	61.4%	-	100%
New Mexico	**Production (kWh/year)**	8,405	1,982	-	10,387
	Fraction	80.9%	19.1%	-	100%
Massachusetts	**Production (kWh/year)**	3,745	5,417	-	9,162
	Fraction	40.9%	59.1%	-	100%
Alaska	**Production**	3,186	6,027	-	9,213

	(kWh/year)				
	Fraction	34.6%	65.4%	-	100%
New Hampshire	**Production (kWh/year)**	3,520	5,508	-	9,028
	Fraction	39%	61%	-	100%
New York	**Production (kWh/year)**	3,561	5,167	-	8,729
	Fraction	40.8%	59.2%	-	100%
Rhode Island	**Production (kWh/year)**	3,805	4,676	-	8,481
	Fraction	44.9%	55.1%	-	100%
Vermont	**Production (kWh/year)**	3,602	4,488	-	8,090
	Fraction	44.5%	55.5%	-	100%
California	**Production (kWh/year)**	8,421	710	-	9,130
	Fraction	92.2%	7.77%	-	100%
Maine	**Production (kWh/year)**	3,669	4,535	-	8,204
	Fraction	44.7%	55.3%	-	100%
Hawaii	**Production (kWh/year)**	7,934	425	-	8,358
	Fraction	94.9%	5.08%	v	100%

Appendix C: Emissions outputs for each stat at 2018 diesel price, 1.0 PV cost multiplier and 1.0 wind turbine cost multiplier for Home application

State		Carbon dioxide (kg/year)	Carbon monoxide (kg/year)	Unburned hydrocarbons (kg/year)	Particulate matter (kg/year)	Sulfur dioxide (kg/year)	Nitrogen oxides (kg/year)
Louisiana	Hybrid System	8,658	54.6	2.38	0.331	21.2	51.3
	Diesel System	13,652	86.1	3.76	0.522	33.4	80.8
Tennessee	Hybrid System	8,510	53.6	2.34	0.325	20.8	50.4
	Diesel System	13,310	83.9	3.66	0.508	32.6	78.8
Minnesota	Hybrid System	8,250	52.0	2.27	0.315	20.2	48.9
	Diesel System	13,036	82.2	3.59	0.498	31.9	77.2
Mississippi	Hybrid System	8,071	50.9	2.22	0.308	19.8	47.8
	Diesel System	13,038	82.2	3.59	0.498	31.9	77.2
Alabama	Hybrid System	7,924	50.0	2.18	0.303	19.4	46.9
	Diesel System	12,926	81.5	3.56	0.494	31.7	76.5
North Dakota	Hybrid System	8,023	50.6	2.21	0.306	19.6	47.5
	Diesel System	12,873	81.1	3.54	0.492	31.5	76.2
Texas	Hybrid System	3,474	21.9	0.956	0.133	8.51	20.6
	Diesel System	12,555	79.1	3.45	0.480	30.7	74.3
Virginia	Hybrid System	7,569	47.7	2.08	0.289	18.5	44.8
	Diesel System	12,388	78.1	3.41	0.473	30.3	73.4
Kentucky	Hybrid System	7,771	49.0	2.14	0.297	19.0	46.0
	Diesel System	12,370	78.0	3.40	0.473	30.3	73.3
Oklahoma	Hybrid System	7,295	46.0	2.01	0.279	17.9	43.2
	Diesel System	12,227	77.1	3.36	0.467	29.9	72.4

Arkansas	**Hybrid System**	7,489	47.2	2.06	0.286	18.3	44.3
	Diesel System	12,116	76.4	3.33	0.463	29.7	71.7
South Carolina	**Hybrid System**	7,280	45.9	2.00	0.278	17.8	43.1
	Diesel System	12,024	75.8	3.31	0.459	29.4	71.2
West Virginia	**Hybrid System**	7,687	48.5	2.11	0.294	18.8	45.5
	Diesel System	11,955	75.4	3.29	0.457	29.3	70.8
North Carolina	**Hybrid System**	7,123	44.9	1.96	0.272	17.4	42.2
	Diesel System	11,734	74.0	3.23	0.448	28.7	69.5
Georgia	**Hybrid System**	6,952	43.8	1.91	0.266	17.0	41.2
	Diesel System	11,617	73.2	3.20	0.444	28.4	68.8
Florida	**Hybrid System**	6,541	41.2	1.80	0.250	16.0	38.7
	Diesel System	11,504	72.5	3.16	0.439	28.2	68.1
Missouri	**Hybrid System**	6,959	43.9	1.91	0.266	17.0	41.2
	Diesel System	11,504	72.5	3.16	0.439	28.2	68.1
South Dakota	**Hybrid System**	7,018	44.2	1.93	0.268	17.2	41.6
	Diesel System	11,267	71.0	3.10	0.430	27.6	66.7
Idaho	**Hybrid System**	3,488	22.0	0.959	0.133	8.54	20.7
	Diesel System	11,261	71.1	3.10	0.430	27.6	66.7
Arizona	**Hybrid System**	3,019	19.0	0.830	0.115	7.39	17.9
	Diesel System	11,185	70.5	3.08	0.427	27.4	66.2
Washington	**Hybrid System**	7,281	45.9	2.00	0.278	17.8	43.1
	Diesel System	11,186	70.5	3.08	0.427	27.4	66.2
Nebraska	**Hybrid System**	6,708	42.3	1.85	0.256	16.4	39.7

	Diesel System	11,253	70.9	3.10	0.430	27.6	66.6
Maryland	**Hybrid System**	6,996	44.1	1.92	0.267	17.1	41.4
	Diesel System	11,001	69.3	3.03	0.420	26.9	65.1
Indiana	**Hybrid System**	6,774	42.7	1.86	0.259	16.6	40.1
	Diesel System	10,901	68.7	3.00	0.416	26.7	64.6
Oregon	**Hybrid System**	5,055	31.9	1.39	0.193	12.4	29.9
	Diesel System	10,552	66.5	2.90	0.403	25.8	62.5
Delaware	**Hybrid System**	4,366	27.05	1.2	0.167	10.7	25.9
	Diesel System	10,176	64.1	2.8	0.389	24.9	60.3
Kansas	**Hybrid System**	4,736	29.9	1.30	0.181	11.6	28.0
	Diesel System	9,945	64.7	2.74	0.380	24.4	58.9
Nevada	**Hybrid System**	4,005	25.2	1.10	0.153	9.81	23.7
	Diesel System	9,931	62.6	2.73	0.379	24.3	58.8
Iowa	**Hybrid System**	4,823	30.4	1.33	0.184	11.8	28.6
	Diesel System	9,743	61.4	2.68	0.372	23.9	57.7
Wyoming	**Hybrid System**	4,143	26.1	1.14	0.158	10.1	24.5
	Diesel System	9,581	60.4	2.64	0.366	23.5	56.7
Ohio	**Hybrid System**	5,017	31.6	1.38	0.192	12.3	29.7
	Diesel System	9,561	60.3	2.63	0.365	23.4	56.6
Montana	**Hybrid System**	3,827	24.1	1.05	0.146	9.37	22.7
	Diesel System	9,160	57.7	2.52	0.350	22.4	54.2
Pennsylvania	**Hybrid System**	3,836	24.2	1.06	0.147	9.39	22.7
	Diesel System	9,161	57.7	2.52	0.350	22.4	54.2

Utah	**Hybrid System**	2,903	18.3	0.798	0.111	7.11	17.2
	Diesel System	8,520	53.7	2.34	0.326	20.9	50.5
Illinois	**Hybrid System**	3,549	22.4	0.976	0.136	8.69	21.0
	Diesel System	8,071	50.9	2.22	0.308	19.8	47.8
Connecticut	**Hybrid System**	3,734	23.5	1.03	0.143	9.14	22.1
	Diesel System	8,043	50.7	2.21	0.307	19.7	47.6
Colorado	**Hybrid System**	2,333	14.7	0.642	0.0891	5.71	13.8
	Diesel System	7,795	49.1	2.14	0.298	19.1	46.2
District of Columbia	**Hybrid System**	3,043	19.2	0.837	0.116	7.45	18.0
	Diesel System	7,733	48.7	2.13	0.295	18.9	45.8
Wisconsin	**Hybrid System**	4,941	31.1	1.36	0.189	12.1	29.3
	Diesel System	7,539	47.5	2.07	0.288	18.5	44.6
New Jersey	**Hybrid System**	4,732	29.8	1.30	0.181	11.6	28.0
	Diesel System	7,364	46.4	2.03	0.281	18.0	43.6
Michigan	**Hybrid System**	4,527	28.5	1.25	0.173	11.1	26.8
	Diesel System	7,105	44.8	1.95	0.271	17.4	42.1
New Mexico	**Hybrid System**	1,562	9.84	0.430	0.0597	3.82	9.25
	Diesel System	6,991	44.1	1.92	0.267	17.1	41.4
Massachusetts	**Hybrid System**	4,309	27.2	1.19	0.165	10.6	25.5
	Diesel System	6,808	42.9	1.87	0.260	16.7	40.3
Alaska	**Hybrid System**	4,629	29.2	1.27	0.177	11.3	27.4
	Diesel System	6,750	42.5	1.86	0.258	16.5	40.0
New Hampshire	**Hybrid System**	4,388	24.7	1.21	0.168	10.7	26.0

	Diesel System	6,720	42.4	1.85	0.257	16.5	39.8
New York	**Hybrid System**	4,098	25.8	1.13	0.157	10.0	24.3
	Diesel System	6,426	40.5	1.77	0.246	15.7	38.1
Rhode Island	**Hybrid System**	3,644	23.0	1.00	0.139	8.92	21.6
	Diesel System	6,427	40.5	1.77	0.246	15.7	38.1
Vermont	**Hybrid System**	3,471	21.9	0.955	0.133	8.50	20.6
	Diesel System	6,262	39.5	1.72	0.239	15.3	37.1
California	**Hybrid System**	836	5.27	0.23	0.0319	2.05	4.95
	Diesel System	6,097	38.4	1.68	0.233	14.9	36.1
Maine	**Hybrid System**	3,563	22.5	0.980	0.136	8.73	21.1
	Diesel System	6,040	38.1	1.66	0.231	14.8	35.8
Hawaii	**Hybrid System**	505	3.18	0.139	0.0193	1.24	2.99
	Diesel System	5,584	35.2	1.54	0.213	13.7	33.1

Appendix D: Electrical production for each stat at 2018 diesel price, 1.0 PV cost multiplier, and 1.0 wind turbine cost multiplier for Commercial building application

State		PV	Diesel Gen.	Wind Turbine	Total
Louisiana	**Production (kWh/year)**	652,799	435,601	-	1,088,399
	Fraction	60%	40%	-	100%
Tennessee	**Production (kWh/year)**	641,641	437,016	-	1,078,657
	Fraction	59.5%	40.5%	-	100%
Minnesota	**Production (kWh/year)**	663,212	448,373	-	1,111,586
	Fraction	59.7%	40.3%	-	100%
Mississippi	**Production (kWh/year)**	661,726	430,745	-	1,092,471
	Fraction	60.6%	39.4%	-	100%
Alabama	**Production (kWh/year)**	668,589	410,629	-	1,079,218
	Fraction	62%	38%	-	100%
North Dakota	**Production (kWh/year)**	673,116	442,414	-	1,115,531
	Fraction	60.3%	39.7%	-	100%
Texas	**Production (kWh/year)**	747,558	381,753	-	1,129,311
	Fraction	66.2%	33.8%	-	100%
Virginia	**Production (kWh/year)**	656,589	440,812	-	1,097,400
	Fraction	59.8%	40.2%	-	100%
Kentucky	**Production (kWh/year)**	621,471	462,408	-	1,083,879
	Fraction	57.3%	42.7%	-	100%
Oklahoma	**Production (kWh/year)**	574,118	497,752	-	1,071,871
	Fraction	53.6%	46.4%	-	100%
Arkansas	**Production (kWh/year)**	655,025	425,979	-	1,081,003
	Fraction	60.6%	39.45	-	100%
South Carolina	**Production (kWh/year)**	677,567	409,996	-	1,087,563
	Fraction	62.3%	37.7%	-	100%
West Virginia	**Production (kWh/year)**	600,206	473,647	-	1,073,854

	Fraction	55.9%	44.1%	-	100%
North Carolina	**Production (kWh/year)**	667,320	428,816	-	1,096,136
	Fraction	60.9%	39.1%	-	100%
Georgia	**Production (kWh/year)**	673,967	408,947	-	1,082,914
	Fraction	62.2%	37.8%	-	100%
Florida	**Production (kWh/year)**	696,817	392,922	-	1,089,739
	Fraction	63.9%	36.1%	-	100%
Missouri	**Production (kWh/year)**	659,868	439,062	-	1,098,929
	Fraction	60%	40%	-	100%
South Dakota	**Production (kWh/year)**	694,265	427,213	-	1,121,478
	Fraction	61.9%	38.1%	-	100%
Idaho	**Production (kWh/year)**	616,186	443,716	-	1,059,902
	Fraction	58.1%	41.9%	-	100%
Arizona	**Production (kWh/year)**	992,050	178,220	-	1,170,269
	Fraction	84.8%	15.2%	-	100%
Washington	**Production (kWh/year)**	619,922	465,538	-	1,085,460
	Fraction	57.1%	42.9%	-	100%
Nebraska	**Production (kWh/year)**	708,179	417,067	-	1,125,246
	Fraction	62.9%	37.1%	-	100%
Maryland	**Production (kWh/year)**	870,668	247,990	-	1,118,658
	Fraction	77.8%	22.2%	-	100%
Indiana	**Production (kWh/year)**	617,932	465,028	-	1,082,960
	Fraction	57.1%	42.9%	-	100%
Oregon	**Production (kWh/year)**	613,667	443,382	-	1,057,049
	Fraction	58.1%	41.9%	-	100%
Delaware	**Production (kWh/year)**	639,671	368,424	79,337	1,087,432
	Fraction	58.8%	33.9%	7.3%	100%
Kansas	**Production (kWh/year)**	562,791	409,465	79,363	1,051,619
	Fraction	53.5%	38.9%	7.55%	100%
Nevada	**Production (kWh/year)**	1,016,835	143,860	-	1,160,696

	Fraction	87.6%	12.4%	-	100%
Iowa	**Production (kWh/year)**	654,277	446,695	-	1,100,972
	Fraction	59.4%	40.6%	-	100%
Wyoming	**Production (kWh/year)**	889,985	250,932	-	1,150,917
	Fraction	78.2%	21.8%	-	100%
Ohio	**Production (kWh/year)**	481,023	537,869	-	1,018,892
	Fraction	47.2%	52.8%	-	100%
Montana	**Production (kWh/year)**	991,911	149,184	-	1,141,095
	Fraction	86.9%	13.1%	-	100%
Pennsylvania	**Production (kWh/year)**	587,390	414,468	73,662	1,075,521
	Fraction	54.6%	38.5%	6.85%	100%
Utah	**Production (kWh/year)**	949,875	207,510	-	1,157,385
	Fraction	82.1%	17.9%	-	100%
Illinois	**Production (kWh/year)**	637,351	444,733	-	1,082,085
	Fraction	58.9%	41.1%	-	100%
Connecticut	**Production (kWh/year)**	630,336	452,099	-	1,082,434
	Fraction	58.2%	41.8%	-	100%
Colorado	**Production (kWh/year)**	942,996	218,503	-	1,161,498
	Fraction	81.2%	18.8%	-	100%
District of Columbia	**Production (kWh/year)**	622,432	464,879	-	1,087,311
	Fraction	57.2%	42.8%	-	100%
Wisconsin	**Production (kWh/year)**	638,690	451,500	-	1,090,190
	Fraction	58.6%	41.4%	-	100%
New Jersey	**Production (kWh/year)**	619,979	457,180	-	1,077,159
	Fraction	57.6%	42.4%	-	100%
Michigan	**Production (kWh/year)**	616,579	475,214	-	1,091,793
	Fraction	56.5%	43.5%	-	100%
New Mexico	**Production (kWh/year)**	672,393	387,570	-	1,059,933
	Fraction	63.4%	36.6%	-	100%
Massachusetts	**Production (kWh/year)**	621,117	429,263	-	1,050,380

	Fraction	59.1%	40.9%	-	100%
Alaska	**Production (kWh/year)**	424,794	606,752	-	1,031,546
	Fraction	41.2%	58.8%	-	100%
New Hampshire	**Production (kWh/year)**	615,991	472,434	-	1,088,426
	Fraction	56.6%	43.4%	-	100%
New York	**Production (kWh/year)**	625,796	461,385	-	1,087,182
	Fraction	57.6%	42.4%	-	100%
Rhode Island	**Production (kWh/year)**	507,295	443,090	77,031	1,027,416
	Fraction	49.4%	43.1%	7.5%	100%
Vermont	**Production (kWh/year)**	600,254	488,354	-	1,088,608
	Fraction	55.1%	44.9%	-	100%
California	**Production (kWh/year)**	1,010,472	165,132	-	1,175,604
	Fraction	86%	14%	-	100%
Maine	**Production (kWh/year)**	611,464	477,003	-	1,088,467
	Fraction	56.2%	43.8%	-	100%
Hawaii	**Production (kWh/year)**	952,021	154,679	18,519	1,125,218
	Fraction	84.6%	13.7%	1.65%	100%

Appendix E: Emissions outputs for each stat at 2018 diesel price, 1.0 PV cost multiplier and 1.0 wind turbine cost multiplier for Commercial building application

State		Carbon dioxide (kg/year)	Carbon monoxide (kg/year)	Unburned hydrocarbons (kg/year)	Particulate matter (kg/year)	Sulfur dioxide (kg/year)	Nitrogen oxides (kg/year)
Louisiana	Hybrid System	291,117	1,835	80.1	11.1	713	1,724
	Diesel System	661,619	4,170	182	25.3	1,620	3,918
Tennessee	Hybrid System	291,911	1,840	80.3	11.2	715	1,729
	Diesel System	661,625	4,171	182	25.3	1,620	3,918
Minnesota	Hybrid System	299,505	1,888	82.4	11.4	733	1,773
	Diesel System	661,619	4,170	182	25.3	1,620	3,918
Mississippi	Hybrid System	287,639	1,813	79.1	11.0	704	1,703
	Diesel System	661,619	4,170	182	25.3	1,620	3,918
Alabama	Hybrid System	274,335	1,729	75.5	10.5	672	1,624
	Diesel System	661,619	4,170	182	25.3	1,620	3,918
North Dakota	Hybrid System	295,545	1,863	81.3	11.3	724	1,750
	Diesel System	661,619	4,170	182	25.3	1,620	3,918
Texas	Hybrid System	255,521	1,611	70.3	9.76	626	1,513
	Diesel System	661,620	4,170	182	25.3	1,620	3,918
Virginia	Hybrid System	294,335	1,855	81.0	11.2	721	1,743
	Diesel System	661,625	4,171	182	25.3	1,620	3,918
Kentucky	Hybrid System	308,773	1,946	84.9	11.8	756	1,828
	Diesel System	661,619	4,170	182	25.3	1,620	3,918
Oklahoma	Hybrid System	332,979	2,099	91.6	12.7	815	1,972
	Diesel System	661,625	4,171	182	25.3	1,620	3,918

Arkansas	**Hybrid System**	284,534	1,794	78.3	10.9	697	1,685
	Diesel System	661,619	4,170	182	25.3	1,620	3,918
South Carolina	**Hybrid System**	273,884	1,726	75.3	10.5	671	1,622
	Diesel System	661,625	4,171	182	25.3	1,620	3,918
West Virginia	**Hybrid System**	316,254	1,993	87.0	12.1	774	1,873
	Diesel System	661,625	4,171	182	25.3	1,620	3,918
North Carolina	**Hybrid System**	286,287	1,805	78.7	10.9	701	1,695
	Diesel System	661,625	4,171	182	25.3	1,620	3,918
Georgia	**Hybrid System**	273,136	1,722	75.1	10.4	669	1,617
	Diesel System	661,619	4,170	182	25.3	1,620	3,918
Florida	**Hybrid System**	262,160	1,653	72.1	10.0	642	1,552
	Diesel System	661,619	4,170	182	25.3	1,620	3,918
Missouri	**Hybrid System**	293,194	1,848	80.6	11.2	718	1,736
	Diesel System	661,619	4,170	182	25.3	1,620	3,918
South Dakota	**Hybrid System**	285,357	1,799	78.5	10.9	699	1,690
	Diesel System	661,619	4,170	182	25.3	1,620	3,918
Idaho	**Hybrid System**	296,429	1,869	81.5	11.3	726	1,755
	Diesel System	661,619	4,170	182	25.3	1,620	3,918
Arizona	**Hybrid System**	118,785	749	32.7	4.54	291	703
	Diesel System	661,619	4,170	182	25.3	1,620	3,918
Washington	**Hybrid System**	311,025	1,961	85.6	11.9	762	1,842
	Diesel System	661,645	4,171	182	25.3	1,620	3,918
Nebraska	**Hybrid System**	279,309	1,761	76.8	10.7	684	1,654

	Diesel System	661,625	4,171	182	25.3	1,620	3,918
Maryland	**Hybrid System**	165,314	1,042	45.5	6.32	405	979
	Diesel System	661,619	4,170	182	25.3	1,620	3,918
Indiana	**Hybrid System**	310,411	1,957	85.4	11.9	760	1,838
	Diesel System	661,619	4,170	182	25.3	1,620	3,918
Oregon	**Hybrid System**	296,921	1,872	81.7	11.3	727	1,758
	Diesel System	661,645	4,171	182	25.3	1,620	3,918
Delaware	**Hybrid System**	245,990	1,551	67.7	9.4	602	1,457
	Diesel System	661,619	4,170	182	25.3	1,620	3,918
Kansas	**Hybrid System**	274,055	1,727	75.4	10.5	671	1,623
	Diesel System	661,619	4,170	182	25.3	1,620	3,918
Nevada	**Hybrid System**	95,845	604	26.4	3.66	235	568
	Diesel System	661,645	4,171	182	25.3	1,620	3,918
Iowa	**Hybrid System**	298,349	1,881	82.1	11.4	731	1,767
	Diesel System	661,619	4,170	182	25.3	1,620	3,918
Wyoming	**Hybrid System**	167,171	1,054	46.0	6.39	409	990
	Diesel System	661,619	4,170	182	25.3	1,620	3,918
Ohio	**Hybrid System**	359,435	2,266	98.9	13.7	880	2,128
	Diesel System	661,625	4,171	182	25.3	1,620	3,918
Montana	**Hybrid System**	99,433	627	27.4	3.80	243	589
	Diesel System	661,645	4,171	182	25.3	1,620	3,918
Pennsylvania	**Hybrid System**	276,966	1,746	76.2	10.6	678	1,640
	Diesel System	661,619	4,170	182	25.3	1,620	3,918

Utah	**Hybrid System**	138,314	872	38.0	5.28	339	819
	Diesel System	661,619	4,170	182	25.3	1,620	3,918
Illinois	**Hybrid System**	297,117	1,873	81.7	11.4	728	1,759
	Diesel System	661,619	4,170	182	25.3	1,620	3,918
Connecticut	**Hybrid System**	302,045	1,904	83.1	11.5	740	1,789
	Diesel System	661,619	4,170	182	25.3	1,620	3,918
Colorado	**Hybrid System**	145,603	918	40	5.56	357	862
	Diesel System	661,619	4,170	182	25.3	1,620	3,918
District of Columbia	**Hybrid System**	310,539	1,957	85.4	11.9	760	1,839
	Diesel System	661,619	4,170	182	25.3	1,620	3,918
Wisconsin	**Hybrid System**	301,656	1,901	83.0	11.5	739	1,786
	Diesel System	661,625	4,171	182	25.3	1,620	3,918
New Jersey	**Hybrid System**	305,423	1,925	84.0	11.7	748	1,809
	Diesel System	661,619	4,170	182	25.3	1,620	3,918
Michigan	**Hybrid System**	317,461	2,001	87.3	12.1	777	1,880
	Diesel System	661,619	4,170	182	25.3	1,620	3,918
New Mexico	**Hybrid System**	258,615	1,630	71.1	9.88	633	1,531
	Diesel System	661,620	4,170	182	25.3	1,620	3,918
Massachusetts	**Hybrid System**	286,962	1,809	78.9	11.0	703	1,699
	Diesel System	661,619	4,170	182	25.3	1,620	3,918
Alaska	**Hybrid System**	406,134	2,560	112	15.5	995	2,405
	Diesel System	661,619	4,170	182	25.3	1,620	3,918
New Hampshire	**Hybrid System**	315,405	1,988	86.8	12.0	772	1,868

	Diesel System	661,619	4,170	182	25.3	1,620	3,918
New York	**Hybrid System**	308,021	1,942	84.7	11.8	754	1,824
	Diesel System	661,619	4,170	182	25.3	1,620	3,918
Rhode Island	**Hybrid System**	295,683	1,864	81.3	11.3	724	1,751
	Diesel System	661,619	4,170	182	25.3	1,620	3,918
Vermont	**Hybrid System**	326,096	2,056	89.7	12.5	799	1,931
	Diesel System	661,619	4,170	182	25.3	1,620	3,918
California	**Hybrid System**	110,062	694	30.3	4.20	270	652
	Diesel System	661,619	4,170	182	25.3	1,620	3,918
Maine	**Hybrid System**	318,546	2,008	87.6	12.2	780	1,886
	Diesel System	661,619	4,170	182	25.3	1,620	3,918
Hawaii	**Hybrid System**	103,106	650	28.4	3.94	252	611
	Diesel System	661,619	4,170	182	25.3	1,620	3,918

Appendix F: Electrical production for each stat at 2018 diesel price, 1.0 PV cost multiplier, and 1.0 wind turbine cost multiplier for Industrial facility application

State		PV	Diesel Gen.	Wind Turbine	Total
Louisiana	**Production (kWh/year)**	3,133,434	6,654,678	-	9,788,112
	Fraction	32%	68%	-	100%
Tennessee	**Production (kWh/year)**	4,057,921	6,078,221	-	10,136,142
	Fraction	40%	60%	-	100%
Minnesota	**Production (kWh/year)**	3,183,419	6,720,987	-	9,904,406
	Fraction	32.1%	67.9%	-	100%
Mississippi	**Production (kWh/year)**	3,151,993	6,654,435	-	9,806,428
	Fraction	32.1%	67.9%	-	100%
Alabama	**Production (kWh/year)**	3,476,662	6,482,639	-	9,959,301
	Fraction	34.9%	65.1%	-	100%
North Dakota	**Production (kWh/year)**	3,841,576	6,287,390	-	10,128,966
	Fraction	37.9%	62.1%	-	100%
Texas	**Production (kWh/year)**	3,588,278	6,346,098	-	9,934,376
	Fraction	36.15	63.9%	-	100%
Virginia	**Production (kWh/year)**	3,414,261	6,566,794	-	9,981,055
	Fraction	34.2%	65.8%	-	100%
Kentucky	**Production (kWh/year)**	2,983,060	6,784,521	-	9,767,581
	Fraction	30.5%	69.5%	-	100%
Oklahoma	**Production (kWh/year)**	3,382,854	6,485,197	18,596	9,886,647
	Fraction	34.2%	65.6%	0.188%	100%
Arkansas	**Production (kWh/year)**	3,144,119	6,668,007	-	9,812,126
	Fraction	32%	68%	-	100%
South Carolina	**Production (kWh/year)**	3,252,321	6,584,863	-	9,837,184
	Fraction	33.1%	66.9%	-	100%
West Virginia	**Production (kWh/year)**	2,880,990	6,869,677	-	9,750,667
	Fraction	29.5%	70.5%	-	100%
North Carolina	**Production**	3,470,063	6,517,781	-	9,987,844

	(kWh/year)				
	Fraction	34.7%	65.3	-	100%
Georgia	**Production (kWh/year)**	3,235,042	6,587,251	-	9,822,293
	Fraction	32.9%	67.1%	-	100%
Florida	**Production (kWh/year)**	3,623,448	6,372,371	-	9,995,819
	Fraction	36.2%	63.8%	-	100%
Missouri	**Production (kWh/year)**	3,431,311	6,549,813	-	9,981,124
	Fraction	34.4%	65.6%	-	100%
South Dakota	**Production (kWh/year)**	3,305,904	6,596,435	-	9,902,338
	Fraction	33.4%	66.6%	-	100%
Idaho	**Production (kWh/year)**	4,298,652	5,939,260	-	10,237,912
	Fraction	42%	58%	-	100%
Arizona	**Production (kWh/year)**	3,968,199	6,139,048	-	10,107,248
	Fraction	39.3%	60.7%	-	100%
Washington	**Production (kWh/year)**	3,223,595	6,726,789	-	9,950,383
	Fraction	32.4%	67.6%	-	100%
Nebraska	**Production (kWh/year)**	3,399,257	6,526,315	-	9,25,572
	Fraction	34.2%	65.8%	-	100%
Maryland	**Production (kWh/year)**	3,218,310	6,702,535	-	9,920,845
	Fraction	32.4%	67.6%	-	100%
Indiana	**Production (kWh/year)**	2,966,073	6,808,137	-	9,774,210
	Fraction	30.3%	69.7%	-	100%
Oregon	**Production (kWh/year)**	3,201,942	6,593,042	-	9,794,984
	Fraction	32.7%	67.3%	-	100%
Delaware	**Production (kWh/year)**	3,070,420	6,734,367	-	9,804,787
	Fraction	31.3%	68.7%	-	100%
Kansas	**Production (kWh/year)**	3,564,509	6,375,745	18,596	9,958,850
	Fraction	35.8%	64%	0.187%	100%
Nevada	**Production (kWh/year)**	4,067,341	6,098,049	-	10,165,390
	Fraction	40%	60%	-	100%
Iowa	**Production**	3,140,528	6,712,282	-	9,852,810

	(kWh/year)				
	Fraction	31.9%	68.1%	-	100%
Wyoming	**Production (kWh/year)**	3,899,934	6,308,044	-	10,207,978
	Fraction	38.2%	61.8%	-	100%
Ohio	**Production (kWh/year)**	2,886,141	6,867,201	-	9,753,342
	Fraction	29.6%	70.4%	-	100%
Montana	**Production (kWh/year)**	3,715,404	6,437,597	-	10,153,001
	Fraction	36.6%	63.4%	-	100%
Pennsylvania	**Production (kWh/year)**	3,054,427	6,832,157	-	9,886,584
	Fraction	30.9%	69.1%	-	100%
Utah	**Production (kWh/year)**	3,799,501	6,274,846	-	10,074,347
	Fraction	37.7%	62.3%	-	100%
Illinois	**Production (kWh/year)**	3,059,285	6,752,957	-	9,812,242
	Fraction	31.2%	68.8%	-	100%
Connecticut	**Production (kWh/year)**	3,025,611	6,788,530	-	9,814,141
	Fraction	30.8%	69.2%	-	100%
Colorado	**Production (kWh/year)**	3,863,959	6,110,877	-	9,974,835
	Fraction	38.7%	61.3%	-	100%
District of Columbia	**Production (kWh/year)**	3,347,632	6,613,947	-	9,961,579
	Fraction	33.6%	66.4%	-	100%
Wisconsin	**Production (kWh/year)**	3,065,713	6,777,772	-	9,843,485
	Fraction	31.1%	68.9%	-	100%
New Jersey	**Production (kWh/year)**	3,223,891	6,701,097	-	9,924,987
	Fraction	32.5%	67.5%	-	100%
Michigan	**Production (kWh/year)**	2,959,581	6,848,184	-	9,807,765
	Fraction	30.2%	69.8%	-	100%
New Mexico	**Production (kWh/year)**	3,697,995	6,235,884	-	9,933,878
	Fraction	37.2%	62.8%	-	100%
Massachusetts	**Production (kWh/year)**	2,995,886	6,812,350	-	9,808,236
	Fraction	30.5%	69.5%	-	100%
Alaska	**Production**	2,336,365	7,330,483	-	9,666,847

	(kWh/year)				
	Fraction	24.2%	75.8%	-	100%
New Hampshire	**Production (kWh/year)**	2,956,759	6,855,815	-	9,812,575
	Fraction	30.1%	69.9%	-	100%
New York	**Production (kWh/year)**	3,003,823	6,790,227	-	9,794,050
	Fraction	30.7%	69.3%	-	100%
Rhode Island	**Production (kWh/year)**	3,043,769	6,766,537	-	9,810,306
	Fraction	31%	69%	-	100%
Vermont	**Production (kWh/year)**	2,881,221	6,922,605	-	9,803,826
	Fraction	29.4%	70.6%	-	100%
California	**Production (kWh/year)**	4,041,889	6,093,074	-	10,134,964
	Fraction	39.9%	60.1%	-	100%
Maine	**Production (kWh/year)**	2,935,026	6,891,036	-	9,826,063
	Fraction	29.9%	70.1%	-	100%
Hawaii	**Production (kWh/year)**	4,125,423	6,026,084	-	10,151,506
	Fraction	40.6%	59.4%	-	100%

Appendix G: Emissions outputs for each stat at 2018 diesel price, 1.0 PV cost multiplier and 1.0 wind turbine cost multiplier for Industrial facility application

State		Carbon dioxide (kg/year)	Carbon monoxide (kg/year)	Unburned hydrocarbons (kg/year)	Particulate matter (kg/year)	Sulfur dioxide (kg/year)	Nitrogen oxides (kg/year)
Louisiana	Hybrid System	4,434,110	27,950	1,220	169	10,858	26,256
	Diesel System	6,192,187	39,032	1,703	237	15,163	36,667
Tennessee	Hybrid System	4,043,130	25,486	1,112	154	9,901	23,941
	Diesel System	6,192,187	39,032	1,703	237	15,163	36,667
Minnesota	Hybrid System	4,476,170	28,215	1,231	171	10,961	26,505
	Diesel System	6,192,187	39,032	1,703	237	15,163	36,667
Mississippi	Hybrid System	4,432,265	27,939	1,219	169	10,854	26,245
	Diesel System	6,192,187	39,032	1,703	237	15,163	36,667
Alabama	Hybrid System	4,312,084	27,181	1,186	165	10,559	25,534
	Diesel System	6,192,187	39,032	1,703	237	15,163	36,667
North Dakota	Hybrid System	4,182,584	26,365	1,150	160	10,242	24,767
	Diesel System	6,192,187	39,032	1,703	237	15,163	36,667
Texas	Hybrid System	4,223,083	26,620	1,162	161	10,341	25,007
	Diesel System	6,192,187	39,032	1,703	237	15,163	36,667
Virginia	Hybrid System	4,374,317	27,573	1,203	167	10,712	25,902
	Diesel System	6,192,187	39,032	1,703	237	15,163	36,667
Kentucky	Hybrid System	4,518,549	28,482	1,243	173	11,065	26,756
	Diesel System	6,192,187	39,032	1,703	237	15,163	36,667
Oklahoma	Hybrid System	4,318,408	27,221	1,188	165	10,575	25,571
	Diesel System	6,192,187	39,032	1,703	237	15,163	36,667

Arkansas	**Hybrid System**	4,446,409	28,028	1,223	170	10,888	26,329
	Diesel System	6,192,187	39,032	1,703	237	15,163	36,667
South Carolina	**Hybrid System**	4,385,817	27,646	1,206	168	10,740	25,970
	Diesel System	6,192,187	39,032	1,703	237	15,163	36,667
West Virginia	**Hybrid System**	4,577,249	28,852	1,259	175	11,209	27,104
	Diesel System	6,192,187	39,032	1,703	237	15,163	36,667
North Carolina	**Hybrid System**	4,341,162	27,364	1,194	166	10,630	25,706
	Diesel System	6,192,187	39,032	1,703	237	15,163	36,667
Georgia	**Hybrid System**	4,384,666	27,639	1,206	168	10,737	25,963
	Diesel System	6,192,187	39,032	1,703	237	15,163	36,667
Florida	**Hybrid System**	4,239,990	26,727	1,166	162	10,383	25,107
	Diesel System	6,192,187	39,032	1,703	237	15,163	36,667
Missouri	**Hybrid System**	4,364,167	27,509	1,200	167	10,687	25,842
	Diesel System	6,192,187	39,032	1,703	237	15,163	36,667
South Dakota	**Hybrid System**	4,392,626	27,689	1,208	168	10,757	26,011
	Diesel System	6,192,187	39,032	1,703	237	15,163	36,667
Idaho	**Hybrid System**	3,940,519	24,839	1,084	151	9,649	23,333
	Diesel System	6,192,187	39,032	1,703	237	15,163	36,667
Arizona	**Hybrid System**	4,085,108	25,750	1,124	156	10,003	24,190
	Diesel System	6,192,226	39,032	1,703	237	15,163	36,667
Washington	**Hybrid System**	4,480,262	28,241	1,232	171	10,971	26,530
	Diesel System	6,192,226	39,032	1,703	237	15,163	36,667
Nebraska	**Hybrid System**	4,345,586	27,392	1,195	166	10,641	25,732

	Diesel System	6,192,187	39,032	1,703	237	15,163	36,667
Maryland	**Hybrid System**	4,466,213	28,153	1,228	171	10,937	26,446
	Diesel System	6,192,187	39,032	1,703	237	15,163	36,667
Indiana	**Hybrid System**	4,532,035	28,567	1,247	173	11,098	26,836
	Diesel System	6,192,187	39,032	1,703	237	15,163	36,667
Oregon	**Hybrid System**	4,380,787	27,614	1,205	167	10,728	25,940
	Diesel System	6,192,226	39,032	1,703	237	15,163	36,667
Delaware	**Hybrid System**	4,487,569	28,287	1,234	171	10,989	26,573
	Diesel System	6,192,187	39,032	1,703	237	15,163	36,667
Kansas	**Hybrid System**	4,244,023	26,752	1,167	162	10,393	25,131
	Diesel System	6,192,187	39,032	1,703	237	15,163	36,667
Nevada	**Hybrid System**	4,060,461	25,595	1,117	155	9,943	24,044
	Diesel System	6,192,226	39,032	1,703	237	15,163	36,667
Iowa	**Hybrid System**	4,472,910	28,195	1,230	171	10,953	26,486
	Diesel System	6,192,187	39,032	1,703	237	15,163	36,667
Wyoming	**Hybrid System**	4,198,985	26,468	1,155	160	10,282	24,864
	Diesel System	6,192,187	39,032	1,703	237	15,163	36,667
Ohio	**Hybrid System**	4,575,381	28,841	1,259	175	11,204	27,093
	Diesel System	6,192,187	39,032	1,703	237	15,163	36,667
Montana	**Hybrid System**	4,286,549	27,020	1,179	164	10,497	25,380
	Diesel System	6,192,226	39,032	1,703	237	15,163	36,667
Pennsylvania	**Hybrid System**	4,550,430	28,683	1,252	174	11,143	26,945
	Diesel System	6,192,187	39,032	1,703	237	15,163	36,667

Utah	**Hybrid System**	4,176,445	26,326	1,149	160	10,227	24,730
	Diesel System	6,192,187	39,032	1,703	237	15,163	36,667
Illinois	**Hybrid System**	4,498,544	28,356	1,237	172	11,016	26,638
	Diesel System	6,192,187	39,032	1,703	237	15,163	36,667
Connecticut	**Hybrid System**	4,512,723	28,446	1,241	172	11,051	26,722
	Diesel System	6,192,187	39,032	1,703	237	15,163	36,667
Colorado	**Hybrid System**	4,064,402	25,620	1,118	155	9,953	24,067
	Diesel System	6,192,187	39,032	1,703	237	15,163	36,667
District of Columbia	**Hybrid System**	4,403,698	27,758	1,211	168	10,784	26,076
	Diesel System	6,192,187	39,032	1,703	237	15,163	36,667
Wisconsin	**Hybrid System**	4,514,634	28,458	1,242	172	11,055	26,733
	Diesel System	6,192,187	39,032	1,703	237	15,163	36,667
New Jersey	**Hybrid System**	4,464,222	28,140	1,228	171	10,932	26,435
	Diesel System	6,192,187	39,032	1,703	237	15,163	36,667
Michigan	**Hybrid System**	4,557,026	28,725	1,253	174	11,159	26,984
	Diesel System	6,192,187	39,032	1,703	237	15,163	36,667
New Mexico	**Hybrid System**	4,151,192	26,167	1,142	159	10,165	24,581
	Diesel System	6,192,187	39,032	1,703	237	15,163	36,667
Massachusetts	**Hybrid System**	4,537,433	28,601	1,248	173	11,111	26,868
	Diesel System	6,192,187	39,032	1,703	237	15,163	36,667
Alaska	**Hybrid System**	4,889,845	30,823	1,345	187	11,974	28,955
	Diesel System	6,192,226	39,032	1,703	237	15,163	36,667
New Hampshire	**Hybrid System**	4,566,400	28,784	1,256	174	11,182	27,040

	Diesel System	6,192,187	39,032	1,703	237	15,163	36,667
New York	**Hybrid System**	4,511,822	28,440	1,241	172	11,048	26,716
	Diesel System	6,192,187	39,032	1,703	237	15,163	36,667
Rhode Island	**Hybrid System**	4,507,271	28,411	1,240	172	11,037	26,689
	Diesel System	6,192,187	39,032	1,703	237	15,163	36,667
Vermont	**Hybrid System**	4,611,722	29,070	1,268	176	11,293	27,308
	Diesel System	6,192,187	39,032	1,703	237	15,163	36,667
California	**Hybrid System**	4,059,845	25,591	1,117	155	9,942	24,040
	Diesel System	6,192,226	39,032	1,703	237	15,163	36,667
Maine	**Hybrid System**	4,588,664	28,924	1,262	175	11,237	27,171
	Diesel System	9,192,187	39,032	1,703	237	15,163	36,667
Hawaii	**Hybrid System**	4,017,449	25,324	1,105	153	9,838	23,789
	Diesel System	6,192,226	39,032	1,703	237	15,163	36,667

Curriculum Vitae

Objective

I am a Ph.D. candidate in Mechanical Engineering at the University of Wisconsin Milwaukee. My research interests are fluid mechanics, turbulence modeling, turbulent flow, hydro turbines, hybrid-renewable energy systems, and net-zero building. I am a Certified Energy Manager, (CEM®), a Renewable Energy Professional, (REP™), and a Certified Measurement and Verification Professional (CMVP®) by the Association of Energy Engineers (AEE), attained 2020.

Qualifications Summary

- Application Engineer since April 2021 in Therma-Stor, which offers QUEST industrial dehumidifiers.
- Research assistant (Team Leader Energy Engineer) since August 2017 in the Industrial Assessment Center of UW-Milwaukee (Participated in 50 assessments).
- Certified Energy Manager, CEM, by Association of Energy Engineers (AEE), attained 2020.
- Three years of experience as a Research Assistant in the Hydro-turbine Lab at UW-Milwaukee with utilizing Star-CCM+ for CFD test, including CAD manipulation and surface repair, rotational domains, thermal analysis, VOF multiphase, phase change, LES unsteady turbulence, mesh deformation tool.
- Experienced in using laboratory test equipment, including velocity meter, programming variable frequency drive (VFD), pressure transducer, thermal camera, wireless thermocouples rotary torque sensors, inline, and magnetic flow meter, combustion analyzer laser tape measure, DAQ, Tachometer, the high-speed camera with analysis software.
- Five years of work experience; Three years as a Technical Support Engineer in the HVAC industry and two years as a Sales Engineer in the HVAC industry.

Experience

April 2021 – Present | Application Engineer

Therma-Stor | Madison, WI

- Interact with engineers, architects, contractors, manufacturer reps, and end-users as a subject matter expert on QUEST products and their applications.
- Provide technical support to the sales organization (internal and external).
- Provide market and customer feedback to Product Management to drive the product roadmap.
- Represent Therma-stor as a technical expert.

- Assist Marketing department

August 2017 – June 2021 | Lead Energy Engineer

DOE-Industrial Assessment Center of UW-Milwaukee| Milwaukee, WI

- Perform ASHRAE level I and II energy audits on industrial facilities across Wisconsin and Illinois as part of the U.S. Department of Energy-Advanced Manufacturing Office program.
- Prepare audit reports delineating the outcomes of the assessment in terms of energy savings, cost reduction in utility bills, and return of investment.
- Analyze and assess equipment, systems, and processes to provide energy savings and improve productivity.
- Evaluate utility bills and carry out a comprehensive analysis to trace the energy usage trend.
- Contact clients, arrange assessments and manage audit teams.
- Conducted 46+ assessments and led 6 energy audits on various industrial facilities.
- Evaluated energy usage and identified over $5 million worth of energy savings.
- Certified by U.S. DOE's IAC program since February 2019.
- The Lead Student for the Center starting November 2019.

August 2017 – June 2021 | Research Assistant

University of Wisconsin-Milwaukee/Global Water Center | Milwaukee, WI

- Working on micro-scale Kaplan hydro-turbine along with several types of hydrofoils:
  1- To investigate and improve the performance of turbines.
  2- To investigate cavitation in hydro-turbines and hydrofoils.

- Utilize STAR-CCM+ as a CFD tool for testing hydro-turbines performance and various design parameters.
- Utilize each of 3D printing, High-Speed Camera, and High-Performance Computing (HPC) clusters.
- Experimental measurements and data analysis for (Hydro turbine performance, Hydrofoil cavitation characteristic) project.

June 2015 – August 2017 | Sales Engineer

PETRA Technical Projects | Oman

- Responsible for developing the best sales techniques to achieve sales targets.

- Perform the tasks of marketing and selling HVAC equipment as well as provide strategies to expand the sales team.
- Handle responsibilities of visiting customer sites to gather requirements and prepare proposals as per the requirement.
- Responsible for conducting doing site surveys to identify issues and provide solutions for the same.
- Perform responsibilities of selling HVAC products to contractors and large-scale distributors.
- Prepares sales engineering reports by collecting, analyzing, and summarizing sales information and engineering and application trends.

July 2012 – June 2015 | Application Engineer / Technical Support

PETRA Engineering for HVAC Industries | Amman, Jordan

- Study received inquiries including the project's technical specifications, schedules & drawings.
- Perform needed analysis to select the most appropriate units to the client's requirements.
- Prepare technical and financial proposals that suit the needed requirements.
- Prepare job orders to the factory with the needed coordination between the sales and production departments.
- Control transmittal and communications with the factory different departments efficiently to guarantee smooth handling of work.

Education

August 2017 – Present | Ph.D. in Engineering

- University of Wisconsin-Milwaukee - Mechanical Engineering Department
- Thesis topic: ***Improvement of Renewable Energy: Cavitation Treatment and Optimization of Hybrid System for Remote Areas***
- GPA of (3.95/4.0)
- Expected Graduation Date: June 2021

January 2013 - September 2015 | M.Sc. of Mechanical Engineering/Energy Systems

- The Hashemite University - Mechanical Engineering Department, Zarqa, Jordan
- GPA of (3.62/4.00), Grade: Excellent
- Thesis Title: ***A stand-alone Hybrid Photovoltaic, Fuel Cell, and Battery System: Case Studies in Jordan***

- Fields of Study: Solar Energy, Renewable Energy Systems, Energy Management, and Energy & Environment

September 2008 - May 2012 | B.Sc. of Mechanical Engineering

- Al-Balqa' Applied University – Faculty of Engineering Technology, Amman, Jordan
- GPA of (3.51/4.00), Grade: Very good **(Ranked the Second position among Batch of 139)**
- Graduation Project/Senior Design: Energy Audit for Administration Building in Faculty of Engineering Technology (Award in Graduation Projects/Senior Design Competition-2013 at Jordan Engineers Association)

Computer Software's

- **STAR-CCM+:** Simulate flow motion (3D simulation, unsteady, turbulent flow, VOF, and rotational motion models) for micro hydro-turbines projects.
- **SolidWorks:** Draw/edit CAD models related to micro hydro-turbines **Hybrid Optimization for Electric Renewable (HOMER) software:** Used for my Doctoral and Master's research to simulate and to study the performance of a Hybrid System in remote areas.

Skills

- **Analytical:** research, problem-solving, data and metrics interpreting, reporting, organization, communication, troubleshooting, diagnostics, creativity, and brainstorming.
- **Critical and Creative Thinking**
- **Management:** leadership, people management, collaboration & teamwork, time management, negotiating, planning, and training.
- **Decision Making:** team and shared decision-making skills.
- **Technical:** writing, spreadsheets, computer, presenting.

Publications

Editorial Services

- Reviewer for the American Society of Mechanical Engineers (ASME) Journal Program.
- Reviewer for the International Journal of Energy for a Clean Environment (IJECE) Journal.
- Reviewer for the Renewable Energy Journal.

Journal Papers:

1. **Qandil, M. D.**, Abbas, A. I., Salem, A. R., Abdelhadi, A. I., Hasan, A., Nourin, F. N., Abousabae, M., Selim, O. M., Espindola, J., and Amano, R. S. (March 4, 2021). "Net Zero Energy Model for Wastewater Treatment Plants." ASME. *J. Energy Resour. Technol*. December 2021; 143(12): 122101. https://doi.org/10.1115/1.4050082
2. **Mohammad D. Qandil**, Ahmad I. Abbas, Saif Al Hamad, Walaa Saadeh, and Ryoichi S. Amano, "Performance of Hybrid Renewable Energy Power System for A Residential Building", Journal of Energy Resources Technology (Accepted for Publication)
3. **Mohammad D. Qandil**, Ahmad I. Abbas, Ahmad I. AbdelHadi, Abdel Rahman Salem, and Ryoichi S. Amano, 2020, "Energy Analysis: Ways to Save Energy and Reduce the Emissions in Wastewater Treatment Plants", International Journal of Energy for a Clean Environment, **DOI:** 10.1615/InterJEnerCleanEnv.2020035138
4. **Mohammad D. Qandil**, Ahmad I. Abbas, Hasan D. Qandil, Muhannad R. Al-Haddad, and Ryoichi S. Amano, "A Stand-Alone Hybrid Photovoltaic, Fuel Cell, and Battery System: Case Studies in Jordan", Journal of Energy Resources Technology, May 2019, Vol. 141, No.11, pp. 111201 (10 pages). https://doi.org/10.1115/1.4043656
5. **Mohammad D. Qandil**, Ahmad I. Abbas, Tarek Elgammal, Ahmad I. AbdelHadi, and Ryoichi S. Amano (August 13, 2020). "Water-Energy Resource Innovation on the Cavitation Characteristics." ASME. J. Energy Resour. Technol. February 2021; 143(2): 022106. https://doi.org/10.1115/1.4047885
6. Hasan, A., Salem, A. R., Hadi, A. A., **Qandil, M.**, Amano, R. S., and Alkhalidi, A. (November 9, 2020). "The Power Reclamation of Utilizing Micro-Hydro Turbines in the Aeration Basins of Wastewater Treatment Plants." ASME. *J. Energy Resour. Technol*. August 2021; 143(8): 081301. https://doi.org/10.1115/1.4048869
7. Juan Espindola, Farah Nazifa Nourin, **Mohammad D. Qandil**, Ahmad I. Abdelhadi, and Ryoichi S. Amano, 2020, "Energy Saving Analysis Using Energy Intensity Usage and Specific Energy Consumption Methods", International Journal of Energy for a Clean Environment. DOI: 10.1615/InterJEnerCleanEnv.v21.i3
8. Ahmad I. AbdelHadi, Salem, A. R., Abbas, A. I., **Mohammad D. Qandil**, and Amano, R. S. (September 28, 2020). "Study of Energy Saving Analysis for Different Industries." ASME. J. Energy Resour. Technol. May 2021; 143(5): 052101. https://doi.org/10.1115/1.4048249
9. Farah Nourin, Ahmad I. Abbas, **Mohammad D. Qandil**, and Amano, R. S. (June 23, 2020). "Analytical Study to Use the Excess Digester Gas of Wastewater Treatment Plants." ASME. J. Energy Resour. Technol. DOI: https://doi.org/10.1115/1.4047603
10. Ahmad I. Abbas, **Mohammad D. Qandil**, Muhannad R. Al-Haddad, and Ryoichi S. Amano, "Investigation of Horizontal Micro Kaplan Hydro Turbine Performance Using Multi-Disciplinary Design Optimization", Journal of Energy Resources Technology, December 2019 https://doi.org/10.1115/1.4045821
11. Ahmad I. Abbas, Ryoichi S. Amano, Mandana S. Saravani, **Mohammad D. Qandil**, and Tomoki Sakamoto, "Optimization of Kaplan Hydroturbine at Very Low Head with Rim-

Driven Generator", Journal of Energy Resources Technology, May 2019, Vol.141, No.11, pp. 111204 (12 pages). https://doi.org/10.1115/1.4043710

12. Ahmad I Abbas, **Mohammad D. Qandil**, Muhannad R. Al-Haddad, Mandana S. Saravani, and Ryoichi S Amano, 2019, "Utilization of Hydroturbines in Wastewater Treatment Plants", Journal of Energy Resources Technology, Vol.141, No.6, pp. 062011 (5 pages). https://doi.org/10.1115/1.4042969
13. A. Alkhalidi, **Mohammad Qandil**, and H. Qandil, 2014, "Analysis of Ocean Thermal Energy Conversion Power Plant using Isobutane as the Working Fluid", Int. J. of Thermal & Environmental Engineering, Volume 7, No.1 (2014) 25-32. DOI: 10.5383/ijtee.07.01.004

Conference Papers (peer-reviewed):

1. **Mohammad D. Qandil**, Ryoichi S Amano, Ahmad I. Abbas, and Muhannad Al-Haddad, 2019, "Energy Consumption, Energy-saving and Emissions Reduction of Wastewater Treatment Plants (WWTPs) in Wisconsin", AIAA Propulsion and Energy 2019 Forum, pages 4239.
2. Ahmad I. Abbas, **Mohammad D. Qandil**, Muhannad R. Al-Haddad, and Ryoichi S. Amano, 2019, "Performance Investigation of Very-Low-Head Kaplan Hydro-Turbines", Proceedings of AIAA SciTech Forum 2019, San Diego, California, USA, DOI: 10.2514/6.2019-0241
3. Ryoichi S. Amano, Ahmad I. Abbas, Abdel Rahman Salem, Ahmad I. AbdelHadi, **Mohammad D. Qandil,** 2019, "Study of industrial energy assessments for different sectors", AIAA Propulsion and Energy 2019 Forum, pages 4238.
4. Ryoichi S. Amano, Ahmad I. Abbas, **Mohammad D. Qandil**, and Muhannad R. Al-Haddad, "Multi-Disciplinary Design Optimization of a Horizontal Micro Kaplan Hydro Turbine." Proceedings of the ASME Turbo Expo 2019: Turbomachinery Technical Conference and Exposition. Volume 8: Microturbines, Turbochargers, and Small Turbomachines; Steam Turbines. Phoenix, Arizona, USA. June 17–21, 2019. V008T26A008. ASME. https://doi.org/10.1115/GT2019-90509
5. **Mohammad D. Qandil**, Tarek Elgammal, Ahmad I Abbas, Ahmad I Abdelhadi, and Ryoichi S Amano, 2019, "Predicting the Cavitation Phenomena Over the Hydrofoil: CFD Validation", AIAA SciTech Forum 2019, DOI: 10.2514/6.2019-0783.
6. Ryoichi S. Amano, Muhannad Al-Haddad, Ahmad Abbas, **Mohammad D. Qandil**, and Mandana Saravani, 2019, "Energy Value Analysis (EVA) of an Office Building: Case Study", AIAA SciTech Forum 2019, Pages 1276.
7. **Mohammad D. Qandil**, Ryoichi S. Amano, and Ahmad I. Abbas, 2018, "A Stand-Alone Hybrid Photovoltaic, Fuel Cell, and Battery System", ASME 2018 12th International Conference on Energy Sustainability collocated with the ASME 2018 Power Conference and the ASME 2018 Nuclear Forum. https://doi.org/10.1115/ES2018-7121
8. Ahmad I. Abbas, **Mohammad D. Qandil**, Muhannad R. Al-Haddad, Mandana S. Saravani, and Ryoichi S. Amano, 2018, "Utilization of Hydro-Turbines in Wastewater Treatment Plants

(WWTPs)", Proceedings of the ASME 2018 Power Conference, Orlando, FL, USA, Paper No. PowerEnergy2018-7349. https://doi.org/10.1115/ES2018-7349

9. Ahmad I. Abbas, Muhannad R. Al-Haddad, Mandana S. Saravani, **Mohammad D. Qandil**, and Ryoichi S. Amano, 2018, "A Comparative Study of Industrial Energy Assessments for Small and Medium-Sized Industrial Facilities", Proceedings of the ASME 2018 Power Conference, Orlando, FL, USA, Paper No. PowerEnergy2018-7550. https://doi.org/10.1115/ES2018-7550

Posters:

1. **Mohammad D. Qandil,** Ahmad I. Abbas and Ryoichi S. Amano, "Optimization for Aeration Treatment for Cavitation Phenomena in Hydrofoil with Different Angle of Attack" 2021 UWM student research poster competition.
2. **Mohammad D. Qandil,** Ahmad I. Abbas and Ryoichi S. Amano, "Optimization of Hybrid Systems for A Residential Building in the Remote Areas" 2020 UWM student research poster competition.
3. Ahmad I. Abbas, **Mohammad D. Qandil** and Ryoichi S. Amano, "Investigation of Newly Developed Rim-Drive Micro and Pico Kaplan Hydro-Turbine Performance" 2020 UWM student research poster competition.
4. **Mohammad D. Qandil,** Ahmad I. Abbas, Abdel Rahman Salem, Ahmad I. AbdelHadi, and Ryoichi S. Amano, 2019, "Energy Consumption, Energy-saving, and Emissions Reduction of Wastewater Treatment Plants (WWTPs) in Wisconsin", AEE World Energy Conference & Expo-2019.
5. **Mohammad D. Qandil,** Muhannad R. Al-Haddad, Ahmad I. Abbas, Mandana S. Saravani, and Ryoichi S. Amano, "Utilization of Hydro-Turbines in Wastewater Treatment Plants (WWTPS)" 2018 UWM student research poster competition.
6. Muhannad R. Al-Haddad, Ahmad I. Abbas, Mandana S. Saravani, **Mohammad D. Qandil,** and Ryoichi S. Amano, "Comparative Study of Industrial Energy Assessments for Small and Medium-Sized Industrial Facilities" 2018 UWM student research poster competition.

Awards and Certificates

- The U.S. Department of Energy (DoE), **Industrial Assessment Center Outstanding Student Award** 2020.
- Certificate for the completion of the **Certified Energy Manager (CEM®)** course by the Association of Energy Engineers (AEE).
- Certificate for the completion of the **Certified Measurement and Verification Professional (CMVP®)** course by the Association of Energy Engineers (AEE).
- Certificate for the completion of the **Renewable Energy Professional (REP™)** course by the Association of Energy Engineers (AEE).

- UWM **Distinguished Dissertation Fellowship** (DDF) 2020-2021 Award.
- UWM **Graduate Student Excellence Fellowship** (GSEF) 2019-2020 Award.
- **ME Chancellor's Awards** (2018, 2020, and 2021).
- National Arab American Association of Engineers and Architects (NAAAEA) scholarship Award 2019.
- Arab American Association of Engineers and Architects – Wisconsin chapter (AAAEA-WI) scholarship Award 2019.
- **Certificate of Achievement**, by the U.S. Department of Energy's Industrial Assessment Center program at the University of Wisconsin Milwaukee.
- Distinguished Award in Graduation Projects Competition for the Year 2013 from the Jordan Engineers Association (JEA).
- The American Institute of Aeronautics and Astronautics (AIAA), certificate of completion, SCIENCE AND TECHNOLOGY FORUM AND EXPOSITION, 2019.
- The American Institute of Aeronautics and Astronautics (AIAA), certificate of completion, AIAA PROPULSION AND ENERGY FORUM, 2019.
- The Association of energy engineering (AEE), certificate of completion, AEE World Energy Conference & Expo- 2019.
- The Association of energy engineering (AEE), certificate of completion, AEE West-2019.
- The Association of energy engineering (AEE), certificate of completion, 2018 World Energy Engineering Congress.

Courses/Training

- **July 2012 – August 2012 | Pumps (Selection & Running) (10 Hours)**
- JEA, (Engineers Training Center) | Zarqa, Jordan
- **September 2011 | Design & Requirements of Fire Fighting Systems (18 Hours)**
- JEA, (Engineers Training Center) | Zarqa, Jordan
- **April 2011 – May 2011 | SolidWorks (30 Hours)**
- JEA, (Engineers Training Center) | Zarqa, Jordan

Languages

- Arabic: Native language.
- English: IELTS Certified.

Professional Memberships

- Association of Energy Engineers (AEE) – Student Member, since 2017.
- American Institute of Aeronautics and Astronautics (AIAA) - Student Member, since 2017.

- Arab American Association of Engineers and Architects (AAAEA)-UWM Chapter president, since 2018.
- AEE–UWM Chapter vice president, since 2017.
- AIAA–UWM Chapter treasurer, since 2017.
- The Jordan Engineers Association (JEA) as a Mechanical Engineer, since 2012.

Other

- **Google Scholar:** https://scholar.google.com/citations?user=haWeOgsAAAAJ&hl=en
- **LinkedIn:** https://www.linkedin.com/in/mohammad-qandil/